UNIVERSITY OF CALIFORNIA,
IRVINE

Precision Black Hole Mass Measurements in Luminous Early-Type Galaxies

DISSERTATION

submitted in partial satisfaction of the requirements
for the degree of

DOCTOR OF PHILOSOPHY

in Physics

by

Benjamin David Boizelle

Dissertation Committee:
Professor Aaron Barth, Chair
Professor David Buote
Associate Professor Michael Cooper

2018

DEDICATION

"I will love the light for it shows me the way, yet I will endure the darkness because it shows me the stars."
– Og Mandino, *The Greatest Salesman in the World*

To Valerie, my light in the darkness

TABLE OF CONTENTS

LIST OF FIGURES

LIST OF TABLES

ACKNOWLEDGMENTS

Financial support for this research was provided by the NSF through grant AST-1614212 and through the National Radio Astronomy Observatory award GSSP SOSPA3-013 SOS. The National Radio Astronomy Observatory is a facility of the National Science Foundation operated under cooperative agreement by Associated Universities, Inc. Travel support for one of one my research trips was provided by AGS Travel Grants.

The initial data for this project was obtained from the W. M. Keck Observatory, which is operated as a scientific partnership among the California Institute of Technology, the University of California and the National Aeronautics and Space Administration. The Observatory was made possible by the generous financial support of the W. M. Keck Foundation. This author recognizes and acknowledges the very significant cultural role and reverence that the summit of Maunakea has always had within the indigenous Hawaiian community. We are most fortunate to have the opportunity to conduct observations from this mountain. New observations made with the NASA/ESA *Hubble Space Telescope* under programs GO-13662 and GO-14920, obtained from the data archive at the Space Telescope Science Institute. STScI is operated by the Association of Universities for Research in Astronomy, Inc. under NASA contract NAS 5-26555. Additional archival observations used in this thesis were obtained from the Hubble Legacy Archive (HLA) under GO programs 5910, 5999, 6094, 9427, & 10911. The HLA is a collaboration between STScI, the Space Telescope European Coordinating Facility (ST-ECF/ESA) and the Canadian Astronomy Data Centre (CADC/NRC/CSA). Lastly, we make use ALMA imaging contained in data sets ADS/JAO.ALMA#2013.1.00229.S, 2013.1.00828.S, 2015.1.00878.S, 2016.1.00854.S, 2016.1.01010.S, and 2017.1.00301.S. ALMA is a partnership of ESO (representing its member states), NSF (USA) and NINS (Japan), together with NRC (Canada), MOST and ASIAA (Taiwan), and KASI (Republic of Korea), in cooperation with the Republic of Chile. The Joint ALMA Observatory is operated by ESO, AUI/NRAO and NAOJ. We acknowledge usage of the NASA/IPAC Extragalactic Database (NED), which is operated by the Jet Propulsion Labratory, California Institute of Technology, under contract with the NASA, as well as of the HyperLeda database.

Some of the text of this dissertation is a reprint of the material as appears in the Astrophysical Journal. Permission to use copyrighted material has been granted by the Astrophysical Journal.

I express greatest appreciation to my advisor Aaron J. Barth for his continued guidance and patience. I also would like to thank David Buote, Michael Cooper, and Jonelle Walsh for their scientific and personal insights, and group members and colleagues for years of friendship and support, including Liuyi Pei, Dan Carson, Daeseong Park, Vivian U, Diego Gonzalez, Dale Mudd, Thomas Schmidt, Dilan Patel, Timothy Carleton, and Andrew Grauss.

I am grateful to my parents and siblings for encouraging my scientific endeavors, in spite of some (minor) damage to hearth and home, and continued encouragement from family as I matured as a researcher. Most of all, I am grateful to my wife who has walked with me and buoyed my spirits.

CURRICULUM VITAE

Benjamin David Boizelle

RESEARCH INTERESTS

Supermassive black holes; Submillimeter/radio astronomy; Active and quiescent galaxy nuclei; Reverberation mapping; Kinematics and properties of circumnuclear gas disks; Low-luminosity active galactic nuclei; Optical and infrared integral-field spectroscopy

EDUCATION

Doctor of Philosophy in Physics & Astronomy **2018**
University of California, Irvine *Irvine, CA*

Master of Science in Physics **2014**
University of California, Irvine *Irvine, CA*

Bachelor of Science in Physics & Astronomy **2012**
Brigham Young University *Provo, UT*

RESEARCH EXPERIENCE

Graduate Research Assistant **2013–2018**
University of California, Irvine *Irvine, California*

Undergraduate Researcher **2010–2012**
Brigham Young university *Provo, UT*

TEACHING EXPERIENCE

Adjunct Faculty **2015–2017**
Santa Ana College *Santa Ana College, CA*

Graduate Teaching Assistant **2012–2014**
University of California, Irvine *Irvine, CA*

Undergraduate Teaching Assistant **2010–2012**
Brigham Young University *Provo, UT*

FIRST AUTHOR REFEREED JOURNAL PUBLICATIONS

ALMA Observations of Circumnuclear Disks in Early Type Galaxies: 12CO(2-1) and Continuum Properties **2017**
The Astrophysical Journal

FIRST AUTHOR PAPERS IN PREPARATION

Measuring the Supermassive Black Hole Mass in NGC 1275: Dynamical Modeling of Ionized and Warm Molecular Gas Observed with *HST* STIS and Keck Adaptive Optics **2018**

High Precision Black Hole Mass Measurement in NGC 3258 from ALMA Observations at 0.09 Arcsecond Resolution **2018**

OTHER REFEREED JOURNAL PUBLICATIONS

Measurement of the Black Hole Mass in NGC 1332 from ALMA Observations at 0.044 Arcsecond Resolution **2016**
The Astrophysical Journal Letters

Towards Precision Black Hole Masses with ALMA: NGC 1332 as a Case Study in Molecular Disk Dynamics **2017**
The Astrophysical Journal

ABSTRACT OF THE DISSERTATION

Precision Black Hole Mass Measurements in Luminous Early-Type Galaxies

By

Benjamin David Boizelle

Doctor of Philosophy in Physics

University of California, Irvine, 2018

Professor Aaron Barth, Chair

The supermassive black hole (BH) census remains very incomplete at the highest masses ($\gtrsim 10^9\ M_\odot$), limiting our understanding of BH/host galaxy co-evolution for the most massive galaxies. I present analysis of circumnuclear ionized atomic and both warm and cold molecular gas kinematics, as well as results of detailed gas-dynamical modeling, for a sample of nearby, luminous early-type galaxies (ETGs). Keck OSIRIS integral-field unit and *Hubble Space Telescope* (*HST*) STIS spectroscopy reveal H_2 1−0 S(1) and Hα in approximately Keplerian rotation within NGC 1275. We build and optimize models of dynamically-warm disk rotation to better constrain its BH mass $M_{\rm BH} = (1.20^{+0.32}_{-0.44}) \times 10^9\ M_\odot$, although significant turbulent velocity dispersion complicates model fitting.

Dynamically cold molecular gas emission is free from nearly all of the systemics that plague $M_{\rm BH}$ determination when using dynamically warm tracers. I present Atacama Large Millimeter/submillimeter Array (ALMA) $\sim 0\farcs3$−resolution CO(2−1) and continuum imaging of a sample of early-type galaxies (ETGs) that host circumnuclear dusty disks. Given their incredible data sensitivities, these dynamically cold disks yield the most sensitive possible tracers of the central gravitational potential. In several targets we detect central velocity upturns that suggest unresolved Keplerian rotation. We find these disks are formally stabilized against fragmentation and gravitational collapse. The continuum emission is in all cases

dominated by a central, unresolved source and appears to be consistent with hot accretion.

I present follow-up, $0\farcs1-$resolution CO(2−1) imaging of one of these promising ETGs – NGC 3258 – to highly resolve its BH sphere of influence and map out the molecular kinematics in exquisite detail. Its very regular, nearly symmetric rotation enables the most detailed thin disk modeling to date. Moderate kinematic twists are incorporated using tilted-ring formalism, and the extended mass profile is amended to allow for a variable stellar mass density profile. Preliminary model optimization returns $M_{\rm BH} = 2.23 \times 10^9\ M_\odot$ with an anticipated total uncertainty of around 5%.

Chapter 1

Introduction

Over the past two decades, increasingly sensitive kinematic studies of galactic nuclei have established that supermassive black holes (BHs; ranging in mass between $\sim 10^6$ and 10^{10} $M_\odot$) are an integral part of the centers of likely every large galaxy (Magorrian et al. 1998; Kormendy & Ho 2013). While contributing negligibly to the overall gravitational potentials of nearby galaxies, supermassive BH masses ($M_{\rm BH}$) are found to correlate strongly with several larger-scale host galaxy properties, especially their stellar velocity dispersion ($\sigma_\star$; Gebhardt et al. 2000; Ferrarese & Merritt 2000) and bulge luminosity (L; Kormendy & Richstone 1995). These local relationships encapsulate a fossil record of black hole/galaxy growth through accretion and merger events, demonstrating co-evolution of the central BH mass and (at least some) host galaxy properties across cosmic time. Due to small intrinsic scatter (~ 0.3 dex), the composite $M_{\rm BH} - \sigma_\star$ and $M_{\rm BH} - L$ local scaling relationships (McConnell & Ma 2013; Kormendy & Ho 2013) are widely employed in predicting BH masses in nearby (and even distant) galaxies across the Hubble sequence.

A better understanding of BH demographics, based on a growing sample of BH masses, reveals more complicated correlations between these central, compact masses and their host

galaxies (e.g., with respect to classical bulges vs. pseudobulges, or scaling with cored vs. coreless ellipticals; Kormendy & Ho 2013). However, this census remains incomplete, especially at the lowest ($\sim 10^6\ M_\odot$) and highest ($\gtrsim 10^9\ M_\odot$) BH masses. Predicted $M_{\rm BH}$ values using large (measured) $\sigma_\star$ are in tension with those derived from the bulge L. This discrepancy reaches an order of magnitude at $10^{10}\ M_\odot$ (Lauer et al. 2007a) due to a precipitous rise in BH mass at $\sigma_\star \gtrsim 270$ km s^{-1} (van den Bosch et al. 2015).

This region of parameter space includes the most massive early-type galaxies (ETGs; encompassing elliptical and S0 galaxies), including brightest cluster galaxies (BCGs) and compact elliptical galaxies (CEGs). BH and galaxy growth for BCGs occurs in the most extreme merger and accretion environments. The few rich-cluster BCGs with accurate BH mass measurements suggest a steeper $M_{\rm BH} - \sigma_\star$ relationship than for typical elliptical galaxies (McConnell et al. 2012), leading to discussion over which relationship is more fundamental (e.g., see Lauer et al. 2007b; Shankar et al. 2016). CEGs, on the other hand, are thought to be local analogs of $z \sim 2$ "red nuggets" (van Dokkum et al. 2010; Yıldırım et al. 2017). These suspected relics appear to have gained the bulk of their stellar mass in the early universe but experienced primarily passive evolution for the past ~ 10 Gyr. The few with confident BH mass measurements (Walsh et al. 2015, 2016, 2017) are offset from canonical $M_{\rm BH} - \sigma_\star$ and $M_{\rm BH} - L$ relationships, suggesting a different evolutionary path for BH and stellar bulge growth. Ongoing programs studying the stellar properties and kinematics of the most massive galaxies (Ma et al. 2014) and relic CEGs (Yıldırım et al. 2017) will determine their BH masses and star formation histories, thereby providing better constraints on the space density of the most massive BHs (Lauer et al. 2007b).

Confidently determining $M_{\rm BH}$ requires disentangling its kinematic signature from that of its host galaxy by resolving tracer kinematics within the dynamical sphere of influence

$$r_{\rm g} \approx {\rm G} M_{\rm BH} / \sigma_\star^2 \,. \tag{1.1}$$

Interior to this radius, the BH dominates over the extended stellar gravitational potential and gives rise to an elevated $\sigma_\star$ within the stellar half-light radius $R_{\rm e}$. To date, roughly 100 supermassive BH masses have been determined to varying precision through dynamical means (Kormendy & Ho 2013), typically by modeling resolved stellar (e.g., van den Bosch & de Zeeuw 2010; McConnell et al. 2012; Rusli et al. 2013b) or ionized atomic gas (e.g., van der Marel & van den Bosch 1998a; Barth et al. 2001) kinematics.

Exploring the slope and intrinsic scatter of these relationships requires highly precise $M_{\rm BH}$ determinations spanning a significant range in mass. The most precise probes are "gold standard" cases of megamaser disks (e.g., Miyoshi et al. 1995; Kuo et al. 2011) that are mapped using Very Long Baseline Interferometry (VLBI) imaging. Their resolved H_2O maser emission originates at radii $\ll r_{\rm g}$ and is in nearly perfect Keplerian rotation. Since megamaser disks tend to be found in edge-on, Type 2 active galactic nuclei (AGN) in late-type galaxies (LTGs) with $M_{\rm BH} \sim 10^7\ M_\odot$, these important (but relatively rare) benchmarks alone cannot probe BH-host galaxy scaling relationships. Instead, the vast majority of extragalactic BH mass measurements are made by modeling optical/near-IR (NIR) spectroscopic observations of stellar or ionized atomic gas kinematics that typically only marginally resolve $r_{\rm g}$. Even for luminous ETGs that tend to have $M_{\rm BH} > 10^8\ M_\odot$, $r_{\rm g}$ is usually on the order of a few tens of parsecs (pc); at a distance of 20 Mpc, this scale corresponds to a few tenths of an arcsecond. Even using adaptive optics (AO), obtaining more than a couple of independent resolution elements across $r_{\rm g}$ remains challenging for the current generation of optical/NIR telescopes.

As a result of only marginally resolving $r_{\rm g}$, both stellar and ionized atomic gas dynamical modeling techniques are subject to potentially serious *systematic* uncertainties that may bias the BH mass determination at the factor of ~ 2 level (van den Bosch & de Zeeuw 2010; Walsh et al. 2010), even while the *statistical* uncertainties in $M_{\rm BH}$ may be more than an order of magnitude smaller. In addition to serious difficulties constructing stellar orbital models for an

entire galaxy, stellar dynamical modeling suffers from uncertainties involving the treatment of the dark matter halo (Gebhardt & Thomas 2009), triaxial orbital structure (van den Bosch & de Zeeuw 2010), and stellar mass-to-light (M/L) ratio gradients (McConnell & Ma 2013). Gas dynamical modeling of circumnuclear disk rotation is appealing for its relative conceptual and computational simplicity, with the added benefit of being nearly insensitive to contributions from an extended dark matter halo or to gradients in the stellar M/L ratio. Indeed, the initial glut of galaxy nuclei kinematic studies (e.g., Ferrarese et al. 1996; Bower et al. 1998) with the *Hubble Space Telescope* (*HST*) primarily focused on obtaining individual or long-slit spectra to detect disk-like gas rotation across galaxy nuclei. However, ionized atomic gas rotation is frequently afflicted by non-circular contributions, as well as large turbulent velocity dispersions, suggesting disk pressure support that (likely) must be incorporated during kinematic modeling. Various approximations (e.g., asymmetric drift; Barth et al. 2001) better reproduce the observed rotation pattern at the cost of modeling simplicity. As a further complication, gas emission (especially cold molecular emission) is often accompanied by coincident, optically-thick dust; circumnuclear dust obscures the central stellar light, leading to an additional (and underappreciated) systematic uncertainty in both the inner stellar luminosity slope and best-fit BH mass (see §3.5).

In the few cases where stellar and ionized gas-dynamical modeling can be applied to the same galaxy, the independently-measured $M_{\rm BH}$ values frequently disagree and factor of $2-4$ discrepancies are common (Kormendy & Ho 2013). Such discrepancies cast significant doubt on the accuracy of these predominant methods to determine $M_{\rm BH}$ values, especially for the most massive BHs (e.g., see de Francesco et al. 2006; Walsh et al. 2010). Additional BH measurement avenues that are free from the potentially serious systematics are crucial to cross-check previously used techniques, enabling investigation of the validity of various modeling assumptions in – and accuracy of – stellar and ionized gas $M_{\rm BH}$ determinations (see esp. the case of NGC 1332; Rusli et al. 2011; Barth et al. 2016a).

Recent CO surveys (Combes et al. 2007; Young et al. 2011; Alatalo et al. 2013) reveal that roughly 10% of all nearby ETGs have significant central cold molecular gas with disk-like morphologies and regular gas rotation. Interferometric observations confirm this molecular gas possesses low turbulent velocity dispersion (Alatalo et al. 2013). Dynamically cold molecular disks are very appealing targets for high angular resolution CO imaging as kinematic observations that probe well within $r_{\rm g}$ avoid *all* of the primary systematics plaguing ionized gas and stellar kinematic modeling. The previous generation of interferometers could resolve $r_{\rm g}$ for a few select targets; even with the prohibitive integration times to detect resolved ($\sim 0\farcs25$) CO emission, Davis et al. (2013) observe rapid central molecular gas rotation to measure the first BH mass using CO kinematics. The Atacama Large Millimeter/submillimeter Array (ALMA) now allows CO imaging at increased sensitivity and significantly higher angular resolution, promising a new avenue for precision BH mass measurement in ETGs and a revolution in our understanding of the high-mass end of the BH mass-host galaxy scaling relationships. Already, ALMA observations have provided the most sensitive possible probes of the central ∼kpc of luminous ETGs and a few precision $M_{\rm BH}$ determinations (Barth et al. 2016a,b; Boizelle et al. 2017; Onishi et al. 2017; Davis et al. 2017, 2018).

In this thesis, I present data that probe the rotational properties of ionized atomic and both warm and cold molecular gas disks at high angular resolution in a large sample of nearby ETGs. Gas properties are studied in detail, and their disk-like kinematics are modeled with a variety of thin disk techniques to determine BH masses and host galaxy properties. This research yields: 1) one of the few comparisons between resolved ionized atomic and warm molecular gas rotational properties within $r_{\rm g}$ and a significant improvement in the confidence of the BH measurement for an important BCG; 2) CO observations of a sample of over twenty dust-disk ETGs, showing dynamically cold rotation that produces the most detailed central ETG mass profiles; 3) identification of rapid central CO emission in at least seven galaxies that suggests marginal resolution of the BH sphere of influence and are prime candidates for

higher-resolution imaging; and 4) the most precise BH mass measurement for a luminous ETG to date. The remainder of the document is organized as follows. Chapter 2 describes the ionized and warm molecular gas kinematics and dynamical modeling of BCG NGC 1275, enabled by *HST* STIS long-slit and Keck OSIRIS integral-field unit (IFU) spectroscopy and ancillary *HST* broadband imaging. Chapter 3 describes cold molecular gas properties and kinematics of a sample of twenty luminous ETGs and three CEGs imaged in the CO(2−1) transition using ALMA. Chapter 4 describes high-resolution ALMA imaging and detailed gas-dynamical modeling of luminous ETG NGC 3258. In Chapter 5 we summarize the main results and discuss prospects for future precision BH mass measurements. The Appendix describes a program to conduct a census of cold molecular gas properties in nearby galaxies and create a kinematic atlas using pipeline data from the ALMA archive.

Chapter 2

Nuclear Gas Kinematics of BCG NGC 1275

The giant cD elliptical NGC 1275 remains one of the most peculiar objects amongst nearby galaxies. Early spectral observations discovered two sets of emission lines, with the high-velocity lines originating from a foreground, infalling spiral galaxy which is spatially co-incident with the center of the BCG (Minkowski 1968; Boroson 1990). Ongoing study of NGC 1275 revealed an active galactic nucleus (AGN) with a Seyfert 1.5 spectrum (Ho et al. 1997a); a subluminal radio jet with evidence for a sub-parsec absorbing disk (Walker et al. 1994; Asada et al. 2006; Fujita et al. 2016), and a very extended, double-lobed Fanaroff-Riley I radio source (3C 84; Chiaberge et al. 1999). The integrated IR light is sufficient to classify it as a luminous IR galaxy (LIRG; Sanders et al. 2003). Strong emission lines are observed at optical (especially Hα; Lynds 1970; Conselice et al. 2001), near-IR (the rovibrational line H_2 1$-$0 S(1); Elston & Maloney 1994; Lim et al. 2012), and millimeter wavelengths (CO; Mirabel et al. 1989; Salomé et al. 2006); the resultant emission-line nebulae are filamentary and very extended ($\sim$ 150 kpc wide). The H_2 1$-$0 S(1)/Hα flux ratio is fairly consistent over the large-scale optical/NIR nebula, and at a value more indicative of a low-ionization

nuclear emission-line region (LINER) than an extended HII region (Heckman et al. 1987; Lim et al. 2012). Emission-line velocity maps suggest that the gas is dynamically supported by rotation about the nucleus on both large ($\sim$ 1.2 kpc; Inoue et al. 1996) and small ($\sim$ 50 pc; Wilman et al. 2005) scales. In addition, filaments and bubbles indicate X-ray cooling flows and past radio jet activity, respectively, which makes Perseus the brightest X-ray cluster in the sky (Fabian et al. 2006). Using 21$-$cm H I absorption line observations, Jaffe (1990) find a large reservoir of $\sim 10^{10}$ $M_{\odot}$ associated with NGC 1275 and in front of the central active nucleus.

As the BCG of the Perseus cluster and one of the nearest (moderately) rich clusters (Abell 426; Abell et al. 1989), $M_{\rm BH}$ determination for NGC 1275 is an important case study for the growth of the central BH in an extreme merger and accretion environment. Noted in the previous chapter, obtaining a BH mass measurement requires spatially resolving tracer kinematics within its sphere of influence $r_{\rm g}$. The kinematics of tracer particles within this physical radius are dominated by the gravitational potential well of the BH. A measured $\sigma_{\star} = 246 \pm 18$ km s^{-1} within the effective radius ($R_{\rm e}$; Smith et al. 1990) and the standard $M_{\rm BH} - \sigma_{\star}$ relationship suggest that $r_{\rm g}$ for NGC 1275 is about 55 pc. At the redshift of NGC 1275 ($z = 0.01796$), including corrections for Local Group infall onto Virgo, the Great Attractor, and the Shapley supercluster (Mould et al. 2000), the BCG lies at a luminosity distance of 76.2 Mpc with a spatial scale of 360 pc arcsec^{-1} (Wright 2006). Its projected $r_{\rm g}$ is therefore expected to be $\sim 0\farcs15$. Given the angular resolution of current optical/NIR spectroscopy, dynamical modeling of this galaxy's central kinematics will require determination of an extended stellar mass profile.

Past studies (Jaffe et al. 2001; Wilman et al. 2002; Scharwächter et al. 2013) have determined that, on both broad ($\sim$ 3 kpc) and nuclear ($\sim$ 100 pc) scales, the H_2 1$-$0 S(1) line in NGC 1275 is most likely collisionally excited with excitation temperature between 1000 and 2000 K. In H_2 1$-$0 S(1) emission line data taken with the UIST integral field unit (IFU) on UKIRT,

Wilman et al. (2005) found evidence for nuclear molecular gas rotation arising from a disk with radius on the order of 50 pc. Assuming purely circular rotation, they estimated $M_{\rm BH}$ to be 3.4×10^8 $M_\odot$ (± 0.18 dex) by measuring the velocity jump of the H_2 line in a single slit across the nucleus; the molecular gas disk disk inclination of 45° was assumed to correspond with the parsec scale radio-jet inclination (see Walker et al. 1994). Their moderate spatial resolution ($\sim$ 0.″4, or roughly a projected 150 pc, full-width at half-maximum; FWHM) observations will suffer from significant point-spread function (PSF) blurring that entangles the spectral features of high-velocity gas near the BH with that of lower velocity gas (in this case far beyond $r_{\rm g}$), resulting only in a lower-bound mass estimate for $M_{\rm BH}$.

Scharwächter et al. (2013) obtained the first high spatial resolution NIR (H and $K-$band) spectroscopy of this galaxy nucleus using the NIFS integral field unit (IFU) at Gemini-North with adaptive optics (AO; for a PSF FWHM of $\sim$ 0.″1). They found roughly Keplerian (albeit largely unresolved) rotational velocity extrema, primarily using the H_2 1−0 S(1) tracer and, to a lesser extent, the [Fe II] λ1644 nm line. Treating the former molecular emission as a thin, rotating disk with a fixed inclination angle range of $(45 \pm 10)^\circ$, more extensive gas-dynamical modeling led them to conclude that $M_{\rm BH} = (8^{+7}_{-2}) \times 10^8$ $M_\odot$. The nuclear molecular gas mass contributions to the combined gravitational potential remain highly uncertain, and they suggest their $M_{\rm BH}$ measurement may only be an upper bound on the intrinsic value. When coupled with the stellar velocity dispersion $\sigma_\star$, this BH mass range agrees with the established $M_{\rm BH} - \sigma_\star$ relation within its 0.3 dex intrinsic scatter (Kormendy & Ho 2013).

Prior to the publication of the Gemini NIFS data, we obtained Keck OSIRIS IFU Kn3−band spectroscopy of the NGC 1275 nucleus spatially resolve the H_2 1−0 S(1) velocity field. As the Keck telescope (with AO) has greater spatial resolution than any previous optical/NIR study of the NGC 1275 nucleus, kinematically modeling these data should provide more confident constraints on the central BH mass. We also obtained new *HST* Space Telescope Imaging Spectrograph (STIS) narrow-slit optical spectroscopy to probe the ionized atomic component

of this disk, as well as *HST* Wide-Field Camera 3 (WFC3) NIR imaging from which to build a more accurate stellar mass profile. In this chapter, we describe both these new observations (the *HST* WFC3 imaging in §2.1, the STIS spectroscopy §2.2, and this OSIRIS IFU data in §2.3) and detailed gas-dynamical modeling results using thin disk (§2.5.1) and Jeans equation (§2.5.2) formalism.

2.1 WFC3 Data

2.1.1 Observations

Previous *HST* imaging programs observed NGC 1275 in both optical (e.g., Holtzman et al. 1992, Martel et al. 1999, Johnstone et al. 2012, Canning et al. 2014) and NIR filters (Donahue et al. 2000). These programs typically investigated faint filamentary features or star clusters, and the necessary, long exposure times caused detector saturation of the active nucleus in all but the MULTIACCUM NICMOS NIR observations. Using these previous NICMOS NIC2 observations that cover the nuclear regions (the central $20'' \times 20''$), Wilman et al. (2005) find that the stellar luminosity (at radii beyond $0\farcs5$) approximately follows a modified Hubble Law profile that implies a stellar mass ($M_\star$) of 2.6×10^7 $M_\odot$ within 100 pc of the BH. This profile's negligibly small stellar mass led both Wilman et al. (2005) and Scharwächter et al. (2013) to ignore stellar contributions when modeling the molecular gas kinematics.

To better constrain the stellar luminosity profile, espeically in the central few tens of pc, we obtained a series of *HST* WFC3 F160W IR channel images on 22 February 2015 in a single orbit as a part of program GO-13662. These new data consist of four primary pointings, each with a set of two 200 s dithered exposures in the STEP100 sequence (NSAMP=9). The primary pointings were dithered in a square pattern that keeps the nucleus in one of the corners, obtaining a total field-of-view (FOV) of $3\farcm45 \times 3\farcm80$. To ensure unsaturated

observations of the active nucleus, we also obtained 16 dithered RAPID (1.7 s each) sub-array images (IRSUB128-FIX, NSAMP=16), dithered in a four-point pattern to sample the PSF in fractional pixel steps. The data were processed through the CALWF3 reduction pipeline, and the sub-array and full images were distortion corrected and combined separately to a uniform ($0\farcs065$ pixel^{-1}) scale and coordinate origin using the DrizzlePac package Astrodrizzle (Gonzaga et al. 2012). Background subtraction was not performed during this process as the BCG halo extends beyond the mosaic spatial scales. The inner $2''$ of the drizzled sub-array image, where S/N is high, was seamlessly overlain onto the drizzled full-frame image. The combined RAPID imaging has a PSF FWHM of $0\farcs18$ and the final mosaic (shown in Figure 2.1) achieves spatial resolution of $\sim 0\farcs2 - 0\farcs22$ at radii beyond $2''$.

We estimated the WFC3 F160W sky background around NGC 1275 based on the larger-scale optical and NIR observations of Schombert (1986) and Prestwich et al. (1997), respectively. These authors show that the BCG stellar luminosity profile falls off as a power-law from $10''$ to $100''$. We therefore model the F160W stellar surface-brightness between these radii as a power-law profile with a constant pedestal level to measure a sky background of 31.6 e$^-$ s^{-1} arcsec^{-2}. This sky value agrees (but is slightly lower by $\sim 15\%$) with the empirical NIR background light models (Buffington et al. 2009; Pirzkal 2014) for the same ecliptic latitude and solar angle.

2.1.2 Stellar Mass Profile

After determining the sky background, we fit the background-subtracted mosaic using the galaxy image-fitting program GALFIT (Peng et al. 2002) at radii $R > 0\farcs8$ from the nucleus. Foreground stars, galaxies, and star clusters, along with the visible dust lanes, were identified and masked using an *HST* F814W-F160W color map, with the archival WFPC2 F814W observations obtained under program GO-11207. The best fit from amongst the GALFIT

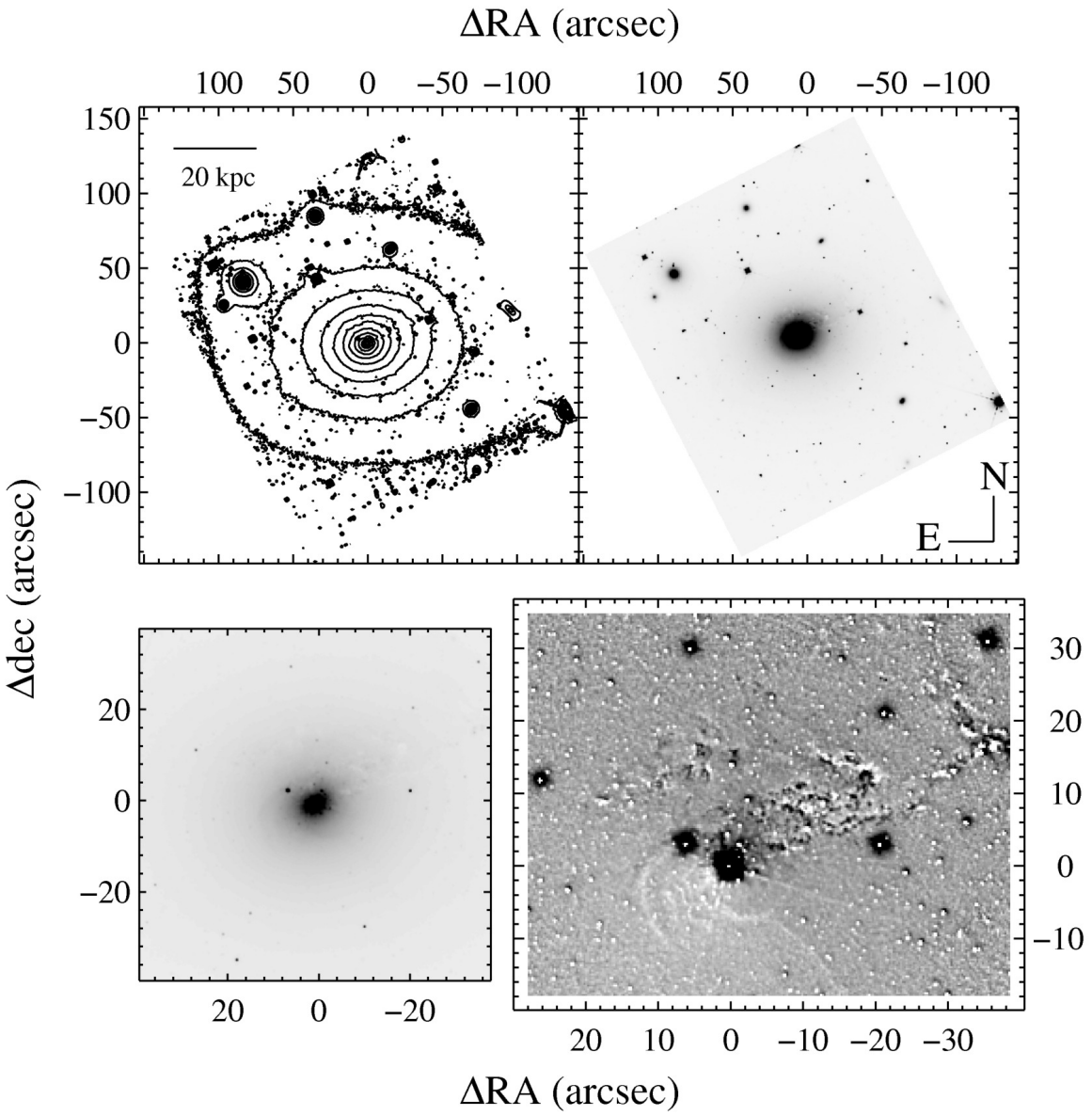

Figure 2.1 NGC 1275 *HST* WFC3 F160W mosaic, shown (*top left*) in contours with logarithmic but arbitrarily spaced intervals, and (*top right*) using an inverted color map. *Bottom Left*: Close-up of the nucleus, showing the strong point-like AGN. *Bottom Right*: Off-center structure map (Pogge & Martini 2002) of the nucleus. Foreground galaxy dust lanes to the north appear as dark filaments, and bright, adjacent areas indicate star forming regions. Faint dots are likely star clusters within the BCG (Brodie et al. 1998), and the bright ripples to the south and east are stellar shells from past mergers (Conselice et al. 2001; Penny et al. 2012). The OSIRIS AO guide star and PSF star is the foreground star approximately 8″ northeast of the nucleus.

functions is a 2D Nuker profile (Lauer et al. 1995) with inner and outer power-law slopes $\gamma = 0.89$ and $\beta = 1.34$, respectively, connected by a transition region with $\alpha = 6.0$ and break radius $R_{\rm b} = 8\farcs4$. We assumed the observed $H-$band mosaic is reddened by a Galactic $E(B-V) = 0.144$ excess from Schlafly & Finkbeiner (2011) in the NASA/IPAC Extragalatic Database (NED). In addition, Mittal et al. (2015) determine a median internal reddening $E(B-V) = 0.14$ for this BCG based on stellar population modeling of the far-UV to far-IR spectral energy distribution of its inner $75''$ ($\sim$ 30 kpc). Treating these Galactic and internal reddening effects as screen and mixed attenuation (see Equation 4.1; also, using the extinction transformations of Rieke & Lebofsky 1985), respectively, we estimated an effective (screen) total extinction $A_H = 0.12$ and $A_K = 0.07$ for NGC 1275. When corrected for this obscuration, the 2D Nuker model contains an integrated $H-$band luminosity of $\sim 10^{11.8}\ L_\odot$ over the full mosaic area.

Modeling the molecular gas kinematics using one Jeans equation technique (described in §2.5.2) requires the stellar luminosity profile to be described as a function of Gaussian components. We therefore applied the Multi-Gaussian Expansion (MGE) formalism (Cappellari 2002) to characterize the F160W mosaic (masked as for the GALFIT modeling). The sum of all constituent Gaussians, when convolved with the telescope PSF MGE, seeks to match the observed surface brightness. The intrinsic 2D profile is given by

$$\Sigma(x', y') = \sum_{j=1}^{N} \frac{L_j}{2\pi\sigma_j'^2 q_j'} \exp\left[-\frac{1}{2\sigma_j'^2}\left(x'^2 + \frac{y'^2}{q_j'^2}\right)\right], \tag{2.1}$$

for all N components with integrated luminosities L_j, dispersions σ_j', and axis ratios q_j'. Primes indicate projected parameters and, when assuming oblate axisymmetry, the stellar MGE parameters are deprojected into $\sigma_j = \sigma_j'$ and $q_j^2 = (q_j'^2 - \cos^2 i)/\sin^2 i$ where i is the assumed galaxy inclination angle (Cappellari 2002; we use $i = 40°$, see §2.5.2). For oblate

axisymmetry, then, the intrinsic stellar mass density along the galaxy's midplane is:

$$\rho(r) = \sum_{j=1}^{N} \frac{\Upsilon_H L_j}{(\sqrt{2\pi}\sigma_j)^3 q_j} \exp\left[-\frac{r^2}{2\sigma_j^2}\right] , \tag{2.2}$$

where Υ_H is the $H-$band stellar mass-to-light ratio. Finally, the circular velocity in the equatorial (disk) plane is (Binney & Tremaine 2008; Cappellari 2002):

$$v_c^2(R) = \sqrt{\frac{2}{\pi}} G \sum_{j=1}^{N} \Upsilon_H L_j \int_0^R \mathrm{d}r \frac{r^2 \exp\left[-\frac{r^2}{2\sigma_j^2}\right]}{\sqrt{R^2 - (1-q_j^2)r^2}} . \tag{2.3}$$

We modeled the *HST* F160W PSF with the Tiny Tim tool (Krist & Hook 2004), generating the model telescope response with a spectral slope ($F_\lambda \propto \lambda^\beta$ with $\beta = -0.65$) that matches nuclear ($0\farcs75$ radius aperture) $0.8 - 2.4$ μm continuum measurements from long-slit spectroscopy (Riffel et al. 2006). To simulate the mosaicing process, copies of this model PSF were dithered and drizzled together in the same manner as the RAPID sub-array images. For use in stellar MGE and later gas dynamical modeling, this composite PSF was decomposed using an MGE sum of ten positive, concentric, circular Gaussians.

The F160W mosaic MGE decomposition (shown along the semi-major axis in Figure 2.2) consists of ten coaxial elliptical Gaussians (see Table 2.1). We estimate the $H-$band mass-to-light ratio Υ_H from stellar population modeling Mittal et al. (2015) that finds up to a quarter of the total stellar mass in NGC 1275 comes from a young population with ages of up to a few hundred Myr. The dominant, old (~ 10 Gyr) stellar population tends towards solar to supersolar metallicity ($Z \approx 0.02-0.05$), and such an old synthetic stellar population (with $B-V \approx 1$; Bruzual & Charlot 2003) are anticipated to have $\Upsilon_H \sim 1$ in solar units (Zibetti et al. 2009). A synthetic population representing the young component (with $B-V \approx 0.2$) is expected to have an order of magnitude smaller Υ_H. These factors combine to give a likely $H-$band mass-to-light ratio of ~ 0.75 $M_\odot/L_\odot$.

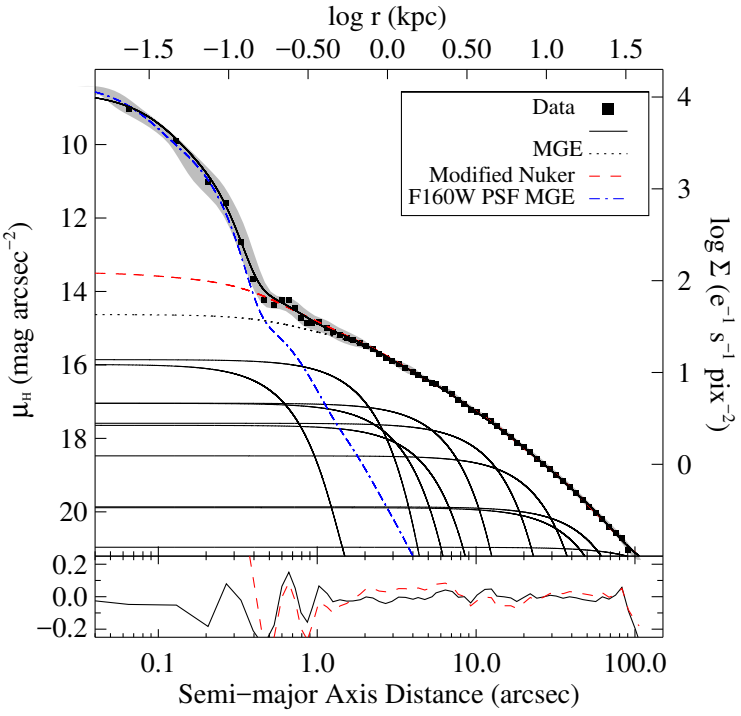

Figure 2.2 Surface brightness profile of the NGC 1275 *HST* F160W mosaic, including the data uncertainties (*shaded region*). Also shown are the composite MGE profiles using the total ($j = 1-10$; *solid*) and lower-bound ($j = 2-10$, assuming the $j = 1$ term is non-stellar; *dotted*) decompositions. The best-fitting Nuker (*dashed*) profile is modified to have a modest ($\gamma = 0.1$) power-law slope for $R \lesssim 0\farcs5$. The scaled Tiny Tim F160W PSF MGE (*dash-dot*) is equivalent to the $j = 1$ galaxy MGE term.

Table 2.1 NGC 1275 $H-$band MGE Parameters

j	log $I_{H,j}$ ($L_\odot$ pc^{-2})	σ'_j (arcsec)	q'_j	log $I_{H,j}$ ($L_\odot$ pc^{-2})	σ'_j (arcsec)	q'_j
	WFC3 F160W MGE			Modified Nuker MGE		
1	7.501	0.037	0.819	4.187	0.243	0.864
2	3.645	0.422	0.960	4.089	0.508	0.863
3	3.636	1.363	0.677	3.761	1.166	0.865
4	3.129	1.968	0.946	3.401	2.619	0.864
5	3.163	3.765	1.000	3.200	6.043	0.865
6	2.868	3.768	0.441	2.776	12.91	0.863
7	3.003	7.957	0.850	2.333	27.62	0.869
8	2.662	15.61	0.850	1.912	61.76	0.851
9	2.314	34.65	0.800	1.569	178.8	0.913
10	1.840	162.5	0.751	–	–	–

Note: Intrinsic NGC 1275 MGE component parameters after decomposing the WFC3 F160W mosaic (*left*) and after modifying the 2D GALFIT Nuker profile fit to have a more modest ($\gamma 0.1$) nuclear power-law slope for radii $R < 0\farcs5$. In the initial MGE, the bright $j = 1$ component models an almost entirely nonstellar, essentially unresolved nucleus. The modified Nuker MGE fit (*right*) is constrained such that $\min(q'_j) \gtrsim 0.85$ for use in JAM modeling (see §2.5.2). Primes indicate projected parameters.

The Seyfert nucleus clearly dominates the central $H-$band surface brightness and is well described by the essentially unresolved, first ($\sigma' \sim 0.5$ pixel) MGE component (Table 2.1). If completely stellar, its integrated light would result in an unreasonably high $\sim 10^{10.4}$ $M_\odot$ within the central 10 pc. What percentage of the $j = 1$ component may be stellar is unknown, and the bright AGN prevents unambiguous *photometric* determination of the stellar luminosity profile for $R \lesssim 0\farcs8$. Krabbe et al. (2000) decompose the nuclear H and $K-$band spectra (integrated within a $1''-$radius aperture) into roughly equal AGN power-law ($F_\lambda \propto \lambda^{-1}$) and hot dust ($T_\mathrm{d} \sim 700$ K) components, but find no appreciable stellar contributions. Riffel et al. (2006) report only weak evidence of the 2.3 μm stellar CO bandheads when the spectra are integrated over the same radius. Many quiescent BCGs show large (~ 300 pc) central core profiles (Lauer et al. 2007a; Rusli et al. 2013a), presumably formed by scouring from a binary BH. The extended, $j = 2-10$ MGE profile is essentially flat within the central arcsecond and serves as a lower-bound approximation to the nuclear stellar luminosity profile. Assuming $\Upsilon_H = 0.75$, this model has a stellar mass of $M_\star \sim 6.4 \times 10^7$ $M_\odot$

contained within a physical radius of 100 pc, higher but roughly consistent with previous NIR estimates (Wilman et al. 2005).

If even a few percent of the $j = 1$ MGE component is stellar in origin, that fraction of light corresponds to a few times 10^8 $M_\odot$ within 50 pc. Given this mass is commensurate with the estimated $M_{\rm BH}$ value, we cannot neglect the possibility that a dense nuclear stellar environment buried under the active nucleus may significantly affect gas disk kinematics. We therefore create a second model stellar luminosity profile that ascribes a portion of the central F160W surface brightness profile to a dense stellar core. The nuclear stellar profiles of a sample of 17 nearby (< 100 Mpc), bright ($M_V \leq -22$ mag), quiescent BCGs with high spatial-resolution imaging (Lauer et al. 2007a; Rusli et al. 2013a) have an average inner power-law slope $\gamma \sim 0.1$ with a typical break radius of ~ 300 pc. To mimic this average BCG behavior, we modified the aforementioned 2D Nuker profile within the inner $0\farcs5$ to break to a much more shallow nuclear power-law slope of $\gamma = 0.1$ (shown in Figure 2.2 and decomposed with a MGE in Table 2.1). This modified Nuker profile contains $M_\star = 2.0 \times 10^8$ $M_\odot$ within a physical radius of 100 pc from the BH. In upcoming dynamical modeling described in §2.5, we employ both stellar profiles to explore the impact of a more substantial nuclear stellar contribution on the best-fitting BH mass.

2.2 STIS Data

2.2.1 Observations and Calibrations

We obtained new *HST* STIS observations of NGC 1275 on 30 December 2016 as the final component of program GO-13662. Observations were made using the $52'' \times 0\farcs1$ aperture and the G750M grating, which is centered on 6581 Å. At the redshift of NGC 1275, this covers the Hα spectral region and includes the [O I] $\lambda\lambda$6300, 6364, Hα, [N II] $\lambda\lambda$6548, 6583, and [S II]

$\lambda\lambda$6716, 6731 emission lines. The 2D spectra have a wavelength scale of 0.554 Å pixel^{-1} and a spatial scale of 0.″0507 pixel^{-1}. The STIS slit was placed in five parallel, adjacent positions with the central slit position centered on the nucleus (in the same method employed by Walsh et al. 2013). To avoid charge transfer efficiency losses, the nucleus was placed at the E1 aperture position. The slit was oriented at a position angle of 53°, which is within $\sim 10°$ of the measured molecular kinematic position angle (PA) of this disk (Scharwächter et al. 2013). We obtained between 3 and 4 spectral observations at each slit position, shifted by 0.″15 along the slit, to facilitate better cosmic ray rejection. Total on-source exposure time for each slit position ranged between about 32 and 46 minutes.

The data were reduced using the standard Space Telescope Science Institute (STScI) pipeline, including trimming the overscan region, removing the bias and dark contributions, and applying flat-fielding corrections. After these processing steps, hot pixels and cosmic rays were removed using the LA-COSMIC routine (van Dokkum 2001). Spectra were geometrically rectified after wavelength and flux calibration; due to the bright nucleus, we applied a wavelet interpolation with PSF convolution is applied to suppress strong artifacts when rectifying the central pointing. For each pointing, the calibrated, rectified spectra were spatially aligned and combined to produce a single 2D spectrum at each slit position.

2.2.2 Spectral Decomposition

In each of the five STIS pointings, we extracted spectra in the cross-dispersion direction out to a radius of $\sim 1''$, beyond which the emission line surface brightness falls beneath the noise. Past a distance of about 0.″25 from the nucleus, multiple spectral rows were binned together to achieve higher signal-to-noise (S/N) emission line profiles. We model the full G750M continuum outside of the emission regions as a second-order polynomial near the nucleus and as a straight line beyond $\sim$ 0.″5. Examples of the continuum-subtracted spectra

are shown in Figure 2.3. The Hα and [N II] lines are strongly blended for locations nearest the central continuum, with high-velocity wings indicating broad Hα emission.

We fit each continuum-subtracted spectrum using the Levenberg-Marquardt least-squares minimization routine MPFIT (Markwardt 2009), including Gaussian components for the [O I] $\lambda\lambda$6300, 6361, narrow Hα, [N II] $\lambda\lambda$6548, 6583, and [S II] $\lambda\lambda$6716, 6731 emission lines. The broad Hα and [O I] λ6300 components are modeled using Gauss-Hermite profiles (van der Marel & Franx 1993), with h_3 and h_4 coefficients accounting for anti-symmetric and symmetric deviations, respectively, from a pure Gaussian function. Within the central $\sim 0\farcs5$, the broad and narrow Hα and the [N II], [S II], and [O I] doublet redshifts are free to assume independent values; at larger angular radii, all emission lines share a common velocity during spectral decomposition. The 3:1 [N II] λ6583/λ6548 flux ratio remains fixed, although we relax this condition when computing uncertainties in the profile fit parameters. Due to the strongly blended Hα+[N II] complex, we force the [N II] lines to have identical widths; beyond $\sim 0\farcs35$ from the nucleus, all narrow lines are constrained to have identical widths. In Figure 2.3, we show examples of this spectral decomposition; also, spatial maps of the narrow Hα flux, line-of-sight (LOS) velocity $v_{\rm LOS}$, and dispersion $\sigma_{\rm LOS}$ are included in Figure 2.5 alongside the Keck OSIRIS emission line moment maps.

2.3 OSIRIS Data

2.3.1 Observations and Calibrations

The nucleus of NGC 1275 was observed using the OH-Suppressing Infra-Red Imaging Spectrograph (OSIRIS; Larkin et al. 2010), then mounted on Keck II, during one half night on UT 30 December 2010. Observations were taken in the narrow-band Kn3 filter that is sensitive to the $\lambda\lambda 2121 - 2229$ nm range and has a wavelength sampling of 0.25 nm pixel^{-1}

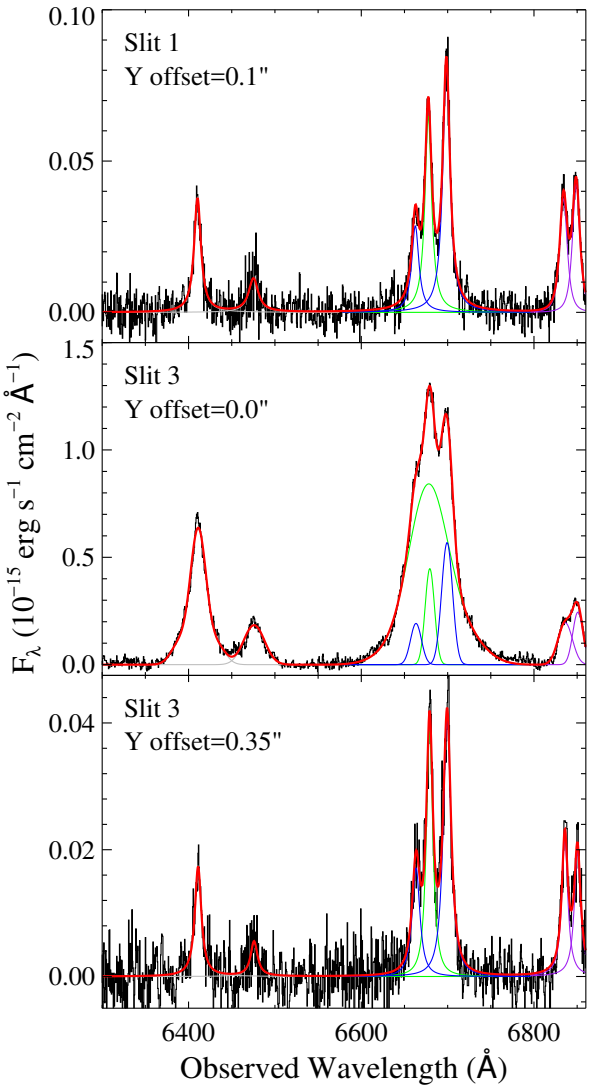

Figure 2.3 Nuclear (slit 3) and off-nuclear (slit 1; see Walsh et al. 2013) continuum-subtracted STIS G750M spectra of NGC 1275. The cross-dispersion distance (Y offset) is indicated. This spectral decomposition simultaneously solves for the underlying continuum emission as well as [O I] $\lambda\lambda$6300, 6364, broad and narrow Hα, [N II] $\lambda\lambda$6548, 6583, and [S II] $\lambda\lambda$6716, 6731 emission line components.

(corresponding to a velocity spacing of $\sim$ 35 km s^{-1}). This filter isolates the redshifted H_2 1$-$0 S(1) emission and also contains the Brγ line; however, due to relatively weak line strength the Brγ line is not as useful as a kinematic tracer. Observations began in the 50 milli-arcsecond (mas) scale, but were changed to the 20 mas scale when the central H_2 surface brightness was determined to be sufficiently high to enable higher-resolution mapping. We obtained 300 s exposures of the nucleus and the off-galaxy sky at a PA of 90° in an object–object–object–sky pattern. In each set, the object frame was dithered by 0.″12 from the first pointing, in the direction perpendicular to the IFU long axis, to remove bad pixels and achieve a larger FOV (1.″4 $\times$ 1.″3 in the 20 mas mode). The total on-source integration time was 90 min in the 20 mas scale. A nearby star (separated by $\sim$ 8″ from the galaxy nucleus; see Figure 2.1) with brightness comparable to the nucleus proved satisfactory as an AO reference star in natural guide-star (NGS) mode. As the 20 mas data cube observes the entire central molecular disk, we focus on describing and modeling these higher spatial resolution IFU observations.

Data were reduced using the OSIRIS data reduction pipeline v2.3, which includes sky-frame subtraction, correcting for crosstalk, cosmic ray cleaning, spectral extraction, and assembling the finished data cube. Spectra were corrected for atmospheric dispersion and telluric absorption (using observations of A0V star HD 21038), placed on a relative flux scale, and wavelength calibrated onto a uniform spectral grid in the heliocentric velocity frame. Since the night was not photometric, we did not apply an absolute flux calibration to the data. The final result is a reduced data cube with one wavelength and two spatial axes (whose spatial pixels are often referred to as spaxels).

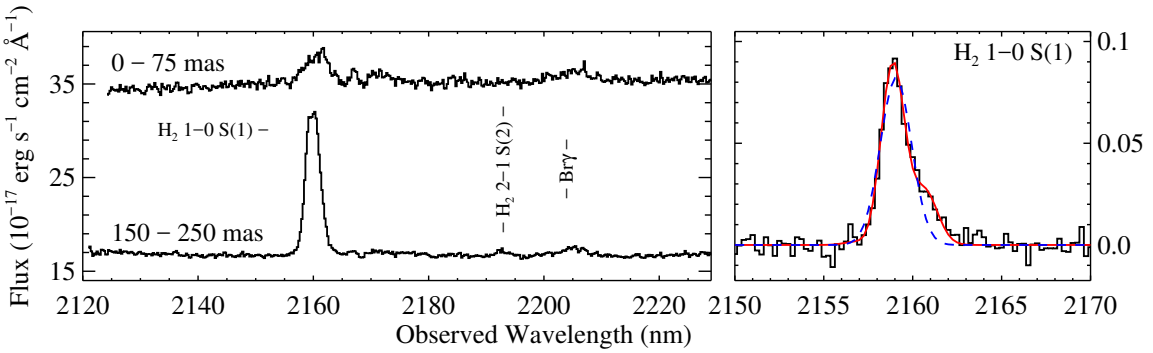

Figure 2.4 *Left*: OSIRIS spectra integrated over a 0.″075 circular radius around the nucleus (*top*) and over a $0.''15 < R < 0.''25$ circular annulus (*bottom*), with no vertical offset applied. The annulus is free of the most significant nuclear light. *Right*: a continuum-subtracted, Voronoi-binned spectrum (containing spectra from three adjacent spaxels) located 0.″15 from the continuum center, highlighting best-fitting Gaussian (*dashed*) and Gauss-Hermite (*solid*) profiles to the H_2 1−0 S(1) LOSVD.

2.3.2 Telescope and Instrumental Properties

The AO guide star was observed for 300 s in the Kn3 filter/20 mas scale combination to create a model of the PSF. The PSF cube was collapsed along the wavelength axis into a 2D image before characterization using GALFIT. A single Moffat profile of form

$$I(r) = I_0 \left[1 + (r/r_m)^2\right]^{-n} \tag{2.4}$$

fits the surface brightness well (see Figure 2.7), with concentration index n and parameter r_m related to the Moffat FWHM $= 2r_m \left(2^{1/n} - 1\right)^{1/2}$. To test the robustness of the fit, we refit the collapsed AO guide star image several hundred times after adding random noise to each spaxel. The random noise in each realization was drawn from a Gaussian distribution with dispersion equal to the best-fit residual standard deviation. From this set of trials, we determine best-fit Moffat profile parameters of $n = 2.78 \pm 0.44$ and FWHM $= 84.2 \pm 2.7$ mas, with an axis ratio $q = 0.91 \pm 0.02$.

To characterize the spatially varying OSIRIS line-spread function (LSF), we model emission

lines in the sky emission line cube with Gaussian profiles in the sky emission line cube. The LSF broadening $\sigma_{\rm LSF}$ is computed by averaging the fitted dispersions for prominent sky lines that lie near the redshifted H_2 wavelength. OSIRIS uses lenslets, and as such the instrumental LSF is not expected to change between point and extended sources at a given lenslet. In the 20 mas spaxel scale, $\sigma_{\rm LSF}$ varies smoothly between 36 and 58 km s^{-1} (with a typical uncertainty $\delta_{\rm LSF} \sim 3$ km s^{-1}) across the IFU FOV.

2.3.3 Emission Line Properties

LOSVD Fitting

We extracted 1D spectra along the wavelength axis from the 20 mas OSIRIS data cube and parametrized the H_2 1−0 S(1) ($\lambda_{\rm rest} = 2122$ nm) line-of-sight velocity distributions (LOSVDs), using MPFIT to model a straight-line continuum and (often) asymmetric line profiles the first four Gauss-Hermite (GH) moments ($v_{\rm LOS}$, $\sigma_{\rm LOS}$, h_3, h_4; van der Marel & Franx 1993). GH h_3 and h_4 coefficients fit to anti-symmetric and symmetric deviations, respectively, from a pure Gaussian LOSVD. The H_2 flux was determined by integrating the continuum-subtracted spectra over $v_{\rm LOS} \pm 3\sigma_{\rm LOS}$. Adjacent spectra were combined using the Voronoi tesselation method (Cappellari & Copin 2003) to achieve an integrated line $({\rm S/N})_{\rm bin} \geq 20$ for spaxels within 0.″3 from the nucleus. Both Gaussian and GH profile fits to the H_2 line of a typical binned spectrum are shown in Figure 2.4. The Brγ ($\lambda_{\rm rest} = 2166$ nm) emission-line parameters were determined using the same method but, due to much lower S/N, the h_3 and h_4 coefficients were fixed to be zero. We see only a hint of H_2 2−1 S(2) signal ($\lambda_{\rm rest} = 2154$ nm; see Figure 2.4), and no strong evidence for additional emission or absorption lines.

The continuum intensity dilutes the H_2 equivalent width within the central 0.″15 to the extent that binning alone is insufficient to reasonably constrain h_3 and h_4. Following a penalized

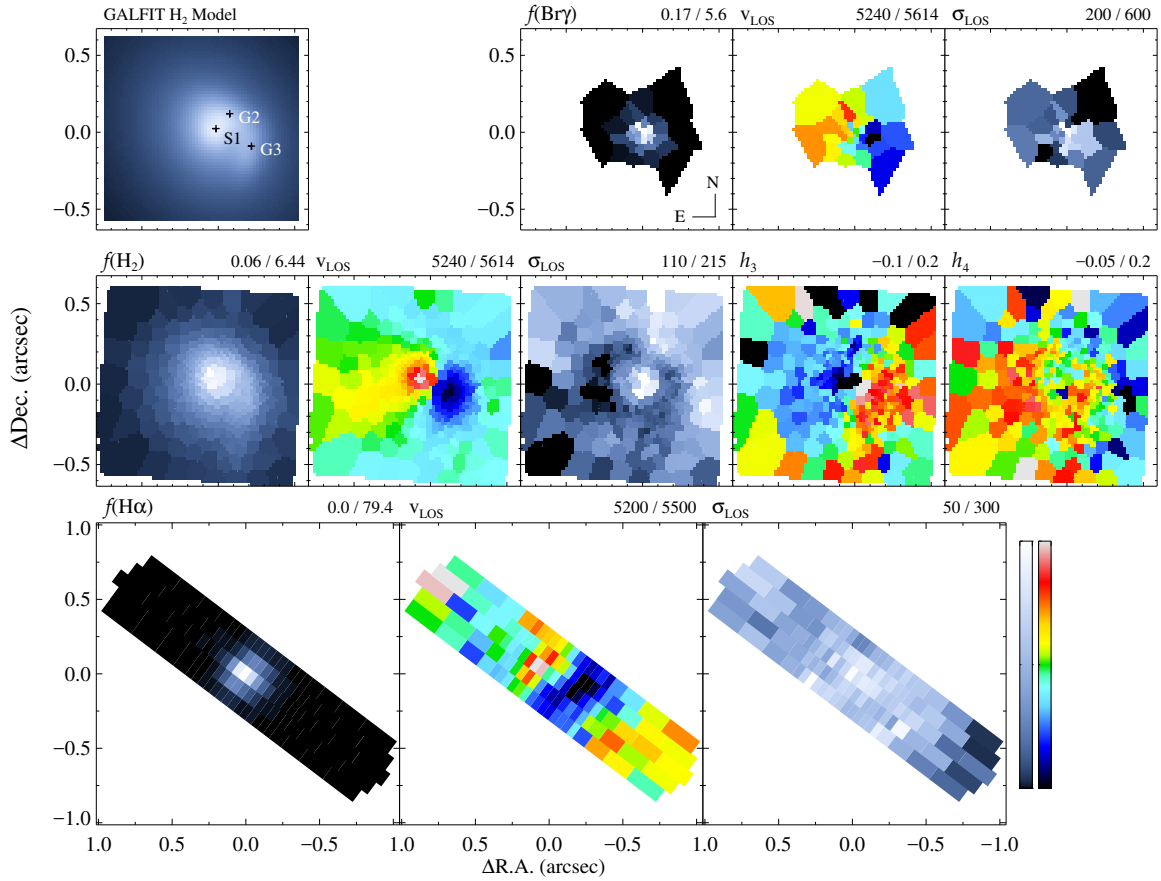

Figure 2.5 NGC 1275 nuclear H_2 1−0 S(1) (*middle row*), Brγ (*top right*), and Hα (*bottom row*) line moment maps determined from Gaussian and Gauss-Hermite (up to h_4) profile fits to the OSIRIS 20 mas data cube and adjacent STIS long-slit spectra. Above each map are numerical ranges corresponding to the low and high ends of the color bars (*bottom right*), with the line-of-sight velocity (v_{LOS}) and line dispersion (σ_{LOS}) ranges in km s^{-1}. STIS Hα maps show the combined broad+narrow flux (in units of 10^{-15} erg s^{-1} cm^{-2}) and the narrow-line velocity and line width measurements; approximate OSIRIS flux values are in units of 10^{-17} erg s^{-1} cm^{-2}. The H_2 flux is modeled using with three GALFIT components S1, G2, and G3 (*top left*; see §2.3.3). The H_2 v_{LOS} is not symmetric – the receding peak reaches ~ 50 km s^{-1} further from v_{sys} than the approaching extremum, and beyond $0\farcs3$ the kinematics are significantly disturbed. H_2 and Hα kinematics appear similar in the central ~ 100 pc, the ionized atomic emission does not show the high-velocity "shelf" eastward of the nucleus.

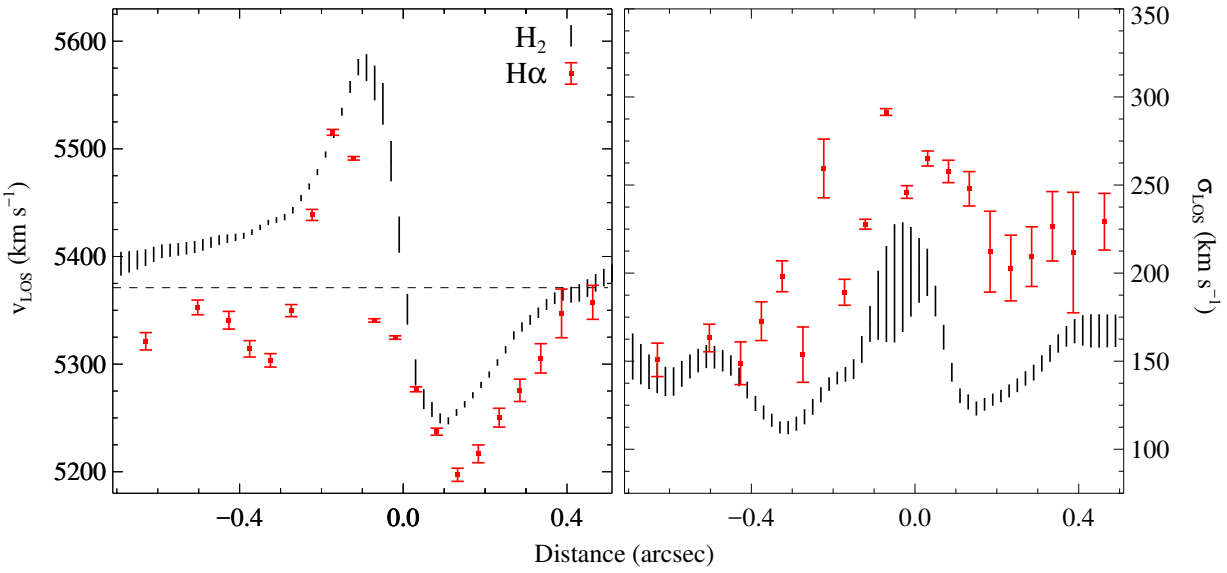

Figure 2.6 Heliocentric velocity (*left*) and dispersion (*right*) profiles for the OSIRIS H_2 1−0 S(1) and STIS Hα emission line observations. Profiles were extracted along the central STIS slit pointing (slit 3) that roughly corresponds to the circumnuclear disk major axis PA. For reference, we include the best-fit systemic velocity obtained from gas-dynamical modeling of the H_2 kinematics (*dashed line*).

fitting method (Emsellem et al. 2004; Cappellari & Emsellem 2004), we adopted a bias ($\beta = 1$) against needlessly large h_3 and h_4 values. Visual inspection of the LOSVD fits indicate that this bias effectively prevents spuriously high moments in all but a few bins, where the h_3 and h_4 values were then arbitrarily confined to be between -0.1 and 0.25.

To place the data on an approximate absolute flux scale, we applied a rough conversion of 2.3×10^{-17} erg s^{-1} cm^{-2} Å^{-1} to each OSIRIS data cube ADU s^{-1} to bring these OSIRIS H_2 1−0 S(1) measurements into agreement with the NIFS flux measurement obtained by integrating over a 0.″25−radius aperture (Scharwächter et al. 2013). Spatial maps of the H_2 1−0 S(1) flux and GH moments are presented in Figure 2.5, as well as those for the Brγ flux, velocity, and dispersion. The H_2 1−0 S(1)/Brγ line ratio increases from ~ 1 at the nucleus to ~ 10 at radii beyond $\sim 0.''2$, with an integrated flux ratio of ~ 9 over the entire OSIRIS FOV. Additional nuclear J−band spectroscopy (at $\sim 1''$ resolution; Rodríguez-Ardila et al.

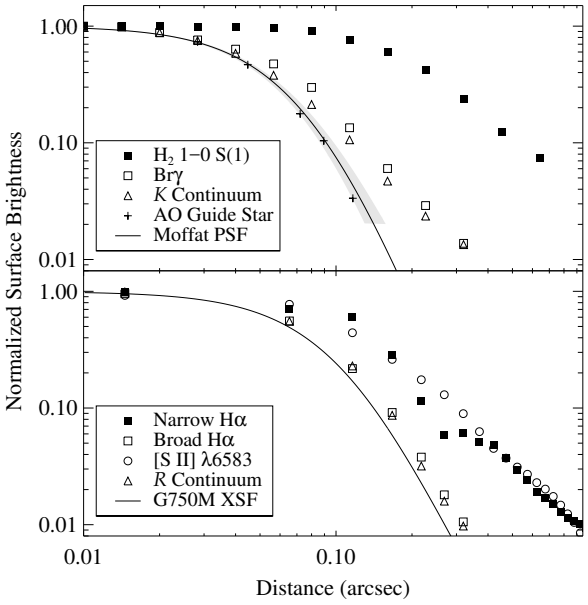

Figure 2.7 Emission line and continuum surface brightness profiles for the Keck OSIRIS (*top*) and *HST* STIS (*bottom*) data. For comparison, the model OSIRIS PSF (with uncertainty ranges; *shaded*) and STIS cross-dispersion PSF profiles are included.

2005) finds an [Fe II] $\lambda 1.257$ μm/Paβ line ratio of ~ 1 when averaged over the larger NIFS FOV. Based on NIR line ratio diagnostics (Riffel et al. 2013), the central H_2 1−0 S(1)/Brγ ratio is typical of a Seyfert; at angular distances $\gtrsim 0\farcs1$ from the nucleus, the increasing H_2 1−0 S(1)/Brγ line ratio and integrated [Fe II]/Paβ measurements indicate the beginning of larger-scale LINER environment at just a few tens of pc that is also observed on kpc scales.

The H_2 flux map shows a feature which extends from the western edge of the disk towards the southwest of the nucleus. Scharwächter et al. (2013) suggest this apparent flux excess may demarcate a streamer connecting the outer (~ 1.2 kpc; see Inoue et al. 1996) rotating gas disk with the inner (~ 100 pc) disk. Molecular gas rotation for $R \lesssim 0\farcs3$ appears ordered without suggestion of radial inflows or outflows. As shown in Figure 2.6, however, there is an asymmetry between the velocity extrema, with the northeast Keplerian peak having greater displacement (by ~ 50 km s^{-1}) from the systemic velocity ($v_{\rm sys}$) than the southwest peak. At radii $R \gtrsim 0\farcs3$ and eastward of the nucleus, $v_{\rm LOS}$ remains elevated above $v_{\rm sys}$ by this

same velocity displacement; at around this angular distance, the eastern H_2 line of nodes twists from a PA of $\sim 68°$ to $\sim 110°$. In addition to these $v_{\rm LOS}$ asymmetries, the observed velocity field between $\sim 0\farcs1 - 0\farcs3$ from the kinematic center falls to the systemic velocity more rapidly with increasing radius (esp. for the eastern velocity peak; see Figure 2.10) than can be explained by simple Keperlian rotation. Gas-dynamical modeling, described in §2.5.1, yields a $v_{\rm sys}$ value for the central ~ 100 pc molecular disk that is inconsistent by over 100 km s^{-1} with previous redshift measurements (e.g., Zabludoff et al. 1990). This tension is mitigated as previous studies determined $v_{\rm sys}$ from the larger-scale, filamentary and asymmetric ionized atomic and molecular emission line nebulae. The nuclear ionized atomic gas appears to have lower $v_{\rm sys}$ by ~ 40 km s^{-1}; the reason for *this* discrepancy is currently not understood.

The Brγ emission is not as spatially extended as the H_2 1−0 S(1) line, and appears to be only marginally resolved in these $0\farcs084-$FWHM OSIRIS data. After aggregating spectra together in a $0\farcs25-$radius aperture about the nucleus, a simple Gaussian profile fit demonstrates the nuclear Brγ LOSVD is significantly more broad than is the central H_2 line emission (~ 380 km s^{-1} compared to ~ 230 km s^{-1}, respectively). Voronoi binning of adjacent spectra prior to line profile fitting does reveal evidence for ionized atomic gas rotation in the NIR that agrees with the better-determined Hα kinematics. Since both ionized atomic and warm molecular emission lines appear to trace the same underlying disk rotation, the discrepancy in $\sigma_{\rm LOS}$ hints that the atomic gas probes closer to the central BH and that the molecular gas may be dissociated within a certain radius.

We form an approximate Kn3 continuum surface brightness map by collapsing the OSIRIS data cube along the spectral axis in the (essentially) line-free regions covering the wavelength ranges $2121 - 2150$, $2170 - 2190$, and $2210 - 2130$ nm. Continuum emission is not always coincident with the emission line flux and rotational centers (e.g., in the case of multiple nuclei, esp. in late-stage mergers; e.g., see U et al. 2013), although for NGC 1275 these NIR

tracers share an origin to within an angular confidence of ~ 15 mas. The H_2 1−0 S(1) and Brγ line emission as well as the NIR continuum are spatially extended when compared to the OSIRIS PSF (with a FWHM resolution of about 30 pc; see Figure 2.7). Decomposition of the nuclear NIR spectrum suggests significant thermal dust emission in addition to the prominent (and likely unresolved) active nucleus (Krabbe et al. 2000), and we expect this former component is responsible for the marginally-resolved Kn3 continuum profile.

Emission-Line Surface Brightness

As the H_2 1−0 S(1) surface brightness shows serious deviations from azimuthal symmetry, we used multiple 2D, non-concentric GALFIT profiles to characterize the observed flux map after convolution with the model OSIRIS PSF. The simplest model without large residuals (shown in Table 2.2 and Figure 2.5) consists of a broad Sérsic (S1) and two Gaussian (G2, G3) components. The broad component S1 ($n = 1.62$, $R_e = 0\farcs55$) lies very near the dynamical center and appears to depict smooth, disk-like emission, while the others (G2 and G3) may suggest localized clumps or streamers of molecular gas which are significantly offset from the center.

A very thin disk with inclination angle i is related to the observed axis ratio q' by $i = \cos^{-1}(q')$. Walker et al. (1994) find evidence for a parsec-scale radio jet that is inclined by 45^{+10}_{-15} degrees with respect to the line of sight; however, later work suggests both higher and lower values (Asada et al. 2006; Abdo et al. 2009). Wilman et al. (2005) and Scharwächter et al. (2013) assume that the molecular gas disk lies along the jet equatorial plane (i.e., $i = 45°$), while the S1 q' value instead suggests $i \sim 30°$ if the molecular disk is truly thin. Gas modeling of thin disks frequently results in at least some degeneracy between the black hole mass M_{BH} and i (see Figure 2.9), and a decrease in the assumed inclination of $\sim 15°$ corresponds to an increase of ~ 0.3 dex in M_{BH}. We performed Monte Carlo simulations to derive constraints on i, adding random noise to each spaxel based on the measured line-

Table 2.2 H_2 Flux GALFIT Parameters

	R_p ($''$)	C_T	R_e ($''$)	n	q	PA (deg)
S1	0.031	47.0	0.55	1.62	0.85	41.4
G2	0.157	4.66	0.29	–	0.58	66.6
G3	0.252	1.80	0.26	–	0.44	-12.8

Note: Sérsic component S1 and Gaussians G2 and G3 of the composite 2D GALFIT model, with S1 representing the broad, disk-like component of the H_2 emission profile. Column R_p indicates the projected distance from the measured continuum center, and C_T is the integrated component flux in units of $\sim 10^{-15}$ erg s^{-1} cm^{-2}.

fitting uncertainties before again modeling the H_2 flux with the S1+G2+G3 GALFIT model. All model parameters were allowed to vary and their total uncertainties determined from the standard deviation of parameter values from several hundred realizations. Under the assumption of a very thin disk, the resulting S1 axis ratio $q' = 0.85 \pm 0.01$ (1σ uncertainties) translates into $i = (32.6 \pm 1.6)^\circ$. As described in §2.5.1, thin-disk modeling agrees with this inclination range; modeling the observed kinematics using a Jeans equation formalism (that accounts for disk thickness; see §2.5.2) instead finds $i \sim 40^\circ$. The average observed $\sigma_{\rm LOS}/v_{\rm LOS}$ ratio (after removing $v_{\rm sys}$) for the bright H_2 emission is roughly unity for $R < 0\farcs3$, suggesting significant pressure support in the molecular disk that may result in a thicker gas distribution.

2.4 Gas Profiles

2.4.1 Atomic and Molecular Gas Mass

We explore the contributions of ionized and molecular gas to its nuclear gravitational potential. Ionized gas mass contributions are estimated by using the total broad and narrow

Hα line flux $f(\mathrm{H}\alpha) = 3.0 \times 10^{-13}$ erg s^{-1} cm^{-2} measured by integrating the STIS flux map over the central disk area. Following Osterbrock & Ferland (2006), and assuming an electron temperature $T \sim 10^4$ K and number density $n_e \sim 400$ cm^{-3} (Ho et al. 1997a), this $f(\mathrm{H}\alpha)$ value suggests only $\sim 1.8 \times 10^6$ $M_\odot$ of ionized gas in the inner $\sim 200 \times 200$ pc^2. The neutral hydrogen fraction $M_{\mathrm{H\,I}}/M_{\mathrm{H\,II}}$ is not known for LINER environments. We simply note that H I in the centers of (late-type) galaxies tends to saturate at a surface mass density of ~ 10 $M_\odot$ pc^{-2} (Leroy et al. 2008; Bigiel et al. 2008), which for a disk-like gas distribution would suggest $M_{\mathrm{H\,I}} \ll M_{\mathrm{H\,II}}$ over the OSIRIS FOV and an overall negligible atomic gas reservoir.

Estimating the total molecular gas reservoir is likewise difficult. Currently, there exist no high-resolution (sub-arcsecond) observations of the NGC 1275 nucleus of cold molecular gas tracers (e.g., CO) of the cold H_2 gas. Using calibrated H_2 1−0 S(1) flux measurements (Scharwächter et al. 2013), the warm H_2−emitting gas mass $M_{\mathrm{H2,warm}} \approx (5.1 \pm 1.0) \times 10^3$ $M_\odot$ contained within a radius of ~ 90 pc from the nucleus. Assuming a globally consistent $L_{\mathrm{H_2\,1-0\,S(1)}} \,/\, M_{\mathrm{H2,cold}}$ ratio based on large-scale (~ 10 kpc) H_2 1−0 S(1) and CO flux measurements (Lim et al. 2012; Salomé et al. 2006), Scharwächter et al. (2013) approximate the associated cold molecular gas $M_{\mathrm{H2,cold}}$ to be $\sim 4 \times 10^8$ $M_\odot$ within (a projected) 50 pc from the central BH. Similarly, Müller Sánchez et al. (2006) and Mazzalay et al. (2013) find a relationship between nuclear (~ 100 pc) $L_{\mathrm{H_2\,1-0\,S(1)}}$ and larger-scale ($\sim$kpc) $M_{\mathrm{H2,cold}}$ in active, late-type galaxies. For NGC 1275, this relationship would suggest $\sim (3.3^{+0.8}_{-1.4}) \times 10^9$ $M_\odot$ of cold molecular gas within 90 pc of its nucleus. However, resolved (albeit asymmetric) central velocity upturns found in both ionized atomic and warm molecular gas kinematics strongly suggests a total (BH+stellar+gas) mass of $\lesssim 10^9$ $M_\odot$ concentrated within the central few tens of pc. Until sub-arcsecond resolution imaging (for instance, with ALMA) of physical cold tracers affords a more unambiguous $M_{\mathrm{H2,cold}}$ determination, we ignore all gas mass contributions and instead assume the circumnuclear ionized atomic and warm molecular gas rotates in the combined potential of the central BH and extended stellar mass profile.

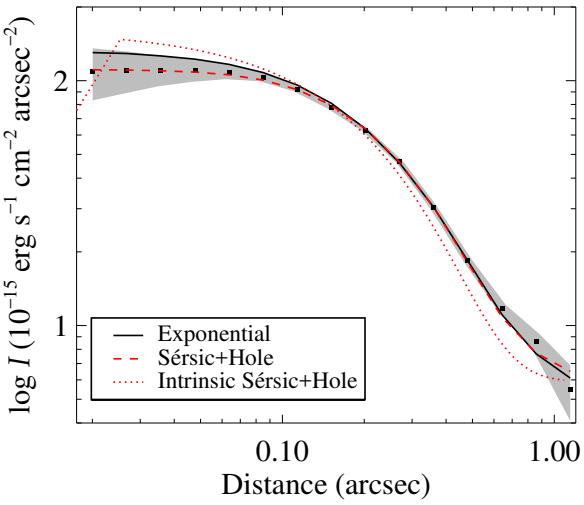

Figure 2.8 Elliptically-averaged H_2 surface brightness along with 1σ uncertainty (*shaded*). Included are PSF-convolved models of an exponential profile ($R_d = 0\farcs16$), as well as a more general Sérsic profile ($n = 0.84$, $R_e = 0\farcs23$) with an r^2 "hole" profile inside $0\farcs03$ to simulate H_2 dissociation (see Equation 2.5). We also plot the intrinsic H_2 "hole" profile for comparison

2.4.2 Molecular Gas Dissociation

While not used here to determine a gas mass profile, the parametric prescription for the intrinsic H_2 1−0 S(1) surface brightness will be folded into gas-dynamical models. The 2D GALFIT (S1+G2+G3) model is utilized in thin-disk tests in §2.5.1; however, this non-concentric fit does not work as an input to the specific Jeans equation modeling technique described in §2.5.2. We therefore used GALFIT to model the intrinsic H_2 flux as a single radially-varying profile with a small pedestal value. First, an exponential disk profile was convolved with the PSF and fit to the elliptically-averaged H_2 surface brightness. We find good agreement from $0\farcs1$ to $1''$ (see Figure 2.8) with a scale radius $R_d = 0\farcs16$ (~ 60 pc) and a small constant term ($\sim 5\%$ of the central H_2 surface brightness). Hicks et al. (2009) fit Sérsic profiles to H_2 disks in other Seyferts, finding several which resemble exponential disks. Those with apparent disk-like rotation have an average best-fitting Sérsic index $n \sim 1.4$ and similar radial scale lengths.

Molecular hydrogen may dissociate within some significant radius from the NGC 1275 active nucleus, with the result that the highest circular velocity regions near the BH will not contribute to the H_2 1−0 S(1) velocity field while still impacting the ionized atomic gas kinematics. For a dissociation radius that is smaller than the spatial resolution (i.e., on the order of a spaxel), this will manifest as a wider Hα/Brγ emission line widths than observed for the warm H_2 line. Work is ongoing to better identify and model faint and blended ionized gas emission, but the current measurements already show the anticipated excess (see comparisons of OSIRIS and STIS kinematics in Figure 2.6). Based on an approximate bolometric luminosity (Levinson et al. 1995), Scharwächter et al. (2013) estimate the dust sublimation radius, as well as an inner bound for radiative dissociation, to be about 0.1 pc. Beyond this, collisions and shocks within turbulent gas may further extend H_2 dissociation. We again modeled the H_2 surface brightness using GALFIT under the assumption of a (potentially sub-spaxel) "hole" in flux, using a Sérsic function for more flexibility in one plausible scenario:

$$I(R) = \begin{cases} I_{\rm h} \left(\frac{R}{R_{\rm h}}\right)^2 & R < R_{\rm h} \\ I_{\rm e} \exp\left[-k\left(\left(\frac{R}{R_{\rm e}}\right)^{1/n} - 1\right)\right] + c_1 & R > R_{\rm h} \end{cases} . \tag{2.5}$$

Constant c_1 is small ($\sim 5\%$ of the peak surface brightness) and $I_{\rm h}$ is scaled so that $I(R)$ remains continuous at hole radius $R_{\rm h}$. Model pixels are subsampled by a factor $s = 30$ to account for the potentially small $R_{\rm h}$ and rebinned prior to PSF convolution and fits to the data. Best-fitting Sérsic parameters $n = 0.84$ and $R_{\rm e} = 0\farcs23$ are not dissimilar from the previous exponential disk modeling results (see Figure 2.8), and assuming this prescription of dissociation, $R_{\rm h} = 0\farcs025$ corresponds to a (possible) "hole" radius of ~ 9 pc. We retain the exponential disk profile when modeling the H_2 kinematics in §2.5.2 and utilize this "hole" profile to approximate the effect of molecular dissociation on the best-fitting $M_{\rm BH}$ value.

2.5 Dynamical Modeling

Circumnuclear rotation has been observed in a handful of galaxies via the H_2 1−0 S(1) emission line, with several showing disk-like behavior amenable to gas-dynamical modeling (e.g., Cen A: Neumayer et al. 2007; NGC 3227, NGC 4151, and NGC 7469: Hicks & Malkan 2008; NGC 404: Seth et al. 2010; NGC 1275: Scharwächter et al. 2013; NGC 4395: den Brok et al. 2015). These molecular tracers are typically treated first as circularly rotating, simple thin disks that are inclined with respect to the line of sight by angle i and rotated on the sky by position angle θ (this formalism was originally applied to model ionized atomic gas rotation; e.g., Macchetto et al. 1997; van der Marel & van den Bosch 1998b; Barth et al. 2001). Additional modeling complexity (e.g., a warped disk) or physical considerations (such as dynamically warm rotation; Neumayer et al. 2007) are infrequently employed to better describe the observed kinematics. We model the NGC 1275 OSIRIS H_2 1−0 S(1) kinematics in §2.5.1 as a geometrically thin disk and later in §2.5.1 by treating the emission as arising from a somewhat oblate gas distribution.

2.5.1 Thin-disk Modeling

Assuming the H_2 emission arises from a physically thin disk, we first model the $v_{\rm LOS}$ data as due to circular rotation (see Barth et al. 2001; Walsh et al. 2010) in the potential of only an extended stellar mass profile and a central BH. A model cube is populated with Gaussian line profiles at each spaxel with parameters determined by the $v_{\rm LOS}$ and $\sigma_{\rm LOS}$ prescriptions and weighted by the intrinsic GALFIT model flux. This procedure allows for a variable disk center ($x_{\rm c}$, $y_{\rm c}$), disk inclination and rotation angles, systemic velocity, and BH mass. Spectral resolution effects are incorporated by LSF convolution (using the measured $\sigma_{\rm LSF}$), and spatial effects by PSF convolution and pixel subsampling and the model cube is then mock-observed by aggregating spectra in the same Voronoi bins and fitting with GH

line profiles to measure the model velocity field. This simple model fails to reproduce the observed H_2 velocity field, and the discrepancy worsens when noting the model line widths are globally much smaller than the observed values. The warm molecular line dispersion far exceeds the combined contributions of thermal motion (for $T \sim 2000$ K, thermal broadening ~ 5 km s^{-1}), instrumental line broadening ($\sigma_{\rm LSF} \lesssim 60$ km s^{-1}), and the effect of intra-spaxel velocity gradients; this excess is highest near the disk center and remains elevated (by ~ 100 km s^{-1}) beyond the primary rotation pattern (i.e., for $R \gtrsim 0\farcs3$). H_2 1$-$0 S(1) rotation observed within other Seyfert nuclei typically show excessive (albeit only at the ~ 30 km s^{-1} level) line widths. However, these other systems tend to show flat or even decreasing $\sigma_{\rm LOS}$ profiles at small radii (Hicks et al. 2009). The remaining line broadening in excess of reasonable modeling and instrumental contributions may be dynamically significant to modeling disk kinematics of NGC 1275 (for treatment of turbulent velocity dispersion $\sigma_{\rm turb}$ frequently treated in ionized gas disks; Verdoes Kleijn et al. 2000; Cretton et al. 2000; Barth et al. 2001) or may be the result of local turbulence within individual gas clouds (van der Marel & Franx 1993). Given that simple thin disk models are unable to reproduce the observed molecular gas $v_{\rm LOS}$, we consider that all excess dispersion is dynamically significant for the molecular gas disk. This $\sigma_{\rm turb}$ is parametrized by the radial form $\sigma_0 \exp(-R/R_0) + \sigma_1$ and incorporated as an asymmetric drift correction (see Barth et al. 2001; Walsh et al. 2010); parameters σ_0, σ_1, and R_0 are allowed to freely vary during model fits.

We briefly present thin-disk results to compare with the $M_{\rm BH}$ determination made by Scharwächter et al. (2013) and using Jeans equation modeling in §2.5.2. We explored the thin-disk goodness-of-fit by using the downhill simplex method (Press et al. 1992) to minimize

$$\chi^2 = \sum_{i=1}^{N} \frac{(v_{{\rm data},i} - v_{{\rm model},i})^2}{\delta v_i^2}. \tag{2.6}$$

where δv was first set to the $v_{\rm LOS}$ 1σ uncertainty in each of the N Voronoi bins. Models are only fit to bins contained within a physical disk radii $r_{\rm fit} \sim 100$ pc ($\lesssim 0\farcs3$ along the disk

major axis) to isolate the most regular region of the observed velocity field. We find that $M_{\rm BH}$ is fairly insensitive to pixel subsampling s above a value of about 2, and we therefore fix $s = 4$ in model creation. Best-fitting parameters σ_0 and σ_1 are found to be 216 and 127 km s^{-1}, respectively, and the scale radius $R_0 = 0\farcs07$. Models that incorporate asymmetric drift corrections much more closely reproduce the observed velocity field, although large correlated residuals remain. We note that this approximation is only strictly appropriate for $\sigma_{\rm turb}/v_{\rm c} \ll 1$ while the best-fitting model approaches a ratio value of 0.6 near the nucleus and remains high out to the edge of the disk-fitting region $r_{\rm fit}$.

Results and Error Budget

Previous gas-dynamical modeling of other circumnuclear disks (e.g., Barth et al. 2001; de Francesco et al. 2006; Walsh et al. 2010) yields best fits with $\chi^2_\nu = \chi^2/\nu \gg 1$ for ν degrees of freedom. Scharwächter et al. (2013) model the NGC 1275 molecular kinematics and determine the minimum $\chi^2_\nu \approx 60$ (over a truncated range in i); even with higher-resolution OSIRIS data and more detailed modeling techniques, our simple thin disk formalism still only poorly ($\chi^2_\nu \approx 40$) matches the observed $v_{\rm LOS}$. In fact, they reveal a more complicated picture, with strong degeneracy $M_{\rm BH}^{-1/2} \propto \sin i$ that favors unreasonably small ($i \lesssim 10^\circ$) inclination angles. Including an asymmetric drift correction both lessens the degeneracy and ameloriates the modeling discrepancies, yielding a best fit of $\chi^2 = 841.3$ over $\nu = 114$ degrees of freedom, or $\chi^2_\nu = 7.38$. The high χ^2_ν may arise due to a combination of significant deviations from simple disk kinematics and underestimated δv, as well as correlated errors between data bins (see Barth et al. 2016b). For now, we have inflated the line-of-sight velocity uncertainties by adding a constant error term $\delta_{\rm c} = 14$ km s^{-1} in quadrature with δv to drive χ^2_ν to unity. Doing this conservatively expands the $M_{\rm BH}$ error budget for model fits that struggle to fully reproduce the observed velocity field. Afterwards, the 1, 2, and 3σ parameter confidence intervals are determined in the standard method by finding where

$\Delta\chi^2 = \chi^2 - \min(\chi^2)$ equals 1, 4, and 9, respectively, if minimized with one fixed parameter, and 2.3, 6.2, and 11.8 if over two parameters.

Modeling Uncertainties: To determine the best-fitting BH mass and inclination angle values, we optimized the thin disk model over an array of fixed $M_{\rm BH}$ and i values to map out the $\chi^2(M_{\rm BH}, i)$ response (see Figure 2.9). Given that degeneracies preclude convergence to reasonable parameters for simple thin disk models, we restrict ourselves to models that apply an asymmetric drift correction. After rescaling the data δv values, the $\Delta\chi^2$ contours outline the statistical uncertainties and yield initial (3σ) determinations of $M_{\rm BH} = \left(0.63^{+0.32}_{-0.17}\right) \times 10^9$ $M_\odot$ and $i = \left(34.3^{+7.8}_{-7.9}\right)^\circ$. This range in i agrees well with the estimate derived from the GALFIT S1 model component as described in §2.3.3.

Figure 2.10 shows that the best-fitting model agrees well with the data velocity profile on the approaching half of the disk. In contrast, the receding peak of the model velocity is in error by ~ 100 km s^{-1}. This discrepancy arises as the disk systemic velocity $v_{\rm sys} = \left(5374^{+2}_{-4}\right)$ km s^{-1} is tightly constrained by the Voronoi bin kinematics near or along the minor axis, with the result being large, asymmetric model velocity residuals. Since the H_2 velocity uncertainties of the innermost Voronoi bins are large, the central several data bins (that include portions of the velocity extrema) are only minor contributors to the overall χ^2 goodness-of-fit measure.

Stellar Mass Profiles: Initial modeling procedures utilize the lower-bound ($j = 2-10$) stellar MGE when creating the intrinsic model velocity field. As thin disk formalism struggles to recreate the observed $v_{\rm LOS}$ values, allowing for a variable Υ_H during model optimization tends to force the $H-$band M/L ratio to very small (or negative) values; therefore, $\Upsilon_H = 0.75$ $M_\odot/L_\odot$ remains fixed in all model iterations. Changing the thin disk model to use the upper-bound modified Nuker profile does yield a slightly lower BH mass determination by $\Delta M_{\rm BH} = -0.7 \times 10^8$ $M_\odot$ and a corresponding increase in best-fit inclination angle of $\Delta i = 2.4^\circ$.

Molecular Dissociation: Folding in the intrinsic, elliptically-averaged H_2 "hole" surface brightness defined by Equation 2.5 instead of the non-concentric GALFIT 2D model does not significantly impact the parameter values after downhill simplex minimization. This is likely due to relatively large nuclear δv values while disk models struggle to simultaneously reproduce both receding/approaching sides of the better-constrained Keplerian-like declining velocity profiles.

Fitting Region: Shrinking the fitting radius $r_{\rm fit}$ to 50 pc does significantly impact the BH mass, yielding $\Delta M_{\rm BH} = 0.25 \times 10^9\ M_\odot$ with a corresponding large decrease in best-fit i. As $r_{\rm fit}$ shrinks, a larger fraction of the total bins within the fitting region come from the major axis Keplerian peaks and the modeling procedure better fits the highest velocity emission on the receding side of the disk. This in turn results in many fewer points sampling the disk minor axis and an increase in the systemic velocity by an unreasonable ~ 10 km s^{-1}. At this time, we do not include $\Delta M_{\rm BH}$ due to a changing $r_{\rm fit}$ into the total error budget in BH mass.

Final Error Budget: Treating the parameter statistical uncertainties and the systematic shift obtained from changing stellar mass profiles as independent, the resulting shifts $\Delta M_{\rm BH}$ and Δi are added in quadrature to the corresponding upper and lower confidence intervals for final BH mass and inclination values and (3σ) uncertainties of $M_{\rm BH} = \left(0.63^{+0.32}_{-0.19}\right) \times 10^9\ M_\odot$ and $i = \left(34.3^{+8.2}_{-7.9}\right)^\circ$. Even with substantial effort, we find only marginal agreement between $v_{\rm LOS}$ and thin disk models with asymmetric drift. As mentioned, this situation becomes less tenable as $\sigma_{\rm turb}/v_{\rm c}$ is globally too large to justify the assumed (but standard) asymmetric drift approximation. We conclude that standard thin-disk models are not well suited to describe warm molecular gas rotation in this particular Seyfert nucleus.

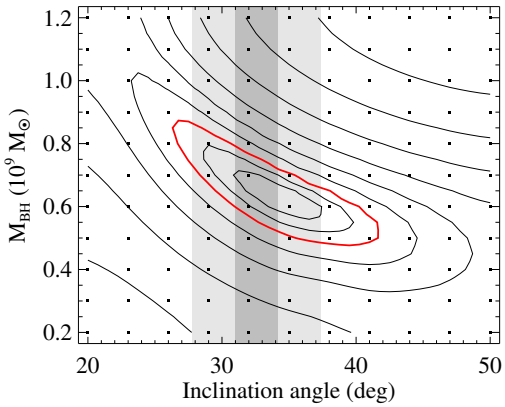

Figure 2.9 Results from thin disk modeling $\chi^2(M_{\rm BH}, i)$ minimization of the warm H_2 kinematics after applying an asymmetric drift correction. The inner three contours are approximate 1, 2, and 3σ confidence intervals, while the rest are logarithmically but arbitrarily spaced. LOS velocity uncertainties were inflated to drive $\chi^2_\nu \to 1$ and thereby conservatively expand these confidence intervals. The broad contour pattern still roughly follows the anticipated (and previously observed; Scharwächter et al. 2013) $M_{\rm BH}^{-1/2} \propto \sin i$ degeneracy which is also seen in Scharwächter et al. (2013). Data points indicate the fixed i and $M_{\rm BH}$ sampling of the parameter space. Shaded regions are the 1 (*dark grey*) and 3σ (*light grey*) confidence ranges on i estimated from the S1 component of GALFIT H_2 surface brightness modeling (see Table 2.2).

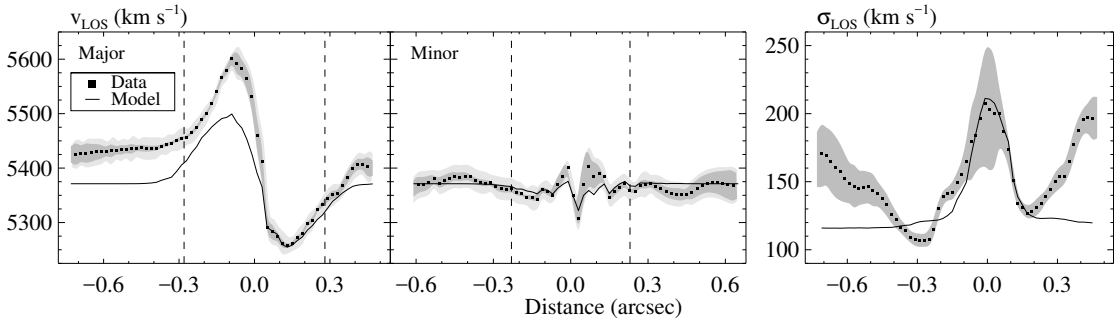

Figure 2.10 Smoothed H_2 1−0 S(1) line-of-sight velocity and dispersion profiles extracted along the major and minor axes (*left*) in $v_{\rm LOS}$ and the major axis (*right*) in $\sigma_{\rm LOS}$, showing both data kinematics and those of the best-fitting model. Shaded regions correspond to the 1σ (*dark grey*) uncertainties in the respective moments, and for the $v_{\rm LOS}$ profiles we also included the expanded uncertainties (*light grey*) that bring χ^2_ν to unity. The demarcated fitting region $r_{\rm fit} = 100$ pc ($R \lesssim 0\farcs3$) (*vertical dashed lines*) avoids the most serious deviations from symmetric rotation, especially that the major axis OSIRIS $v_{\rm LOS}$ profile does not return to $v_{\rm sys}$ on the receding side of the disk.

2.5.2 Jeans Modeling

The kinematic warmth of the NGC 1275 H_2 1−0 S(1) emission (where $\sigma_{\rm turb} \sim v_{\rm c}$) appears typical of physically warm molecular gas tracers within Seyfert nuclei on sub-kpc scales (Hicks et al. 2009), suggesting significant vertical motion in addition to the observed disk-like rotation. Standard thin disk formalism is neither able to model a potentially thick disk nor to incorporate its impact on the observed kinematics and, as a result, the $M_{\rm BH}$ determination using thin-disk gas-dynamical modeling may seriously underpredict the true BH mass.

In an attempt to better model the molecular $v_{\rm LOS}$ data, we employ a Jeans equation method that treats the tracer particles as originating from a rotating, oblate spheroidal gas distribution. Jeans equation modeling has previously been used to characterize [Fe II] λ1644 nm (Häring-Neumayer et al. 2006) and H_2 1−0 S(1) (Neumayer et al. 2007) velocity fields in Centaurus A by approximating a geometrically thin but kinematically hot disk. To reproduce the H_2 1−0 S(1) emission line disk rotation in NGC 1275, we used the Jeans Anisotropic MGE (JAM; Cappellari 2008) method that is implemented to reproduce integral-field stellar kinematics of fast-rotator ETGs (e.g., Scott et al. 2009; Cappellari et al. 2012, 2013; Cappellari 2016) and that is comparable to more intensive Schwarzschild orbit superposition modeling (Cappellari 2008; Leung et al. 2018). JAM generalizes the semi-isotropic asymmetric Jeans equation by an approximation in cylindrical coordinates that assumes a linear relationship between $\overline{v_z^2}$ and $\overline{v_R^2}$ in the anisotropy $\beta_z \equiv 1 - \overline{v_z^2}/\overline{v_R^2}$. This anisotropic Jeans equation implementation takes as inputs the intrinsic inclination and rotation angles i and θ, the kinematic center ($x_{\rm c}$, $y_{\rm c}$), (potentially) spatially-varying β_z value, dynamical M/L ratio, and tracer luminosity and galaxy mass MGE components; the modeling returns $v_{\rm LOS}$ and $v_{\rm RMS}^2 = v_{\rm LOS}^2 + \sigma_{\rm turb}^2$ values for the rotating system at desired (projected) locations.

To tailor the JAM procedure to model our warm molecular gas disk, we assume the kinematic

tracer luminosity profile is formed from an MGE of the intrinsic 2D GALFIT exponential disk profile fit (detailed in §2.4.2) to the H_2 flux map, while the initial (lower-bound) stellar MGE is expected to be a close proxy for the extended mass profile. In the future, we will explore additional, more flexible extended mass prescriptions that will better account for potential dust obscuration and stellar M/L gradients. The assumed oblate axisymmetry of the system requires that $\cos^2 i < q'^2_j$ for each observed axis ratio q'_j in MGEs of both the extended mass and gas luminosity surface brightness profiles. Individual stellar MGE components do not possess any physical significance; however, the minimum stellar q'_j value constrains the lowest inclination angle allowable as a JAM input. We therefore re-measured the modified Nuker MGE, constraining the minimum q' to increasingly larger values until the global χ^2 fit had increased by a moderate ($\sim 5\%$) amount. At $\min(q'_j) = 0.85$, this minimum projected axis ratio corresponds to a lower-bound intrinsic $i = 32°$ and should just barely cover the best-fit inclination angle from thin-disk modeling results. If the gas physical density is roughly exponential in both radius r and height z, i.e., is proportional to$\exp(-r/r_0)\exp(-z/z_0)$, the disk thickness can be estimated by the edge-on scale length ratio $h = z_0/r_0$ that relates intrinsic and observed disk properties by $\cos^2 i \approx (q'^2 - h^2)/(1 - h^2)$ (Holmberg 1958). Even for a moderately thick disk ($h \sim 0.5$), to first order ($\sim 10\%$ accuracy at $i \sim 40°$) this relationship preserves $q' \approx \cos i$. The H_2 surface brightness MGE $q' \sim 0.85$ values remain fixed during modeling, so the changing input i effectively sets the disk thickness.

Parameters $M_{\rm BH}$, i, θ, $x_{\rm c}$, $y_{\rm c}$, and β_z are allowed to varying at each JAM model iteration in the downhill simplex (Press et al. 1992) minimization process. Stellar Υ_H was again fixed to 0.75 $M_\odot/L_\odot$. For the most part, physically imposed parameter constraints (e.g., $M_{\rm BH} > 0$, $\beta_z \leq 1$) are sufficient to ensure reasonable models; however, leaving anisotropy otherwise free results in $\beta_z \to -\infty$ even without a significant χ^2 improvement for $\beta_z \lesssim 0.05\%$. With no *a priori* anisotropy expectation for disk-like gaseous rotation, we elect to treat the warm H_2 kinematics as an analogue of fast-rotator ETG stellar cores (that show $\beta_z \gtrsim 0$; Cappellari et al. 2007) and adopt a positivity constraint on this parameter. The (spherical) anisotropy

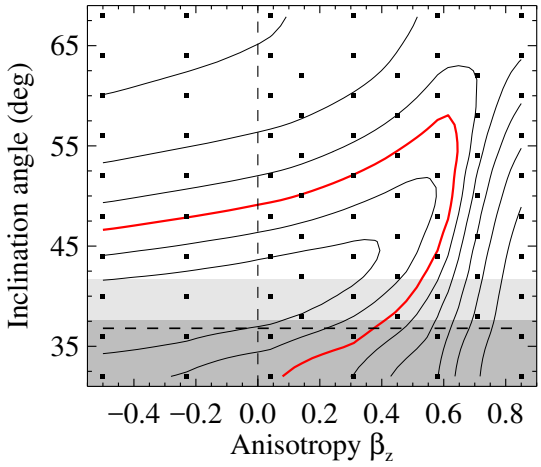

Figure 2.11 Results from JAM modeling $\chi^2(i, \beta_z)$ minimization of the warm H_2 $v_{\rm RMS}$ velocity field, sampled at fixed i and β_z values as indicated. The inner three contours are approximate 1, 2, and 3σ confidence intervals, while the rest are logarithmically but arbitrarily spaced. The vertical dashed line is the later-imposed $\beta_z \geq 0$. Shaded regions show the 1 (*dark grey*) and 3σ (*light grey*) confidence intervals on i from thin disk modeling that employs an asymmetric drift correction, while also containing the 3σ upper limit (*dashed line*) on i based on multi-function GALFIT modeling of the H_2 surface brightness.

for a variety of both rotating and non-rotating mock galaxies demonstrates that β correlates positively with GH h_4 moment (van der Marel & Franx 1993; see also Figure 2.5), suggesting constraining $\beta_z \in [0, 1]$ for this system may be reasonable.

Disk systemic velocity is removed and the instrumental and thermal line broadening terms are subtracted in quadrature from the respective $v_{\rm LOS}$ and $\sigma_{\rm LOS}$ profiles prior to constructing the RMS velocity field. At this stage we consider all excess σ to be dynamically significant. At radii $\gtrsim 0\farcs2$, this turbulent velocity dispersion dominates over the rotation pattern in the $v_{\rm RMS}$ (see Figure 2.13). At some radius from the nucleus, the warm H_2 emission will arise primarily from the larger-scale emission-line nebula that does not share the orderly circumnuclear circumnuclear disk rotation. To focus on the kinematics contributions from regions that show the most regular rotation, these models are matched to the observed RMS kinematics for Voronoi bins within an elliptical fitting radius $r_{\rm fit} = 0\farcs2$ (corresponding to ~ 70 pc).

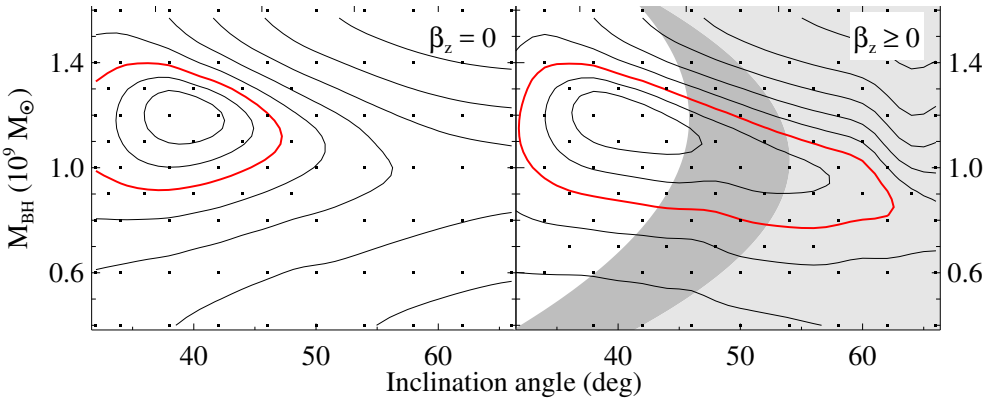

Figure 2.12 Results of $\chi^2(M_{\rm BH}, i)$ minimization using the JAM procedure to reproduce the warm H_2 $v_{\rm RMS}$ data, first fixing anisotropy $\beta_z = 0$ (*left*) and then allowing β_z to vary between zero and unity (*right*). The $M_{\rm BH}$ and i parameter space is sampled at fixed points as indicated. The inner three contours are approximate 1, 2, and 3σ confidence intervals, while the rest are logarithmically but arbitrarily spaced. Shaded regions (*at right*) show where the $\beta_z \geq 0$ values exceeds the 1 (*dark grey*) and 3σ (*light grey*) limits determined for that fixed i during $\chi^2(i, \beta_z)$ minimization as shown in Figure 2.11.

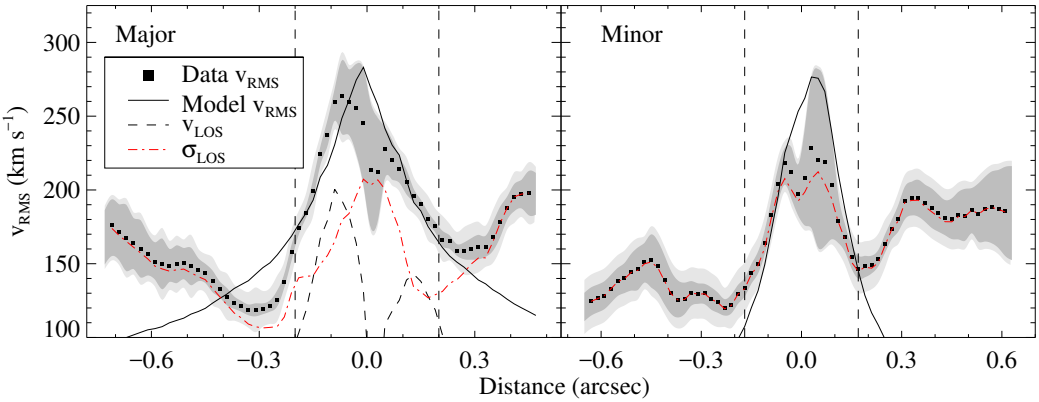

Figure 2.13 Smoothed H_2 1−0 S(1) line-of-sight RMS velocity profiles along the major (*left*) and minor (*right*) axes, showing both the data and best-fitting model. Thermal and LSF broadening contributions have been removed from the $\sigma_{\rm LOS}$ profile. Given the unequal magnitude of the $v_{\rm LOS}$ peaks and the slightly off-center, high $\sigma_{\rm LOS}$ values, major and minor profiles show qualitatively different shapes. Shaded regions show both the initial $v_{\rm RMS}$ uncertainties (*dark grey*) and those expanded to bring $\chi^2_{\rm dof}$ to unity (*light grey*). Data $\sigma_{\rm LOS}$ dominates over the primary $v_{\rm LOS}$ at larger radii, so we limited the χ^2 fitting region to $r_{\rm fit} = 70$ pc ($R \lesssim 0\farcs2$; demarcated by vertical dashed lines) to avoid the large increases in $\sigma_{\rm LOS}$ that JAM modeling is unable to reproduce.

Results and Error Budget

We determined best-fitting parameter values and confidence intervals from JAM modeling in the same manner as done under the assumption of thin-disk rotation. Inclusion of the anisotropy parameter somewhat complicates the modeling process since β_z positively correlates with i (interestingly enough, opposite to stellar JAM results of some ETGs; Cappellari 2008). We therefore present χ^2 minimization results over both the (i, β_z) and $(M_{\rm BH}, i)$ planes in Figures 2.11 and 2.12. These efforts yield a best-fit model with $\chi^2 = 229.9$ over 38 degrees of freedom, with the resultant $\chi^2_\nu = 6.05$. Due to the elevated reduced chi-squared level, we incorporate additional uncertainty $\delta_{\rm c} = 11$ km s^{-1} in quadrature to the error-propagated uncertainty in $v_{\rm RMS}$. Inflating the RMS velocity error bars conservatively broadens the confidence intervals by a factor of about three. Exploring the entire β_z parameter space shows that $\chi^2(\beta_z)$ is nearly flat for increasingly negative anisotropy values, and enforcing positivity during $\chi^2(i, \beta_z)$ minimization constrains the disk inclination to be between 37° and 43° (at 1σ confidence).

Minimizing χ^2 over the $(M_{\rm BH}, i)$ parameter space shows a much smaller (but still discernible) degeneracy between the BH mass and disk inclination than revealed in thin disk modeling results. We favor $\beta_z = 0$ based on the observed $\chi^2(i, \beta_z)$ trend and the assumption this dynamically warm gas disk is similar to fast-rotator ETG stellar kinematics. The best-fitting $M_{\rm BH}$ value and confidence intervals appear to be nearly insensitive to changes in anisotropy, and so we run tests at fixed BH mass and inclination while allowing a freely-varying $\beta_z \in [0, 1]$. As anticipated, relaxing constraints on β_z produces large changes in the i confidence ranges. We do not attempt to explore the hyperplane behavior at fixed $(M_{\rm BH}, i, \beta_z)$ points; instead, we exclude regions of the $\chi^2(M_{\rm BH}, i, \beta_z \geq 0)$ minimization results where the free anisotropy takes values that lie outside $\chi^2(i, \beta_z)$ contours at the same fixed i. Of course, $i \gtrsim 48°$ is also excluded when minimizing $\chi^2(M_{\rm BH}, i, \beta_z = 0)$; however, this region lies beyond the existing 3σ contours. As shown in Figure 2.12, the permitted parameter

space for free anisotropy is no longer in tension with minimization with fixed $\beta_z = 0$ and suggests the choice of anisotropy has a relatively small impact on the best-fitting $M_{\rm BH}$ and i values.

Modeling Uncertainties: From χ^2 minimization in the $(M_{\rm BH}, i)$ plane (assuming $\beta_z = 0$), the JAM modeling finds respective best-fit BH mass and intrinsic inclination determinations, along with 3σ uncertainty ranges, of $(1.20^{+0.22}_{-0.28}) \times 10^9\ M_\odot$ and $(39.1^{+8.1}_{-7.1})^\circ$. The lower uncertainty bound on i corresponds to the minimum permissible inclination angle ($\sim 32^\circ$) that is set by the minimum stellar MGE q' value. However, the best-fit inclination value determined here is significantly removed from this hard limit and should not impact our analysis. The approximation relating h, the best-fit intrinsic i, and the observed H_2 emission $q' \approx 0.85$ suggests a molecular scale length ratio $h \sim 0.5$. A radial disk scale length $r_0 \sim 60$ pc (assumed from $R_{\rm d}$ in §2.4.1) then correlates to a vertical disk scale height $z_0 \sim 30$ pc, which agrees with the estimated scale heights of other warm molecular gas disks in Seyfert nuclei (Hicks et al. 2009).

Anisotropy: Allowing $\beta_z \in [0, 1]$ during χ^2 minimization at fixed points in the $(M_{\rm BH}, i)$ planes yields only a slight decrease ($\Delta M_{\rm BH} \approx 10^7\ M_\odot$) in the best-fit BH mass. The intrinsic i determination and confidence intervals are significantly altered, but the $\chi^2(i, \beta_z)$ results exclude nearly all of the expanded χ^2 contours. As such, we do not include the effects of anisotropy on the $M_{\rm BH}$ and i uncertainties.

Non-dynamical σ: We consider the effect on $M_{\rm BH}$ if a significant portion of the data dispersion is considered to be non-dynamical in origin. We subtract a constant ~ 25 km s^{-1} from $\sigma_{\rm LOS}$ (roughly 20% of the turbulent velocity profile component σ_1 as determined by thin-disk dynamical modeling) and re-calculate $v_{\rm RMS}$. Any larger reduction in $\sigma_{\rm LOS}$ creates two distinct peaks in $v_{\rm RMS}$ due to asymmetric $v_{\rm LOS}$ contributions, and current model optimization settles its kinematic centers on the location of the primary peak. Lowering the pedestal level of $\sigma_{\rm turb}$ decreases the BH mass by $2 \times 10^8\ M_\odot$ while increasing the best-fit inclination by

$\sim 4^\circ$.

Stellar Mass Profile: JAM modeling that instead utilizes the modified Nuker stellar MGE at the same Υ_H value returns a $M_{\rm BH}$ value that is slightly lower by 1.2×10^8 $M_\odot$ without any significant impact on the disk inclination.

Molecular Gas Dissociation: Using the piecewise H_2 profile that possesses a central hole in emission (Equation 2.5) instead of the exponential disk model results in an increased BH mass by 1.3×10^8 $M_\odot$ while the inclination angle remains unchanged.

Fitting Radius: The initial fitting radius $r_{\rm fit} = 70$ pc samples only the primary rotation pattern. Including Voronoi bins out to a radius of 100 pc (as done for thin-disk modeling of $v_{\rm LOS}$) yields $\Delta M_{\rm BH} \sim -10^8$ $M_\odot$ while the best-fit inclination falls precipitously to the lowest allowed 32° value and the minimum χ^2_ν increases by over 30%. Much of the worsened fit is due to the inclusion of $\sigma_{\rm LOS}$ contributions that appear unrelated to the disk-like kinematic features.

Symmetrized $v_{\rm RMS}$: The asymmetry in H_2 velocity extrema (that are discrepant by ~ 50 km s^{-1} from $v_{\rm sys}$) along with high but slightly off-center line dispersions, create an irregular nuclear RMS velocity field that reaches a maximum value ~ 3 spaxels from the dynamical center. We further bound the BH mass error budget symmetrizing the $v_{\rm RMS}$ data, first reflecting the Voronoi-binned RMS velocity data from one side of the disk across the minor axis and refitting using JAM modeling; afterwards, this process is repeated using data points from the other side of the disk. The BH mass determination changes by $\Delta M_{\rm BH} = (-2.6, 1.6) \times 10^8$ $M_\odot$ and the inclination angle by $\Delta i = (1.6, -1.1)^\circ$, respectively. As expected when symmetrizing somewhat asymmetric data points, the χ^2 fit signficantly improves (by a factor of ~ 2).

Final Error Budget: As for the thin disk modeling results, the sources of systemic uncertainty addressed above are assumed to be independent, with the $\Delta M_{\rm BH}$ and Δi shifts added in

quadrature to the corresponding statistical uncertainty values. This yields parameter values with (3σ) total error budgets of $M_{\rm BH} = (1.20^{+0.32}_{-0.44}) \times 10^9\ M_\odot$ and $i = (39.1^{+9.2}_{-7.1})^\circ$. These JAM determinations are not formally inconsistent with thin disk dynamical model results at the 3σ level.

Even though JAM modeling produces a somewhat better fit to $v_{\rm RMS}$ than did thin disk models to $v_{\rm LOS}$, comparisons between data and model $v_{\rm RMS}$ fields in Figures 2.13 and 2.14 demonstrate the limitations of current gas-dynamical techniques when treating kinematically warm disk-like rotation. Key among these difficulties is the continued inability of models to recreate the rapid descent of the eastern $v_{\rm LOS}$ extremum. The observed $v_{\rm RMS}$ is slightly double-peaked within the inner $\sim 0\farcs1$, although this feature is largely hidden during the χ^2 fitting by the large uncertainties in the central $\sigma_{\rm LOS}$ which are propagated into the final $v_{\rm RMS}$ error budget.

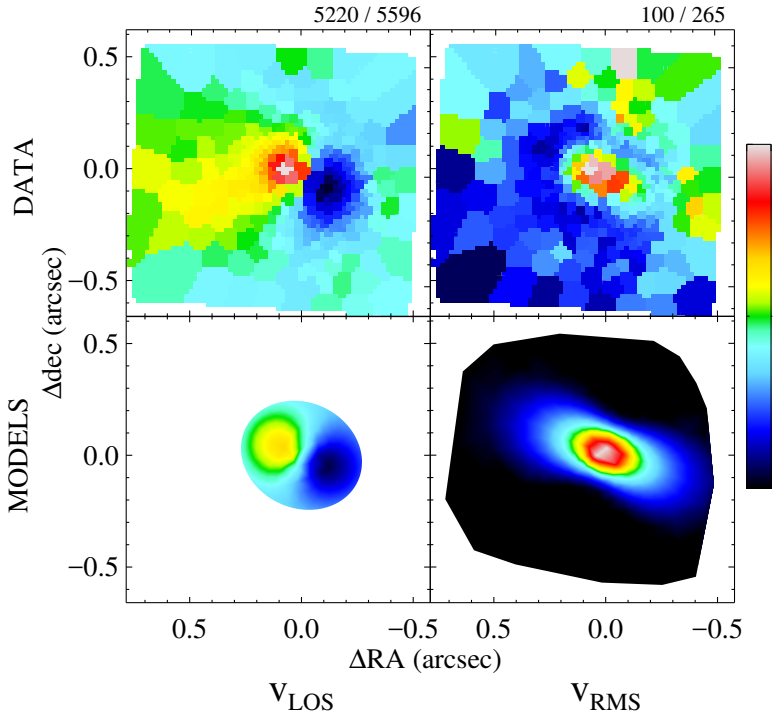

Figure 2.14 H_2 1−0 S(1) $v_{\rm LOS}$ and $v_{\rm RMS}$ data (*top*) and the best-fitting thin disk and Jeans equation dynamical modeling results (*bottom*), respectively. The thin disk results are taken from models that incorporate an asymmetric drift correction, and we implement the Jeans equation using the JAM method. The thin disk model $v_{\rm LOS}$ is shown only for $r_{\rm fit}$ = 100 pc, while we include a larger radial extent for the best-fitting JAM RMS model to highlight discrepancies arising from large $\sigma_{\rm turb}$ values beyond $r_{\rm fit}$. Velocity ranges (in km s^{-1}) above the data LOS and RMS velocities correspond to the low and high colorbar ranges.

Chapter 3

ALMA Observations of Luminous Early-Type Galaxies

An early consensus held ETGs were nearly devoid of gas and dust (Hubble 1926; de Vaucouleurs 1959; Sandage 1961). The first challenge to this paradigm came from optical spectroscopy that revealed the presence of ionized interstellar gas (e.g., Mayall 1958; Minkowski & Osterbrock 1959; Osterbrock 1960; for a more recent survey, refer to Bassett et al. 2017). Later, radio observations of ETGs detected neutral hydrogen on large (several kpc) scales (e.g., Balkowski et al. 1972; Knapp et al. 1985; Wardle & Knapp 1986), and X-ray observations uncovered reservoirs of hot, diffuse gas within and around some cluster and isolated ETGs (e.g., Forman et al. 1979; Nulsen et al. 1984). Soon afterwards, the *Infrared Astronomical Satellite* (*IRAS*) discovered significant mid to far-IR excess in ETGs originating from thermal dust emission (e.g., Jura 1986; Knapp et al. 1989). Imaging surveys from the ground and with *HST* also detected dust in absorption in the centers of roughly half of all early-type galaxies (Ebneter & Balick 1985; Ebneter et al. 1988; van Dokkum & Franx 1995; Verdoes Kleijn et al. 1999; Tomita et al. 2000; Tran et al. 2001; Laine et al. 2003; Lauer et al. 2005). In about 10% of these ETGs, *HST* imaging revealed round, morphologically

regular disks (typically with sub-kpc radii) that trace a dense, cold component of the nuclear environment. Early CO observations of several early-type targets with bright far-IR emission confirmed the presence of molecular gas with $\sim 50\%$ detection rates (e.g., Sage & Wrobel 1989; Wiklind et al. 1995). While at much coarser spatial resolution than *HST* imaging, these gas observations suggested that up to a tenth of nearby ETGs might possess molecular gas that is both detectable in CO emission and in disk-like rotation on small scales.

Two prominent surveys – SAURON (de Zeeuw et al. 2002) and ATLAS^{3D} (Cappellari et al. 2011) – observed CO in representative (Combes et al. 2007) and volume-limited (Young et al. 2011; Alatalo et al. 2013) samples of nearby ETGs, respectively. In the latter survey, Young et al. (2011) detect CO emission in about a quarter of their galaxies, and Young et al. (2014) determine that $\sim 40\%$ of nearby ETGs harbor significant ($\gtrsim 10^8\ M_\odot$) molecular and/or atomic gas reservoirs. Nearly half of the ATLAS^{3D} galaxies with interferometric detections (just over 10% of their full sample) have disk-like CO morphologies, while the rest show ring-like and non-axisymmetric CO structures (Alatalo et al. 2013). Even at moderate resolution (beam FWHM $\gtrsim 3''$, corresponding to $\sim$ kpc scales), these mm-wavelength interferometric observations demonstrate that disk-like CO morphologies tend to correlate with regular gas rotation in ETGs. The gas kinematic axes are typically aligned with the galaxy photometric axes, although often with moderate ($\sim 30^\circ$) disk warping. Higher resolution ($\sim 0\farcs25$) observations confirm low turbulent velocity dispersions (~ 10 km s^{-1}) on scales of a few tens of parsecs from the galaxy centers (e.g., Utomo et al. 2015). ATLAS^{3D} galaxies with regular, circularly rotating molecular gas disks tend to have coincident, morphologically round dust features, indicating that dust morphology is tied to the dynamical coldness of the underlying gas disk.

Prior to early science observations with the ALMA, only a few ETGs were suitable candidates for BH mass measurements using other arrays. The previous generation of mm/sub-mm interferometers could resolve r_g for many nearby ETGs (Davis 2014), but only a small

percentage of these galaxies have detectable quantities of rapidly rotating cold gas in their nuclei. In the first successful case, Davis et al. (2013) observed CO kinematics from within $r_{\rm g}$ and demonstrated the capacity of cold molecular gas to constrain BH masses. At its full capability, ALMA now delivers about an order of magnitude increase in sensitivity and angular resolution over previous arrays. Even in configurations with sub-km maximum baselines, this array is capable of routinely measuring gas kinematics within $\sim r_{\rm g}$ for many nearby ETGs.

In addition to resolving gas kinematics to pursue BH mass measurements, such ALMA observations are capable of probing molecular gas morphologies and chemistries, along with continuum properties, for a statistically significant number of early-type galaxy nuclei. For example, using resolved gas kinematics and derived radial mass profiles reveals whether the molecular gas disks are (at least formally) stable against gravitational fragmentation and the likelihood they host recent/ongoing star formation (Toomre 1964). Observations of certain chemical tracers are expected to yield accurate column density measurements and estimates of gas-phase metallicities across the disks (Bayet et al. 2012). Thermal continuum and CO isotopologue measurements will together place spatially-resolved constraints on gas and dust temperatures, H_2 volume densities, gas-to-dust ratios, and the CO-to-H_2 conversion factor; the last of these is not well understood for ETGs or for the inner $\sim$ kpc of galaxies in general (Sandstrom et al. 2013).

In ALMA Cycle 2, we began a program to determine sub-arcsecond scale ^{12}CO(2$-$1) morphologies and kinematics in ETGs following a two-step process. First, we obtain sufficiently high angular resolution observations to detect high-velocity gas originating from within the BH sphere of influence. Then, when such gas is found, we conduct deeper, higher-resolution ALMA observations to map out the disk kinematics within $r_{\rm g}$ and accurately measure the BH masses. In this ongoing program, we select targets from the larger sample of dust-disk ETGs that have large (estimated) $r_{\rm g}$. In this chapter, we describe ALMA observations of

twenty-three of our currently observed galaxies and characterize their CO(2−1) emission and kinematics. For the first seven galaxies observed in Cycle 2, we also present their resolved and unresolved continuum properties. Dynamical modeling for one galaxy has already been presented (Barth et al. 2016b,a) and future work will focus on modeling the CO(2−1) kinematics for the remainder of the sample.

3.1 Sample Selection

Targets for these Cycles 2 through 5 observations were selected from ETG candidates with morphologically round dust disks as seen in *HST* images. Ho et al. (2002) demonstrated that the presence of circularly symmetric dust lanes in S0 and late-type galaxies tends to correlate with regular, symmetric ionized gas velocity fields, and we expect this trend to hold for their molecular gas kinematics. We imposed an additional selection criterion that the estimated angular $r_{\rm g}$ sizes should be large (here, $\gtrsim 0\farcs3$) in projection along the major axis as $M_{\rm BH}$ measurements are easiest for galaxies having large projected $r_{\rm g}$. The candidates observed in Cycle 2 as part of Program 2013.1.00229.S are NGC 1332, NGC 1380, NGC 3258, NGC 3268, NGC 6861 and IC 4296. In Program 2013.1.00828.S, ALMA observed NGC 4374 (M84), while data for an additional object were not taken. In Cycle 3, program 2015.1.00878.S observed NGC 2872, NGC 3078, NGC 3557, NGC 4697, NGC 4786, and NGC 5838. In Cycle 4, program 2016.1.01010.S obtained imaging of CEGs NGC 384, PGC 11179, and UGC 2698. Finally, program 2017.1.00301.S in Cycle 5 covered ETGs NGC 3245, NGC 3271, NGC 3585, NGC 4261, NGC 5193, ESO 208-G21, and ESO 322-G08. Three additional galaxy nuclei remain to be observed in Cycle 5.

These targets are luminous (typically $M_{K_s} \lesssim -24$ mag), nearby ($D_L \sim 12$ to 100 Mpc; $z \sim 0.0034$ to 0.023) galaxies whose closest large neighbors usually lie $\gtrsim 2'$ away in projection. Luminosity distances (D_L; see Table 3.1) for sixteen galaxies were derived using distance

moduli measured by surface brightness fluctuations (Mei et al. 2000; Tonry et al. 2001; Jensen et al. 2003), supplemented with estimates for three galaxies made using the Fundamental Plane (Willick et al. 1997; Lauer et al. 2007b) and for one from the Tully-Fisher relationship (Theureau et al. 2007). Approximate D_L values for the three CEGs were adopted from Yıldırım et al. (2017). The dust disks are very apparent in *HST* structure maps (e.g., see Figure 3.1), which highlight clumpy and filamentary dust (Pogge & Martini 2002). For the Cycle 2 sample, we also constructed two-band *HST* color maps (e.g., F555W−F814W; also Figure 3.1), which show more smoothly distributed dust. The NGC 4374 color map reveals that, beyond $\sim 1''$ from the nucleus, the dust is concentrated in an asymmetric dust lane. Despite its somewhat irregular dust morphology, we included NGC 4374 in our sample as *HST* spectroscopy shows ionized gas in regular rotation within the central $0\farcs5$ (e.g., Bower et al. 1997; Walsh et al. 2010), and ALMA offers the possibility of carrying out a direct comparison of circumnuclear CO and ionized gas kinematics.

Seven of these ETGs have prior $M_{\rm BH}$ measurements. The NGC 1332 BH mass was previously measured to be $(1.45 \pm 0.20) \times 10^9\ M_\odot$ using stellar dynamical modeling (Rusli et al. 2011), while Humphrey et al. (2009) find a much lower mass of $(0.52^{+0.41}_{-0.28}) \times 10^9\ M_\odot$ using X-ray gas hydrostatic equilibrium constraints. The BHs in NGC 3585 and NGC 6861 were also measured with stellar dynamical modeling to have masses of $(3.4^{+1.5}_{-0.6}) \times 10^9\ M_\odot$ (Gültekin et al. 2009) and $(2.0 \pm 0.2) \times 10^9\ M_\odot$ (Rusli et al. 2013b). The BHs in NGC 3245, NGC 4261, and NGC 4374, and IC 4296 were measured to have masses of $(2.1 \pm 0.5) \times 10^8\ M_\odot$ (Barth et al. 2001), $(4.9 \pm 1.0) \times 10^8\ M_\odot$ (Ferrarese et al. 1996), $(9.25^{+0.98}_{-0.87}) \times 10^8\ M_\odot$ (Walsh et al. 2010) and $(1.34^{+0.21}_{-0.19}) \times 10^9\ M_\odot$ (Dalla Bontà et al. 2009), respectively, using ionized gas dynamical modeling. In the first BH mass measurement to resolve $r_{\rm g}$ with ALMA, Barth et al. (2016a) model high-resolution ($0\farcs044$) Cycle 3 NGC 1332 CO(2−1) observations and determine its BH mass to be $(6.64^{+0.65}_{-0.63}) \times 10^8\ M_\odot$. Based solely on averages over several velocity dispersion measurements in the HyperLeda catalog (Makarov et al. 2014; see Table 3.1) and the $M_{\rm BH} - \sigma_\star$ relationship (Kormendy & Ho 2013), the remaining sixteen

ETGs have expected BH masses ranging from $\sim (0.08 - 4.2) \times 10^9\ M_\odot$. The projected r_g for our sample range between $\sim 0\farcs14$ and $0\farcs71$ and should be at least nearly resolved with the ALMA observations presented here.

3.2 Observations and Imaging

Our ALMA Band 6 observations consisted of single pointings with three ~ 2 GHz bandwidth spectral windows, the first centered on the redshifted ^{12}CO$(2-1)$ 230.538 GHz line and the remaining two measuring the continuum at observed frequencies of ~ 226 and ~ 245 GHz. Targets were observed with channel widths of $0.49 - 3.91$ MHz and 15.6 MHz (corresponding to velocity channel widths of $0.62 - 5.09$ and 19.8 km s^{-1}) for the line and continuum spectral windows, respectively. The observations were flux calibrated using Titan, Ceres, and Ganymede when available, supplemented with ALMA quasar catalog sources (such as J0334−4008 and J2056−4719) when no solar system standards were nearby. These flux standards combine to give $\lesssim 10\%$ flux scale uncertainty at any time (Fomalont et al. 2014). We therefore propagate a 10% uncertainty into all flux and flux density measurements. Data were processed using versions 4.2.2, 4.5, 4.7.2, and 5.1.1 of the Common Astronomy Software Application (CASA; McMullin et al. 2007) and the ALMA pipeline. Image deconvolution was performed using the CASA CLEAN task. As each target possesses a nuclear continuum source, we applied continuum phase self-calibration to most of the data sets with the exception of NGC 384, NGC 3245, NGC 3271, NGC 3258, NGC 3585, NGC 5193, PGC 11179, and UGC 2698, whose nuclear continuum dynamical ranges did not improve with self-calibration. We also applied amplitude self-calibration to the data sets of four of the brightest continuum sources, NGC 3557, NGC 4261, NGC 4374 and IC 4296. On-source integration times ranged from 20 to 50 minutes, with typical rms noise levels of ~ 400 μJy beam^{-1} per 20 km s^{-1} channel, and ~ 40 μJy beam^{-1} after imaging of the continuum spec-

Table 3.1 Galaxy Sample Characteristics

Galaxy	Type	M_{K_s} (mag)	$\sigma_\star$ (km s^{-1})	D_L (Mpc)	$v_{\rm sys}$ (km s^{-1})	Scale (pc/arcsec)	b / a (dust) ($''$)
(1)	(2)	(3)	(4)	(5)	(6)	(7)	(8)
Cycle 2							
NGC 1332	S0	−24.69 (0.17)	313	22.3 (1.8)	1524	107	0.28 / 2.1
NGC 1380	SA0	−24.30 (0.17)	211	17.1 (1.4)	1877	82	1.5 / 4.8
NGC 3258	E1	−24.21 (0.25)	257	31.9 (3.9)	2792	148	0.7 / 1.1
NGC 3268	E2	−24.50 (0.24)	235	33.9 (3.9)	2800	161	1.2 / 2.4
NGC 4374	E1	−25.04 (0.11)	275	17.9 (0.9)	1017	86	0.35 / 1.5
NGC 6861	SA0	−24.47 (0.33)	414	27.3 (4.5)	2829	130	2.0 / 8.0
IC 4296	E	−25.88 (0.16)	329	47.4 (3.7)	3737	213	0.25 / 0.8
Cycle 3							
NGC 2872	E2	−24.65 (0.37)	273	47.4 (8.7)[a]	3196	225	0.16 / 0.35
NGC 3078	E2/3	−24.85 (0.28)	243	35.2 (4.9)	2580	168	0.13 / 0.63
NGC 3557	E3	−26.10 (0.21)	266	45.7 (4.6)	3088	217	0.59 / 0.97
NGC 4697	E6	−23.99 (0.14)	165	11.8 (0.8)	1241	57	0.81 / 3.4
NGC 4786	cD pec	−25.27 (0.37)	286	62.8 (11.6)[a]	4647	296	0.32 / 0.61
NGC 5838	SA0	−24.15 (0.34)	274	22.2 (3.8)[a]	1341	107	1.7 / 4.1
Cycle 4							
NGC 384	E3	−23.83 (0.06)	244	59 (1)[c]	4233	277	1.22 / 2.07
PGC 11179	S0	−23.45 (0.06)	291	94 (2)[c]	6861	437	1.05 / 2.04
UGC 2698	E	−25.18 (0.07)	363	89 (2)[c]	6421	415	0.38 / 0.78
Cycle 5							
NGC 3245	SA0	−23.74 (0.19)	207	20.9 (1.9)	1326	100	0.7 / 1.5
NGC 3271	SB0	−25.47 (0.37)	247	53.3 (9.8)[b]	3804	252	1.0 / 1.7
NGC 3585	E6	−24.80 (0.17)	212	20.0 (1.7)	1434	96	0.1 / 0.45
NGC 4261	E2/3	−25.24 (0.19)	297	31.6 (2.8)	2212	151	0.4 / 0.90
NGC 5193	E pec	−24.67 (0.15)	204	46.8 (3.2)	3711	222	0.4 / 1.0
ESO 208-G21	SAB0	−22.79 (0.20)	148	13.6 (1.3)	1085	66	0.7 / 3.8
ESO 322-G08	SA0	−24.05 (0.47)	202	37.3 (9.0)	2996	178	1.8 / 5.9

Note: Col. (2): Galaxy type, taken from de Vaucouleurs et al. (1991). Col. (3): K_s-band magnitude and uncertainty from the 2MASS catalogue (Skrutskie et al. 2006), including the uncertainty in the luminosity distance D_L. Col. (4): Central stellar velocity dispersion from the HyperLeda database (Makarov et al. 2014). Col. (5): Luminosity distance and uncertainties determined primarily from surface brightness fluctuations by Mei et al. (2000), Tonry et al. (2001), and Jensen et al. (2003) including a Cepheid zero-point correction (Mei et al. 2005), supplemented with those measured using the Fundamental Plane (Willick et al. 1997; Lauer et al. 2007a; *a*) and Tully-Fisher (Theureau et al. 2007; *b*) relations, and those (*c*) adopted from Yıldırım et al. (2017). Col. (6): Systemic velocity $v_{\rm sys}$ taken from the NASA/IPAC Extragalactic Database (NED). Col. (7): Angular scale derived from the assumed D_L. Col. (8): Dust disk minor/major axis radii typically measured from two-band *HST* color images. For NGC 4374, these values are of the central dust disk and do not include the large-scale dust lane.

tral window data into a single image. The average angular resolution of these observations range between $\sim 0\farcs15$ and $0\farcs48$ (see Table 3.2), corresponding to a typical projected spatial resolution of ~ 50 pc.

The continuum of each measurement set was imaged using both natural weighting for the greatest sensitivity to faint, extended emission, and Briggs weighting (Briggs 1995) with robustness parameter $r = 0.5$ for a good trade-off between resolution and sensitivity. We further explored the frequency dependence of the continuum by imaging the visibilities into multiple, separate continuum-only spectral window images. To isolate the molecular emission, the continuum contributions were first removed in the *uv* plane from the spectral window containing the CO(2−1) line. The resultant continuum-subtracted visibilities were then imaged into data cubes using Briggs weighting ($r = 0.5$) with 20 km s^{-1} channels if we observe high S/N CO emission, and 40 km s^{-1} channels using natural weighting otherwise. Velocities were calculated in the barycentric frame using the optical definition of radial velocity. Spatial pixel sizes varied for each target and were chosen to adequately sample the beam minor axis.

3.3 CO(2−1) Properties

Inspection of the continuum-subtracted image cubes reveals significant CO(2−1) line emission across many channels for nearly all of these twenty-three ETGs. We also detect both CO(2−1) emission (at low S/N) and absorption in NGC 4374 and IC 4296, while only faint line emission for NGC 3585 and NGC 4261. Figure 3.1 shows integrated intensity maps for the Cycle 2 targets, made by summing the image cubes over the channel ranges that show line emission. For the two galaxies in this subsample that have faint CO emission, the intensity maps show the cubes collapsed over ±400 km s^{-1} from the systemic velocity ($v_{\rm sys}$). Within the primary beam half-power width ($\sim 25''$), no CO line emission is detected outside these

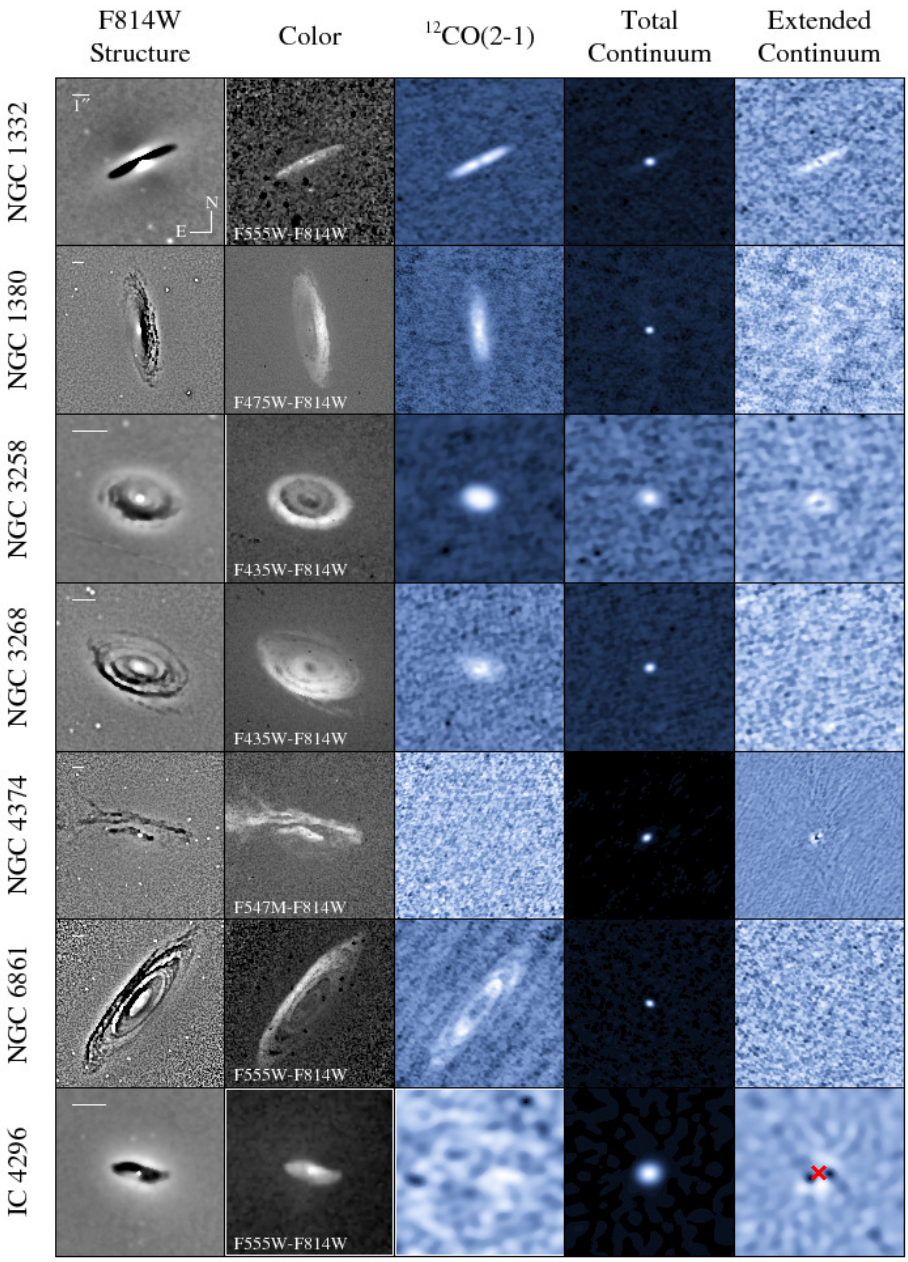

Figure 3.1 Comparison of *HST* structure (Pogge & Martini 2002) and two-band color maps with the ALMA Cycle 2 CO(2-1) emission line and ~ 236 GHz continuum images. *HST* images are in linear gray scale while the ALMA images are displayed logarithmically. Bright regions in the structure maps indicate an excess of light, and darker regions in the color maps indicate bluer colors. The $1''$ angular scale bar in each *HST* structure map applies to the subsequent ALMA images. Structure and color maps reveal regular dust disk morphology in all cases, and dust lanes for NGC 4374 at radii past $r \gtrsim 1''$. The CO(2−1) intensity maps are constructed by collapsing the ALMA data cubes over velocity channels that show (or are expected to show) CO emission. Continuum maps are constructed by imaging the spectral windows over all channels that do not contain line emission. The extended continuum images are residual maps after modeling (and subtracting) the central peak continua in the *uv* plane. Point-source over-subtraction of the bright IC 4296 nucleus (at the location of the "×") leads to the east-west imaging artifacts alongside its real extended continuum emission.

Table 3.2 ALMA Observational Parameters

Galaxy (1)	Obs. Date (2)	$t_{\rm obs}$ (min) (3)	Baseline (m) min / max (4)	$b_{\rm maj}$ / $b_{\rm min}$ ($''$) (5)	Freq. Range / Bandwidth (GHz) (6)	Self-Cal (7)
			Cycle 2			
NGC 1332	2014-09-01	22.3	33 / 1091	0.32 / 0.23	226.4 – 246.1 / 5.9	p
NGC 1380	2015-06-11 2015-09-18	22.8	21 / 783 41 / 2125	0.24 / 0.18	226.2 – 245.9 / 5.9	p
NGC 3258	2014-07-21 2015-06-12	22.4	18 / 784 21 / 784	0.48 / 0.40	225.5 – 245.1 / 5.9	–
NGC 3268	2014-07-21 2015-06-12	22.3	18 / 784 21 / 784	0.45 / 0.40	225.5 – 245.1 / 5.9	p
NGC 4374	2015-08-16	50.9	43 / 1574	0.35 / 0.26	227.2 – 246.6 / 7.9	ap
NGC 6861	2014-09-01	23.9	34 / 1091	0.32 / 0.23	225.5 – 245.1 / 5.9	p
IC 4296	2014-07-22	29.6	18 / 780	0.52 / 0.43	224.8 – 244.4 / 5.9	ap
			Cycle 3			
NGC 2872	2016-07-21	21.7	15 / 1090	0.36 / 0.29	212.0 – 231.5 / 7.8	p
NGC 3078	2016-07-21	19.7	15 / 1090	0.44 / 0.28	212.0 – 231.5 / 7.8	p
NGC 3557	2016-07-21	19.7	15 / 1090	0.37 / 0.26	212.0 – 231.1 / 7.8	ap
NGC 4697	2016-07-23	20.7	15 / 1110	0.29 / 0.27	213.0 – 232.5 / 7.8	p
NGC 4786	2016-07-23	20.2	15 / 1110	0.35 / 0.27	226.1 – 244.8 / 7.8	p
NGC 5838	2016-06-22 2016-08-18	21.2 21.2	15 / 704 15 / 1462	0.30 / 0.28	213.0 – 232.3 / 7.8	p
			Cycle 4			
NGC 384	2016-10-13	27.2	16 / 3143	0.30 / 0.16	226.4 – 244.0 / 5.9	–
PGC 11179	2017-07-08	25.2	16 / 2647	0.29 / 0.16	224.4 – 242.1 / 5.9	–
UGC 2698	2017-08-19	34.3	21 / 3696	0.20 / 0.10	224.7 – 242.6 / 5.9	–
			Cycle 5			
NGC 3245	2017-12-28	42.3	15 / 2516	0.23 / 0.17	226.5 – 246.2 / 7.8	–
NGC 3271	2018-01-17	29.2	15 / 1397	0.28 / 0.27	224.7 – 244.2 / 7.8	–
NGC 3585	2018-01-17	29.2	15 / 1397	0.32 / 0.25	226.5 – 246.2 / 7.8	–
NGC 4261	2018-01-19	31.2	15 / 1397	0.31 / 0.28	225.9 – 245.5 / 7.8	ap
NGC 5193	2018-01-15	28.7	15 / 2386	0.26 / 0.23	224.8 – 244.4 / 7.8	–
ESO 208-G21	2018-01-15	31.2	15 / 2386	0.29 / 0.21	226.7 – 246.4 / 7.8	p
ESO 322-G08	2018-01-18	29.2	15 / 1397	0.29 / 0.25	225.9 – 245.5 / 7.8	p

Note: Properties of the ALMA observations. Col. (3): On-source integration time. Col. (4): Minimum and maximum baselines of the specific array configurations. Col. (5): Synthesized beam major and minor axes FWHM when using natural weighting for CO-faint galaxies NGC 4374 and IC 4296, and Briggs weighting ($r = 0.5$) for the remainder. Col. (6): Frequency range including the continuum basebands, followed by the combined bandwidth of all spectral windows. Col. (7): Indicates phase-only (p) or amplitude and phase (ap) continuum self-calibration.

dust disk regions. In the next section, we discuss the emission properties of the CO-bright subsample, and afterwards we investigate the emission and absorption characteristics of the four CO-faint targets.

3.3.1 CO-Bright Galaxies

The bright CO(2−1) emission seen in Cycle 2 galaxies NGC 1332, NGC 1380, NGC 3258, NGC 3268, and NGC 6861 directly coincides with optically thick dust disks as seen in the structure maps of the corresponding optical *HST* images; initial inspection of archival *HST* imaging of the remaining ALMA targets appears consistent with their molecular emission spatial extent. Image cubes reveal clear rotation about the nuclear continuum sources. To visualize their rotational properties, we integrated the flux densities in each channel over the elliptical regions coinciding with the optical dust disks. These CO velocity profiles (shown in Figures 3.2 through 3.5) exhibit nearly symmetric double-horned features characteristic of rotating disks with emission ranging between (a line-of-sight) ±300 and ±500 km s^{-1} from $v_{\rm sys}$. We also constructed a position-velocity diagram (PVD; also shown in Figures 3.2 through 3.5) for each galaxy by extracting a slice along the major axis as determined from the average disk position angle (measured in §3.3.1). Extraction widths were set to the CLEAN beam FWHM projected along the disk major axis. A central rise in the PVD envelope to high velocity at small radius, which indicates a massive, compact object at the disk center, is unambiguously observed only in PVDs for NGC 1332, NGC 3258, NGC 3557, and ESO 208-G21, with a marginal detection in NGC 1380 and NGC 4697 within the central $\sim 0\farcs1$. (Note also the very strong upturn seen in borderline CO-faint galaxy NGC 4261.) The NGC 6861 PVD shows a clear $\sim 2''$−wide hole in CO emission; for NGC 384, NGC 5193, and NGC 5838 we see evidence for a similar lack of emission on small scales.

For a disk whose line emission primarily originates within the sphere of influence of a mas-

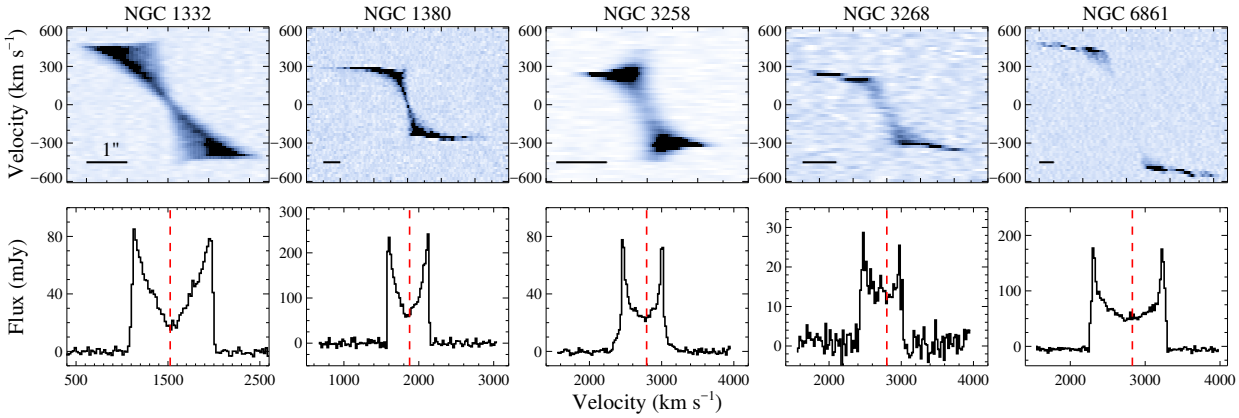

Figure 3.2 *Top*: CO(2−1) position-velocity diagrams (PVDs) for the Cycle 2 CO-bright galaxies, extracted with a width equal to the synthesized beam FWHM projected onto the disk major axis. To bring out faint emission, we display these PVDs using a negative, arcsinh color scale. Central velocity upturns are observed in NGC 1332 and NGC 3258, with the possible addition of NGC 1380. *Bottom*: Velocity profiles of these targets, formed by spatially integrating over the optical dust disk regions for each 20 km s^{-1} wide channel. The dashed lines indicate the host galaxy $v_{\rm sys}$, as reported in the NASA/IPAC Extragalactic Database (NED).

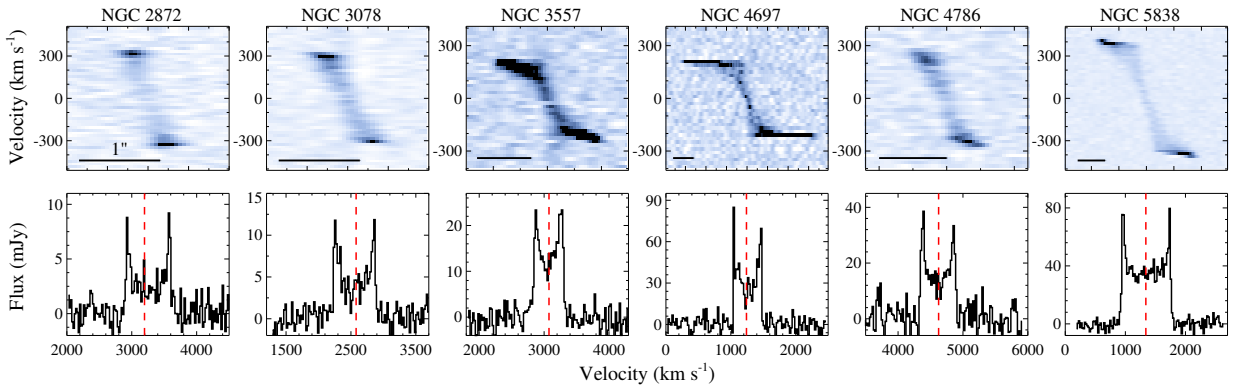

Figure 3.3 CO(2−1) PVDs and velocity profiles for the Cycle 3 CO-bright galaxies, extracted in the same manner as the Cycle 2 sample.

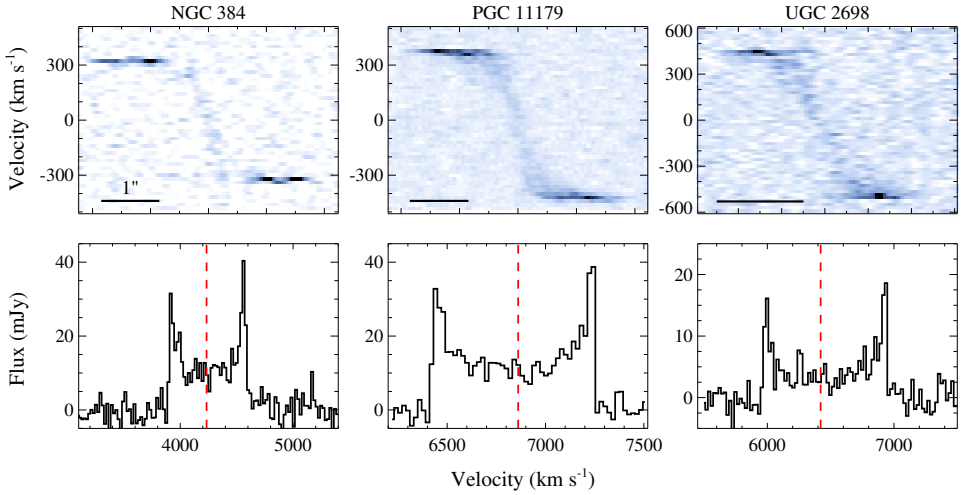

Figure 3.4 CO(2−1) PVDs and velocity profiles for the Cycle 4 CO-bright galaxies, extracted in the same manner as the Cycle 2 sample.

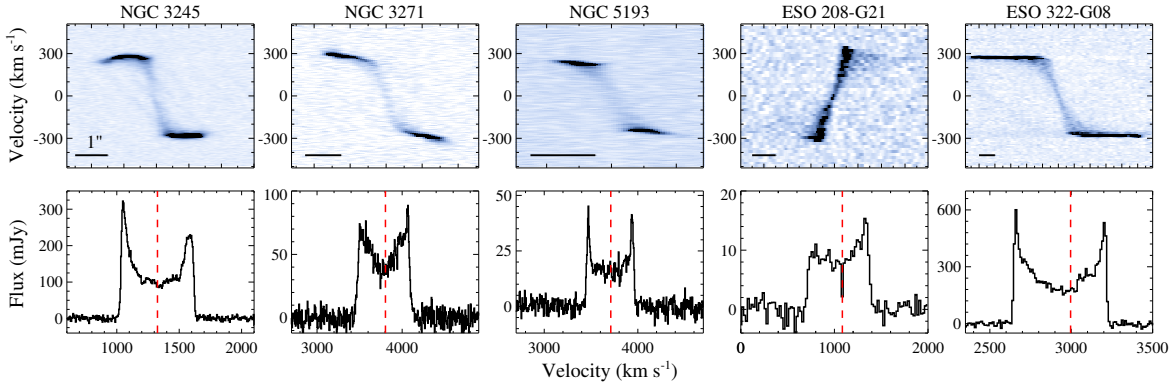

Figure 3.5 CO(2−1) PVDs and velocity profiles for the Cycle 5 CO-bright galaxies, extracted in the same manner as the Cycle 2 sample.

sive object, the double-horned peaks in its velocity profile suggest near-perfect Keplerian rotation. This is not the case for the roughly kpc-scale disks in our CO-bright sample. Comparing the velocity profiles to the PVDs, we find that most of the contributions to the peaks of the double-horned profiles originate far ($\gtrsim$ 100 pc) from the disk centers, at which radii the extended stellar mass profiles typically dominate over the BH mass. At velocities beyond these peaks (e.g., for NGC 1380, NGC 3268, NGC 6861, and ESO 208-G21), the sharp decline in integrated flux density is the result of flat (or nearly flat) rotation curves in the outer disk regions. The Keplerian velocity signatures detected in the PVDs of NGC 1332, NGC 3258, NGC 3557, and ESO 208-G21 appear only as faint, high-velocity wings in their respective velocity profiles.

CO surveys conducted with single-dish telescopes generally cannot resolve circumnuclear gas disk rotation within nearby galaxies, although velocity profiles from these observations can determine line luminosities (or upper limits) and velocity ranges for a substantial number of ETGs. Such surveys have shown, for instance, that the CO detection rate may be slightly environment-dependent (i.e., field vs. cluster; Young et al. 2011) and that the CO emission velocity width strongly correlates with the host galaxy mass (the CO Tully-Fisher relationship; Ho 2007; Davis et al. 2011a). However, the detection of a double-horned profile in low angular resolution observations does not necessarily indicate that the galaxy will be a good candidate for $M_{\rm BH}$ determination. These CO-bright PVDs demonstrate that the line emission originating from within $r_{\rm g}$ is generally faint, and is not detected beyond a deprojected velocity of $\sim$ 600 km s^{-1} for these five galaxies. In the absence of strong, broad ($\sim$ 1000 km s^{-1} from $v_{\rm sys}$) velocity wings, spatially resolved data are necessary to confidently detect the BH kinematic signature. Based on PVDs from Cycles 2 through 5, we find that interferometric observations with a spatial resolution that corresponds to $\sim r_{\rm g}$ appear to be sufficient to identify high-velocity, central gas emission.

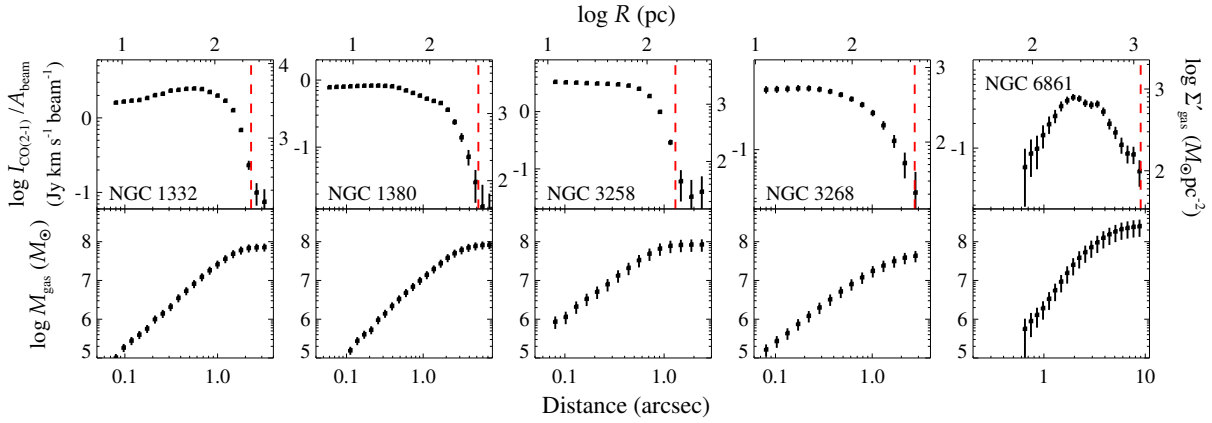

Figure 3.6 Radial CO(2−1) surface brightness profiles for the Cycle 2 group (*top*), averaged on elliptical annuli using average position angles and axis ratios from Table 3.5. The right vertical axes indicate the corresponding projected surface mass densities in units of $M_\odot$ pc^{-2}. The dashed lines show the radial extent of the optically opaque dust features in the *HST* images. Cumulative gas mass profiles (*bottom*) assuming $\alpha_{\rm CO} = 3.1\ M_\odot$ pc^{-2} (K km s^{-1})$^{-1}$ and incorporating the expected helium contributions.

Line Profile Fitting

To characterize the velocity fields of the nineteen CO-bright disks, we parametrize the line profiles at each spatial pixel with Gauss-Hermite (GH) profiles (van der Marel & Franx 1993), including the flux, Gaussian line-of-sight (LOS) velocity $v_{\rm LOS}$ and dispersion $\sigma_{\rm LOS}$, and higher-order terms (h_3, h_4, ...) that account for symmetric (even terms) and anti-symmetric (odd) deviations from a purely Gaussian profile. The $\sim 0\farcs3$−resolution beam size entangles CO emission across large ($\sim$ 50 pc) physical regions. Especially near the nucleus, emission from a wide range of intrinsic velocities becomes spectrally and spatially blended. Within their central beam areas, the PVDs show broad velocity envelopes with complex and asymmetric line profiles (see Barth et al. 2016b). We use h_3 and h_4 components in all spectral fits, and include h_5 and h_6 when modeling the more complicated and higher S/N line profiles in NGC 1332 and NGC 3258 for which h_5 and h_6 remain large outside of the central beam area. To measure line parameters with higher precision, adjacent spectra are combined together based on their line S/N using the Voronoi binning method (Cappellari & Copin 2003). This spatial binning primarily affects regions near the edge of the CO-emitting

disks, although it also proves useful for the central 2″ of NGC 6861 and for fainter CEG disks in NGC 384 and UGC 2698. There are no *a priori* limits on these GH coefficients, especially given the level of beam smearing. We fix limits of $|h_3, h_4| < 0.35$ (and $|h_5, h_6| < 0.25$ when fitting the NGC 1332 and NGC 3258 emission) that allows for reasonable line profile fits while avoiding model line shapes with strong double-peaked features. We determine the formal uncertainty of each GH term by adding random Gaussian noise to each Voronoi-binned spectrum with dispersion equal to the line residual standard deviation of its GH profile fit. The resampled spectrum is again fit with a GH profile to measure new line parameters; this process is repeated several hundred times for each binned spectrum, and we set the formal uncertainties of each coefficient to the standard deviation of all its resampled fit values.

Maps of the CO(2−1) line flux, $v_{\rm LOS}$ and $\sigma_{\rm LOS}$, and GH coefficients are shown for each galaxy in Figures 3.7 through 3.10. Line flux in the observed frame (in Jy km s^{-1}) for each binned spectrum is determined by integrating the profile between $v_{\rm LOS} \pm 3\sigma_{\rm LOS}$. The CO(2−1) flux maps are spatially coincident with, and similar in shape to, the optical dust disks. In addition to essentially smooth emission (in NGC 3245, NGC 3258, and NGC 4786), these flux maps also reveal the presence of rings (in NGC 384, NGC 3271, NGC 5193, NGC 5838, and NGC 6861), small-scale central CO deficits (in NGC 1332, NGC 6861,ESO 208-G21, and ESO 322-G08), and large-scale clumps (in NGC 3078, NGC 3268, and NGC 3557). Cycles 3 and 4 observations of the respective molecular disks of NGC 1332 at $\sim 0\farcs044$ resolution (Barth et al. 2016a) and NGC 3258 at $\sim 0\farcs1$ resolution (see Chapter 4) do show significantly more CO(2−1) substructure than their Cycle 2 flux maps, suggesting that clumpy emission on $10 - 20$ pc scales is standard for these circumnuclear disks.

The molecular gas kinematics of the five CO-bright galaxies are dominated by regular, disk-like rotation. For the Cycle 2 subsample, we characterize deviations from coplanar, circular rotation in Figures 3.11 and 3.12. Visual inspection shows moderate kinematic warping in

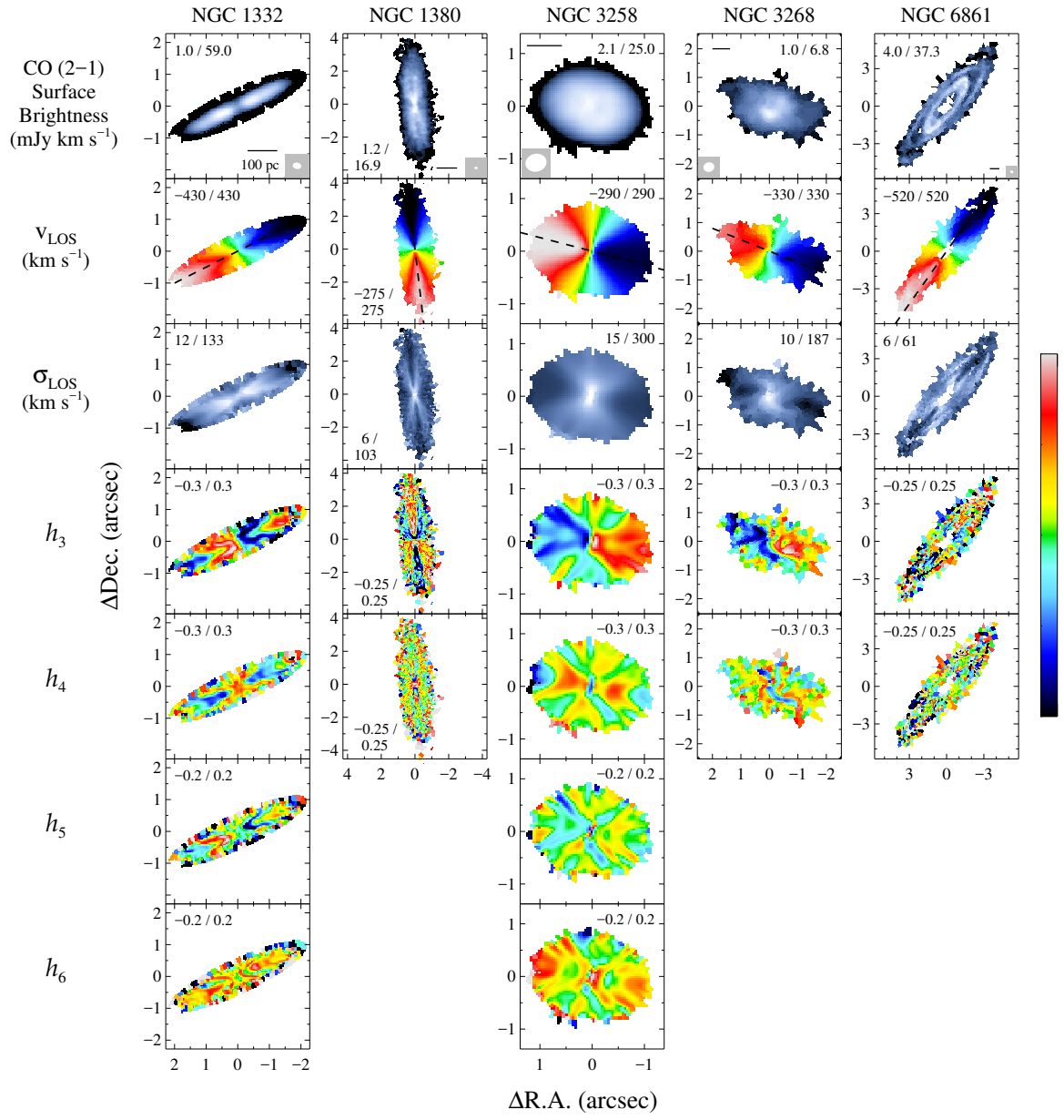

Figure 3.7 CO(2−1) line parameters for the Cycle 2 CO-bright galaxies, parametrized using Gauss-Hermite (GH) polynomials. Shown are the CO(2−1) surface brightness maps, along with maps for the line-of-sight velocity $v_{\rm LOS}$ and dispersion $\sigma_{\rm LOS}$, and GH moments from h_3 up to h_6. The galaxy systemic velocities have been removed from $v_{\rm LOS}$. The scale bar in each CO flux map denotes a physical 100 pc, and alongside is shown the beam size. At the disk edges (largely undisplayed) and near the center of NGC 6861, the individual spectra were Voronoi binned spatially to achieve sufficient S/N to fit the line profiles. For each target, its kinematic maps are displayed down to the flux limit where its $v_{\rm LOS}$ field remains well behaved. The values provided alongside the parameter maps are the minimum and maximum data values that correspond to the ranges in intensity or color. Superimposed dashed lines on each $v_{\rm LOS}$ profile are the stellar photometric major axes position angles measured from *HST* images.

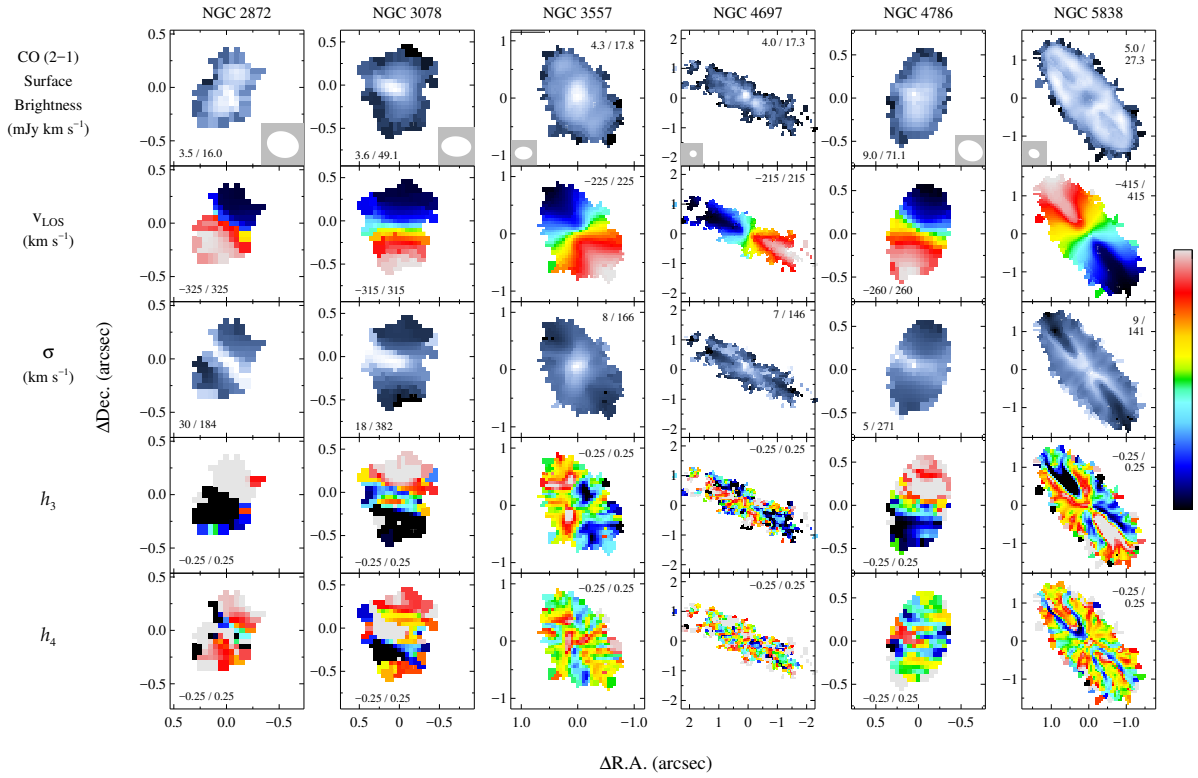

Figure 3.8 CO(2−1) line parameters for the Cycle 3 CO-bright galaxies, as for the Cycle 2 sample, shown for GH moments up to h_4.

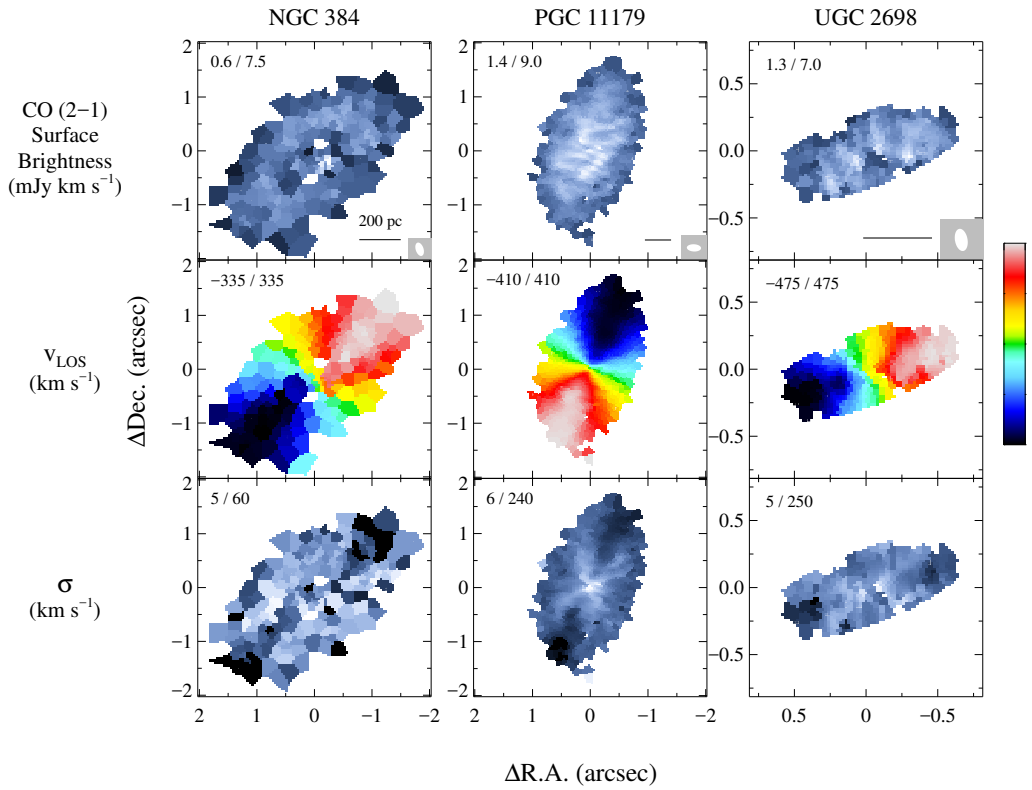

Figure 3.9 CO(2−1) line parameters for the Cycle 4 CO-bright galaxies, as for the Cycle 2 sample, without including higher-order (h_3 and h_4) GH moments in the line-profile fitting.

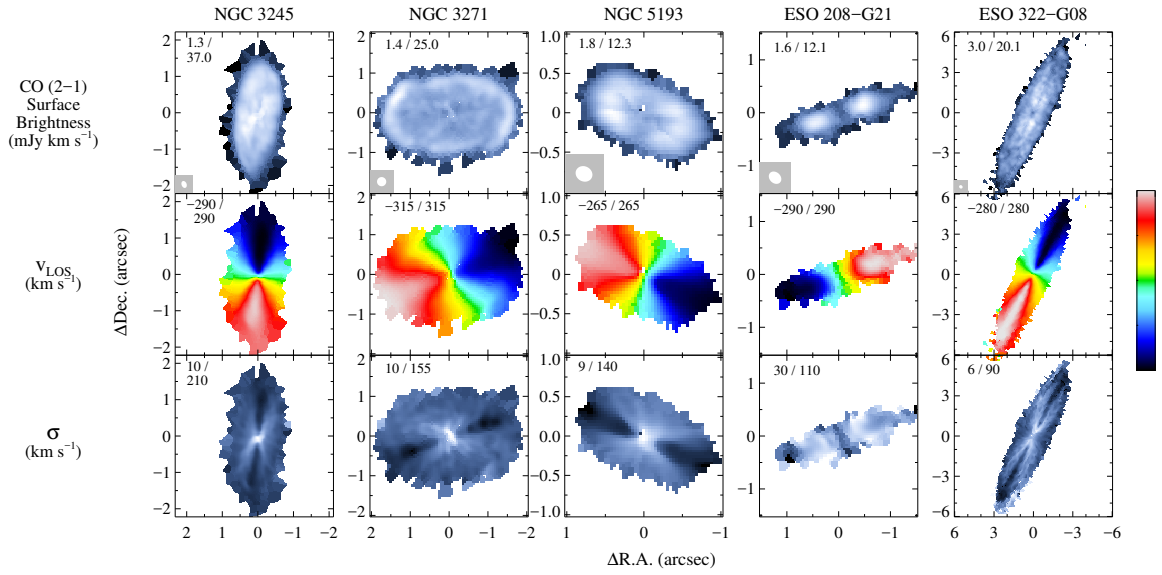

Figure 3.10 CO(2−1) line parameters for the Cycle 5 CO-bright galaxies, as for the Cycle 2 sample, without including higher-order (h_3 and h_4) GH moments in the line-profile fitting.

NGC 384, NGC 3245, NGC 3271, NGC 3268, and ESO 208-G21; the disk kinematics for the remaining CO-bright subsample appear to be fairly relaxed. In all cases, stellar photometric major axis position angles (PAs), measured from the inner several kpc of *HST* images, agree to within $\lesssim 5°$ with the average CO kinematic axes. This does not necessarily mean that the molecular gas is aligned with the stellar kinematics, since mismatches between *stellar* photometric and kinematic axes can exist in ETGs. However, Krajnović et al. (2011) find that the stellar photometric and kinematic axes nearly always agree to within $\sim 10°$ for fast-rotating ETGs. In addition, luminous ($M_{K_s} \lesssim -24$ mag) ETGs with molecular (and/or H I, H II) gas nearly always show kinematic alignment between stellar and gaseous rotation (Davis et al. 2011b). For the Cycle 2 galaxies, previously published IFU spectroscopy of NGC 1332 (Rusli et al. 2011), NGC 1380 (Ricci et al. 2014), and NGC 6861 (Rusli et al. 2013b) shows that their molecular gas disks co-rotate (to an accuracy of $\lesssim 5°$) with respect to their stars. Spatially resolved stellar kinematics are not currently available for NGC 3258 and NGC 3268. For those of the remaining CO-bright ETGs that have appreciable stellar rotation, we anticipate good agreement between the observed molecular gas kinematics and

any net galaxy rotation.

Line dispersions generally increase towards the disk kinematic centers due to beam smearing. The exceptions are NGC 384, NGC 1332, NGC 6861, UGC 2698, and ESO 208-G21, all of which appear to possess low (if any) CO surface brightness in their central beam areas. X-shaped features appear in twelve $\sigma_{\rm LOS}$ maps, and the high CO line widths forming these features are due to beam smearing of large velocity gradients at these locations. These gradients are lowest along the major axes near the disk edges, where the observed line dispersions typically fall to between 6 and 15 km s^{-1} with measurement uncertainties of ~ 1 km s^{-1}. For comparison, the gas sound speed c_s is expected to be $\sqrt{\gamma_d k_B T_d/(\mu m_p)} \sim 0.3$ km s^{-1} for an assumed $T_d \sim 30$ K (typical for molecular gas in other ETGs; Bayet et al. 2013), specific heat $\gamma_d \sim 1$, and mean molecular mass $\mu \sim 2.5$ for the predominantly H_2+He disks. For several of these galaxies, including NGC 1380, NGC 3245 , NGC 4697, NGC 5193, NGC 5838, NGC 6861, PGC 11179, and ESO 322-G08, the measured minimum line widths ($\sigma_{\rm LOS} \lesssim 10$ km s^{-1}) are much smaller than the standard 20 km s^{-1} channel widths. We tested the accuracy of our line width fits by re-imaging the visibilities for two of the data sets – NGC 1380 and NGC 6861 – into ~ 4 km s^{-1} channels; line profile fits to these more finely sampled data cubes show line widths that agree to within ~ 1 km s^{-1} with those measured in cubes with coarser velocity channel spacing. Even though the effect is lowest near the disk edges and along the major axes, portions of the lowest observed $\sigma_{\rm LOS}$ values are still the result of beam smearing. In future work, we will detail gas-dynamical modeling to constrain the intrinsic gas line widths as a function of radius.

Surface Brightness and Mass Profiles

For the CO-bright galaxies, line intensities $I_{\rm CO(2-1)}$ integrated over the emitting areas range between ~ 5 and 150 Jy km s^{-1} (see Table 3.3). The associated H_2 mass is determined by computing $M_{\rm H_2} = \alpha_{\rm CO} L'_{\rm CO}$, where CO luminosity $L'_{\rm CO}$ is related to observables (Carilli &

Walter 2013) by:

$$L'_{\rm CO} = 3.25 \times 10^7 S_{\rm CO}\Delta v \frac{D_L^2}{(1+z)^3 \nu_{\rm obs}^2} \text{ K km s}^{-1} \text{ pc}^2 \,. \tag{3.1}$$

The utilized line intensity $S_{\rm CO}\Delta v$ is typically of the $J = 1 - 0$ transition, and D_L is the galaxy luminosity distance. We convert our integrated CO(2−1) flux measurements into H_2 masses using average R_{21} and $\alpha_{\rm CO}$ values from a sample of nearby, late-type galaxies (Sandstrom et al. 2013), assuming $R_{21} = I_{\rm CO(2-1)}/I_{\rm CO(1-0)} \approx 0.7$ (corresponding to an excitation temperature $T_{\rm ex} \sim 5 - 10$ K; e.g., Lavezzi et al. 1999) to transform the CO(2−1) line intensities into estimated CO(1 − 0) values, and using $\alpha_{\rm CO} = 3.1\ M_\odot$ pc^{-2} (K km s^{-1})$^{-1}$ as the extragalactic mass-to-luminosity ratio. The average molecular hydrogen mass for the CO-bright targets (listed in Table 3.4), is $\sim 10^8\ M_\odot$, although the most appropriate CO-to-H_2 conversion factor for our sample (or ETGs in general) is not currently known. For comparison, decomposing the Cycle 2 *HST* F814W imaging using an MGE (assuming an $I-$band mass-to-light ratio $\Upsilon_I \approx 5\ M_\odot/L_\odot$; e.g., Walsh et al. 2012) indicates a total stellar mass on the order of $10^9\ M_\odot$ when integrated out to a radius of 100 pc. In addition to substantial scatter (0.3 dex) about the average $\alpha_{\rm CO}$ for extragalactic sources, Sandstrom et al. (2013) find that this mass-to-light ratio typically decreases by a factor of ~ 2 (and in some cases by nearly an order of magnitude) in the central kpc of late-type galaxies. Given the large scatter in $\alpha_{\rm CO}$, the derived gas masses are subject to potentially large systematic uncertainties. Measuring and modeling CO spectral line energy distributions (SLEDs) for these galaxies should allow a more precise $\alpha_{\rm CO}$ determination (even using only spatially resolved, low$-J$ lines observable with ALMA; e.g., Saito et al. 2017).

The total atomic hydrogen mass of late-type galaxies often dominates the total molecular gas mass (e.g., Bigiel et al. 2008) while in ETGs the total $M_{\rm H_2} \gtrsim M_{\rm H\,I}$ (see Serra et al. 2012; Alatalo et al. 2013). Only three galaxies in our Cycle 2 subsample have H I detections or upper limits based on 21-cm observations – NGC 1332 with $\log(\ M_{\rm H\,I}/M_\odot) \sim 8.8$ (Balkowski

Table 3.3 ^{12}CO(2−1) Measurements

Galaxy (1)	RMS Noise (mJy beam^{-1}) (2)	$R_{\rm d}$ (pc) (3)	$I_{\rm CO(2-1)}$ (Jy km s^{-1}) (4)	$\Delta v_{\rm CO(2-1)}$ (km s^{-1}) (5)	W_{50} (km s^{-1}) (6)
Cycle 2					
NGC 1332	0.40	256	39.94 (3.99)	1000	880
NGC 1380	0.39	426	78.35 (7.84)	580	560
NGC 3258	0.35	164	23.89 (2.39)	880	580
NGC 3268	0.45	373	10.73 (1.07)	620	580
NGC 4374	0.47	–	4.81 (0.70)	750	–
NGC 6861	0.62	784	93.93 (9.39)	1040	980
IC 4296	0.41	–	0.76 (0.18)	600	–
Cycle 3					
NGC 2872	0.53	89	2.41 (0.28)	770	680
NGC 3078	0.46	86	3.51 (0.38)	730	625
NGC 3557	0.43	187	7.52 (0.79)	610	460
NGC 4697	0.46	193	15.84 (1.65)	430	420
NGC 4786	1.51	189	10.25 (0.50)	570	540
NGC 5838	0.50	222	33.53 (3.38)	890	810
Cycle 4					
NGC 384	0.47	568	10.11 (1.10)	730	675
PGC 11179	0.46	941	12.89 (1.33)	820	820
UGC 2698	0.44	319	5.25 (0.61)	960	960
Cycle 5					
NGC 3245	0.67	184	84.38 (8.44)	620	580
NGC 3271	0.82	485	33.62 (3.38)	700	600
NGC 3585	0.61	–	1.01 (0.13)	690	–
NGC 4261	0.60	–	4.34 (0.54)	950	–
NGC 5193	0.60	263	10.36 (1.05)	530	500
ESO 208-G21	0.31	238	6.11 (0.63)	730	640
ESO 322-G08	1.15	1436	154.01 (15.43)	590	570

Note: Molecular gas properties from CO(2−1) flux measurements. Col. (2): The rms background noise per 20 km s^{-1} channel of the Briggs weighted ($r = 0.5$) image cube. For NGC 4374 and IC 4296, these noise levels are per 40 km s^{-1} channel in naturally-weighted image cubes. Col. (3): The intrinsic radial extent of the CO emission from surface brightness measurements. Col. (4): Integrated CO(2−1) flux measurements over the entire dust disks. For NGC 4374, this $I_{\rm CO(2-1)}$ measurement only integrates over the inner ($\sim 1''$ radius) dust disk. Col. (5): Velocity range over which CO(2−1) emission is detected. Col. (6): Width of the CO velocity profile at 50% of the peak intensity. We give (1σ) uncertainties on $I_{\rm CO(2-1)}$ (in parantheses) that incorporate a 10% uncertainty in the absolute flux scaling.

Table 3.4 ^{12}CO(2−1) Disk Parameters

Galaxy (1)	$L'_{\rm CO(2-1)}$ (10^6 K km s^{-1} pc^{-2}) (2)	$M_{\rm gas}$ (10^7 $M_\odot$) (3)	$N_{\rm H_2}$ (10^{21} cm^{-2}) (4)
	Cycle 2		
NGC 1332	12.1 (2.3)	7.3 (1.4)	71
NGC 1380	14.0 (2.7)	8.4 (1.6)	37
NGC 3258	14.1 (3.8)	8.5 (2.3)	29
NGC 3268	7.6 (1.9)	4.6 (1.2)	11
NGC 4374	0.94 (0.17)	0.57 (0.10)	4.0
NGC 6861	42.6 (14.8)	25.6 (8.9)	19
IC 4296	1.03 (0.30)	0.62 (0.18)	9.8
	Cycle 3		
NGC 2872	3.28 (1.26)	1.98 (0.76)	80
NGC 3078	2.64 (0.79)	1.59 (0.47)	153
NGC 3557	9.51 (2.16)	5.73 (1.30)	40
NGC 4697	1.34 (0.23)	0.81 (0.14)	13
NGC 4786	24.3 (9.4)	14.7 (5.7)	115
NGC 5838	10.1 (3.6)	6.1 (2.2)	44
	Cycle 4		
NGC 384	21.2 (2.4)	12.8 (1.5)	9.9
PGC 11179	68.1 (7.6)	41.0 (4.6)	13
UGC 2698	24.9 (3.1)	15.0 (1.9)	44
	Cycle 5		
NGC 3245	22.4 (4.7)	13.5 (2.8)	126
NGC 3271	57.7 (22.0)	34.7 (13.2)	37
NGC 3585	0.25 (0.05)	0.15 (0.03)	53
NGC 4261	2.63 (0.05)	1.58 (0.34)	28
NGC 5193	13.7 (2.3)	8.3 (1.4)	44
ESO 208-G21	0.69 (0.15)	0.41 (0.09)	5.8
ESO 322-G08	129.7 (63.9)	78.1 (38.5)	18

Note: Molecular gas properties from CO(2−1) flux measurements. Col. (2): Integrated line surface brightness temperature. Col. (3): Integrated gas mass of the molecular disk, assuming $\alpha_{\rm CO}$ = 3.1 $M_\odot$ pc^{-2} (K km s^{-1})$^{-1}$, a CO(2−1)/CO(1−0)≈ 0.7 line ratio, and including contributions from helium. We give (1σ) uncertainties on $L'_{\rm CO(2-1)}$ and $M_{\rm gas}$ in parentheses; these include a 10% uncertainty in the absolute flux scaling, and we also propagate uncertainties in D_L into the $L'_{\rm CO(2-1)}$ and $M_{\rm gas}$ confidence ranges. Col. (4): Estimated H_2 column densities made by averaging these $M_{\rm gas}$ masses over the CO disk radius $R_{\rm d}$ (or, for the CO-faint targets, their central dust disk areas).

1979), NGC 1380 with $\log(M_{\rm H\,I}/M_\odot) < 8.6$ (Huchtmeier & Richter 1989), and NGC 4374 with $\log(M_{\rm H\,I}/M_\odot) \sim 9.3$ (Davies & Lewis 1973). Beam sizes for these H I observations are several arcminutes (corresponding to several tens of kpc), and neutral hydrogen envelopes tend to be much more extended than the molecular gas profiles. For late-type galaxies, Leroy et al. (2008) and Bigiel et al. (2008) find that the H I surface mass density $\Sigma_{\rm H\,I}$ saturates at $\sim 10\ M_\odot\ {\rm pc}^{-2}$ and that molecular contributions dominate when $\Sigma_{\rm H_2+H\,I} \gtrsim 14\ M_\odot\ {\rm pc}^{-2}$. Assuming that any neutral hydrogen is also in a disk-like configuration and this HI saturation limit applies to the ~ 500 pc radii circumnuclear gas disks in our ETG sample, neutral hydrogen should contribute at most $\sim 10^7\ M_\odot$ to the gas mass $M_{\rm gas}$ over the CO-emitting regions. Assuming only negligible atomic gas contributions, we estimate total gas masses by $M_{\rm gas} = M_{\rm H_2}(1 + f_{\rm He})$ where $f_{\rm He} = 0.36$ is the estimated mass-weighted helium fraction.

Our nineteen CO-bright galaxies have estimated $M_{\rm gas}$ values that span a wide range between $(0.04 - 7.8) \times 10^8\ M_\odot$, with a median of a little under $10^8\ M_\odot$ (see Table 3.4). These results are similar to the interferometric ($\sim 4''$ beam) gas measurements from a subsample of the ATLAS$^{\rm 3D}$ ETG survey, which finds $M_{\rm H_2}$ in the range of $(0.6 - 21.4) \times 10^8\ M_\odot$ for their CO-detected galaxies (using an $\alpha_{\rm CO} \approx 6.5$; Alatalo et al. 2013), and those with disk-like gas morphology and rotation have a median $M_{\rm H_2} \approx 4.5 \times 10^8\ M_\odot$. As expected, these ALMA observations reveal more faint CO emission due to roughly an order of magnitude higher sensitivity. After adjusting for different $\alpha_{\rm CO}$ values, the ATLAS$^{\rm 3D}$ galaxies with interferometric data have a median H_2 mass that is four times larger than the median of our $M_{\rm H_2}$ values. This discrepancy is likely the result of ATLAS$^{\rm 3D}$ interferometric targets being selected from the brightest and largest CO sources in a full single-dish survey (Young et al. 2011).

Projected surface brightness and mass profiles shown in Figure 3.6 have been constructed for the Cycle 2 targets by averaging their CO flux in elliptical annuli centered on the continuum

peaks; we fix the ellipse major axis PAs and axis ratios to the average kinemetry fit values as described later. Even at this moderate ($\sim$ 50 pc) spatial resolution, the NGC 1332 and NGC 6861 CO profiles reach their maximal surface brightnesses at $0\farcs5$ and $1\farcs9$ from rotation centers, respectively, instead of peaking around the disk centers. The intrinsic radial size $R_{\rm d}$ of these disks is estimated by $R_{\rm d}^2 = R'^2_{\rm d} - \sigma^2_{\rm beam,CO}$ where $R'_{\rm d}$ is the observed radial CO(2$-$1) extent and $\sigma_{\rm beam,CO}$ is the Gaussian dispersion size of the synthesized beam projected along the disk major axis. To within 20%, these intrinsic disk sizes measured using CO emission are equivalent to those inferred from the largest angular extent of the optical dust disks (Table 3.1) from *HST* two-band color maps.

Surface densities were corrected for the effects of inclination, i.e., $\Sigma_{\rm gas} = \Sigma'_{\rm gas} \cos i$, where $\Sigma'_{\rm gas}$ is the observed surface density and i is the estimated disk inclination (derived from kinematic decomposition; see Table 3.5). We find that the deprojected gas mass surface densities of our Cycle 2 CO-bright galaxies peak between $10^{2.3}$ and $10^{3.2}$ $M_\odot$ pc^{-2}, while $\Sigma_{\rm gas}$ averaged over the full disk areas ranges from $\sim 10^{1.8}$ to $10^{2.4}$ $M_\odot$ pc^{-2}. The observed average surface mass densities agree well with the average $\Sigma_{\rm H\,I+H_2}$ values from the ATLAS$^{\rm 3D}$ survey (Alatalo et al. 2013; Davis et al. 2013). This consistency indicates that radial size and not internal structure is the likely driver of the median mass difference between our ALMA targets and the ATLAS$^{\rm 3D}$ interferometric sample. We derive representative column densities $N_{\rm H_2} \sim (1-7) \times 10^{22}$ cm^{-2} by averaging the total $M_{\rm H_2}$ values over the elliptical CO-emitting disk areas. If we then assume a disk thickness $h \sim 0.1 R_{\rm d}$ (e.g., Boselli et al. 2014), the corresponding volume-averaged $\rm H_2$ densities $n_{\rm H_2}$ range between $\sim$ 10 and 200 cm^{-3}. These $N_{\rm H_2}$ values are typical of dusty disks in ETGs, while the estimated $n_{\rm H_2}$ are a couple orders of magnitude lower than predicted from theoretical models (Bayet et al. 2013); this discrepancy can be resolved if the molecular gas is clumpy with a filling factor much below unity. A Galactic $N_{\rm H_2}/A_V = 2.21 \times 10^{21}$ cm^{-2} mag^{-1} (Güver & Özel 2009) ratio implies $A_V \sim 5-30$ mag for homogeneous disks (and is highest for the nearly edge-on orientations). As expected for dusty disks that bisect galaxies, these extinction estimates are significantly

higher than A_V estimates derived from two-band *HST* color maps (with peak A_V ranging between ~ 0.5 and 1.5 mag for our Cycle 2 targets), which method treats the dust disks as foreground (local) obscuration (Figure 3.1; see also Kreckel et al. 2013). In §3.5, we discuss large systematic uncertainties that are introduced into the central stellar mass profiles by high extinction across our targets' circumnuclear regions, as well as the implications for BH mass measurements.

Kinematic Properties

We characterize the magnitude of kinematic twists in the Cycle 2 CO-bright sample using the kinemetry formalism and code of Krajnović et al. (2006). This program performs a harmonic decomposition of a velocity field on elliptical annuli. At each semi-major axis distance R we measure a kinematic position angle Γ, axis ratio q, and harmonic coefficients k_1 and k_5 for that annulus. Coefficient k_1 measures the rotation extremes along the line of nodes (the locus of velocity extrema along elliptical annuli); if $\Gamma(R)$ is roughly constant, then k_1 follows $v_{\rm LOS}$ along the semi-major axis. The k_5 coefficient quantifies deviations from pure rotation and is useful in conjunction with k_1. Kinemetry identifies multiple kinematic elements (e.g., kinematically decoupled components) in the LOS velocity field by the presence of abrupt changes in the PA or flattening ($\Delta\Gamma \gtrsim 10^\circ$ or $\Delta q \gtrsim 0.1$), a double-peaked k_1 profile, or a peak in k_5/k_1 (at the level of $\gtrsim 0.1$). Reconstructed model maps in Figure 3.11 use only the circular velocity terms from kinemetry fits, demonstrating good agreement with the observed velocity fields to (typically) $\lesssim 10$ km s^{-1}. In Figure 3.12 we show the radial kinemetry fits for these five CO-bright ETGs and in Table 3.5 we report the best-fitting $v_{\rm sys}$ that minimizes residuals, as well as the average (and total ranges of) Γ and q values. The best-fitting recessional velocities are discrepant with those taken from NED by between 20 and 40 km s^{-1}. For each of these disks, the ellipse axis ratio q decreases with increasing R. Simple models of thin disk rotation show a similar increase in q with decreasing radius, where

Table 3.5 Kinemetry Parameters

Galaxy	$v_{\rm sys}$ (km s^{-1})	$\overline{\Gamma}$ / $\Delta\Gamma$ (°)	$\overline{q}$ / Δq	i (°)	$\overline{b}$ (pc)	$M(R < 2, 5\overline{b})$ (10^9 $M_\odot$)
(1)	(2)	(3)	(4)	(5)	(6)	(7)
NGC 1332	1561	121.8 / 8.4	0.26 / 0.22	80	29	6.20
NGC 1380	1855	187.1 / 3.2	0.27 / 0.08	75	17	1.54
NGC 3258	2758	76.6 / 4.1	0.86 / 0.28	45	65	5.03
NGC 3268	2760	68.7 / 27.8	0.62 / 0.24	55	69	3.14
NGC 6861	2800	140.9 / 3.9	0.32 / 0.33	75	36	8.83

Note: Molecular gas disk properties of the Cycle 2 CO-bright galaxies from kinemetry fits to the CO(2−1) $v_{\rm LOS}$ maps. Col. (2): Best-fitting heliocentric systemic velocity which minimized the kinemetry residuals. Col. (3) and (4): The average (and the maximum range in) position angle Γ and ellipse axis ratio q. Col. (5): Estimated gas disk inclination derived using the thin-disk approximation $i \sim \cos^{-1} q_{\rm min}$ where $q_{\rm min}$ is the minimum axis ratio from the kinemetry modeling. Col. (6): Physical size corresponding to the geometrically-average beam FWHM $\overline{b}$. Col. (7): Estimated mass enclosed within a radius corresponding to $2\overline{b}$ (or $5\overline{b}$) for moderately (or highly; $i \gtrsim 75°$) inclined disks.

beam smearing effectively circularizes the kinemetry results. Assuming these disks are indeed thin, we approximate the inclination i by $\cos^{-1} q_{\rm min}$, where $q_{\rm min}$ is the minimum observed axis ratio. These kinematic inclination angles correlate well (to within a few percent) with those estimated from dust disk morphologies (i.e., $\cos^{-1}[b/a]$ from Table 3.1). Kinematic twists tend to be mild ($\lesssim 10°$) except in the case of NGC 3268 – where $\Delta\Gamma$ approaches 30° – and k_5/k_1 values are consistently low. Each molecular disk appears to be composed of a single, slightly warped, rotating component.

We use these kinemetry results to estimate the circular speed $v_{\rm c} \approx k_1/\sin i$ and probe the enclosed mass profiles in these five ETGs as a function of radius. At $\sim$ 50 pc spatial resolution, beam smearing mixes emission from far-removed locations in the disk, especially along the minor axis, and dilutes the line-of-sight velocities that are intrinsically highest along the line of nodes. For highly-inclined ($i \gtrsim 80°$) disks, dynamical modeling of the NGC 1332 CO(2−1) image cube indicates that $k_1/\sin i$ approximates the intrinsic $v_{\rm c}$ to $\lesssim 10\%$ accuracy only beyond a radius of $\sim 5\overline{b}$ (Barth et al. 2016b; see their Figure 15), where $\overline{b}$ is the

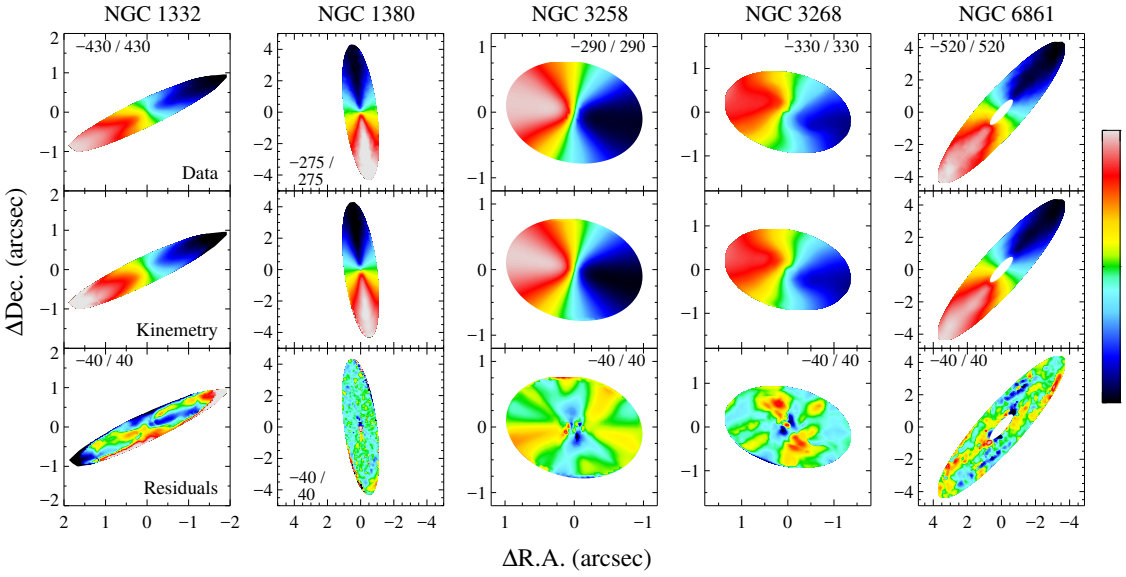

Figure 3.11 Kinemetry modeling results, showing the (*top*) highest S/N regions of the $v_{\rm LOS}$ profiles along with (*middle*) kinemetry models that only include the circular velocity components and (*bottom*) residual maps that indicate generally small ($\lesssim$ 10 km s^{-1}) deviations from circular velocity. The velocity ranges corresponding to the color scaling in the observed $v_{\rm LOS}$ images likewise apply to the kinemetry model maps.

geometric mean of the synthesized beam major and minor axis FWHMs. More moderately inclined disks ($i \sim 45°$) show $k_1/\sin i \approx v_{\rm c}$ beyond a radius of $\sim 2\bar{b}$ (see the high-resolution NGC 3258 CO imaging in §4). We expect that the intrinsic rotation curves of the remaining moderately inclined ($i \approx 55°$; NGC 3268) galaxy can be approximated beyond a radius of $\sim 2\bar{b}$, and likewise beyond $\sim 5\bar{b}$ for the two additional, very inclined ($i \approx 75°$; NGC 1380, NGC 6861) galaxies we have not yet dynamically modeled. We therefore estimate the masses $M(r < 2,5\bar{b})$ of these galaxies enclosed within projected radii of either $2\bar{b}$ or $5\bar{b}$, finding a relatively broad range of $\sim (1.5-8.8)\times10^9\ M_\odot$ (Table 3.5). By design, $\bar{b} \sim r_{\rm g}$ for this Cycle 2 sample, so these enclosed masses are dominated by stellar and not BH mass contributions.

We now explore possible disk formation mechanisms in light of these kinemetry results. Dusty, gas-rich disks in ETGs may be either internally generated by *in situ* stellar evolution and feedback or externally accreted by gas inflow and merging. In the first scenario, *in situ* dusty disk formation may be the result of either the cooling of a hot halo (Lagos et al. 2014)

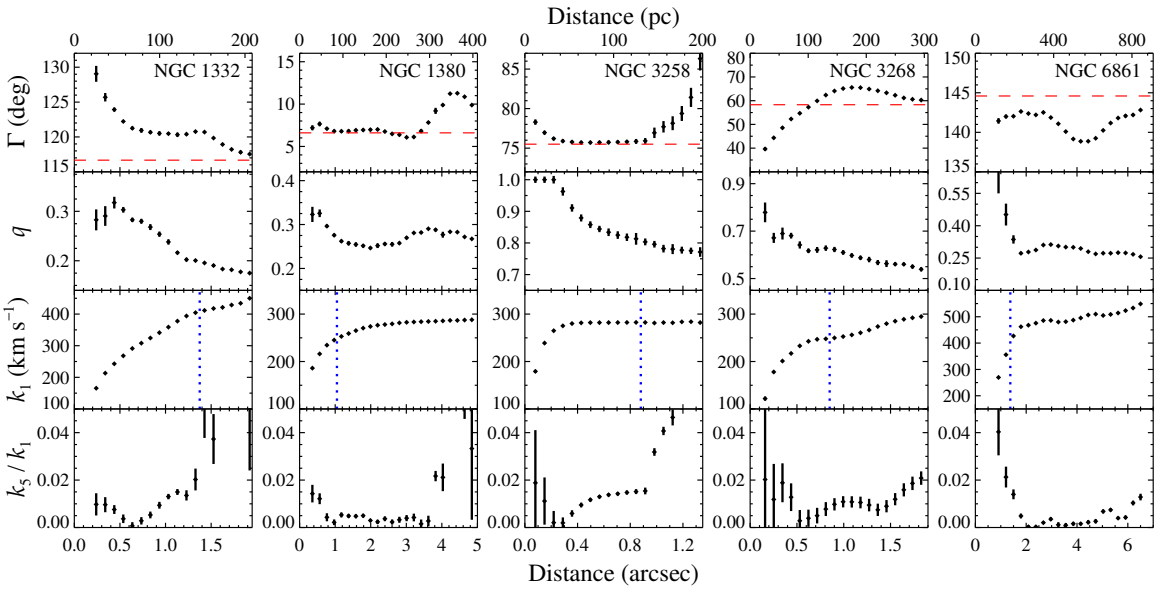

Figure 3.12 Results of the kinemetry expansion of each $v_{\rm LOS}$ field. Kinematic twists of the line of nodes are indicated by a changing position angle Γ, though the average Γ values generally agree very well with the host galaxy stellar photometric major axes position angles (dashed lines). Axis ratio q is related to the gas disk inclination angle, while the k_5/k_1 ratio characterizes the level of non-circular motion in the velocity fields. Vertical (dotted) lines alongside the k_1 profiles indicate the $2\overline{b}$ ($5\overline{b}$) distance at which we expect $k_1/\sin i \approx v_{\rm c}$ for moderately (highly) inclined disks.

or evolved (primarily AGB) stars that inject gas and dust into the interstellar medium at a significant rate (e.g., Bloecker 1995). Dusty disks that originate from stellar evolution will be closely aligned and co-rotate with the stars. In the second scenario, externally accreted gas streams or mergers with gas-rich galaxies are responsible for the high CO and optically thick dust detection rates. Based on frequent kinematic mismatches ($\sim$ 40% of the ATLAS$^{\rm 3D}$ sample having $\geq 30^\circ$ discrepancy) between molecular/ionized gas and stars in fainter ($M_K > -24$) ETGs, Davis et al. (2011b) estimated that at least half of all field ETGs externally acquire their gas. Without ongoing accretion, the gas will relax into the galaxy plane on Gyr timescales (van de Voort et al. 2015) and become photometrically (though perhaps not kinematically, if the gas rotates counter to the stars; e.g., Davis et al. 2011b) indistinguishable from material entering the gas phase *in situ* (following the episodic settling pattern; Lauer et al. 2005). However, Lagos et al. (2015) find that smooth gas accretion (e.g., cooling) onto an initially relaxed molecular disk from a misaligned hot halo can promote and

maintain large discrepancies between the stellar and gaseous rotation axes. Both scenarios face the complication that dust should be destroyed by thermal sputtering from the hot interstellar medium on relatively short timescales (perhaps up to 100 Myr; see Clemens et al. 2010). Uncertainties in the dust destruction and gas depletion (due to star formation) timescales, as well as in the minor merger rate, make extracting an *in situ* formation fraction from surveys of ETGs problematic at best (see Davis & Bureau 2016; Bassett et al. 2017). As Martini et al. (2013) suggest, these disks may be formed by a combination of internal and external formation mechanisms, such that minor mergers "seed" the ETGs with central gas and dust disks, and stellar evolution and halo gas cooling replenishes the cold circumnuclear disks with gas and dust.

Our ETGs were selected for ALMA imaging based on morphologically round dust disks. The Cycle 2 CO-bright subsample molecular gas disks co-rotate with the stars (to within a few degrees) and, based on their kinematic decomposition, we find that their *in situ* formation is as plausible a scenario as the accretion and settling of external gas. For similarly round, clean dust disks (and for dusty ETGs in general), other observational constraints are needed to determine the disk origins. Firstly, if these disks form primarily from the accretion and settling of satellite gas and dust, with little time ($\ll$Gyr) for chemical enrichment from stellar mass loss, their gas-phase metallicities and dust-to-gas mass ratios should be consistent with those of low-mass galaxies as opposed to the products of late stellar evolution within luminous ETGs. Spatially mapping various metallicity indicators is possible with optical (e.g., Storchi-Bergmann et al. 1994; Pettini & Pagel 2004) and mm/sub-mm (Bayet et al. 2012) emission line measurements, and a determination of the dust-to-gas ratio, which scales linearly with metallicity, can be made by modeling far-IR (and potentially spatially-resolved, high-frequency ALMA) observations (e.g., Davis et al. 2017). Secondly, deep photometric imaging of galaxies reveals post-merger signatures such as stellar streams or shells (e.g., Duc et al. 2015), and H I surveys of nearby ETGs often find large-scale disks/rings that are kinematically mismatched with respect to the stellar rotation (e.g., Serra et al. 2012). Even

for morphologically round dust disks in ETGs, systems showing recent merger activity on large scales may preferentially host less relaxed circumnuclear disks as demonstrated by the level ($\Delta\Gamma$) of kinematic warping.

Molecular Gas Stability

Unless stabilized against gravitational fragmentation, a thin, rotating molecular disk is prone to collapse into star-forming clouds. Understanding the stability of the gas disks has implications for both their star formation rates and their disk depletion times (Davis et al. 2014). Toomre (1964) established a local stability criterion Q that can be applied to gas disks based on the gas sound speed c_s and deprojected surface mass density $\Sigma_{\rm gas}$:

$$Q_{\rm gas} \equiv \frac{c_s \kappa}{\pi G \Sigma_{\rm gas}} \, . \tag{3.2}$$

Here, the epicyclic frequency κ is defined by $\kappa^2 = R\, d\Omega^2/dR + 4\Omega^2$, and the angular velocity is $\Omega = v_{\rm c}/R$ with $v_{\rm c}$ the circular velocity at radius R. We use $k_1/\sin i$ profiles to approximate $v_{\rm c}$ for our Cycle 2 subsample, and reiterate that this approximation is expected to hold beyond an angular radius of $\sim 2\overline{b}$ ($\sim 5\overline{b}$) for moderately (highly) inclined disks. Since c_s is much lower than the observed line dispersions, we instead assume that the intrinsic line dispersion contributes more to the gas stability than does thermal pressure. We therefore replace c_s with the minimum observed $\sigma_{\rm LOS}$ for each disk. If the intrinsic line widths of the cold molecular gas strongly increase towards the disk center (for which there is little evidence at high angular resolution; see Utomo et al. 2015; Barth et al. 2016b), then $Q_{\rm gas}$ will likewise increase at small radii. Toomre Q values above unity are typically considered stable against gravitational fragmentation, although numerical simulations find that disk instabilities are not fully damped out in regions where Q is only slightly above unity (e.g., Li et al. 2005).

We show $Q_{\rm gas}$ as a function of radius in Figure 3.13 for our first five CO-bright targets, finding

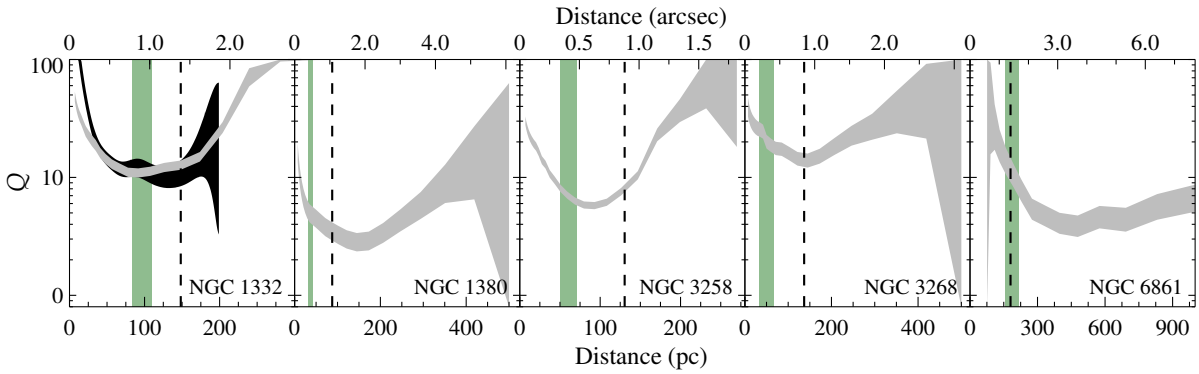

Figure 3.13 Analysis of the molecular gas stability in the Cycle 2 CO-bright galaxies using the Toomre Q parameter (shown with uncertainties indicated by the gray shaded regions). These gas disks appear to be formally stable (i.e., $Q_{\rm gas} > 1$) against gravitational fragmentation. The dashed vertical lines correspond to $2\bar{b}$ (or $5\bar{b}$), at which distance from the nucleus the observed LOS velocities are nearly equal to the intrinsic speeds. The shaded vertical regions indicate the projected sphere of influence $r_{\rm g}$, determined by estimating the BH mass using the stellar velocity dispersion in Table 3.1 and the $M_{\rm BH} - \sigma_\star$ relationship (Kormendy & Ho 2013). For NGC 1332, we include a $Q_{\rm gas}$ profile derived from ALMA Cycle 3 $0\farcs044-$resolution gas dynamical modeling (darker regions; Barth et al. 2016a).

that $Q_{\rm gas} > 1$ for all radii where k_1 is a good proxy for the line-of-sight velocity profile. For all these targets, this formal stability measure persists after we include the uncertainties in k_1 and $\Sigma_{\rm gas}$, along with reasonable uncertainties in the inclination angle ($\delta i \sim 2^\circ$) and minimum line widths ($\delta\sigma_{\rm LOS} \sim 1$ km s^{-1}). Some portion of the minimum observed $\sigma_{\rm LOS}$ is likely due to rotational broadening and beam smearing (see also Barth et al. 2016b), and dynamically modeling the CO-bright disk rotation is under way to determine the intrinsic line widths. Initial modeling results suggests that the observed $\min(\sigma_{\rm LOS})$ exceeds the intrinsic widths by at most a factor of two. As a result, $Q_{\rm gas}$ is expected to decrease slightly but should remain above unity.

Cosmological simulations demonstrate that gas disks within ETGs tend to be stable against fragmentation due to larger BH masses and more centrally concentrated stellar profiles than in late-type galaxies (i.e., morphological quenching by bulge growth; Kawata et al. 2007; Martig et al. 2009, 2013). In addition, many ETGs do not possess stellar disks that otherwise would increase the self-gravity of co-spatial gaseous disks. Martig et al. (2013) suggest that increased shear (often defined by the logarithmic shear rate $\Gamma_{\rm sh} = -d\ln\Omega/d\ln R$; Julian &

Toomre 1966) as a result of bulge growth is the primary stabilizer of ETG gas disks. Since the CO-bright rotation curves are nearly flat from the middle of the disks to the outer edges, the epicyclic frequencies ($\kappa^2 = 2\Omega^2[2 - \Gamma_{\rm sh}]$) are dominated at these radii by high angular speeds and not their logarithmic shear rates. The increase in $Q_{\rm gas}$ near the disk edges is the result of the $\Sigma_{\rm gas}$ profiles declining faster than the epicyclic frequencies. However, a strong intrinsic velocity rise due to the central BH (that is not seen in the $v_{\rm LOS}$ maps due to the $\overline{b} \sim r_{\rm g}$ resolution) will result in much higher κ values within the projected $r_{\rm g}$ radius. We explored the inner $Q_{\rm gas}$ profile of NGC 1332 using $\sim 0\farcs044-$resolution Cycle 3 CO(2−1) observations that more fully map out the rotation speed within $r_{\rm g}$ (Barth et al. 2016a). The circular velocity for this profile is derived from the radial mass profile of the best-fitting full-disk dynamical modeling results. At this higher resolution, the observed rotation speed along the major axis is less beam-smeared, and we find that the radial κ profile of NGC 1332 rises more steeply within the central ~ 50 pc. This corroborates with previous simulations, showing that the central BH does further stabilize the central disk regions of dust-disk ETGs.

Notwithstanding formal stability ($Q > 1$), suppressed star formation still occurs in both simulated and real ETG disks. Based on excess mid-IR flux, Davis et al. (2014) find evidence for low star formation rates in ETGs with average $\Sigma_{\rm gas}$ and rotational properties similar to that of our sample. We expect the CO emission to be clumpy when observed at high angular resolution, with surface mass densities peaking above the values suggested by the elliptically-averaged $\Sigma_{\rm gas}$ profiles (§3.6; see also Utomo et al. 2015). In addition, turbulence and non-circular orbits will create pockets of sufficiently high gas density to be self-gravitating and collapse (see Hopkins & Christiansen 2013). The presence of a coincident stellar disk lowers the total Toomre Q parameter ($Q_{\rm tot}^{-1} = Q_{\star}^{-1} + Q_{\rm gas}^{-1}$), although for our S0 galaxies we do not expect the effect to be more pronounced than for the Milky Way (i.e., a factor of ~ 2 lower in the solar neighborhood; see Wang & Silk 1994). Measuring $Q_{\rm tot}$ on sufficiently small scales (i.e., giant molecular cloud sizes) to fully investigate molecular gas stability requires deeper, more highly resolved CO observations to map out the molecular gas distribution and full disk

dynamical modeling (with an extinction-corrected stellar mass profile). An alternate (and complementary) method to test disk stability is to directly look for evidence of star forming regions. We identify one such potential location $\sim 1''$ east of the nucleus in NGC 3268. This region is significantly bluer in the *HST* color map, while its structure map suggests a light excess. Confirming star formation at this or other locations should be possible using optical IFU spectroscopy to resolve ionized gas emission, or by modeling sub-arcsecond continuum spectral energy distributions (SEDs).

3.3.2 CO-Faint Galaxies

We constructed velocity profiles for NGC 3585, NGC 4261, NGC 4374, and IC 4296 (shown in Figures 3.14 through 3.17, respectively) by integrating the image cube flux densities in each $10-40$ km s^{-1} channel over their $\lesssim 2''-$wide optical dust disks (described by the major/minor axes in Table 3.1). The resulting profiles are very different from the clean, symmetric, double-horned shapes that we observe for the CO-bright subsample. We do detect CO(2−1) emission, but at much lower ($\sim 5-10\sigma$) significance than the remainder of our ETG galaxies. Their PVDs, extracted along the central dust disk major axes, show faint evidence of disk-like rotation. In all four galaxies, careful inspection of the image cubes reveals regions of statistically significant ($\geq 3\sigma$ in a $10-40$ km s^{-1} channel) emission across many channels that spatially coincide with the optically thick dust absorption and that shows outlines of the full disk rotation. The NGC 3585 and IC 4296 PVDs and approximate velocity maps are consistent with no central high-velocity emission above the background level (although it cannot be ruled out due to the coarse, $0\farcs5$ resolution). The NGC 4374 data show hints of a velocity upturn within $r_{\rm g}$ with emission spanning at least 700 km s^{-1} directly across the nucleus.

The NGC 4261 molecular emission spans at least 950 km s^{-1} and clearly traces central

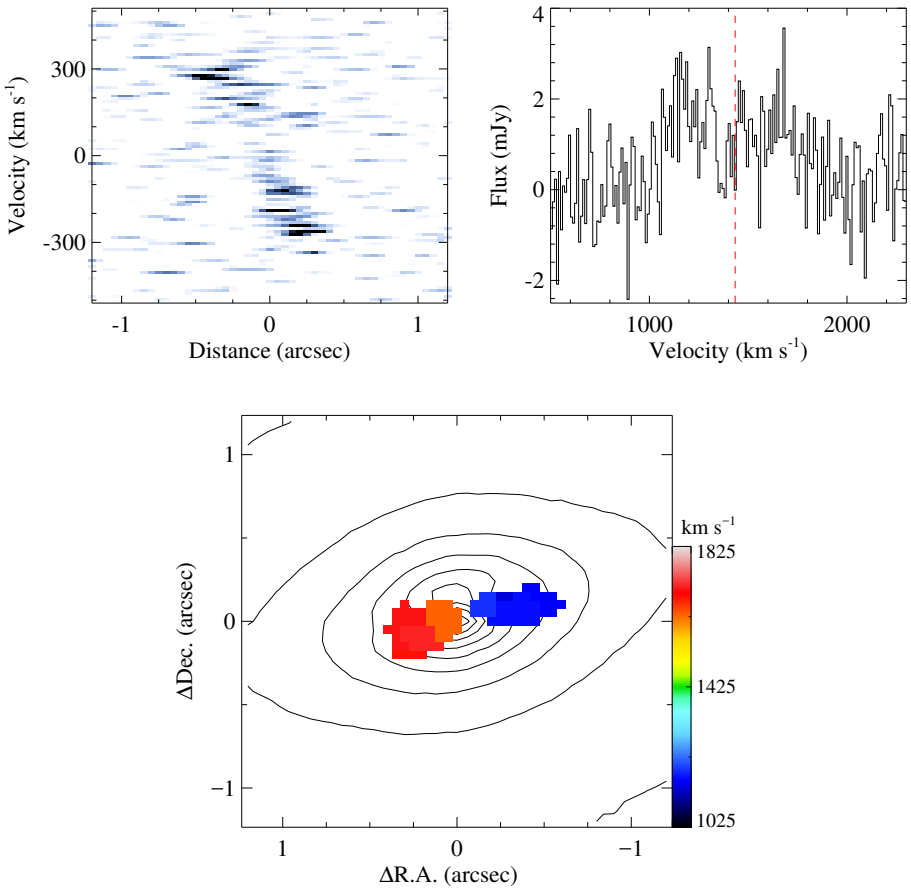

Figure 3.14 NGC 3585 CO(2−1) emission and absorption characteristics. *Top Left*: PVD extracted along the dust disk major axis, using the same negative color scale as the CO-bright target PVDs that displays emission as being darker. *Top Right*: Velocity profiles formed by integrating only over the inner, $\sim 0\farcs5$ radius dust disk in each 20 km s^{-1} channel. The dashed lines indicate the host galaxy $v_{\rm sys}$ as reported in NED. *Bottom*: Contour map of the *HST* F475W surface brightness with coordinates centered on the nuclear 1.3 mm continuum. Regions of the image cube showing faint CO emission are overlaid with a color mapping that corresponds to the channel velocity.

velocity upturns due to a massive BH; Ferrarese et al. (1996) estimate its $M_{\rm BH} \sim 5 \times 10^8\ M_\odot$ from *HST* FOS spectroscopy, although without detailed data modeling and more complicated ionized gas kinematics revealed by later *HST* STIS observations (Noel-Storr et al. 2003). The estimated $r_{\rm g} \sim 0\farcs16$ appears inconsistent with (a little asymmetric) strong Keplerian-like emission line features detected in observations with a $0\farcs3$ synthetic beam size, suggesting a BH mass that is perhaps a factor of three higher. The stellar kinematics from IFU spectroscopy show some rotation along the stellar photometric axes; however, the molecular disk is rotating *counter* to the larger-scale ($R \gtrsim 10''$; Krajnović et al. 2011) stellar kinematics and we find agreement between the stellar photometric and CO kinematic axes at the 10° level. This molecular disk appears to be inconsistent with *in situ* formation.

IFU data for NGC 4374 show almost no evidence for stellar rotation (Emsellem et al. 2011), and the galaxy is expected to be (mildly) triaxial; stellar photometric axes of this slow rotator are misaligned by nearly 90° with respect to the inner dust disk major axis, the ionized gas kinematics (e.g., Walsh et al. 2010), and now seemingly also the cold molecular gas rotation. Long-slit spectroscopy of NGC 3585 and IC 4296 suggests somewhat significant (~ 100 km s^{-1}) stellar rotation that is roughly consistent with the stellar photometric axes (for IC 4296: PA $\sim 60-70°$, Efstathiou et al. 1980, Killeen et al. 1986; for NGC 3585: PA $\sim 97°$, Gültekin et al. 2009) and appears to co-rotate to within about 10° with the faint CO emission (see Figures 3.14 and 3.17).

Even when imaged into 40 km s^{-1} channels, CO(2−1) absorption is apparent in NGC 4374 and IC 4296 against their strong nuclear continuum sources. While extragalactic CO absorption is not frequently observed due to low equivalent widths, ALMA's high-angular resolution and sensitivity allow its detection against some nearby active nuclei (e.g., Davis et al. 2014; Rangwala et al. 2015). To better characterize these two absorption-line systems, we also imaged their visibility data (without continuum subtraction) into cubes with 1.28 km s^{-1} channels. The primary absorption in IC 4296 is consistent with the galaxy's

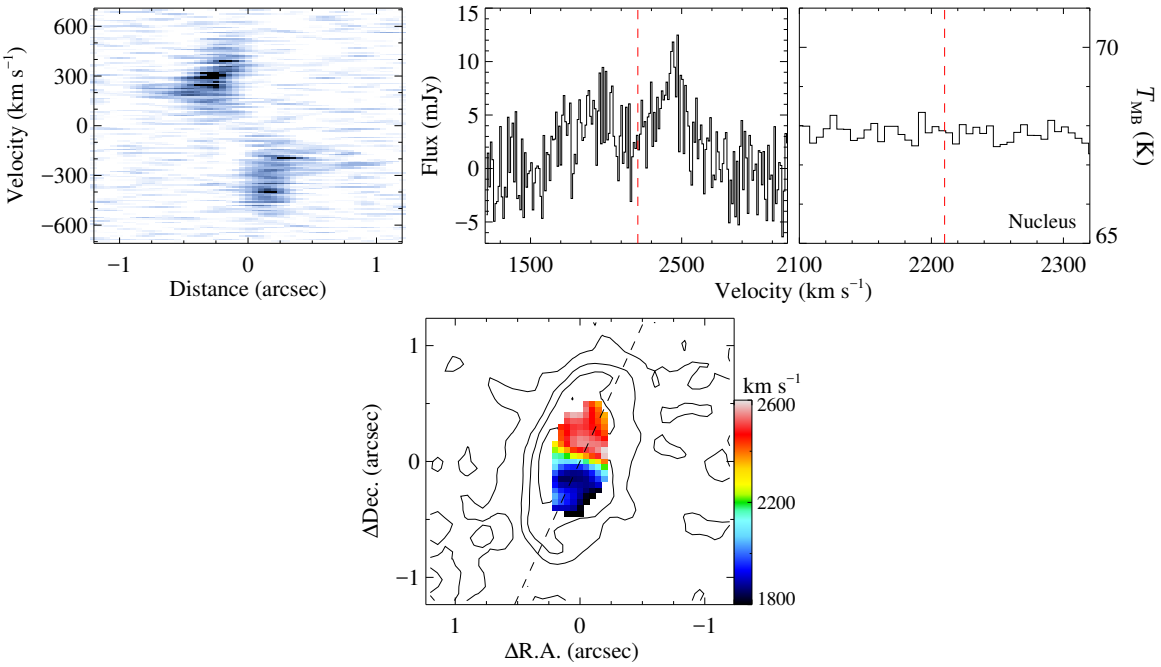

Figure 3.15 NGC 4261 CO(2−1) emission and absorption characteristics. *Top Left*: PVD extracted along the dust disk major axis, using the same negative color scale. The bright central feature is the strong nuclear CO absorption. *Top Right*: Velocity profiles formed by (*left*) integrating only over the inner, $\sim 1''$ radius dust disk in each 10 km s^{-1} channel, and by (*right*) measuring the main beam brightness temperature of the nuclear continuum source, imaged in roughly 5.08 km s^{-1} channels. The dashed lines indicate the host galaxy $v_{\rm sys}$ as reported in NED. *Bottom*: Contour map of the *HST* F547M−F791W image, with coordinates centered on the nuclear 1.3 mm continuum. Regions of the image cube showing faint CO emission are overlaid with a color mapping that corresponds to the channel velocity. The dashed line indicates the larger-scale photometric stellar major axis PA measured from *HST* imaging.

assumed systemic velocity (Table 3.1), although there may be a small secondary absorption feature $\sim$ 15 km s^{-1} redward of $v_{\rm sys}$. The CO(1$-$2) transition seen in the nucleus of NGC 4374, however, is redshifted by $\sim$ 100 km s^{-1} from the $v_{\rm sys}$ value derived using stellar kinematics (Emsellem et al. 2004) and by $\sim$ 50 km s^{-1} with respect to the best-fitting $v_{\rm sys}$ from ionized gas dynamical modeling (e.g., Walsh et al. 2010). The absorption lines in these two galaxies have narrow widths ($\lesssim$ 7 km s^{-1} FWHM) that are only slightly smaller than the minimum line widths in our CO-bright subsample. Maximum absorption depths are (-3.26 ± 0.74) and (-5.25 ± 0.35) K with integrated absorption intensities $W_{\rm CO(2-1)}$ of (19.4 ± 2.5) and (44.3 ± 1.4) K km s^{-1} for NGC 4374 and IC 4296, respectively. From these $W_{\rm CO(2-1)}$ measurements we estimate corresponding H$_2$ column densities $N_{\rm H_2} = X_{\rm CO} W_{\rm CO(1-0)}$ of (4.7 ± 0.6) $\times$ 10^{21} cm^{-2} and (1.1 ± 0.3) $\times$ 10^{22} cm^{-2} after assuming an absorption depth ratio CO(1$-$2)/CO(0$-$1)$\approx$ 0.6 (based on ^{13}CO absorption line ratios; e.g., see Eckart et al. 1990) and a CO-to-H$_2$ conversion factor $X_{\rm CO}$ corresponding to $\alpha_{\rm CO}$ = 3.1 $M_{\odot}$ pc^{-2} (K km s^{-1})$^{-1}$ (Sandstrom et al. 2013). Since the $\alpha_{\rm CO}$ and CO(1$-$2)/CO(0$-$1) values carry large systematic uncertainties, and faint nuclear CO emission may somewhat dilute these equivalent widths, these $N_{\rm H_2}$ estimates are much more uncertain than indicated by the formal associated uncertainties. NGC 3585 does not possess a strong nuclear continuum source (see Table 3.7). Interestingly enough NGC 4261, our brightest Band 6 source, shows no evidence of CO absorption even after re-imaging the data using (the online 8$\times$ native) $\sim$ 5 km s^{-1} channel spacing. While Jaffe & McNamara (1994) report CO(2$-$1) absorption at $\sim$ 2236 km s^{-1}, Okuda et al. (2013) find no such evidence when investigated at greater sensitivity.

While the CO-faint galaxy line profiles are dominated by noise on a pixel-by-pixel basis, we estimate total CO(2$-$1) emission fluxes by integrating their velocity profiles outside of the absorption features and over the velocities where faint emission is detected in the PVDs (ranging from $\pm$320 to $\pm$600 km s^{-1}). The central disks of these CO-faint galaxies have low integrated CO(2$-$1) fluxes ($<$ 5 Jy km s^{-1}; see Table 3.3) with corresponding total (molecular and helium) gas masses of $\sim$ 10$^{6-7}$ $M_{\odot}$ (see Table 3.4). For completeness, we

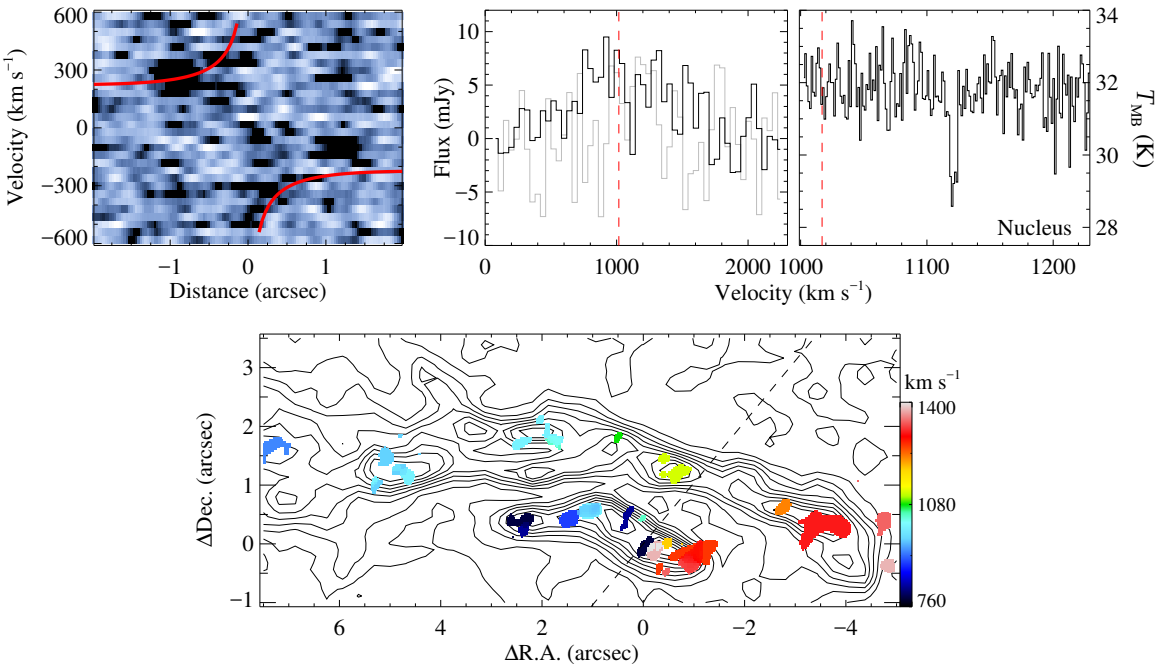

Figure 3.16 NGC 4374 CO(2−1) emission and absorption characteristics. *Top Left*: PVD extracted along the dust disk major axis, using the same negative color scale. For comparison, we include a model $v_{\rm LOS}$ profile (solid curve) assuming the $M_{\rm BH} = 10^{8.9}\ M_{\odot}$ and a stellar mass profile measured by Walsh et al. (2010). *Top Right*: Velocity profiles formed by (*left*) integrating only over the inner, $\sim 1''$ radius dust disk (*dark profile*) and only over the outer dust lane (*light profile*) in each 40 km s^{-1} channel, and by (*right*) measuring the main beam brightness temperature of the nuclear continuum source, imaged in 1.28 km s^{-1} channels. The dashed lines indicate the host galaxy $v_{\rm sys}$ as reported in NED. *Bottom*: Contour map of the *HST* F547M−F814W image (see Figure 3.1), with coordinates centered on the nuclear 1.3 mm continuum. Regions of the image cube showing faint CO emission are overlaid with a color mapping that corresponds to the channel velocity. The dashed line indicates the larger-scale photometric stellar major axis PA measured from *HST* imaging.

also measure a velocity profile for the larger-scale, outer dust lane in NGC 4374 (included in Figure 3.16) and find a possible CO detection with $I_{\rm CO(2-1)} = (1.6 \pm 1.1)$ Jy km s^{-1} when integrated over the same $\pm$520 km s^{-1} velocity range. Previous single-dish (CSO: Knapp & Rupen 1996; IRAM 30m: Combes et al. 2007, Ocaña Flaquer et al. 2010) observations of NGC 4374 found at best only a tentative CO detection (corresponding to $I_{\rm CO(2-1)} = 8.8 \pm 1.6$ Jy km s^{-1}), while similar (APEX: Prandoni et al. 2010) observations of IC 4296 found only an upper limit of $I_{\rm CO(2-1)} < 20$ Jy km s^{-1} (corresponding to $M_{\rm H_2} \lesssim 10^{8.7}$ $M_\odot$). Single-dish and interferometric imaging (JCMT: Jaffe & McNamara 1994; NoMA and IRAM PdBI: Okuda et al. 2013) do not identify any CO emission in NGC 4261, with their most stringent (3σ) upper limits suggesting $I_{\rm CO(2-1)} \lesssim 2$ Jy km s^{-1} that is not bourne out by our CO(2$-$1) measurement. No previous NGC 3585 CO observations are extant.

IRAS far-IR data, which are sensitive to thermal emission from both clumpy, optically opaque dust as well as additional diffuse dust, suggest total dust masses of $\sim 10^{3.6-5.9}$ $M_\odot$ in these four galaxies (Ocaña Flaquer et al. 2010; Amblard et al. 2014). The ratio of our $M_{\rm H_2+He}$ measurements for these dusty disks (even including the NGC 4374 outer dust lane) and the associated (total) thermal dust masses are consistent with a fiducial 100:1 gas-to-dust mass ratio (de Ruiter et al. 2002).

When these $M_{\rm H_2}$ masses are averaged over optically thick dust disk regions, the estimated H_2 column densities are approximately 7.7×10^{22} cm^{-2} (NGC 3585), 3.4×10^{22} cm^{-2} (NGC 4261), 4.0×10^{21} cm^{-2} (NGC 4374) and $\sim 9.8 \times 10^{21}$ cm^{-2} (IC 4296). Without even considering the large total flux uncertainties ($\sim 15 - 25\%$), the CO emission-derived $N_{\rm H_2}$ estimates for the Cycle 2 targets are consistent with those from integrated absorption line intensities. After correcting for inclination effects (assuming $i \sim 75^\circ$), the average deprojected H_2+He surface mass densities are comparable (between $\sim 10^{1.4-2.4}$ $M_\odot$ pc^{-2}) to the CO-bright subsample (whose average $\Sigma_{\rm gas}$ values range from $10^{1.8-2.4}$ $M_\odot$ pc^{-2}.

It is not yet clear why the central disks of these four galaxies are underluminous in CO(2$-$1)

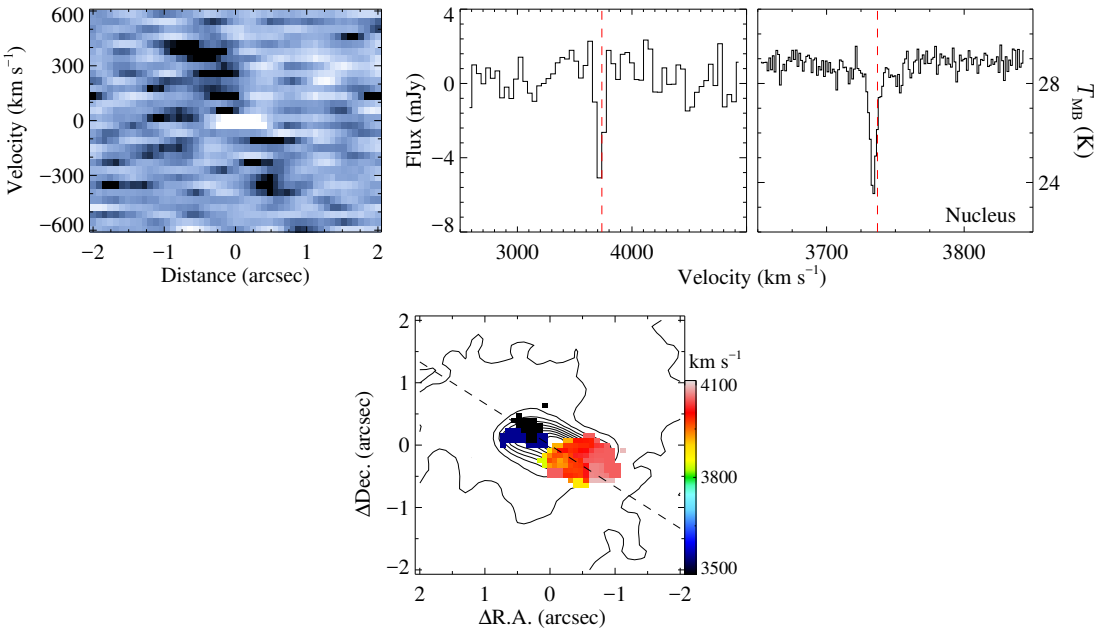

Figure 3.17 IC 4296 CO(2−1) emission and absorption characteristics. *Top Left*: PVD extracted along the dust disk major axis, using the same negative color scale. The bright central feature is the strong nuclear CO absorption. *Top Right*: Velocity profiles formed by (*left*) integrating only over the inner, $\sim 1''$ radius dust disk in each 40 km s^{-1} channel, and by (*right*) measuring the main beam brightness temperature of the nuclear continuum source, imaged in 1.28 km s^{-1} channels. The dashed lines indicate the host galaxy $v_{\rm sys}$ as reported in NED. *Bottom*: Contour map of the *HST* F555W−F814W image (see Figure 3.1), with coordinates centered on the nuclear 1.3 mm continuum. Regions of the image cube showing faint CO emission are overlaid with a color mapping that corresponds to the channel velocity. The dashed line indicates the larger-scale photometric stellar major axis PA measured from *HST* imaging.

compared to the CO-bright subsample. Intriguingly, their dusty disks show greater excess in *HST* color maps while having less total gas mass than the similarly sized and inclined NGC 1332 dust disk, suggesting these CO-faint disks may possess larger dust column densities. Using their average $N_{\rm H_2}$ values, NGC 4374 and IC 4296 have $A_V \leq 4$ mag extinction estimates. However, the dusty disk in NGC 1332 has a very large $A_V \sim 30$ mag estimated from its average $N_{\rm H_2}$ and possesses over an order of magnitude larger H_2 reservoir. NGC 4261 (Ferrarese et al. 1996), NGC 4374 (Bower et al. 1997), and IC 4296 (Annibali et al. 2010) all possess significant nuclear ionized gas emission, perhaps indicating that their dust disks are associated with large H I or ionized gas reservoirs. Lower estimated $\Sigma_{\rm H_2+He}$ values for at least NGC 4374 and IC 4296 suggest parity between the surface mass densities of atomic and molecular gas components. These two targets along with NGC 4261 are Fanaroff-Riley (FR) type-I radio galaxies (Fanaroff & Riley 1974) having both large (Killeen et al. 1986; Laing & Bridle 1987; Piner et al. 2001) and small-scale (Harris et al. 2002; Pellegrini et al. 2003; Kolokythas et al. 2015) radio jets. The CO-bright galaxies and NGC 3585 are not known to contain radio jets (Large et al. 1981). These three FR I targets show strong 1.3 mm nuclear continua relative to the CO-bright targets (see Table 3.7), and their extended 1.3 mm continuum profiles may be small-scale ($\sim$ 100 pc; see §3.4.1) nuclear jets. The luminosities and energetics of active nuclei may dissociate a significant portion of the H_2 (Müller-Sánchez et al. 2013), giving rise to smaller molecular gas reservoirs, or excite the CO into higher$-J$ transitions more efficiently than in normal galaxies (compare to the NGC 4151 active nucleus, which has significant warm H_2 rovibrational emission yet is undetected in low$-J$ CO transitions; Storchi-Bergmann et al. 2009; Dumas et al. 2010).

From optical *HST* imaging, nuclear dust features are found in a third to half of nearby FR sources in the 3CR and B2 radio catalogs, frequently appearing as morphologically regular disks (de Koff et al. 2000; Capetti et al. 2000; de Ruiter et al. 2002). CO-detected FR galaxies have an average $M_{\rm H_2} \gtrsim 10^8\ M_\odot$ (although with only $\sim$ 50% detection rates; e.g., Ocaña Flaquer et al. 2010). Our four CO-faint galaxies are either at or (in the case of IC 4296) an

order of magnitude below the CO detection threshold in these earlier surveys. We suspect that a large fraction of previously CO-undetected FR galaxies will show emission (with at least partially resolved gas kinematics) when observed with ALMA in relatively short ($\sim$ 1 hr per target) on-source integrations. Such observations will allow investigation of the physical conditions (e.g., molecular gas kinematics, disk dynamical coldness) of the large-scale dusty disks that power these radio galaxy nuclei. Furthermore, ALMA CO observations of a statistically unbiased sample of radio-loud and radio-quiet ETGs will reveal whether there exists any correlation between the molecular gas mass or surface density and the nuclear radio (and mm/sub-mm) continuum intensity.

3.4 Continuum Properties

All twenty-three ALMA targets show significant continuum emission concentrated near the galaxy centers. For our CO-bright (CO-faint) targets, the locations of the continuum peaks listed in Table 3.6 agree with the line kinematic centers to $\lesssim \overline{b}/5$ ($\sim \overline{b}/2$). Since at least some level of nuclear activity is seen in most ETGs (Ho et al. 1997b; Nyland et al. 2016), the centrally peaked continua in our sample may be dominated by emission from low-luminosity AGN (LLAGN). Other sources may include thermal and free-free emission from (AGN or stellar) photoionized regions, and thermal emission from cool dust grains. Through a combination of $uv-$plane modeling and spectral fitting, we investigate the continuum emission properties of our Cycle 2 sample.

3.4.1 Surface Brightness Modeling

When imaged with natural weighting, most of our Cycle 2 targets (with the exception of NGC 3268 and NGC 6861) show significant extended emission (see Figure 3.1). We model

Table 3.6 Continuum Centroid Positions

Galaxy	Peak Position (J2000) α	δ
(1)	(2)	(3)
Cycle 2		
NGC 1332	03:26:17.234	−21:20:06.81
NGC 1380	03:36:27.573	−34:58:33.84
NGC 3258	10:28:53.550	−35:36:19.78
NGC 3268	10:30:00.654	−35:19:31.55
NGC 4374	12:25:03.745	12:53:13.11
NGC 6861	20:07:19.469	−48:22:12.47
IC 4296	13:36:39.040	−33:57:57.18
Cycle 3		
NGC 2872	09:25:42.536	11:25:55.75
NGC 3078	09:58:24.585	−26:55:36.04
NGC 3557	11:09:57.647	−37:32:21.05
NGC 4697	12:48:35.898	−05:48:02.46
NGC 4786	12:54:32.410	−06:51:33.90
NGC 5838	15:05:26.248	02:05:57.32
Cycle 4		
NGC 384	01:07:25.014	32:17:33.80
PGC 11179	02:57:33.669	05:58:37.07
UGC 2698	03:22:02.899	40:51:50.06
Cycle 5		
NGC 3245	10:27:18.382	28:30:26.61
NGC 3271	10:30:26.505	−35:21:34.05
NGC 3585	11:13:17.093	−26:45:17.44
NGC 4261	12:19:23.215	05:49:29.69
NGC 5193	13:31:53.524	−33:14:03.55
ESO 208-G21	07:33:56.228	−50:26:34.57
ESO 322-G08	12:25:37.738	−39:19:11.02

Note: Nuclear continuum centroid location, in hh:mm:ss and dd:mm:ss format, from multi-frequency synthesis imaging of line-free channels prior to any any self-calibration. The astrometric precision of these observations is $\sim 0\farcs01$.

Table 3.7 Continuum Emission Properties

Galaxy	RMS Noise (μJy beam^{-1})	$S_{\rm nuc}$ (mJy)	$\alpha_{\rm nuc}$	$S_{\rm ext}$ (mJy)	$\alpha_{\rm ext}$
(1)	(2)	(3)	(4)	(5)	(6)
Cycle 2					
NGC 1332	28.2	$8.53\ (^{+0.88}_{-1.13})$	-0.44 (0.11)	$2.05\ (^{+0.50}_{-0.35})$	2.60 (2.05)
NGC 1380	26.8	$6.05\ (^{+0.64}_{-1.14})$	1.62 (0.17)	$2.35\ (^{+0.67}_{-0.40})$	6.10 (1.95)
NGC 3258	21.4	$0.44\ (^{+0.18}_{-0.24})$	0.90 (2.09)	$0.47\ (^{+0.27}_{-0.09})$	3.18 (2.69)
NGC 3268	27.0	3.45 (0.61)	-0.28 (0.30)	< 0.39	–
NGC 4374	53.8	$126.0\ (^{+13.1}_{-16.1})$	-0.21 (0.02)	$3.47\ (^{+7.17}_{-0.68})$	-0.56 (1.03)
NGC 6861	34.1	22.6 (2.29)	-0.27 (0.05)	< 2.04	–
IC 4296	164.4	$212.1\ (^{+21.4}_{-22.0})$	0.10 (0.02)	$2.59\ (^{+1.28}_{-0.69})$	–
Cycle 3					
NGC 2872	32.1	6.45	–	–	–
NGC 3078	102	90.3	–	–	–
NGC 3557	31.5	20.4	–	–	–
NGC 4697	25.9	0.23	–	–	–
NGC 4786	26.8	0.66	–	–	–
NGC 5838	25.6	3.45	–	–	–
Cycle 4					
NGC 384	28.5	1.02	–	–	–
PGC 11179	27.7	0.45	–	–	–
UGC 2698	26.6	1.45	–	–	–
Cycle 5					
NGC 3245	26.5	2.07	–	–	–
NGC 3271	29.3	0.39	–	–	–
NGC 3585	25.5	0.65	–	–	–
NGC 4261	53.2	251.6	–	–	–
NGC 5193	23.3	1.50	–	–	–
ESO 208-G21	19.3	20.1	–	–	–
ESO 322-G08	22.0	3.05	–	–	–

Note: Spatial and spectral properties of the nuclear and extended continua. We only present Cycles 3-5 peak continuum flux densities. Col. (2): The rms background noise in the naturally-weighted continuum images. Col. (3): Peak flux densities at an observed frequency of ~ 236 GHz. Asymmetric uncertainties for $S_{\rm nuc}$ and $S_{\rm ext}$ arise from first fitting the continua as completely unresolved sources in the uv plane and afterwards requiring that the extended emission monotonically decreases with radius. Col. (4): Spectral indices (where $S_\nu \propto \nu^\alpha$) of the unresolved emission using measurements of the peak continuum levels in separate spectral windows $\gtrsim 6$ GHz apart. Col. (5): Flux densities (or 3σ upper limits) of the extended continuum profiles, integrated over the optical dust disk regions. The uncertainties in $S_{\rm nuc}$ and $S_{\rm ext}$ tend to be dominated by the ($\sim 10\%$) uncertainty in the absolute flux calibration. Col. (6): Spectral indices of the extended emission using $S_{\rm ext}$ measurements of the extended continuum levels in separate spectral windows.

and subtract the central point sources in the uv plane prior to re-imaging the visibilities and isolating the extended continua. This point-source subtraction may leave a slight depression in the center of the extended continuum emission (e.g., for NGC 3258) and can also introduce imaging artifacts (in the case of IC 4296). For targets with significant extended emission, we account for possible over-subtraction of the point source by performing the $uv-$plane point-source subtraction with consecutively lower unresolved flux density values until the extended emission in the image plane has a roughly monotonically decreasing central profile (Figure 3.18). We take this as an appropriate upper bound to the extended continuum emission.

We determine the central unresolved ($S_{\rm nuc}$) and extended ($S_{\rm ext}$) continuum emission values (Table 3.7) by measuring the peak intensities from $uv-$plane modeling and by integrating the extended emission, respectively. For NGC 3268 and NGC 6861, we integrate over their optical dust disk regions to determine 3σ upper limits on their extended emission. For the remainder of the sample, we only integrate the extended emission out to the radius where negative sidelobes begin to decrease the $S_{\rm ext}$ values. Uncertainties in the tabulated flux densities include changes in $S_{\rm nuc}$ and $S_{\rm ext}$ when we force the point-source subtraction to produce centrally peaked extended continuum profiles. We separate these $S_{\rm nuc}$ measurements into mm-faint and mm-bright ($S_{\rm nuc} > 100$ mJy) nuclear sources for convenience during later discussion. We note that the two mm-bright galaxies NGC 4374 and IC 4296 are also the brightest radio (FR I) sources.

The resolved continuum profiles of NGC 1332, NGC 1380, and NGC 3258 follow the shapes and orientations of their optical dust disks. Since continuum emission above ~ 200 GHz is usually dominated by thermal reprocessing of starlight (e.g., Condon 1992), this consistency suggests a thermal origin for $S_{\rm ext}$. Dust absorption is apparent in *HST* images, so the dominant thermal source is likely cold ($T \sim 30$ K; Bendo et al. 2003; Galametz et al. 2012) dust grains. However, LLAGN and central star formation photoionize and heat their surround-

ings, and Bremsstrahlung emission from ionized atomic gas with electron temperatures of $\sim 10^4$ K may also contribute to the mm/sub-mm continuum emission. Long-slit spectroscopy of NGC 1380, NGC 3258, NGC 3268, NGC 4374, and IC 4296 reveals photoionized gas with low Hβ line luminosities ($\lesssim 10^{38}$ erg s^{-1}) and low densities ($n_e \lesssim 10^3$ cm^{-3}) within the central $2'' \times 2''$ (Annibali et al. 2010) that are typical of "dwarf" Seyfert nuclei (Ho et al. 1997a). Based on Balmer line decrements, the extinction in the observed ionized gas regions is low ($A_V \lesssim 1.5$ mag; Annibali et al. 2010), suggesting that the ionized gas emission is physically distinct from the molecular gas regions. In the scenario where the ionized gas exists around and between clumpy, optically thick ($A_V \gtrsim 10$) clouds, at most half of the intrinsic Hβ line emission will be heavily obscured (in the case of a uniformly opaque molecular disk). We therefore expect that the observed L(Hβ) values underestimate the total Hβ luminosity by no more than a factor of two. Ulvestad et al. (1981) derive a relationship between the Balmer narrow line flux and the low-frequency thermal flux density of low density environments. For a $\sim 10^4$ K emitting region, we expect that the nuclear photoionized gas in these galaxies should produce at most only a few μJy of thermal continuum emission at 230 GHz. Thermal emission from dust and not photoionized gas is therefore the most likely $S_{\rm ext}$ source for the Cycle 2 CO-bright galaxies NGC 1332, NCG 1380, and NGC 3258.

The continuum residuals of the mm-bright sources NGC 4374 and IC 4296 extend roughly perpendicular to the orientation of their optical dust disks, and are therefore not likely related to thermal emission. Instead, these extended features may trace resolved synchrotron jets on tens of pc scales. Sub-arcsecond resolution radio observations show an inner jet position angle of $\sim 170 - 180^\circ$ for NGC 4374 (Jones et al. 1981; Harris et al. 2002) and $\sim 140^\circ$ for IC 4296 (Pellegrini et al. 2003), while we estimate the orientations of the residual continuum emission to be at about 135° and 140°, respectively. Continuum observations at additional (esp. lower) frequencies of equivalent or greater angular resolution should allow for a more confident interpretation of the mm-bright $S_{\rm ext}$ profiles.

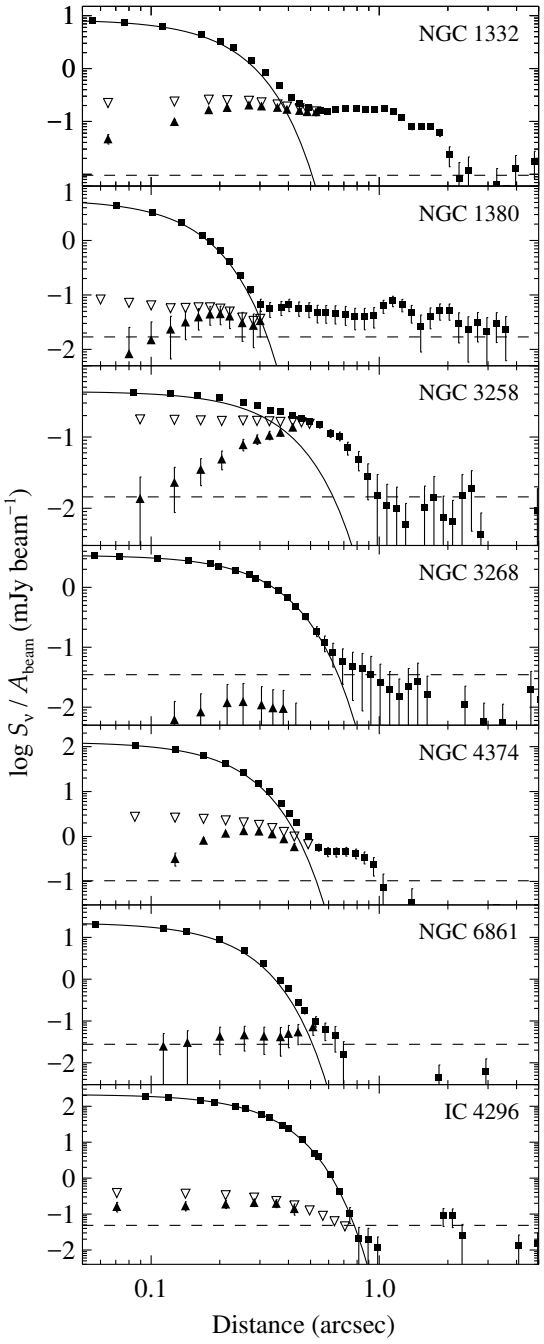

Figure 3.18 Continuum surface brightness profiles of the naturally-weighted Cycle 2 continuum images. The central peak component is modeled as an unresolved source in the *uv* plane, as represented by the accompanying scaled synthesized beam profiles (solid curves). The extended continua are first measured (filled diamonds) after removing the best-fit point source from the visibilities. When these fits yield significant nuclear residuals (in all cases except for NGC 3268 and NGC 6861), we subtract slightly lower, but still centrally-dominant, point source flux densities in the *uv* plane until the image plane residuals are a monotonically decreasing function of radius (open diamonds). Horizontal (dashed) lines show the rms sidelobe noise levels which are determined by measuring the surface brightness beyond the optical dust disk radii.

3.4.2 Spectral Fitting

The continua within the central beam areas are heavily dominated by unresolved emission for all Cycle 2 targets except NGC 3258 (although its peak unresolved emission still exceeds the resolved continuum by at least a factor of two). To measure crude mm-wavelength spectral indices, we imaged the continuum-only spectral windows into individual continuum maps with frequency separations of ~ 20 GHz. The unresolved nuclei were again subtracted in the *uv* plane (as described in §3.4.1) to determine $S_{\rm nuc}$ and $S_{\rm ext}$ values for each spectral window image. Nuclear and extended spectral indices were measured at an observed ~ 236 GHz by modeling the unresolved and (where detected) resolved continuum emission as a power law ($S_\nu \propto \nu^\alpha$).

The unresolved 1.3 mm continuum spectral indices $\alpha_{\rm nuc}$ of these seven ETGs range from -0.44 to 1.62 (see Table 3.7), and are roughly consistent with both the radio spectral indices and flux densities of other LLAGNs (Nagar et al. 2001; Nemmen et al. 2014). These spectral slopes are likely to result from some nuclear thermal dust emission (with index $\alpha_{\rm th} \sim 3-4$; see Draine 2003, 2006) surrounding a compact active nucleus, consisting of an accretion disk and perhaps a synchrotron jet (with $\alpha_{\rm syn} \sim -0.7$). In starburst galaxies (e.g., M82; Carlstrom & Kronberg 1991, Condon 1992), free-free emission from ionized stellar winds may also contribute (with $\alpha_{\rm ff} \sim -0.1$ to 0.4 at mm/sub-mm wavelengths; see Pascucci et al. 2012), but our Cycle 2 galaxies do not show any signs of significant nuclear star formation. The central engines of LLAGN are expected to be powered by hot accretion flows (such as advection-dominated accretion; Narayan & Yi 1994, Narayan & Yi 1995). Given plausible accretion model parameters and the previous $M_{\rm BH}$ measurements for this sample, our measured $\alpha_{\rm nuc}$ values are consistent with the predicted 1.3 mm spectral index for hot accretion flows (Yuan & Narayan 2014; see their Figure 1); however, a mixture of optically thin synchrotron and thermal emission can equally well reproduce this range in spectral slopes. Additional ALMA ($\sim 100-900$ GHz) continuum measurements, along with

sub-arcsecond radio flux densities, would enable us to confidently identify the dominant nuclear mm/sub-mm emission sources (e.g., see Alatalo et al. 2015).

Based on the spatial correspondance between the CO emission or radio jet orientation, the extended continuum profiles in our sample appear to originate from either thermal (with $\alpha_{\rm th} \sim 3-4$) or nonthermal ($\alpha_{\rm syn} \sim -0.7$) sources, respectively. The resolved continuum spectral indices $\alpha_{\rm ext}$ for NGC 1332, NGC 1380, and NGC 3258 (in Table 3.7) are all consistent with a purely thermal origin. As the cold dust in these disks is likely at a temperature of ~ 30 K, the 1.3 mm flux densities lie very far down on the Rayleigh-Jeans tail of thermal emission. Measuring $S_{\rm ext}$ across higher frequency ALMA bands will allow for more accurate $\alpha_{\rm ext}$ values and provide more useful constraints on the physical state of the dust. The extended continuum of NGC 4374 is inconsistent with a predominantly thermal source; due to large uncertainties inherent in extracting a weak extended source that is barely resolved, we cannot state with certainty that its $\alpha_{\rm ext}$ measurement is strong evidence for a resolved synchrotron jet.

3.5 Prospects for Black Hole Mass Measurement

The primary motivation for these Cycles 2 through 5 observations is to detect high-velocity rotation from within $r_{\rm g}$. In cases where the central velocity upturns are unambiguously detected, we plan to propose for higher spatial resolution ALMA observations to fully map and dynamically model the molecular gas kinematics. Barth et al. (2016b,a) have demonstrated the efficacy of this two-stage process for NGC 1332, measuring its $M_{\rm BH}$ to 10% precision. By comparison, BH mass measurements via stellar or ionized gas dynamical modeling typically produce 20-50% uncertainties on $M_{\rm BH}$ (Kormendy & Ho 2013) that often do not address potentially serious systematic uncertainties. High-resolution ALMA observations can provide crucial cross-checks for BH masses measured by stellar dynamical modeling or other

methods: for example, Barth et al. (2016a) use higher-resolution ALMA data to rule out a previous stellar dynamical BH mass measurement for NGC 1332 at high confidence. While ALMA has the capacity to highly resolve $r_{\rm g}$ and produce tight BH mass constraints for nearby galaxies, the majority of ETGs are not suitable targets for such studies. Roughly half of all ETGs show optically thick dust features, while only about 10% of these have morphologically regular dust disks (e.g., van Dokkum & Franx 1995; Tran et al. 2001). We have shown that the majority of such dust disk candidates should be detectable in CO with relatively short integration times using ALMA. To enable BH mass measurements, the observed disks need to be in circular rotation with low turbulence (low intrinsic $\sigma/v_{\rm c}$) and have high-velocity emission originating from within $r_{\rm g}$. Only 7/23 of our sample show central velocity upturns on spatial scales comparable to $r_{\rm g}$, although we cannot rule out low central surface brightness CO emission in several others. In addition, highly inclined disks are more difficult to model due to strong beam smearing effects that dilute the major axis rotation when the sphere of influence projected along the minor axis ($r_{\rm g}\cos i$; see Barth et al. 2016b) is not well resolved. Based on these findings, we expect that only a few percent of nearby ETGs will be good targets for highly precise BH mass measurements with ALMA. The barrier here is slightly higher than finding regular kinematics in circumnuclear ionized gas disks for BH mass measurements (though for different reasons), where the success rate without any pre-selection is somewhat less than 20% (Kormendy & Ho 2013). When rapid molecular rotation is detected within $r_{\rm g}$, however, the low turbulence and modest levels of disk warping make these ETG disks prime candidates for high-resolution ALMA observations.

In the sample PVDs we do not detect any CO(2−1) emission with deprojected velocity over $\sim$ 600 km s^{-1}; this suggests that most CO emission does not originate from deep within the BH sphere of influence. Observing denser gas tracers (including higher-J CO lines) at similar (or higher) angular resolutions will clarify whether molecular gas is abundant in the central few tens of parsecs of CO-bright ETGs. If such tracers are absent, the ubiquitous mm continuum sources are candidates to have dissociated or disrupted the inner molecular

disks. Observations of dusty disks in additional ETGs may reveal whether a correlation exists between the nuclear continuum intensity $S_{\rm nuc}$ and the presence of holes (as with NGC 6861, which has the brightest $S_{\rm nuc}$ of the Cycle 2 CO-bright subsample) or potential depressions (as with NGC 1332) in the inner emission-line surface brightness profiles.

For late-type galaxies, which tend to be gas-rich, a similar fraction may also be good candidates for BH mass measurement, and cold molecular gas tracers have already been observed at arcsecond to sub-arcsecond scales in some nuclei (e.g., García-Burillo et al. 2014; Onishi et al. 2015; García-Burillo et al. 2016). While observations of late-type galaxies are now approaching the resolution required to unambiguously detect the BH kinematic influence, complications such as spiral structure and radial flows may cause strong deviations from purely circular rotation that will be difficult to model (e.g., García-Burillo et al. 2016). Late-type galaxies also tend to have much lower $M_{\rm BH}$ values than do luminous ETGs, and the smaller BH spheres of influence for nearby spirals are more difficult to resolve with ALMA.

Obtaining an accurate stellar mass profile is essential when modeling the kinematics of ALMA observations that do not highly resolve molecular rotation within $r_{\rm g}$. *HST* imaging of these ETGs indicates that dust obscuration extends from roughly the outer edge of CO emission down to the nuclei. If the gas and dust are uniformly distributed in these disks, the average H_2 column densities derived from CO intensities suggest average visual extinctions of $A_V \sim 5-30$ mag; using standard extinction transformations (Rieke & Lebofsky 1985), we expect between 0.5 and 3 mag of $K-$band extinction of the stellar light that originates from *behind* the dust disks of our targets. The slopes of the central stellar luminosity profiles will therefore remain somewhat low (but to an uncertain amount) even if high spatial resolution NIR imaging is obtained. We find that uncertainties in the inner slope of the stellar surface brightness profile produce changes in the best-fitting $M_{\rm BH}$ determination from gas-dynamical modeling that are larger than the statistical BH mass uncertainties (Barth et al. 2016b; see also Figure 3.19). To minimize systematic errors from an uncertain stellar mass profile, the

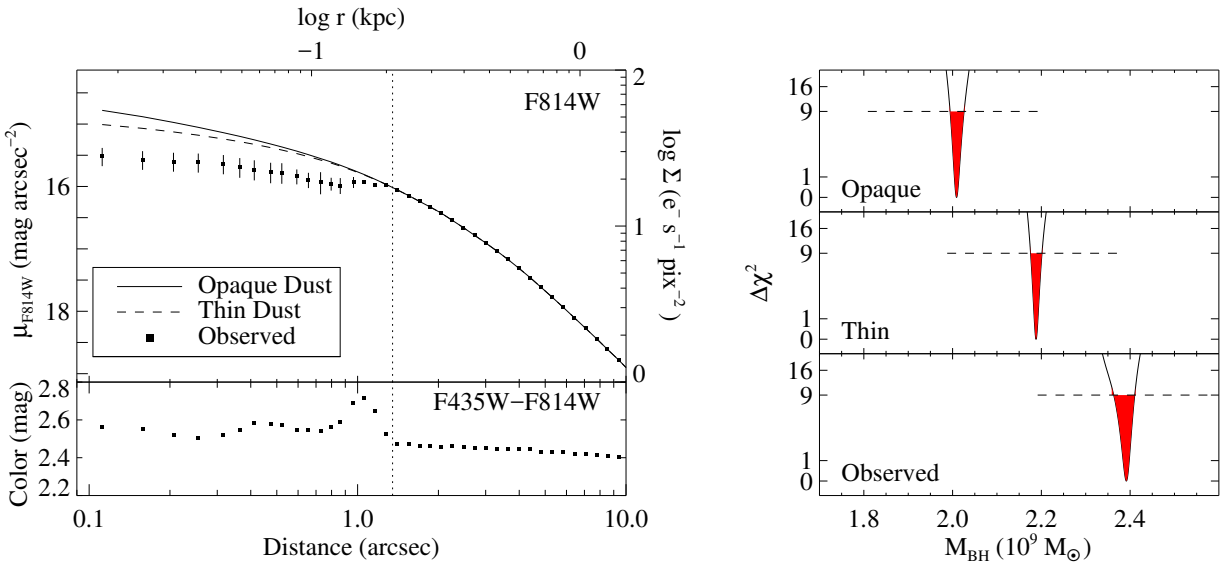

Figure 3.19 *Left*: NGC 3258 stellar surface brightness and color profiles derived from *HST* ACS/WFC F435W and F814W imaging. Only the central region is shown to highlight the dust extinction within the central arcsecond. Two additional model stellar luminosity profiles are included that assume either all (*solid line*) or half (*dashed*) of the central host galaxy light originating from *behind* the disk is obscured. For reference, the outer edge of the dust disk is indicated by the dotted line. *Right*: Preliminary gas-dynamical modeling results of the Cycle 2 NGC 3258 CO(2−1) imaging data, showing $\chi^2(M_{\rm BH})$ minimization curves that utilize stellar mass profiles derived from luminosity profiles that assume all (*top*), half (*middle*), and none (*bottom*) of the central galaxy light *behind* the disk is obscured. The dashed lines indicate the $\Delta\chi^2 = \chi^2 - \min(\chi^2) = 9$ level (for ~ 6000 degrees of freedom) and demarcate the 3σ statistical uncertainty ranges (*shaded*) for each of the host galaxy luminosity models. The total uncertainty captured by this range of possible input stellar mass models is $(2.0 - 2.4) \times 10^9\ M_\odot$, while the statistical uncertainty assuming any one of these host galaxy prescriptions in on the order of $\sim 2\%$.

optimal situation is to procure NIR imaging to mitigate extinction effects while obtaining ALMA observations that highly resolve the BH sphere of influence along both the disk major and minor axes. Ideally, this requires several independent resolution elements across the projected minor axis $r_{\rm g} \cos i$. Given the need for reasonable S/N while highly resolving $r_{\rm g}$, accurately measuring BH masses in ETGs is nontrivial, even with ALMA. Even without highly resolved observations, or in disks that show no central, rapid rotation, dynamical modeling is still capable of constraining or placing upper limits on $M_{\rm BH}$ after accounting for reasonable uncertainties in the inner slope of the stellar profile.

Gas-dynamical modeling of ALMA observations has the potential to produce some of the most accurately measured BH masses (Barth et al. 2016a) after the Milky Way BH (Ghez

et al. 2008; Gillessen et al. 2009) and a few determined using H_2O maser disks (e.g., Miyoshi et al. 1995; Kuo et al. 2011). Since only a few percent of nearby ETGs are likely to be good candidates for these high-resolution studies, careful sample selection is required. We have demonstrated that target pre-selection based on regular dust morphology produces a very high CO detection rate. ALMA observations with spatial resolution roughly matching $r_{\rm g}$ are sufficient to identify significant high-velocity molecular emission that justifies follow-up, high-resolution observations. This two-stage process is necessary to identify high-quality targets for long-baseline studies and to make optimal use of precious ALMA observing time.

Chapter 4

Precision Black Hole Mass Measurement of NGC 3258

NGC 3258 is one of two brightest group galaxies (the other is NGC 3268) that dominate the central regions of the Antlia cluster, a somewhat poor (Ferguson & Sandage 1990) yet nearby cluster. At a distance $D_L \sim 31.9$ Mpc, the disk radius of $\sim 1''$ corresponds to about 150 pc. ALMA Cycle 2 observations of this galaxy revealed strong central velocity upturns in its CO(2−1) emission line PVD (Figure 3.2). However, with a geometrically-averaged synthetic beam size $\overline{b} \sim 0\farcs44$ – roughly a quarter of the disk diameter – its central high-velocity emission is relegated to higher-order line moments. Compared to velocity upturns observed in the PVDs of at least six other ETGs in our sample (see Chapter 3), NGC 3258 shows the most Keplerian-like velocity signature, indicating significant molecular emission originating from radii $\ll r_{\rm g}$. Simple gas-dynamical modeling of the Cycle 2 data cube (shown in Figure 3.19) constrains its $M_{\rm BH}$ value to the range $(1.95 - 2.45) \times 10^9\ M_\odot$, resulting in an anticipated $r_{\rm g} \sim 0\farcs9$ that is nearly the entire disk radius (see Table 3.1). Uncertainties introduced by an optically-thick dust disk dominate over the statistical uncertainties in $M_{\rm BH}$ for an assumed stellar luminosity profile (see also Barth et al. 2016b).

Our first high-resolution ALMA observations in Cycle 3 imaged the NGC 1332 CO(2−1) emission with $\overline{b} \sim 44$ mas. These data disentangled the high-velocity along the line of nodes from the lower-velocity gas emission that, in Cycle 2 imaging, is beam smeared into the major axis due to its high disk inclination ($i \approx 80°$). Detailed dynamical modeling of the high-resolution data cube refines its $M_{\rm BH}$ determination made previously using Cycle 2 data (Barth et al. 2016b). Due in part to its disk inclination and low central CO surface brightness, the best-fit $M_{\rm BH}$ value is accompanied by a total error budget at the 10% level. Models are fit to data points within the central 50 pc ($\lesssim 2\ r_{\rm g}$), completely avoiding systematics associated with the choice of stellar mass profile; its BH mass measured at this level of precision invalidates a previous stellar dynamical modeling result (Rusli et al. 2011) at very high significance. Similarly well-resolved molecular gas observations of our most promising ALMA targets should enable $M_{\rm BH}$ determinations to equal (or better) precision. These valuable measurements will help anchor the BH mass-host galaxy scaling relationships at high $M_{\rm BH}$ and provide crucial cross-checks of other avenues of BH mass measurement.

In this chapter, we present higher angular resolution ($\overline{b} \sim 0\farcs1$, or roughly 15 pc spatial resolution) ALMA CO(2−1) imaging of the dusty disk in NGC 3258. Given its moderate inclination angle ($i \sim 45°$), these data provide about a dozen independent resolution elements across the minor axis $r_{\rm g} \cos i$, yielding the most highly resolved BH sphere of influence of any luminous ETG. Modeling of the exquisite molecular gas kinematics confirms the disk is in slightly warped but dynamically cold rotation. We describe detailed gas-dynamical modeling and preliminary results that suggest a final BH mass measurement with a $\lesssim 5\%$ precision. To mitigate the impact of dust obscuration and explore connections between the dust disk and molecular gas emission, we obtain and model ancillary optical/NIR broadband observations.

4.1 CGS Data

Constructing an accurate stellar luminosity profile for a relatively nearby, luminous galaxy such as NGC 3258 requires high angular resolution imaging to capture the central stellar behavior. Deep, lower-resolution observations out to several times the half-light radius $R_{\rm e}$ enable full characterization of the galaxy bulge/disk as well as detection/exploration of a possible extended stellar halo. Here, we briefly describe broadband imaging acquired by the Carnegie-Irvine Galaxy Survey (CGS; Ho et al. 2011). This survey targets 600 nearby southern hemisphere galaxies using the Las Campanas Observatory, obtaining $BVRI$ images with a $9' \times 9'$ FOV; for NGC 3258, these data cover the stellar surface brightness out to ~ 50 kpc (corresponding to about $5R_{\rm e}$; Lauberts & Valentijn 1989) from the nucleus.

To avoid the "red halo" PSF effect (Huang et al. 2013), we only use the cosmic-ray cleaned $V-$band CGS data of NGC 3258 (with $V \sim 26.9$ mag arcsec^{-2} limit; see Figure 4.1) to determine the large-scale stellar behavior. All other galaxies and foreground stars are masked prior to measuring the stellar surface brightness profile in regions that are spaced equally in position angle and logarithmically in radius (out to nearly $300''$; Cappellari 2002). These $V-$band profile measurements are later spliced with the $H-$band surface brightness profile to enable proper background subtraction of the smaller FOV *HST* data and thereby extend the MGE fit (Figure 4.1) by a factor of three in radius.

4.2 *HST* Data

4.2.1 Archival ACS Observations and Dust Obscuration

A previous *HST* program (GO-9427; Häring-Neumayer et al. 2006) obtained deep (38 and 89 min on-source, respectively) ACS/WFC F435W and F814W imaging of NGC 3258. We

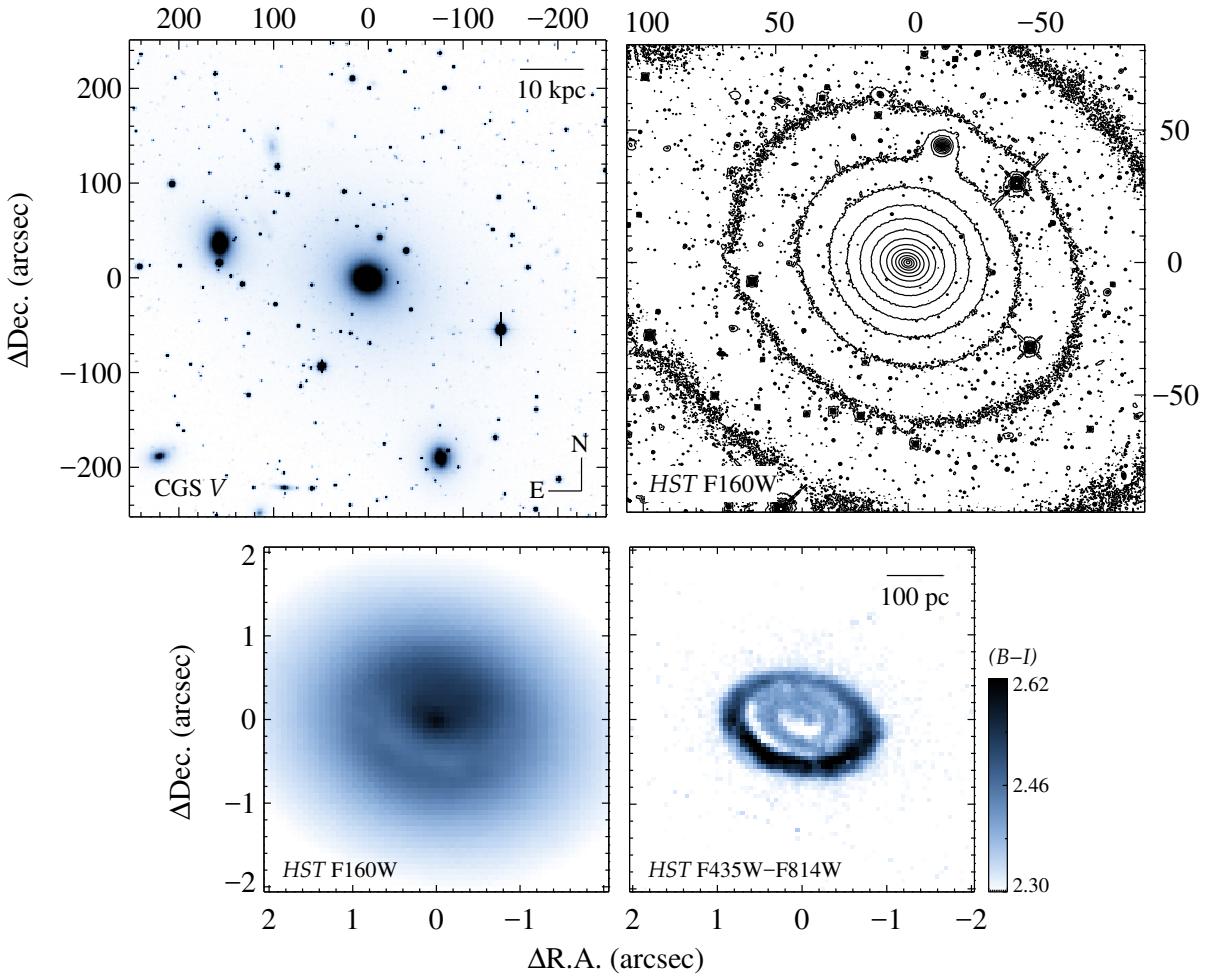

Figure 4.1 Stellar imaging data for NGC 3258. Wide-field ($\sim 9' \times 9'$; *top left*) $V-$band image from the Carnegie-Irvine Survey (CGS), shown in an inverted color scale, of this brightest group galaxy. A new *HST* F160W mosaic ($\sim 3\farcs0 \times 3\farcs4$; *top right*) better constrains the surface brightness in the central ~ 20 kpc. The entire $2''-$wide dust disk (*bottom*) is clearly visible in the *HST* ACS F435W-F814W color map and, at least for the near side of the disk, in the F160W mosaic.

processed the raw images using the CALACS pipeline, afterwards combining the distortion-corrected ACS images in each filter onto a uniform pixel scale and origin using the DrizzlePac package Astrodrizzle (Gonzaga et al. 2012). Since the galaxy fills the images, background subtraction was not performed at this stage. Upon inspection, these data reveal a morphologically round, optically thick circumnuclear dust disk $\sim 2\farcs2$ wide (corresponding to roughly 330 pc) that is nearly azimuthally symmetric in its structure map (see Fig. 3.1). An F435W-F814W color map (see Fig. 4.1) shows the regions of highest obscuration appear to trace out two rings with average distances of about $0\farcs4$ and $0\farcs8$ from the nucleus.

If treated as a foreground screen (as have others), the peak $B-I$ color excess in the outer dust-disk annulus suggests a modest $A_V \sim 0.3$ mag (assuming $R_V = 3.1$; Cardelli et al. 1989). Instead, the disk appears to be a geometrically-thin disk embedded in the galaxy midplane, where an intrinsic A_V only obscures the stellar light originating from *behind* this disk. The disk-averaged H_2 column density N_{H_2} of NGC 3258, inferred from ALMA Cycle 2 CO(2−1) flux measurements and a Galactic N_{H_2}/A_V conversion factor (Güver & Özel 2009), suggests a much higher $A_V \sim 10$ mag extinction of the stellar light originating from behind the dusty disk (Boizelle et al. 2017). This estimate translates into significant obscuration well into the NIR, hinting that dust extinction will still impact stellar surface brightness profiles derived from even $K-$band imaging.

We model this dust obscuration by creating a mock galaxy cube of stellar luminosity densities to determine the fraction of the total light that originates from in front (p), within (f), and behind ($q = 1-p-f$) the galaxy midplane (see Viaene et al. 2017) at each projected spatial position. The cube is populated by deprojecting the stellar surface brightness (described by the F160W MGE in §4.2.3), accounting for both galaxy inclination and oblateness. The wavelength-dependent attenuated light F'_λ as a fraction of its intrinsic value F_0 is:

$$\frac{F'_\lambda}{F_{\lambda,0}} \approx \frac{(1-f)(p/q)}{p/q+1} + f\left[\frac{1-10^{-A_\lambda/2.5}}{0.921A_\lambda}\right] + \left[\frac{1-f}{p/q+1}\right] 10^{-A_\lambda/2.5}\,, \tag{4.1}$$

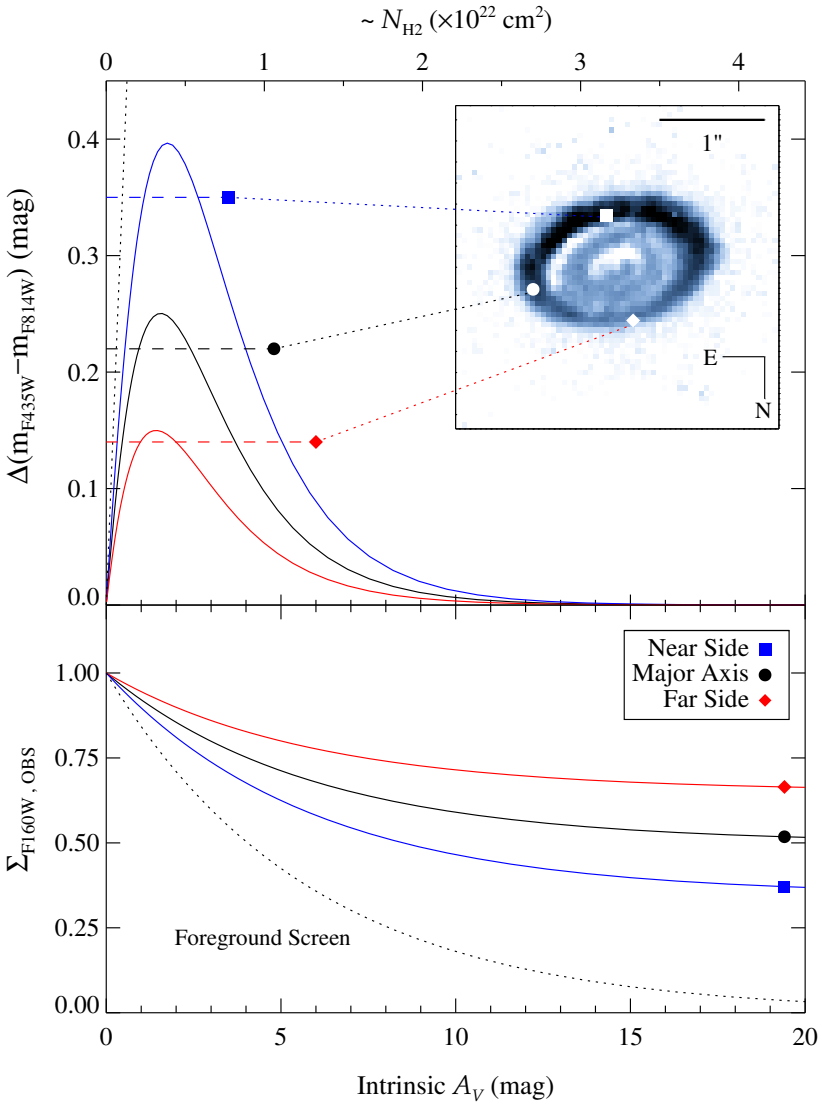

Figure 4.2 Results of modeling *HST* NGC 3258 imaging, creating a mock galaxy with a geometrically thin, inclined dusty disk embedded in its midplane. *Top*: Predicted changes to the model $\Delta(m_{\rm F435W} - m_{\rm F814W})$ profiles as a function of the intrinsic A_V, shown to agree with the observed F435W-F814W color excess at three locations in the physical dust disk. *Bottom*: The anticipated effect of disk A_V on the normalized *HST* F160W surface brightness profile at the same three disk locations. The dotted curves in both panels show the model $\Delta(m_{\rm F435W} - m_{\rm F814W})$ and $\Sigma_{\rm F160W}$ profiles if we instead assume the extinction is due to an entirely foreground screen.

with an anticipated color excess in the observed *HST* ACS filters:

$$\Delta(m_{\rm F435W} - m_{\rm F814W}) = -2.5\log_{10}\left[\left(\frac{F'_{\rm F435W}}{F_{\rm F435W,0}}\right)\left(\frac{F'_{\rm F814W}}{F_{\rm F814W,0}}\right)^{-1}\right] . \quad (4.2)$$

Using a Cardelli et al. (1989) $R_V = 3.1$ extinction law, we determine model color excesses as a function of intrinsic A_V at various spatial locations across the optically thick disk. Extracted $\Delta(m_{\rm F435W} - m_{\rm F814W})$ profiles at three disk locations (see Fig. 4.2) show model color excess curves that reach a maximum at $A_V \sim 1.5-2$ mag. Rapidly declining "observed" color with increasing A_V is the results of diminishing contributions from increasingly reddened background stellar light. At near and far sides of the disk, the observed peak $m_{\rm F435W} - m_{\rm F814W}$ values in the outer annulus (with radii ranging from $0\farcs6-1\farcs0$; see Figure 4.6) agree well with the model $\Delta(m_{\rm F435W} - m_{\rm F814W})$ maxima. These results strongly suggest the decrease in central color interior to $\sim 0\farcs7$ is due to heavy ($A_V \gtrsim 5$) obscuration and not any optical thinning of the inner disk. This simplistic model is illustrative only: actually recovering the intrinsic stellar surface brightness will require accounting for dust geometry/distributions and realistic radiative transfer (e.g., Camps & Baes 2015), star formation regions, etc. Constraining the possible components of such detailed dust modeling will necessitate spatially resolved optical-to-NIR spectroscopy or imaging in multiple filters across the same wavelength range.

4.2.2 WFC3 Observations

We obtained *HST* WFC3/IR channel F110W and F160W ($H-$band) imaging of the galaxy in one orbit on 5 June 2017 as a part of program GO-14920. $H-$band imaging consisted of a single exposure in a four-point mosaic pattern to obtain a wider $3\farcm4\times3\farcm1$ FOV with the nucleus always kept in one corner. The F160W data were obtained in the STEP50 (NSAMP=12) sequence for a total integration time of 23 min. These new data were processed through the CALWF3 pipeline, corrected for distortions, and combined to a uniform ($0\farcs065$ pixel^{-1})

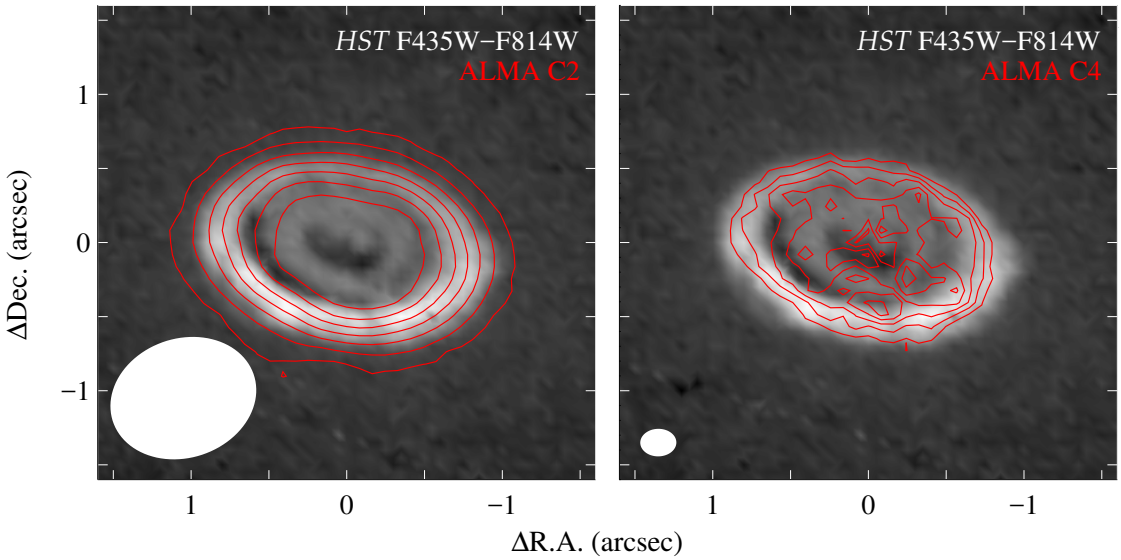

Figure 4.3 *HST* F435W-F814W color map shown with the ALMA CO(2−1) surface brightness maps (overlain, contours) for the Cycle 2 (*left*) and Cycles 2+4 (*right*) data sets. In this latter comparison, the ALMA angular resolution best matches that of the *HST* optical imaging. The optically thick dust disk outer radius agrees closely with the CO emission extent. ALMA synthetic beams are included in each figure. The outer annulus of highest $(B - I)$ color extends from $\sim 0\farcs6 - 1\farcs0$ while the majority of the CO flux originates from *within* this annulus.

scale and origin using the DrizzlePac package Astrodrizzle (Gonzaga et al. 2012). As the galaxy halo light extends beyond the $\sim 2'$ radial extent of the *HST* mosaic, background subtraction was not performed during this process. In future work, these *HST* ACS and WFC3 observations will be utilized to perform pixel-based spectral energy distribution (SED) radiative transfer modeling across the disk. At present, the $H-$band imaging is used to constrain a stellar mass profile that is *less* impacted by dust attenuation.

4.2.3 Stellar Mass Profile

In the same manner as CGS $V-$band data, we masked foreground stars and galaxies in the $H-$band mosaic and measured its stellar surface brightness profile out to $\sim 100''$. A composite surface brightness profile is formed by scaling the $V-$band measurements to match the *HST* data in the overlap region between $70'' - 90''$ at multiple position angles. At this stage, a uniform sky background is also subtracted from the NIR mosaic, and the final $V-$band scaling and NIR background values minimizes residuals at these radii. We note the optical/NIR splicing process assumes that negligible $V - H$ color gradients observed around one arcminute extends far beyond $\sim R_{\rm e}$. This composite $H-$band profile is then parameterized by an MGE consisting of 13 coaxial elliptical Gaussians (shown in Figure 4.4) that are corrected for the expected Galactic reddening of $A_H \sim 0.041$ mag (Schlafly & Finkbeiner 2011).

Based on mock galaxy simulations described in §4.2.1, the central dust disk may obscure the $H-$band light originating from *behind* the disk by ~ 1 mag. We assume the intrinsic stellar surface brightness is a smoothly declining function of radius that connects to the observed profile beyond the disk radius of $\sim 1''$ but is elevated at interior radii. Borrowing techniques used to modify the central surface brightness profile of NGC 1275 (see §2.1.2) and NGC 3258 (in early Cycle 2 dynamical modeling; see Figure 3.19), an additional stellar luminosity

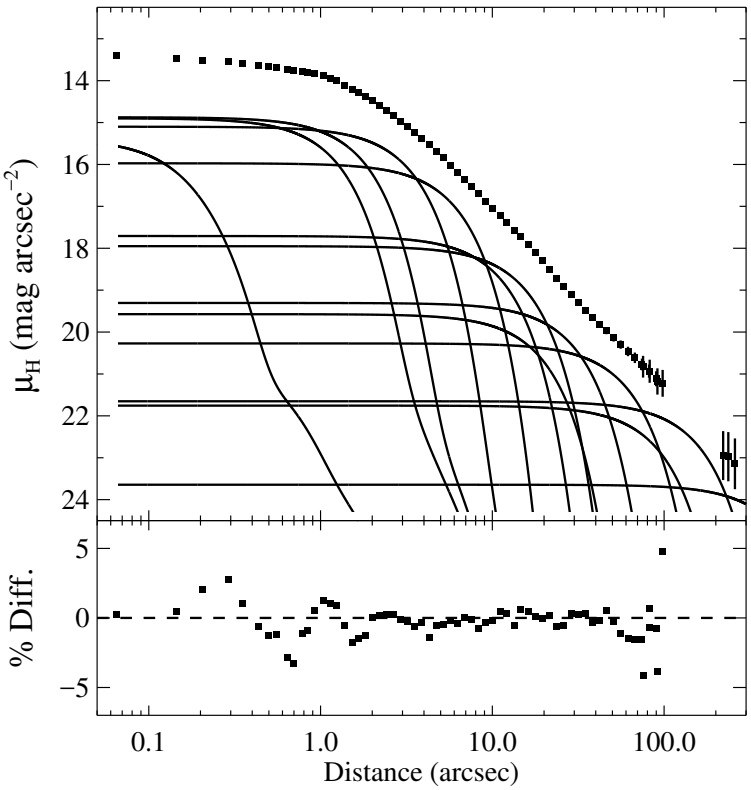

Figure 4.4 Multi-Gaussian Expansion of the *HST* WFC3 F160W surface brightness profile after splicing in the CGS $V-$band imaging at radii beyond $\sim 70''$. The central depression in stellar slope is still evident interior to the dust-disk radius of $1''$. The break in data points at around $2'$ is the result of masking out a neighboring galaxy.

profile is created with a steeper central slope to correct for a plausible intrinsic $A_H \sim 0.75$ mag in the central few pixels (corresponding to half of the stellar light behind the midplane being obscured). This model approximation follows the corrected profile shown in Fig. 4.4.2; for use in gas-dynamical modeling of CO(2−1) kinematics, the modified surface brightness profile is also decomposed using an MGE.

4.3 ALMA Data

4.3.1 Observations and Imaging

Higher angular resolution ALMA imaging of NGC 3258 were obtained in three execution blocks on 7-8 August 2017 in Program 2016.1.00854.S. These observations consisted of a single pointing with three $\sim$ 2 GHz bandwidth spectral windows spanning $227.5 - 245.0$ GHz. The primary window centered on the redshifted ^{12}CO(2−1) 230.538 GHz line that was observed in our Cycle 2 sample, and the remaining two measured the continuum at ∼228.4 and ∼243.0 GHz. Given the observed CO line widths (of $\lesssim 5$ km s^{-1}; Boizelle et al. 2017), this target was imaged using 3.91 MHz channel widths (after an 8× online channel averaging to reduce data rates) in the emission line spectral window and 15.6 MHz spacing when measuring continuum-only spectral windows (corresponding to velocity sampling of $\sim$ 5.08 and 20.3 km s^{-1}, respectively). The data were obtained under good to moderate weather conditions (PWV between $0.3 - 1.0$ mm) and flux calibrated using J1037−2934 and J1107−4449 from the ALMA quasar catalog. The precision of these flux standards combine to give roughly 10% uncertainty in all subsequent flux and flux density measurements (Fomalont et al. 2014).

The visibilities were processed using version 4.7.2 of the CASA pipeline. As the nuclear continuum source in NGC 3258 is very weak ($S_{\rm nuc} \sim 0.2$ mJy, consistent with Cycle 2

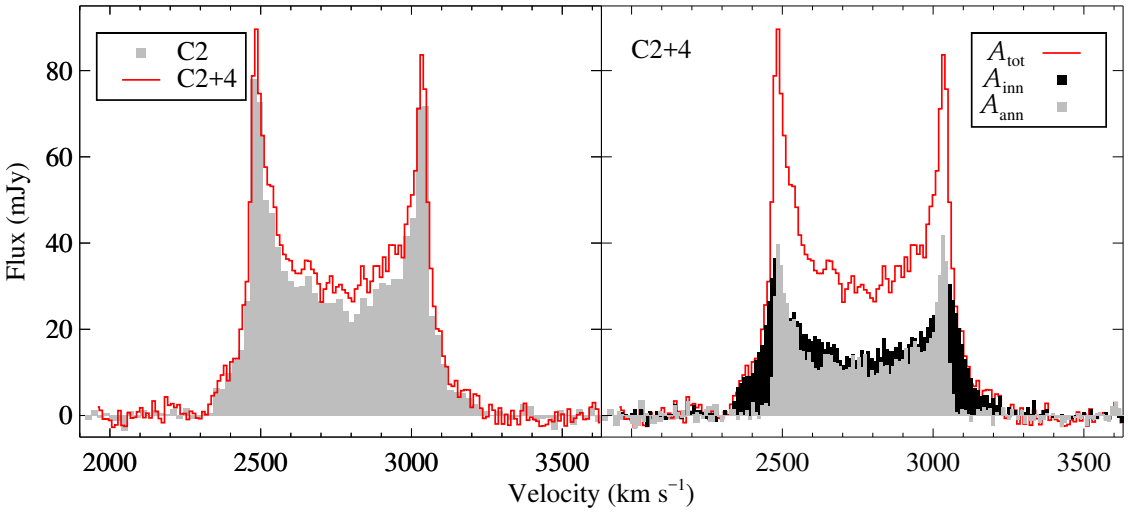

Figure 4.5 NGC 3258 CO(2−1) emission velocity profiles, integrated over the respective emission-line areas. *Left*: Comparison between the Cycle 2 and Cycles 2+4 profiles, integrated over the respective emission-line areas. The flux density increase is primarily the result of performing a multiscale deconvolution. *Right*: Velocity profiles formed by integrating the Cycle 2+4 flux densities over the entire elliptical disk area ($A_{\rm tot}$), within a radius of $0\farcs6$ ($A_{\rm inn}$), and in an annulus with major axis radii ranging from $0\farcs6 - 1\farcs0$ ($A_{\rm ann}$).

measurements; see Table 3.7), we did not attempt any continuum phase self-calibration on this data set. The continuum was imaged using CASA TCLEAN deconvolution with both natural and Briggs weighting (Briggs 1995; with robust parameter $r = 0.5$). A pixel size of $0\farcs015$ adequately samples the beam minor axis. After $uv-$plane removal of faint continuum emission, the visibilities were imaged into data cubes with 7.81 MHz channels (twice the native binning, so ~ 10.1 km s^{-1}) using Briggs ($r = 0.5$) weighting. Velocities were calculated in the barycentric frame using the optical definition of radial velocity. On-source integration time of 135.2 min enable a typical rms sensitivity level of ~ 0.265 mJy beam^{-1} in ~ 10 km s^{-1} channels and ~ 12.0 μJy beam^{-1} after multi-frequency synthesis imaging of the continuum-only channels. (To compare the relative sensitivities of Cycles 2 and 4 data sets, imaging the latter visibilities into 20 km s^{-1} channels achieves an rms sensitivity of ~ 0.108 mJy beam^{-1} compared to ~ 0.35 mJy beam^{-1} for the former observations; see Table 3.3.) With baselines ranging between $21 - 3696$ m, this data set achieves a synthetic

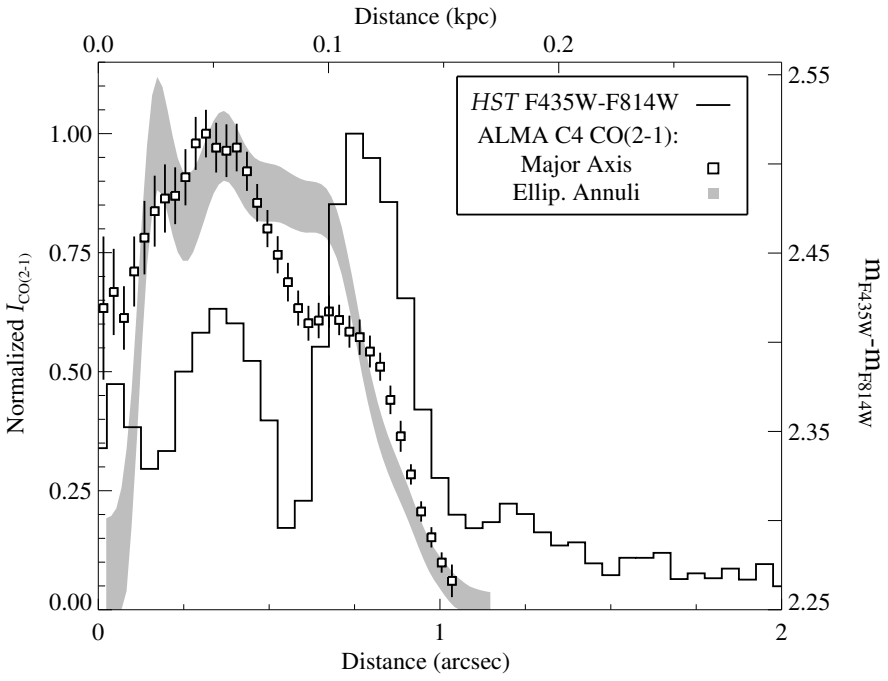

Figure 4.6 Normalized NGC 3258 CO(2−1) surface brightness profiles, extracted along the disk major axis and averaged over elliptical annuli with axis ratio $q = \cos i$ using the best-fitting $i \approx 49°$ from dynamical modeling. Shown for comparison, the *HST* F435W-F814W color profile, extracted along the disk major axis, highlights the observed color excess does not faithfully trace the molecular gas reservoir.

beam size of $\sim 0\farcs11 \times 0\farcs08$ with a major axis PA=88°. The resulting maximum recoverable scale of $1\farcs2$ is only slightly larger than the disk radius as measured from *HST* color maps. Integrated Cycles 2 and 4 flux measurements do not suggest that some smooth CO emission is resolved out. To better explore the emission line properties at this high angular resolution, we simultaneously imaged the Cycles 2 and 4 continuum-subtracted visibilities together using a multiscale deconvolution, yielding an rms sensitivity of ~ 0.228 mJy beam^{-1} in the same channel binning, albeit with a slightly degraded synthetic beam size of $\sim 0\farcs12 \times 0\farcs09$ due to the inclusion of additional small-baseline data.

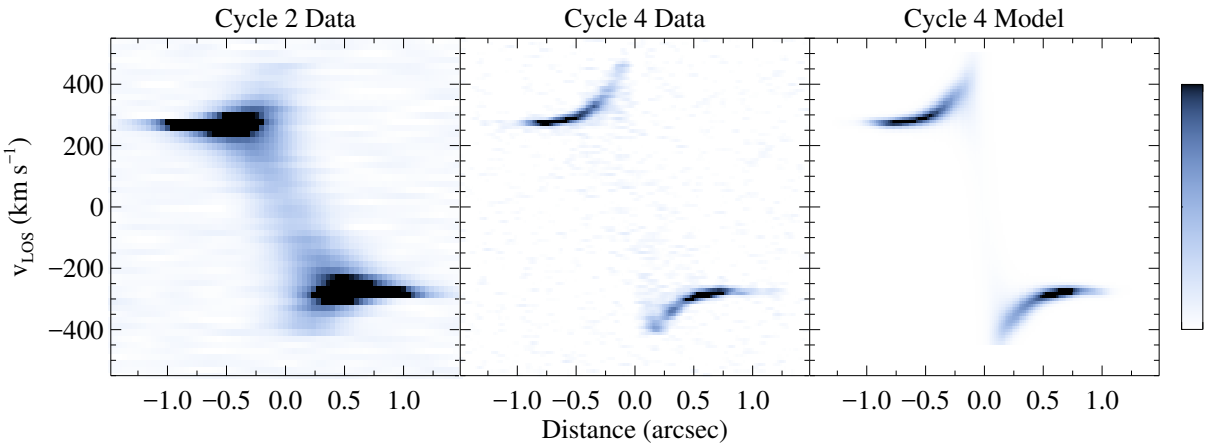

Figure 4.7 NGC 3258 ALMA CO(2−1) PVDs for the Cycle 2 (*left*) and Cycle 4 (*middle*) imaging at angular resolutions of $\sim 0\farcs44$ and $\sim 0\farcs1$, respectively, extracted at a PA of 75° with a width equal to their respective synthetic beam sizes. The galaxy systemic velocity is removed from the observed line-of-sight velocities. We note that the Cycle 4 observations confirm our previous suspicion of some asymmetry in the Keplerian velocity upturns, especially an apparent high-velocity ($\gtrsim$ 450 km s^{-1}) emission deficit in the approaching side of the disk. The model PVD (*right*) is constructed from thin disk models that include non-parametric fits to both the kinemtic warping and the stellar mass density profile as well as a radial-varying prescription for the CO line width.

4.3.2 Emission Line Properties

In the Cycle 2+4 data cube, CO(2−1) emission is clearly detected in channels spanning 910 km s^{-1}. The highest velocity emission is detected on either side of the nucleus. Integrating its flux densities in each channel over the elliptical disk area, as shown in Figure 4.5, yields a velocity profile that is fully consistent (within the flux calibration accuracy) to that derived from the Cycle 2 data set and a $I_{CO(2-1)} = 24.8$ Jy km s^{-1}. Extracting a position-velocity diagram along the disk major axis (at a PA$\approx$ 77°; see Fig. 4.7) now reveals a resolved locus of high-velocity emission that traces approximately Keplerian rotation extending to within the synthesized beam FWHM (roughly 17 pc) of the kinematic center.

We parameterize the line profiles at each spatial pixel with GH profiles that include the h_3 and h_4 coefficients. Due to the more than four times improvement in angular resolution over

the initial data set, the higher-order line moments tend to be negligible ($|h_3, h_4| \lesssim 0.05$) during line fitting. Disk regions are Voronoi-binned to ensure approximately equal S/N per bin during spectral fitting, although this spectral aggregation only significantly impacts the spatial sampling of the outer disk regions. The resultant maps of CO(2−1) line flux, $v_{\rm LOS}$, and $\sigma_{\rm LOS}$ are shown in Figure 4.8. The CO emission now appears clumpy, suggesting at least marginal resolution of some large giant molecular clouds. The apparent central hole matches the separation in high-velocity emission across the nucleus in the PVD. Within the central 75 pc, the line-of-sight velocity field shows a smooth increase (by $\sim 15°$) in disk PA and fully resolved, symmetric velocity upturns. Even though Cycle 2 imaging did resolve $r_{\rm g} \cos i \approx 0\farcs6$ for this disk, its GH-fit $v_{\rm LOS}$ map (see Figure 3.7) only showed constant average velocity down nearly to the nucleus. Recovering Keplerian structure in the measured velocity field appears to require *highly* resolving the BH sphere of influence along the minor axis. Deprojecting the LOS velocity extrema indicates maximum circular velocities of ± 610 km s^{-1}. Line widths are broadest at the disk center and the measured dispersions are elevated due to beam smearing together large velocity gradients above and below the disk major axis, along which axis the minimum $\sigma_{\rm LOS}$ falls below 7 km s^{-1}.

Cycle 2 imaging shows the CO(2−1) emission coincides directly with the $\sim 2''$−wide optically thick dust disk, albeit at such coarse angular resolution as to prohibit any detailed investigation of the dust disk/CO surface brightness correspondence. Shown at higher resolution ($\overline{b} \sim 0\farcs1$) in Figure 4.3 and extracted along the disk major axis in Figure 4.6, the observed CO emission now appears decoupled from the *HST* F435W-F814W color excess profile. Whereas the region of highest $m_{\rm F435W} - m_{\rm F814W}$ lies within the outer ($0\farcs6 - 1\farcs0$) elliptical annulus, its integrated $I_{\rm CO(2-1)} = 10.1$ Jy km s^{-1} is lower than the 14.7 Jy km s^{-1} measured when integrated over the interior ellipse (see Figure 4.5). The average surface brightness $I_{\rm CO(2-1)}/A_{\rm beam}$ over the outer and inner regions is 0.09 and 0.23 Jy km s^{-1} beam^{-1}, respectively. This further supports the claim that, at radii interior to $\sim 0\farcs7$, the disk is so optically thick (with $A_V \gtrsim 4 - 5$ mag) that light behind this embedded dust is

ineffective in producing a more reddened color.

4.4 Dynamical Modeling

These regular CO kinematics are very amenable to detailed gas-dynamical modeling. However, their exquisite kinematics and surface brightness maps reveal moderate deviations from purely co-planar rotation of a smoothly-distributed CO-emitting disk. We first test the assumptions of simple thin disk rotation to then compare with results from a more complex framework. This method will allow measurement of systematics associated with using an oversimplified model. Efforts are ongoing, and here we present only *preliminary* gas-dynamical results. In future work, we will model disk rotation in the *uv* plane to avoid errors associated with image deconvolution. For now, we follow the forward modeling method of Barth et al. (2016a,b) to create and optimize a model cube in the image plane. This method populates a model cube with Gaussian line profiles at each spatial position, whose line centroids and widths are determined by the combined BH+stellar mass circular velocity profile and a model for the line dispersion. Model line profiles at each spatial position are weighted by a Lucy-Richardson deconvolution of the CO(2−1) line flux. We convolve each velocity channel with a synthetic beam profile to approximate beam smearing. Both data and model cubes are downsampled (by a factor of 5) to create "pixels" that are about the size of one synthesized beam and and thereby much less sensitive to correlated errors (see Barth et al. 2016b). The NGC 3258 $r_{\rm g}$ value encompasses essentially the entire dusty disk, so we set the fitting radius $r_{\rm fit}$ to the edge of disk emission at $1''$. Optimizing fits to the downsampled cubes using the entire disk radius and roughly a hundred velocity channels results in about 4×10^4 degrees of freedom.

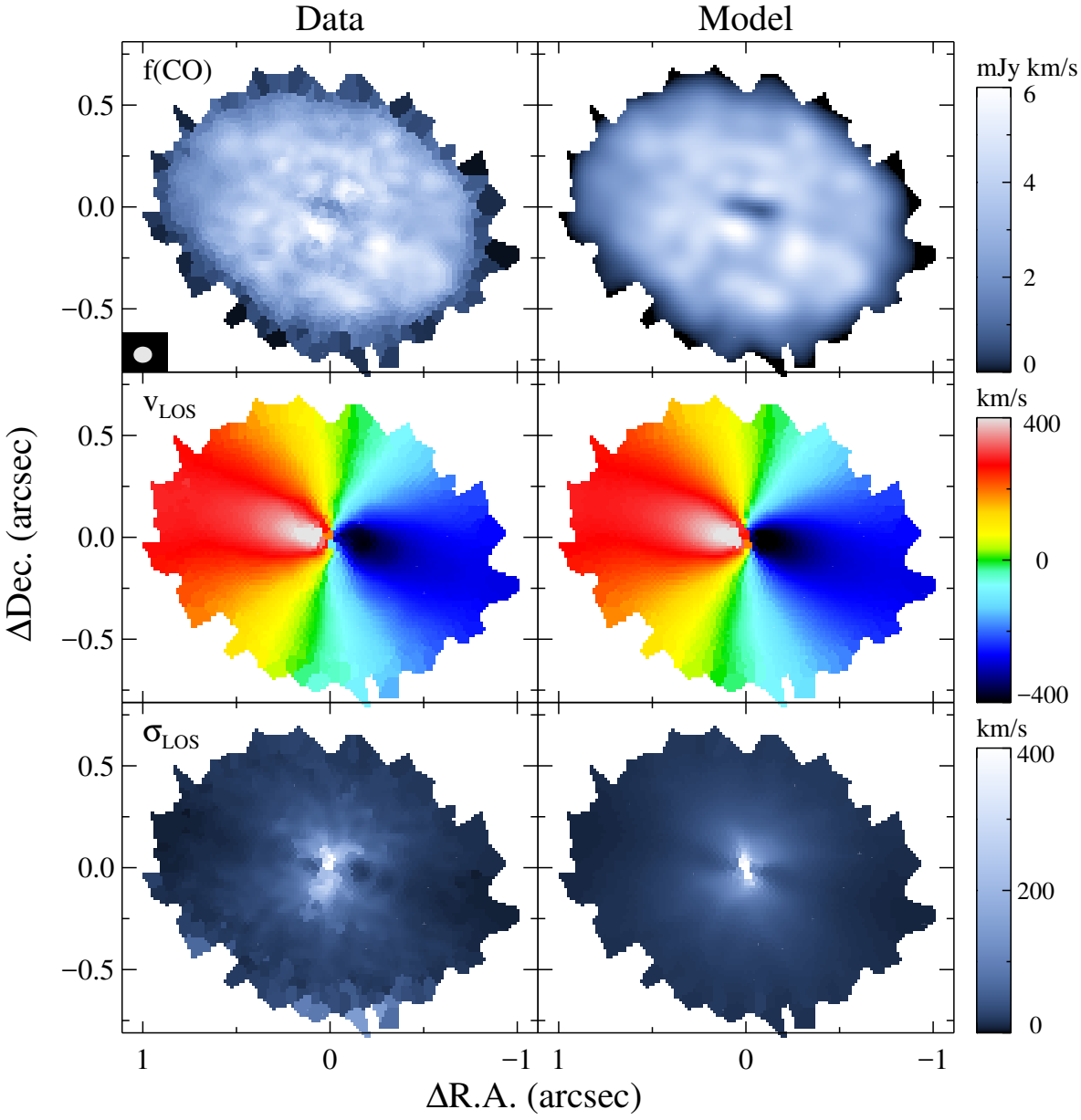

Figure 4.8 Maps of CO(2−1) GH line profile fits to the Cycle 2+4 NGC 3258 data cube (*left*) and best-fitting thin disk model (*right*) that includes non-parametric prescriptions of a tilted-ring disk model and the central stellar mass density. Shown are the integrated/model line emission and the LOS velocity and dispersion fields.

4.4.1 Simple Thin Disk Modeling

The most simple thin disk model that is sufficiently flexible to reproduce the CO(2−1) rotation pattern takes as free parameter inputs the $M_{\rm BH}$ value, $H-$band M/L ratio Υ_H, (fixed) disk inclination i and position angle θ, a constant line width (flat dispersion profile σ_1; see §2.5.1), disk kinematic center ($x_{\rm c}$, $y_{\rm c}$), and average disk redshift z. Comparison of the preliminary $M_{\rm BH}$ determination with mass constraints derived from modeling the Cycle 2 data cube (see Figure 3.19) suggests strong central $I-$band extinction. We therefore utilize the model $H-$band stellar luminosity profile described in §4.2.3 that corrects for a loss of half of the stellar light originating from *behind* the disk plane.

Allowing all parameters to freely vary in a downhill simplex χ^2 minimization process (Press et al. 1992) finds a best-fit $\chi^2_\nu = 1.23$ with parameter values $M_{\rm BH} = 2.12 \times 10^9$ $M_\odot$, $\Upsilon_H = 2.2$ $M_\odot/L_\odot$, $i = 49.2°$, $\theta = 77.0°$, $\sigma_1 = 10.27$ km s^{-1}, and $z = 0.0091254$. The disk kinematic center is constrained to be $\lesssim 5$ pc of the Band 6 nuclear continuum peak location. We optimized the simple thin disk model at fixed BH masses (see Figure 4.11), finding a very well-defined, Gaussian-like minimum in the $\chi^2(M_{\rm BH})$ curve. From this minimization, we confirm the preferred BH mass and estimate the statistical measurement uncertainties (bounded by $\Delta\chi^2 \leq 9$) to be at the 0.5% level in BH mass. Several systematic uncertainties related to the choice of stellar luminosity profile, prescription for emission line widths, etc., are expected to introduce shifts in the best-fitting BH mass that far exceed its statistical uncertainty range. Inspection of the model fit residuals also demonstrate the need for a more flexible stellar circular velocity profile as well as a more general prescription for disk structure.

4.4.2 Detailed Disk Modeling

Construction of more general models of thin disk rotation is warranted based on the incredible data quality and nearly symmetric disk kinematics. We note these new models (described

below) pioneer the study of highly resolved molecular gas disks. While the following additions or adjustments do improve the overall model fits (see Figure 4.8 for a comparison of data and model line moment maps), spatial substructure and spectral line complexity keep χ^2_ν elevated over unity. Parameter value statistical uncertainties are unreasonably narrow (at the $\sim 0.2\%$ level in some cases). This is in large part due to the number of degrees of freedom contained in the fitting region, of which the actual disk emission occupies only a small fraction (a little less than 6% of the total degrees of freedom). This dilutes the χ^2_ν value and produces overly confident parameter measurements via $\Delta\chi^2$ methods. Restricting the fits to data cube regions within $r_{\rm fit}$ that contain or are near CO emission predictably worsens the goodness-of-fit measure. A portion of the significantly elevated χ^2_ν level is due to sidelobe noise in each velocity channel that cannot be replicated by convolution of the model emission with a simple elliptical synthesized beam. Modeling the rotation in the uv plane is expected to produce much more precise parameter determinations, although no study has yet explored the systematics associated with optimizing disk models directly to visibility data.

Kinematic Twists

The most easily justified adjustment to the simple thin disk model is to allow the disk position angle θ and axis ratio $q(\approx \cos i)$ to vary in some manner as some function of radius. We adopted a tilted-ring model (e.g., see Neumayer et al. 2007) to describe a warped disk where $\theta \rightarrow \theta(R)$ and $q \rightarrow q(R)$, favoring a non-parametric prescription that allows these parameters to vary at specific radii (instead of just fixing $\theta(R)$ and $q(R)$ to a kinematic expansion of $v_{\rm LOS}$; Krajnović et al. 2006; see also Neumayer et al. 2007) and are interpolated at intermediate values. Tilted-ring models do not in general preserve the one-to-one correspondence between projected (sky) coordinates and physical disk location that underpins thin-disk model simplicity. However, the mild, smoothly varying twists observed in the $v_{\rm LOS}$

data do not create any significant overlap between neighboring "rings". Incorporating disk warping while retaining the remainder of the simple thin disk formalism does not produce much better fits to the data as its $\chi^2_\nu = 1.22$ over the same degrees of freedom. The tilted-ring model does, however, increase the best-fit BH mass to 2.28×10^9 $M_\odot$; this change is due to a portion of the model velocity field near the disk center being folded away from the line-of-sight direction (due to decreasing q; see Figure 4.9). The change in BH mass from this one model adjustment far exceeds the statistical $M_{\rm BH}$ error budget, a useful reminder that the uncertainties of model parameters derived from such pristine, high-resolution ALMA observations are systematics-driven.

Central Stellar Density Profile

The approximate stellar luminosity profile used for the previous trials was constructed to correct for an assumed obscuration of half of the central stellar surface brightness originating from *behind* the disk. The intrinsic stellar luminosity surface brightness profile is not expected to behave in this exact manner. Given the quality of the kinematic data out to large radii ($\sim$ 150 pc) where the stellar mass profile begins to dominate the galaxy potential, we expect that dynamical modeling will be able to constrain the stellar contributions to the radial circular velocity. After determining the stellar luminosity density profile by deprojecting the MGE of this modified stellar profile (see Equation 2.2), this density $\rho_\star$ is allowed to vary within the dust disk radius by changing $\rho_\star(R)$ at fixed radii and interpolating between these points (see Figure 4.10). Each new density profile is numerically integrated (using Equation 2.3) to create the stellar contributions to the gas circular velocity profile for that model iteration. The non-parametric stellar density model is required to smoothly vary to ensure the optimization produces a physical stellar density profile $\rho_\star$ at all radii. χ^2 minimization of models that address disk warping as well as incorporate a variable stellar luminosity density profile produce a better overall fit $\chi^2_\nu = 1.19$ but only a modest change

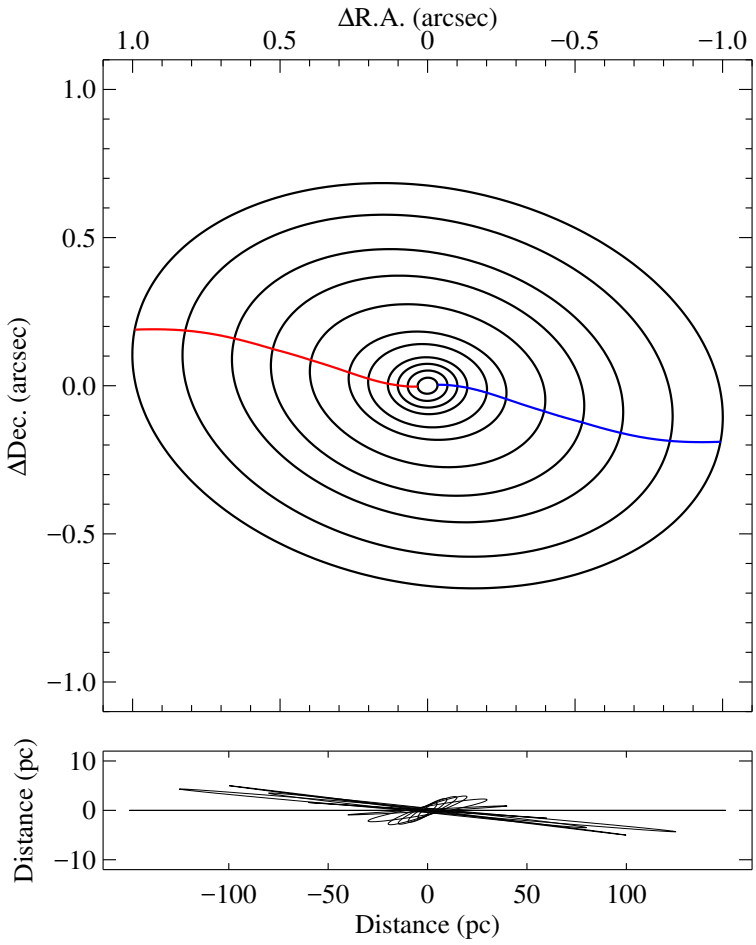

Figure 4.9 Best-fitting tilted-ring model to describe the NGC 3258 CO kinematics, shown (*top*) as seen in projection with the solid lines indicating the line of nodes for the receding (*left/red*) and approaching (*right/blue*) sides of the disk. Also, seen (*bottom*) with the outermost ring being observed edge-on to highlight the physical deviations associated with the kinematic warping from coplanar rotation.

in BH mass to $2.23 \times 10^9\ M_\odot$.

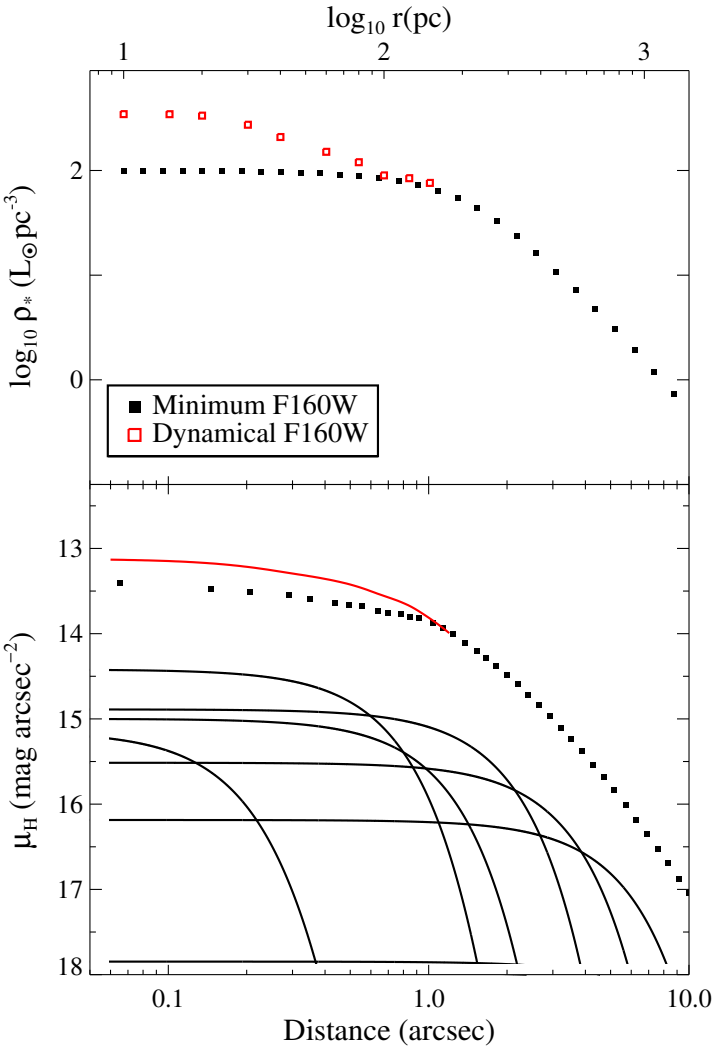

Figure 4.10 NGC 3258 stellar luminosity density (*top*) and surface brightness (*bottom*) profiles, first for the lower-bound case detailed in §4.2.3 and then after optimizing the stellar density values during detailed dynamical models that allow $\rho_\star$ in the inner 150 pc to vary as a function of radius.

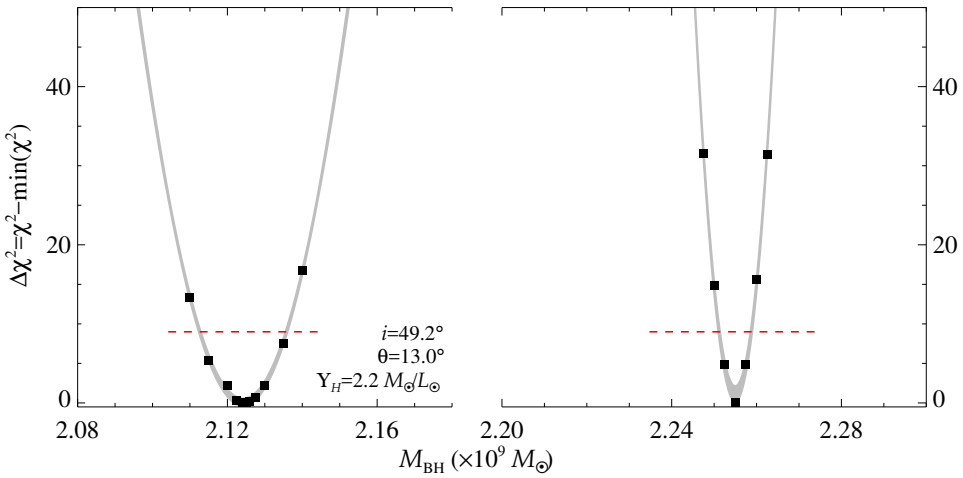

Figure 4.11 Results from minimizing χ^2 over fixed BH mass for the simple thin disk model (*left*; with best-fitting disk parameters indicated) and after including disk kinematic warping, a free stellar mass density profile, and a radially-varying intrinsic line width (*right*), highlighting only the mass range that shows the best agreement. The ordinate values are scaled to show the $\Delta\chi^2 = \chi^2 - \min(\chi^2)$ values, included with the (shaded) uncertainty ranges from simple Gaussian fits to these $\Delta\chi^2$ values. The 3σ uncertainty ranges in $M_{\rm BH}$ (where $\Delta\chi^2 \leq 9$; *dashed lines*) are demarcated.

Chapter 5

Conclusions

This thesis focuses on measuring the BH masses of luminous ETGs using resolved gas kinematic observations. The research is divided into detailing the properties and kinematic modeling of dynamically warm tracers in a single galaxy NGC 1275, describing the CO(2−1) observations and properties of a sample of dust-disk ETGs, and, for one of these CO-bright galaxies, performing state-of-the-art thin disk dynamical modeling on high-resolution imaging. In this chapter, we review the major results and discuss the ongoing and future work on these data.

5.1 NGC 1275 Ionized Atomic and Warm Molecular Gas Kinematics

We presented new observations of NGC 1275, the BCG of one of the most well-studied clusters. These observations consist of *HST* WFC3 F160W imaging and STIS G750M spectroscopy at adjacent pointings across the nucleus, along with Keck OSIRIS (with AO) Kn3 IFU spectroscopy of the galaxy's central arcsecond. The data were analyzed to determine

the stellar mass profile and to measure and compare the ionized atomic and warm molecular kinematics. Detailed dynamical models were then constructed and fit to the observed kinematics to obtain a more precise BH mass for this iconic galaxy. The main results of this project are as follows:

1. The Hα and H_2 1$-$0 S(1) velocity fields show coincident, resolved Keplerian-like upturns within the central 0.″3 (roughly 100 pc) from the continuum peak. At least for the H_2 emission, the receding peak has greater displacement (by $\sim$ 50 km s^{-1}) from the systemic velocity. Due to greater S/N and spatial coverage, the warm molecular emission and line-of-sight velocity reveals more disturbed morphology and kinematics beyond this radius. The Hα dispersion profile shows somewhat broader (by $\sim$ 75 km s^{-1}) lines than found for H_2, suggesting that the warm molecular line is a somewhat more dynamically cold tracer of the central potential. Interestingly, both the atomic and molecular velocity upturns descend more rapidly to the $v_{\rm sys}$ than can be explained by simple Keplerian rotation.

2. The Seyfert emission appears to be essentially unresolved (at $\sim$ 0.″2 resolution) in *HST* $H-$band imaging and dominates over any stellar light in the central $\sim$ 100 pc. Keck OSIRIS Kn3 continuum emission (with a factor of $\sim$ 2 better angular resolution) appears to be marginally resolved, likely due to spatially extended hot dust emission. The *HST* mosaic is parameterized using an MGE, although the active nucleus prevents characterization of the central stellar contributions. To complement this lower-bound measurement, an effective upper-bound stellar profile is constructed by modifying a best-fit Nuker profile to have a small but non-zero inner stellar slope. These stellar luminosity models are used when modeling the observed H_2 $v_{\rm LOS}$ and $v_{\rm RMS}$ kinematics; early tests suggest the lower-bound stellar MGE is preferred.

3. The total gas mass remains unknown from emission-line observations of these physically hot/warm tracers. However, the presence of resolved Keplerian upturns limits the cold molecular gas mass to a factor of several less than is suggested by the $L(H_2) - M_{\rm cold}$ relation

for late-type galaxies. This may suggest a more efficient H_2 1−0 S(1) heating mechanism in the nucleus of NGC 1275.

4. To at least marginally fit the H_2 velocity field, thin disk modeling requires the addition of an asymmetric drift correction, ostensibly to approximate gas pressure support to the disk. The best-fit BH mass determined by this method $M_{\rm BH} = \left(0.63^{+0.32}_{-0.19}\right) \times 10^9\ M_\odot$ is degenerate with disk inclination angle $i = \left(34.3^{+8.2}_{-7.9}\right)^\circ$ (both 3σ uncertainties). This fit is unsatisfying both due to a high χ^2_ν value and its inability to explain the asymmetric velocity extrema directly across the nucleus. In addition, this approximation is not strictly valid given the high $\sigma_{\rm turb}/v_{\rm c} \approx 0.6$ over the molecular disk.

5. A better-motivated Jeans equation method, implemented with JAM to fit the $v_{\rm RMS}$ data, allows for significant vertical gas motion and approximates a thick disk. We find the anisotropy parameter β_z tends towards negative numbers and is positively correlated with i; assuming the H_2 emission is qualitatively similar to the stellar kinematics of fast-rotator ETGs, we fix $\beta_z = 0$ and determine $M_{\rm BH} = \left(1.20^{+0.32}_{-0.44}\right) \times 10^9\ M_\odot$ (3σ uncertainties) with a slightly larger $i = (39.1^{+9.2}_{-7.1})^\circ$ value. This mass range lies slightly above the $M_{\rm BH} - \sigma_\star$ relationship but is consistent within the intrinsic scatter. However, we note that both thin disk and Jeans equation modeling of the central kinematics demonstrate the fundamental inability of these models to accurately match the full shape and extremes of the data $v_{\rm LOS}$ and $v_{\rm RMS}$ profiles. We suspect that the AGN environment, which is responsible for the warm gas emission in the nucleus, also introduces the kinematic warmth ("puffiness") into the velocity fields that is difficult to recreate.

5.2 ALMA CO(2−1) Observations of Early-Type Galaxies

We presented ALMA Band 6 observations at $\sim 0\farcs3$ resolution of a sample of twenty-three ETG nuclei that were selected based on their optical dust disk morphologies. ^{12}CO(2−1) line and ~ 236 GHz continuum properties are extracted from the imaging data. In addition to line visualizations (velocity profiles, PVDs, GH moment maps, etc.) for the entire sample, we analyze the disk kinematic properties and molecular gas stability, as well as continuum spatial and spectral properties for the Cycle 2 targets. The main results of this project are as follows:

1. Nineteen of these are detected in CO(2−1) emission at high S/N, arising from disks with total gas masses of $\sim 10^{7-9}$ $M_\odot$ and average deprojected mass surface densities on the order of 100 $M_\odot$ pc^{-2}. The remaining four show faint but unambiguous CO emission with somewhat lower ($\sim 10^{6-9}$ $M_\odot$ and $\lesssim 50$ $M_\odot$ pc^{-2}) total gas masses and average surface mass densities. Two of these CO-faint galaxies also show strong CO(2−1) absorption coincident with their mm-bright nuclear continua.

2. In all CO-bright cases, line-of-sight velocity maps indicate nearly circular rotation about the disk centers and confirm that disky dust morphology is a good predictor of a significant molecular gas reservoir that is in regular rotation. Warping of the gas disks, although evident in every CO-bright case, is both smooth and generally of low magnitude ($\lesssim 10°$, except for NGC 384, NGC 3268, NGC 3271, NGC 3557, ESO 208-G21). Based on low line dispersions and regular gas kinematics, we find that our CO-bright targets possess dynamically cold gas disks.

3. Seven disks show velocity upturns in CO emission within $\sim r_g$ that indicate partial resolution of the BH kinematic signature. Even in the best of cases with moderate angular

beam size, BH mass measurement errors are dominated by systematics associated with the uncertain, dust-obscured central stellar surface brightness. These are prime candidates for high-resolution molecular gas observations to fully map out emission line kinematics and highly resolve $r_{\rm g}$ along their disk minor axes. Such follow-up imaging will permit $M_{\rm BH}$ determinations that are insensitive to all major modeling systematics that plague stellar and ionized gas dynamical measurements.

4. We explore the stability of the Cycle 2 molecular disks against fragmentation and gravitational collapse using the Toomre Q test. For the outer regions of these disks, $Q_{\rm gas}$ lies significantly above unity. Based on higher-resolution observations of NGC 1332 and NGC 3258, we expect this stability measure to extend within $r_{\rm g}$.

5. Each galaxy in our sample possesses a centrally-dominant, unresolved nuclear 1.3 mm continuum source that is most likely accretion powered. For the Cycle 2 sample, the 236 GHz nuclear continuum spectral slopes are typically well described by standard ADAF models of low-luminosity AGN. Subtracting their unresolved emission reveals significant extended emission in five of the seven galaxies. The extended continuum features in the CO-bright galaxies coincide with the optical dust disks, and we determine that their extended continuum spectral indices are consistent with a thermal dust origin. However, the extended continuum features in the two CO-faint galaxies are oriented nearly perpendicular to their optical dust disks and may trace marginally resolved synchrotron jets on < 100 pc scales.

5.3 High-resolution ALMA CO(2−1) Imaging of NGC 3258

We presented $\sim 0\farcs1-$resolution ALMA CO(2−1) imaging of elliptical galaxy NGC 3258. These follow-up observations probe the molecular gas properties at four times higher angular

resolution than our prior CO imaging of this galaxy, well within the BH sphere of influence. These data comprise the most sensitive probe of any luminous ETG to date, enabling detailed dynamical modeling to determine a very precise BH mass. The preliminary results of this ongoing project are as follows:

1. We highly resolve the central kinematics with over ten independent resolution elements across the BH sphere of influence. The $v_{\rm LOS}$ data show distinct, almost perfectly symmetric Keplerian velocity upturns. The observed CO emission line flux shows a clumpy distribution with a central hole in emission, suggesting the CO-emitting gas probes to within about 20 pc of the central BH.

2. The bulk of the CO emission arises from the central disk region; slightly less than half of the flux is associated with the outer annulus, where the observed $B-I$ color excess reaches a maximum. We model the color change for a mock galaxy as a function of intrinsic disk A_V, determining that the central disk regions are likely so obscured that the stellar light from *behind* the dust disk plane no longer significantly impacts the optical colors.

3. Detailed gas-dynamical modeling, accounting for moderate disk warping using a tilted-ring model and a central stellar luminosity density that varies as a function of radius, reproduces very well the observed CO(2−1) line properties. The best-fitting BH mass is $\sim 2.23 \times 10^9$ $M_\odot$; we expect a final precision of $\lesssim 5\%$ based on various remaining systematics.

Bibliography

Abdo, A. A., Ackermann, M., Ajello, M., et al. 2009, ApJ, 699, 31

Abell, G. O., Corwin, Jr., H. G., & Olowin, R. P. 1989, ApJS, 70, 1

Alatalo, K., Davis, T. A., Bureau, M., et al. 2013, MNRAS, 432, 1796

Alatalo, K., Lacy, M., Lanz, L., et al. 2015, ApJ, 798, 31

Amblard, A., Riguccini, L., Temi, P., et al. 2014, ApJ, 783, 135

Annibali, F., Bressan, A., Rampazzo, R., et al. 2010, A&A, 519, A40

Asada, K., Kameno, S., Shen, Z.-Q., et al. 2006, PASJ, 58, 261

Balkowski, C. 1979, A&A, 78, 190

Balkowski, C., Bottinelli, L., Gouguenheim, L., & Heidmann, J. 1972, A&A, 21, 303

Barth, A. J., Boizelle, B. D., Darling, J., et al. 2016a, ApJ, 822, L28

Barth, A. J., Darling, J., Baker, A. J., et al. 2016b, ApJ, 823, 51

Barth, A. J., Sarzi, M., Rix, H.-W., et al. 2001, ApJ, 555, 685

Bassett, R., Bekki, K., Cortese, L., et al. 2017, ArXiv e-prints, arXiv:1704.08433

Bayet, E., Davis, T. A., Bell, T. A., & Viti, S. 2012, MNRAS, 424, 2646

Bayet, E., Bureau, M., Davis, T. A., et al. 2013, MNRAS, 432, 1742

Bendo, G. J., Joseph, R. D., Wells, M., et al. 2003, AJ, 125, 2361

Bigiel, F., Leroy, A., Walter, F., et al. 2008, AJ, 136, 2846

Binney, J., & Tremaine, S. 2008, Galactic Dynamics: Second Edition (Princeton University Press)

Bloecker, T. 1995, A&A, 297, 727

Boizelle, B. D., Barth, A. J., Darling, J., et al. 2017, ApJ, 845, 170

Boroson, T. A. 1990, ApJ, 360, 465

Boselli, A., Cortese, L., & Boquien, M. 2014, A&A, 564, A65

Bower, G. A., Heckman, T. M., Wilson, A. S., & Richstone, D. O. 1997, ApJ, 483, L33

Bower, G. A., Green, R. F., Danks, A., et al. 1998, ApJ, 492, L111

Briggs, D. S. 1995, in Bulletin of the American Astronomical Society, Vol. 27, American Astronomical Society Meeting Abstracts, 1444

Brodie, J. P., Schroder, L. L., Huchra, J. P., et al. 1998, AJ, 116, 691

Bruzual, G., & Charlot, S. 2003, MNRAS, 344, 1000

Buffington, A., Bisi, M. M., Clover, J. M., et al. 2009, Icarus, 203, 124

Camps, P., & Baes, M. 2015, Astronomy and Computing, 9, 20

Canning, R. E. A., Ryon, J. E., Gallagher, J. S., et al. 2014, MNRAS, 444, 336

Capetti, A., de Ruiter, H. R., Fanti, R., et al. 2000, A&A, 362, 871

Cappellari, M. 2002, MNRAS, 333, 400

—. 2008, MNRAS, 390, 71

—. 2016, ARA&A, 54, 597

Cappellari, M., & Copin, Y. 2003, MNRAS, 342, 345

Cappellari, M., & Emsellem, E. 2004, PASP, 116, 138

Cappellari, M., Emsellem, E., Bacon, R., et al. 2007, MNRAS, 379, 418

Cappellari, M., Emsellem, E., Krajnović, D., et al. 2011, MNRAS, 413, 813

Cappellari, M., McDermid, R. M., Alatalo, K., et al. 2012, Nature, 484, 485

—. 2013, MNRAS, 432, 1862

Cardelli, J. A., Clayton, G. C., & Mathis, J. S. 1989, ApJ, 345, 245

Carilli, C. L., & Walter, F. 2013, ARA&A, 51, 105

Carlstrom, J. E., & Kronberg, P. P. 1991, ApJ, 366, 422

Chiaberge, M., Capetti, A., & Celotti, A. 1999, A&A, 349, 77

Clemens, M. S., Jones, A. P., Bressan, A., et al. 2010, A&A, 518, L50

Combes, F., Young, L. M., & Bureau, M. 2007, MNRAS, 377, 1795

Condon, J. J. 1992, ARA&A, 30, 575

Conselice, C. J., Gallagher, III, J. S., & Wyse, R. F. G. 2001, AJ, 122, 2281

Cretton, N., Rix, H.-W., & de Zeeuw, P. T. 2000, ApJ, 536, 319

Dalla Bontà, E., Ferrarese, L., Corsini, E. M., et al. 2009, ApJ, 690, 537

Davies, R. D., & Lewis, B. M. 1973, MNRAS, 165, 231

Davis, T. A. 2014, MNRAS, 443, 911

Davis, T. A., & Bureau, M. 2016, MNRAS, 457, 272

Davis, T. A., Bureau, M., Cappellari, M., Sarzi, M., & Blitz, L. 2013, Nature, 494, 328

Davis, T. A., Bureau, M., Onishi, K., et al. 2017, ArXiv e-prints, arXiv:1703.05248

Davis, T. A., Bureau, M., Young, L. M., et al. 2011a, MNRAS, 414, 968

Davis, T. A., Alatalo, K., Sarzi, M., et al. 2011b, MNRAS, 417, 882

Davis, T. A., Young, L. M., Crocker, A. F., et al. 2014, MNRAS, 444, 3427

Davis, T. A., Bureau, M., Onishi, K., et al. 2018, MNRAS, 473, 3818

de Francesco, G., Capetti, A., & Marconi, A. 2006, A&A, 460, 439

de Koff, S., Best, P., Baum, S. A., et al. 2000, ApJS, 129, 33

de Ruiter, H. R., Parma, P., Capetti, A., Fanti, R., & Morganti, R. 2002, A&A, 396, 857

de Vaucouleurs, G. 1959, Handbuch der Physik, 53, 275

de Vaucouleurs, G., de Vaucouleurs, A., Corwin, Jr., H. G., et al. 1991, Third Reference Catalogue of Bright Galaxies. (New York: Springer)

de Zeeuw, P. T., Bureau, M., Emsellem, E., et al. 2002, MNRAS, 329, 513

den Brok, M., Seth, A. C., Barth, A. J., et al. 2015, ApJ, 809, 101

Donahue, M., Mack, J., Voit, G. M., et al. 2000, ApJ, 545, 670

Draine, B. T. 2003, ARA&A, 41, 241

—. 2006, ApJ, 636, 1114

Duc, P.-A., Cuillandre, J.-C., Karabal, E., et al. 2015, MNRAS, 446, 120

Dumas, G., Schinnerer, E., & Mundell, C. G. 2010, ApJ, 721, 911

Ebneter, K., & Balick, B. 1985, AJ, 90, 183

Ebneter, K., Davis, M., & Djorgovski, S. 1988, AJ, 95, 422

Eckart, A., Cameron, M., Genzel, R., et al. 1990, ApJ, 365, 522

Efstathiou, G., Ellis, R. S., & Carter, D. 1980, MNRAS, 193, 931

Elston, R., & Maloney, P. 1994, Infrared Astronomy with Arrays: The Next Generation, ed I. S. McLean (Dordrecht: Kluwer)

Emsellem, E., Cappellari, M., Peletier, R. F., et al. 2004, MNRAS, 352, 721

Emsellem, E., Cappellari, M., Krajnović, D., et al. 2011, MNRAS, 414, 888

Fabian, A. C., Sanders, J. S., Taylor, G. B., et al. 2006, MNRAS, 366, 417

Fanaroff, B. L., & Riley, J. M. 1974, MNRAS, 167, 31P

Ferguson, H. C., & Sandage, A. 1990, AJ, 100, 1

Ferrarese, L., Ford, H. C., & Jaffe, W. 1996, ApJ, 470, 444

Ferrarese, L., & Merritt, D. 2000, ApJ, 539, L9

Fomalont, E., van Kempen, T., Kneissl, R., et al. 2014, The Messenger, 155, 19

Forman, W., Schwarz, J., Jones, C., Liller, W., & Fabian, A. C. 1979, ApJ, 234, L27

Fujita, Y., Kawakatu, N., Shlosman, I., & Ito, H. 2016, MNRAS, 455, 2289

Galametz, M., Kennicutt, R. C., Albrecht, M., et al. 2012, MNRAS, 425, 763

García-Burillo, S., Combes, F., Usero, A., et al. 2014, A&A, 567, A125

García-Burillo, S., Combes, F., Ramos Almeida, C., et al. 2016, ApJ, 823, L12

Gebhardt, K., & Thomas, J. 2009, ApJ, 700, 1690

Gebhardt, K., Bender, R., Bower, G., et al. 2000, ApJ, 539, L13

Ghez, A. M., Salim, S., Weinberg, N. N., et al. 2008, ApJ, 689, 1044

Gillessen, S., Eisenhauer, F., Trippe, S., et al. 2009, ApJ, 692, 1075

Gonzaga, S., Hack, W., Fruchter, A., & Mack, J. 2012, The DrizzlePac Handbook, `http://drizzlepac.stsci.edu`

Gültekin, K., Richstone, D. O., Gebhardt, K., et al. 2009, ApJ, 695, 1577

Güver, T., & Özel, F. 2009, MNRAS, 400, 2050

Häring-Neumayer, N., Cappellari, M., Rix, H.-W., et al. 2006, ApJ, 643, 226

Harris, D. E., Finoguenov, A., Bridle, A. H., Hardcastle, M. J., & Laing, R. A. 2002, ApJ, 580, 110

Heckman, T. M., Armus, L., & Miley, G. K. 1987, AJ, 93, 276

Hicks, E. K. S., Davies, R. I., Malkan, M. A., et al. 2009, ApJ, 696, 448

Hicks, E. K. S., & Malkan, M. A. 2008, ApJS, 174, 31

Ho, L. C. 2007, ApJ, 669, 821

Ho, L. C., Filippenko, A. V., & Sargent, W. L. W. 1997a, ApJS, 112, 315

—. 1997b, ApJ, 487, 568

Ho, L. C., Li, Z.-Y., Barth, A. J., Seigar, M. S., & Peng, C. Y. 2011, ApJS, 197, 21

Ho, L. C., Sarzi, M., Rix, H.-W., et al. 2002, PASP, 114, 137

Holmberg, E. 1958, Meddelanden fran Lunds Astronomiska Observatorium Serie II, 136, 1

Holtzman, J. A., Faber, S. M., Shaya, E. J., et al. 1992, AJ, 103, 691

Hopkins, P. F., & Christiansen, J. L. 2013, ApJ, 776, 48

Huang, S., Ho, L. C., Peng, C. Y., Li, Z.-Y., & Barth, A. J. 2013, ApJ, 766, 47

Hubble, E. P. 1926, ApJ, 64, doi:10.1086/143018

Huchtmeier, W. K., & Richter, O.-G. 1989, A General Catalog of HI Observations of Galaxies. The Reference Catalog., 350

Humphrey, P. J., Buote, D. A., Brighenti, F., Gebhardt, K., & Mathews, W. G. 2009, ApJ, 703, 1257

Inoue, M. Y., Kameno, S., Kawabe, R., et al. 1996, AJ, 111, 1852

Jaffe, W. 1990, A&A, 240, 254

Jaffe, W., Bremer, M. N., & van der Werf, P. P. 2001, MNRAS, 324, 443

Jaffe, W., & McNamara, B. R. 1994, ApJ, 434, 110

Jensen, J. B., Tonry, J. L., Barris, B. J., et al. 2003, ApJ, 583, 712

Johnstone, R. M., Canning, R. E. A., Fabian, A. C., et al. 2012, MNRAS, 425, 1421

Jones, D. L., Sramek, R. A., & Terzian, Y. 1981, ApJ, 247, L57

Julian, W. H., & Toomre, A. 1966, ApJ, 146, 810

Jura, M. 1986, ApJ, 306, 483

Kawata, D., Cen, R., & Ho, L. C. 2007, ApJ, 669, 232

Killeen, N. E. B., Bicknell, G. V., & Ekers, R. D. 1986, ApJ, 302, 306

Knapp, G. R., Guhathakurta, P., Kim, D.-W., & Jura, M. A. 1989, ApJS, 70, 329

Knapp, G. R., & Rupen, M. P. 1996, ApJ, 460, 271

Knapp, G. R., Turner, E. L., & Cunniffe, P. E. 1985, AJ, 90, 454

Kolokythas, K., O'Sullivan, E., Giacintucci, S., et al. 2015, MNRAS, 450, 1732

Kormendy, J., & Ho, L. C. 2013, ARA&A, 51, 511

Kormendy, J., & Richstone, D. 1995, ARA&A, 33, 581

Krabbe, A., Sams, III, B. J., Genzel, R., Thatte, N., & Prada, F. 2000, A&A, 354, 439

Krajnović, D., Cappellari, M., de Zeeuw, P. T., & Copin, Y. 2006, MNRAS, 366, 787

Krajnović, D., Emsellem, E., Cappellari, M., et al. 2011, MNRAS, 414, 2923

Kreckel, K., Groves, B., Schinnerer, E., et al. 2013, ApJ, 771, 62

Krist, J., & Hook, R. 2004, The Tiny Tim User's Guide, `http://www.stsci.edu/hst/observatory/focus/TinyTim`

Kuo, C. Y., Braatz, J. A., Condon, J. J., et al. 2011, ApJ, 727, 20

Lagos, C. d. P., Davis, T. A., Lacey, C. G., et al. 2014, MNRAS, 443, 1002

Lagos, C. d. P., Padilla, N. D., Davis, T. A., et al. 2015, MNRAS, 448, 1271

Laine, S., van der Marel, R. P., Lauer, T. R., et al. 2003, AJ, 125, 478

Laing, R. A., & Bridle, A. H. 1987, MNRAS, 228, 557

Large, M. I., Mills, B. Y., Little, A. G., Crawford, D. F., & Sutton, J. M. 1981, MNRAS, 194, 693

Larkin, J., Barczys, M., McElwain, M., et al. 2010, OSIRIS User's Manual, `http://www.astro.ucla.edu/~irlab/osiris/`

Lauberts, A., & Valentijn, E. A. 1989, The surface photometry catalogue of the ESO-Uppsala galaxies

Lauer, T. R., Ajhar, E. A., Byun, Y.-I., et al. 1995, AJ, 110, 2622

Lauer, T. R., Faber, S. M., Gebhardt, K., et al. 2005, AJ, 129, 2138

Lauer, T. R., Gebhardt, K., Faber, S. M., et al. 2007a, ApJ, 664, 226

Lauer, T. R., Faber, S. M., Richstone, D., et al. 2007b, ApJ, 662, 808

Lavezzi, T. E., Dickey, J. M., Casoli, F., & Kazès, I. 1999, AJ, 117, 1995

Leroy, A. K., Walter, F., Brinks, E., et al. 2008, AJ, 136, 2782

Leung, G. Y. C., Leaman, R., van de Ven, G., et al. 2018, MNRAS, 477, 254

Levinson, A., Laor, A., & Vermeulen, R. C. 1995, ApJ, 448, 589

Li, Y., Mac Low, M.-M., & Klessen, R. S. 2005, ApJ, 626, 823

Lim, J., Ohyama, Y., Chi-Hung, Y., Dinh-V-Trung, & Shiang-Yu, W. 2012, ApJ, 744, 112

Lynds, R. 1970, ApJ, 159, doi:10.1086/180500

Ma, C.-P., Greene, J. E., McConnell, N., et al. 2014, ApJ, 795, 158

Macchetto, F., Marconi, A., Axon, D. J., et al. 1997, ApJ, 489, 579

Magorrian, J., Tremaine, S., Richstone, D., et al. 1998, AJ, 115, 2285

Makarov, D., Prugniel, P., Terekhova, N., Courtois, H., & Vauglin, I. 2014, A&A, 570, A13

Markwardt, C. B. 2009, in Astronomical Society of the Pacific Conference Series, Vol. 411, Astronomical Data Analysis Software and Systems XVIII, ed. D. A. Bohlender, D. Durand, & P. Dowler, 251

Martel, A. R., Baum, S. A., Sparks, W. B., et al. 1999, ApJS, 122, 81

Martig, M., Bournaud, F., Teyssier, R., & Dekel, A. 2009, ApJ, 707, 250

Martig, M., Crocker, A. F., Bournaud, F., et al. 2013, MNRAS, 432, 1914

Martini, P., Dicken, D., & Storchi-Bergmann, T. 2013, ApJ, 766, 121

Mayall, N. U. 1958, in IAU Symposium, Vol. 5, Comparison of the Large-Scale Structure of the Galactic System with that of Other Stellar Systems, ed. N. G. Roman, 23

Mazzalay, X., Saglia, R. P., Erwin, P., et al. 2013, MNRAS, 428, 2389

McConnell, N. J., & Ma, C.-P. 2013, ApJ, 764, 184

McConnell, N. J., Ma, C.-P., Murphy, J. D., et al. 2012, ApJ, 756, 179

McMullin, J. P., Waters, B., Schiebel, D., Young, W., & Golap, K. 2007, in Astronomical Society of the Pacific Conference Series, Vol. 376, Astronomical Data Analysis Software and Systems XVI, ed. R. A. Shaw, F. Hill, & D. J. Bell, 127

Mei, S., Silva, D., & Quinn, P. J. 2000, A&A, 361, 68

Mei, S., Blakeslee, J. P., Tonry, J. L., et al. 2005, ApJ, 625, 121

Minkowski, R. 1968, AJ, 73, 842

Minkowski, R., & Osterbrock, D. 1959, ApJ, 129, 583

Mirabel, I. F., Sanders, D. B., & Kazes, I. 1989, ApJ, 340, L9

Mittal, R., Whelan, J. T., & Combes, F. 2015, MNRAS, 450, 2564

Miyoshi, M., Moran, J., Herrnstein, J., et al. 1995, Nature, 373, 127

Mould, J. R., Huchra, J. P., Freedman, W. L., et al. 2000, ApJ, 529, 786

Müller Sánchez, F., Davies, R. I., Eisenhauer, F., et al. 2006, A&A, 454, 481

Müller-Sánchez, F., Prieto, M. A., Mezcua, M., et al. 2013, ApJ, 763, L1

Nagar, N. M., Wilson, A. S., & Falcke, H. 2001, ApJ, 559, L87

Narayan, R., & Yi, I. 1994, ApJ, 428, L13

—. 1995, ApJ, 452, 710

Nemmen, R. S., Storchi-Bergmann, T., & Eracleous, M. 2014, MNRAS, 438, 2804

Neumayer, N., Cappellari, M., Reunanen, J., et al. 2007, ApJ, 671, 1329

Noel-Storr, J., Baum, S. A., Verdoes Kleijn, G., et al. 2003, ApJS, 148, 419

Nulsen, P. E. J., Stewart, G. C., & Fabian, A. C. 1984, MNRAS, 208, 185

Nyland, K., Young, L. M., Wrobel, J. M., et al. 2016, MNRAS, 458, 2221

Ocaña Flaquer, B., Leon, S., Combes, F., & Lim, J. 2010, A&A, 518, A9

Okuda, T., Iguchi, S., & Kohno, K. 2013, ApJ, 768, 19

Onishi, K., Iguchi, S., Davis, T. A., et al. 2017, MNRAS, 468, 4663

Onishi, K., Iguchi, S., Sheth, K., & Kohno, K. 2015, ApJ, 806, 39

Osterbrock, D. E. 1960, ApJ, 132, 325

Osterbrock, D. E., & Ferland, G. J. 2006, Astrophysics of gaseous nebulae and active galactic nuclei

Pascucci, I., Gorti, U., & Hollenbach, D. 2012, ApJ, 751, L42

Pellegrini, S., Venturi, T., Comastri, A., et al. 2003, ApJ, 585, 677

Peng, C. Y., Ho, L. C., Impey, C. D., & Rix, H.-W. 2002, AJ, 124, 266

Penny, S. J., Forbes, D. A., & Conselice, C. J. 2012, MNRAS, 422, 885

Pettini, M., & Pagel, B. E. J. 2004, MNRAS, 348, L59

Piner, B. G., Jones, D. L., & Wehrle, A. E. 2001, AJ, 122, 2954

Pirzkal, N. 2014, The Near Infrared Sky Background, Tech. rep.

Pogge, R. W., & Martini, P. 2002, ApJ, 569, 624

Prandoni, I., Laing, R. A., de Ruiter, H. R., & Parma, P. 2010, A&A, 523, A38

Press, W. H., Teukolsky, S. A., Vetterling, W. T., & Flannery, B. P. 1992, Numerical recipes in FORTRAN. The art of scientific computing

Prestwich, A. H., Joy, M., Luginbuhl, C. B., Sulkanen, M., & Newberry, M. 1997, ApJ, 477, 144

Rangwala, N., Maloney, P. R., Wilson, C. D., et al. 2015, ApJ, 806, 17

Ricci, T. V., Steiner, J. E., & Menezes, R. B. 2014, MNRAS, 440, 2419

Rieke, G. H., & Lebofsky, M. J. 1985, ApJ, 288, 618

Riffel, R., Rodríguez-Ardila, A., & Pastoriza, M. G. 2006, A&A, 457, 61

Riffel, R. A., Storchi-Bergmann, T., & Winge, C. 2013, MNRAS, 430, 2249

Rodríguez-Ardila, A., Riffel, R., & Pastoriza, M. G. 2005, MNRAS, 364, 1041

Rusli, S. P., Erwin, P., Saglia, R. P., et al. 2013a, AJ, 146, 160

Rusli, S. P., Thomas, J., Erwin, P., et al. 2011, MNRAS, 410, 1223

Rusli, S. P., Thomas, J., Saglia, R. P., et al. 2013b, AJ, 146, 45

Sage, L. J., & Wrobel, J. M. 1989, ApJ, 344, 204

Saito, T., Iono, D., Xu, C. K., et al. 2017, ApJ, 835, 174

Salomé, P., Combes, F., Edge, A. C., et al. 2006, A&A, 454, 437

Sandage, A. 1961, The Hubble atlas of galaxies

Sanders, D. B., Mazzarella, J. M., Kim, D.-C., Surace, J. A., & Soifer, B. T. 2003, AJ, 126, 1607

Sandstrom, K. M., Leroy, A. K., Walter, F., et al. 2013, ApJ, 777, 5

Scharwächter, J., McGregor, P. J., Dopita, M. A., & Beck, T. L. 2013, MNRAS, 429, 2315

Schlafly, E. F., & Finkbeiner, D. P. 2011, ApJ, 737, 103

Schombert, J. M. 1986, ApJS, 60, 603

Scott, N., Cappellari, M., Davies, R. L., et al. 2009, MNRAS, 398, 1835

Serra, P., Oosterloo, T., Morganti, R., et al. 2012, MNRAS, 422, 1835

Seth, A. C., Cappellari, M., Neumayer, N., et al. 2010, ApJ, 714, 713

Shankar, F., Bernardi, M., Sheth, R. K., et al. 2016, MNRAS, 460, 3119

Skrutskie, M. F., Cutri, R. M., Stiening, R., et al. 2006, AJ, 131, 1163

Smith, E. P., Heckman, T. M., & Illingworth, G. D. 1990, ApJ, 356, 399

Storchi-Bergmann, T., Calzetti, D., & Kinney, A. L. 1994, ApJ, 429, 572

Storchi-Bergmann, T., McGregor, P. J., Riffel, R. A., et al. 2009, MNRAS, 394, 1148

Theureau, G., Hanski, M. O., Coudreau, N., Hallet, N., & Martin, J.-M. 2007, A&A, 465, 71

Tomita, A., Aoki, K., Watanabe, M., Takata, T., & Ichikawa, S.-i. 2000, AJ, 120, 123

Tonry, J. L., Dressler, A., Blakeslee, J. P., et al. 2001, ApJ, 546, 681

Toomre, A. 1964, ApJ, 139, 1217

Tran, H. D., Tsvetanov, Z., Ford, H. C., et al. 2001, AJ, 121, 2928

U, V., Medling, A., Sanders, D., et al. 2013, ApJ, 775, 115

Ulvestad, J. S., Wilson, A. S., & Sramek, R. A. 1981, ApJ, 247, 419

Utomo, D., Blitz, L., Davis, T., et al. 2015, ApJ, 803, 16

van de Voort, F., Davis, T. A., Kereš, D., et al. 2015, MNRAS, 451, 3269

van den Bosch, R. C. E., & de Zeeuw, P. T. 2010, MNRAS, 401, 1770

van den Bosch, R. C. E., Gebhardt, K., Gültekin, K., Yıldırım, A., & Walsh, J. L. 2015, ApJS, 218, 10

van der Marel, R. P., & Franx, M. 1993, ApJ, 407, 525

van der Marel, R. P., & van den Bosch, F. C. 1998a, AJ, 116, 2220

—. 1998b, AJ, 116, 2220

van Dokkum, P. G. 2001, PASP, 113, 1420

van Dokkum, P. G., & Franx, M. 1995, AJ, 110, 2027

van Dokkum, P. G., Whitaker, K. E., Brammer, G., et al. 2010, ApJ, 709, 1018

Verdoes Kleijn, G. A., Baum, S. A., de Zeeuw, P. T., & O'Dea, C. P. 1999, AJ, 118, 2592

Verdoes Kleijn, G. A., van der Marel, R. P., Carollo, C. M., & de Zeeuw, P. T. 2000, AJ, 120, 1221

Viaene, S., Sarzi, M., Baes, M., Fritz, J., & Puerari, I. 2017, MNRAS, 472, 1286

Walker, R. C., Romney, J. D., & Benson, J. M. 1994, ApJ, 430, L45

Walsh, J. L., Barth, A. J., Ho, L. C., & Sarzi, M. 2013, ApJ, 770, 86

Walsh, J. L., Barth, A. J., & Sarzi, M. 2010, ApJ, 721, 762

Walsh, J. L., van den Bosch, R. C. E., Barth, A. J., & Sarzi, M. 2012, ApJ, 753, 79

Walsh, J. L., van den Bosch, R. C. E., Gebhardt, K., et al. 2015, ApJ, 808, 183

—. 2017, ApJ, 835, 208

—. 2016, ApJ, 817, 2

Wang, B., & Silk, J. 1994, ApJ, 427, 759

Wardle, M., & Knapp, G. R. 1986, AJ, 91, 23

Wiklind, T., Combes, F., & Henkel, C. 1995, A&A, 297, 643

Willick, J. A., Courteau, S., Faber, S. M., et al. 1997, ApJS, 109, 333

Wilman, R. J., Edge, A. C., & Johnstone, R. M. 2005, MNRAS, 359, 755

Wilman, R. J., Edge, A. C., Johnstone, R. M., et al. 2002, MNRAS, 337, 63

Wright, E. L. 2006, PASP, 118, 1711

Yıldırım, A., van den Bosch, R. C. E., van de Ven, G., et al. 2017, MNRAS, 468, 4216

Young, L. M., Bureau, M., Davis, T. A., et al. 2011, MNRAS, 414, 940

Young, L. M., Scott, N., Serra, P., et al. 2014, MNRAS, 444, 3408

Yuan, F., & Narayan, R. 2014, ARA&A, 52, 529

Zabludoff, A. I., Huchra, J. P., & Geller, M. J. 1990, ApJS, 74, 1

Zibetti, S., Charlot, S., & Rix, H.-W. 2009, MNRAS, 400, 1181

Appendix A

ALMA Archive Modeling

In recent ALMA Cycles, about 4000 hours of 12-m observation time have been offered yearly, with roughly a quarter of the high-priority (grade A+B) projects focusing on galaxy and galactic nuclei studies. Already, the ALMA archive contains a significant number of data sets seeking to detect continuum and emission line properties in a diverse set of nearby galaxies. Depending on the impetus for these approved proposals (e.g., sensitive absorption line studies using bright nuclear continuum sources, detailed kinematic studies and dust/gas mass measurements in late-stage mergers, diagnostic line-ratio maps to determine gas chemistry and nuclear excitation mechanisms, etc.), the published data products may vary by author. The raw visibilities and pipeline-created data products (continuum maps and emission line data cubes) are publicly available on the ALMA archive after a year-long proprietary period. However, the large data sizes (with individual data cubes and visibilities being at the GB and tens of GB levels, respectively) and, at times, complicated gas kinematics dissuade casual inspection and analysis of the archival pipeline products. Because of the potential value to the scientific community, this author advocates for the creation of some kind of census or kinematic atlas of nearby galaxies observed using ALMA.

Given the heterogeneous angular resolution (from just a few milli-arcsec to $\sim 5''$ depending on the frequency band and array configuration) and target galaxy type (from spirals and early-type galaxies to irregulars and mergers/luminous IR galaxies), the wide range in on-source integration times, and the chosen spectral windows (covering a variety of emission lines) in these projects, such a complete atlas may have little (initial) statistical value. However, the quick-look information of this atlas project (detailed below) will enable identification of data subsets (nuclear disks, rings, kinematic warps, etc.) that are not readily discernible via inspection of the pipeline data cube and will serve as a launchpad for more detailed studies.

A.1 Description of Methodology

In its current iteration, this pipeline modeling program interactively creates various visualizations for quick inspection and analysis. The pipeline data cubes tend to be enormous (typically between 480×480 and 960×960 spatial pixels and between 480 and 960 spectral channels), and most computer languages struggle to preserve such large (several GB) files in memory and afterwards split out new arrays. Command-line prompts are therefore implemented, allowing for easy data cube cropping and subsampling. The data cube is then collapsed along the frequency axis (between the user-supplied spatial boundaries and channel numbers of interest) to produce a crude flux density map that may include continuum emission in addition to the desired line emission/absorption features.

Since this program focuses (for now) on line features, while common, bright nuclear continuum sources are not always properly removed (especially by early pipeline routines), the user can subtract a (localized) continuum source by selecting both the continuum contamination region on the collapsed flux density map and (multiple) line-free channels in the plot of integrated flux density versus frequency. As determined by the user in a graphical interface, the region (and those mentioned later) can either be elliptical or bounded by an $N-$vertex

polygon. The continuum source is modeled as a linearly varying function of frequency and scaled to agree with each spectrum contained in the region to better reveal line absorption or emission. This simple method is no substitute for $uv-$plane continuum subtraction; however, it remains very useful to identify and characterize absorption hiding in a bright nuclear continuum source.

Faint emission is often heavily obscured when collapsing the data cube over a large number of channels. To better identify line features that will be included in further analysis, the user can, either channel-by-channel or in a series of collapsed frequency "chunks", interactively identify regions containing emission. From the general collapsed flux density map or the aforementioned improvement, the user detemines the spatial region containing emission/absorption. Each slice of the cube is integrated over this region to determine the total flux density as a function of velocity/frequency. Command-line prompts query for the (galaxy) systemic velocity and then the minimum/maximum range over which emission/absorption is observed. The integral of this velocity profile over the velocity extrema give an estimate of the source's true flux (in Jy km s^{-1}). If the spatial region used to measure the velocity profile does not include faint emission or includes an excess number of "background" pixels, the returned flux estimate will underestimate or be a dilution of the true integrated flux.

Having ascertained the integrated line flux, the program proceeds to determine the spatial line moments maps (flux, line-of-sight velocity, and line width) by fitting Gaussian functions to the observed line profiles at each spatial location in the fitting region. For better line-profile fitting, the program bins the constructed flux density map using Voronoi tesselation (Cappellari & Copin 2003) to achieve roughly equal spectral S/N in all bins. This program allows for iterative changing of the threshold S/N to ensure sufficiently smooth line moment maps while fully spatially sampling the brightest line features.

The final visualization this program creates is a position-velocity diagram (PVD). Experience

has shown that rapidly rotating gas about a central BH tends to be of low surface brightness, and unresolved/marginally resolved Keplerian upturns are best identified in PVDs. As the flux maps of many interacting systems tend to be chaotic (and in general clean disk rotation, e.g., seen in our ALMA ETG observing project, is an exception), many of the galaxies and/or emission line systems observed with ALMA may have no clear major/minor axes. The user is therefore prompted to select an axis from a graphical interface; the program then extracts the PVD slice from the data cube.

Lastly, the program compiles these four visualizations (collapsed flux density map, velocity profile, PVD, and line moment maps) into a single image for quick inspection and comparison with other targets. Additional essential information, such as the synthetic beam angular size, RMS sensitivity limit in the native channel binning, and estimated total line flux are included in the finished archival modeling product. The underlying data for these visualizations is also saved in text and FITS files for later incorporation into a kinematic atlas of galaxies observed with ALMA.

A.2 Atlas Data Products

Shown below are a few of the best archival data products for a variety of late and early-type galaxies, as well as those in the late stages of merging, created by this author (with the collaboration of Dilan Patel). In addition to exploring multiple rotational CO transitions (e.g., CO(1-0): Figure A.3; CO(6-5): Figure A.2), dense gas tracers (e.g., CN: Figure A.4) and CO isotopologues (e.g., ^{13}CO: Figure A.13) are sometimes sufficiently bright to detect and map. Occasionally, absorption line features are detectable in front of bright nuclear emission (e.g., Figures A.6 and A.12) after post-pipeline continuum subtraction.

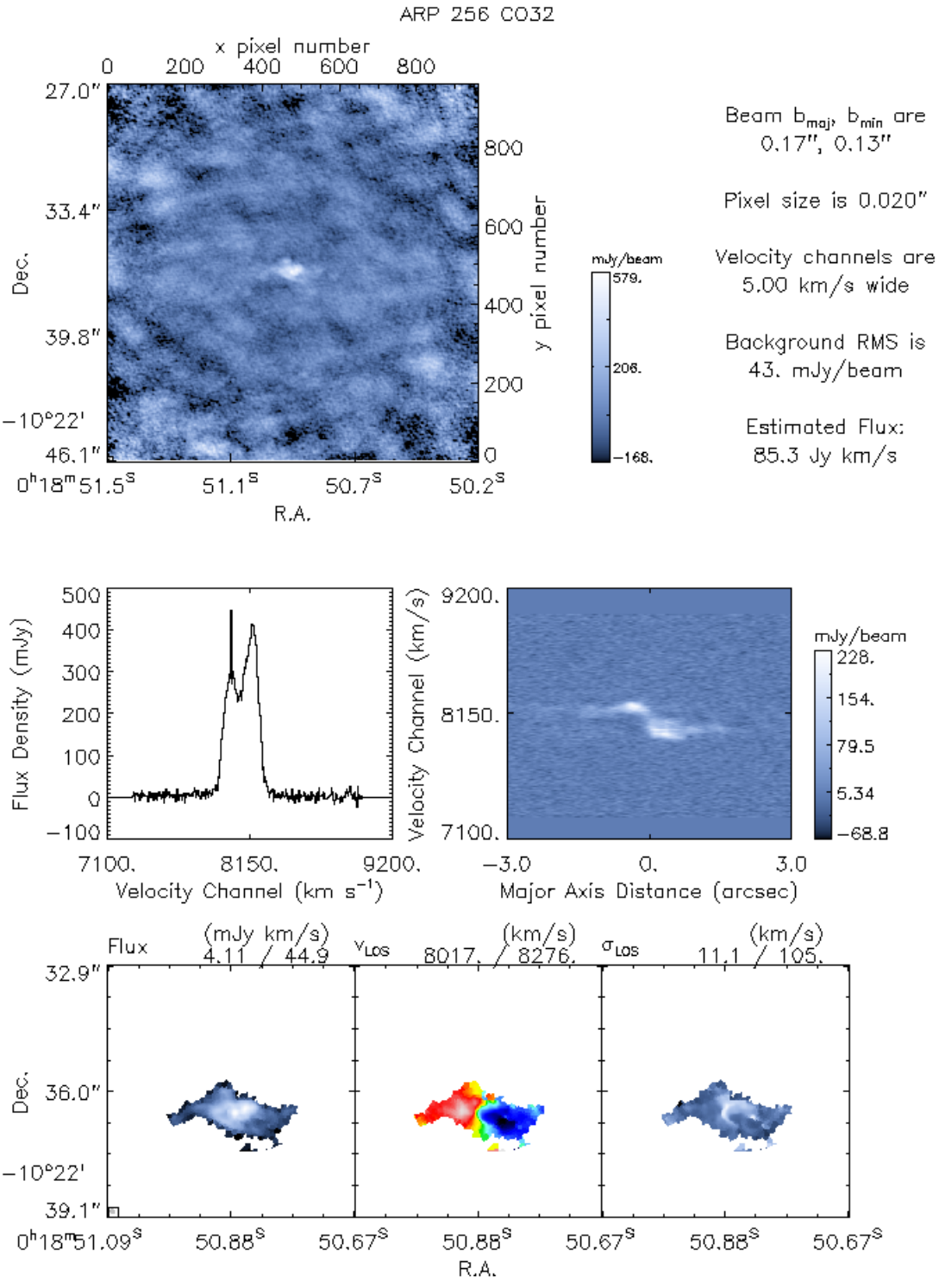

Figure A.1 Arp 256 CO(3-2) archive data visualizations from Project 2013.1.00814.S

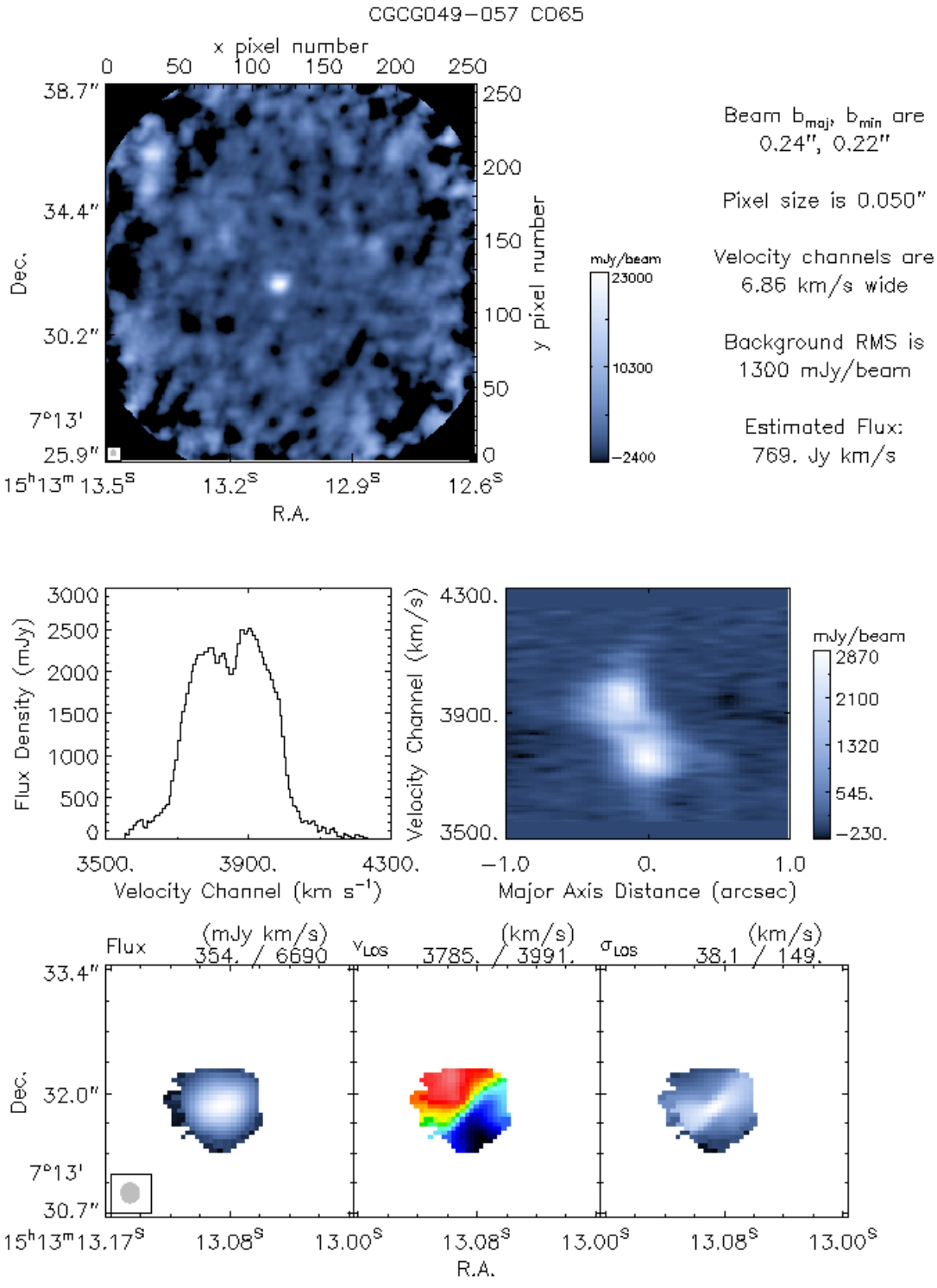

Figure A.2 CGCG049-057 CO(6-5) archive data visualizations from Project 2013.1.00524.S

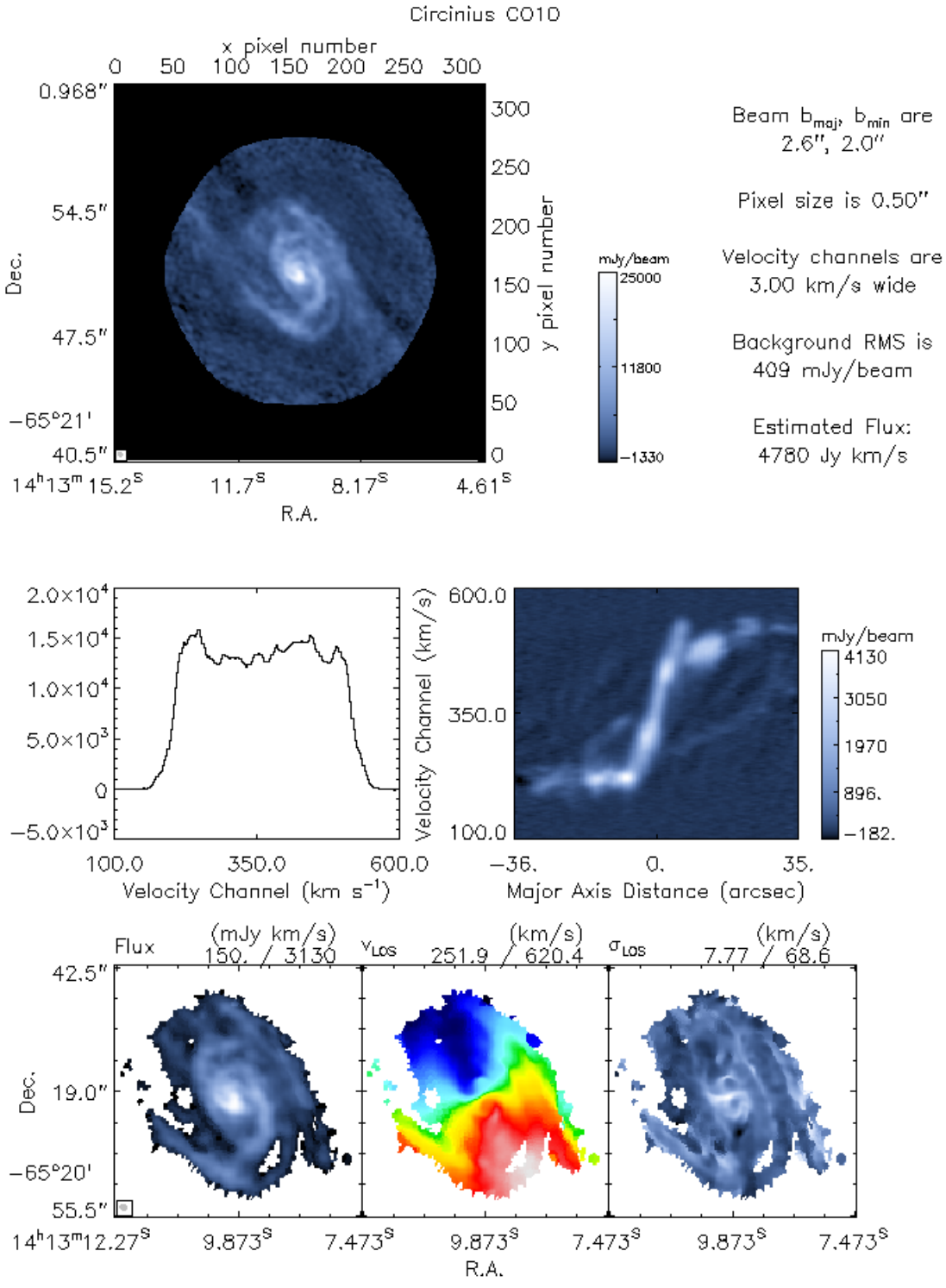

Figure A.3 Circinus CO(1-0) archive data visualizations from Project 2013.1.00247.S

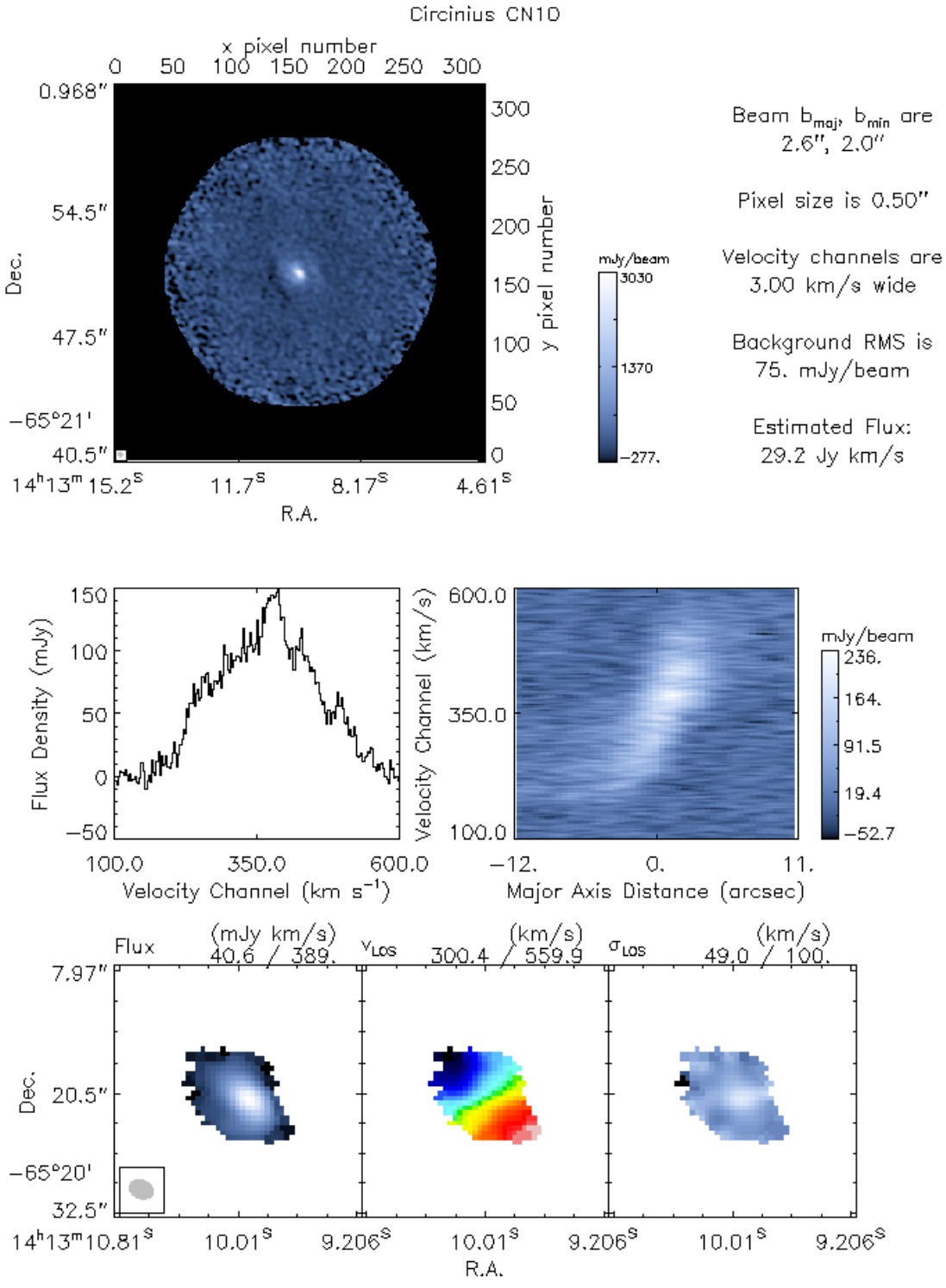

Figure A.4 Circinus CN(1-0) archive data visualizations from Project 2013.1.00247.S

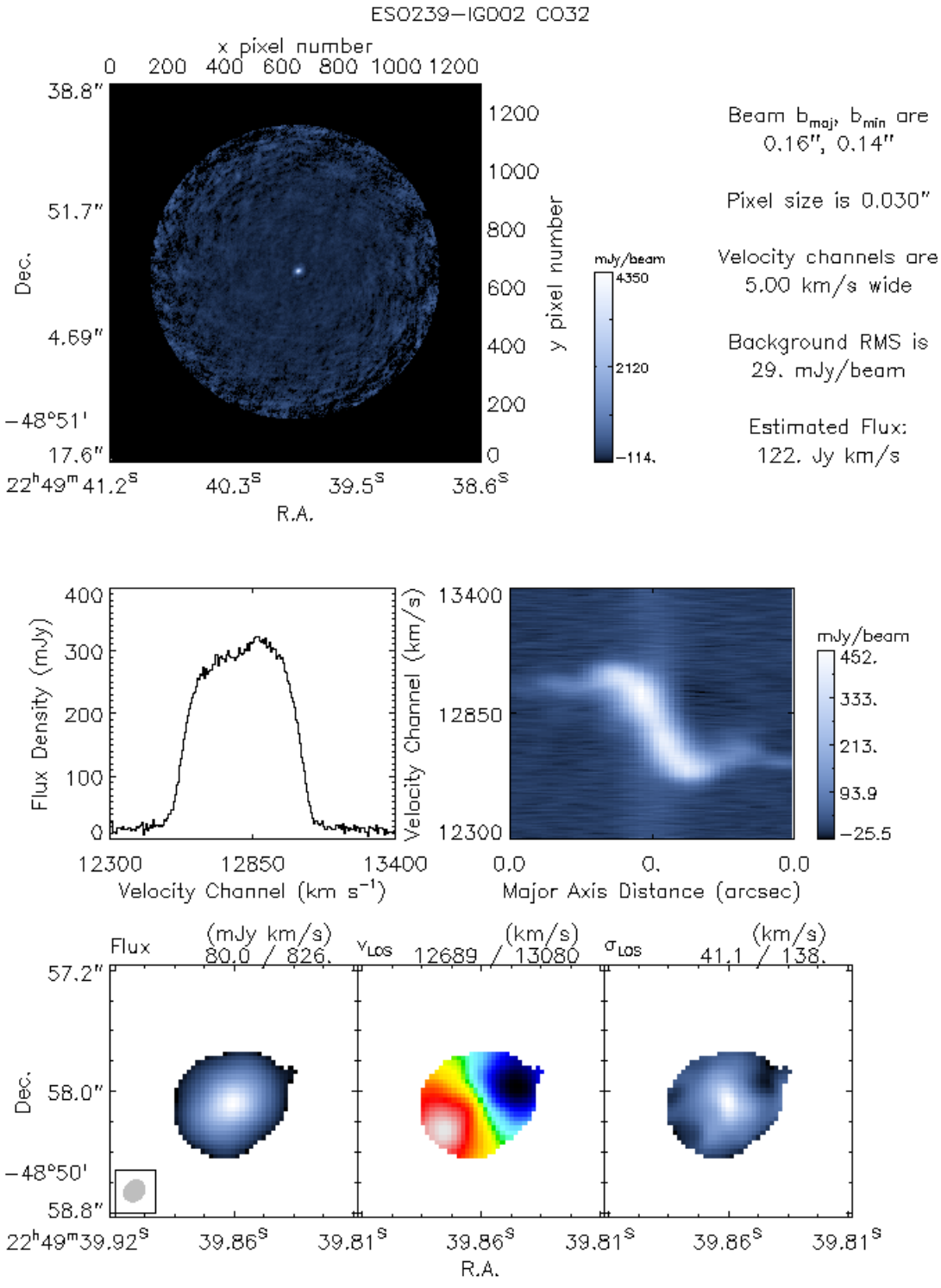

Figure A.5 ESO239-IG002 CO(3-2) archive data visualizations from Project 2013.1.00814.S

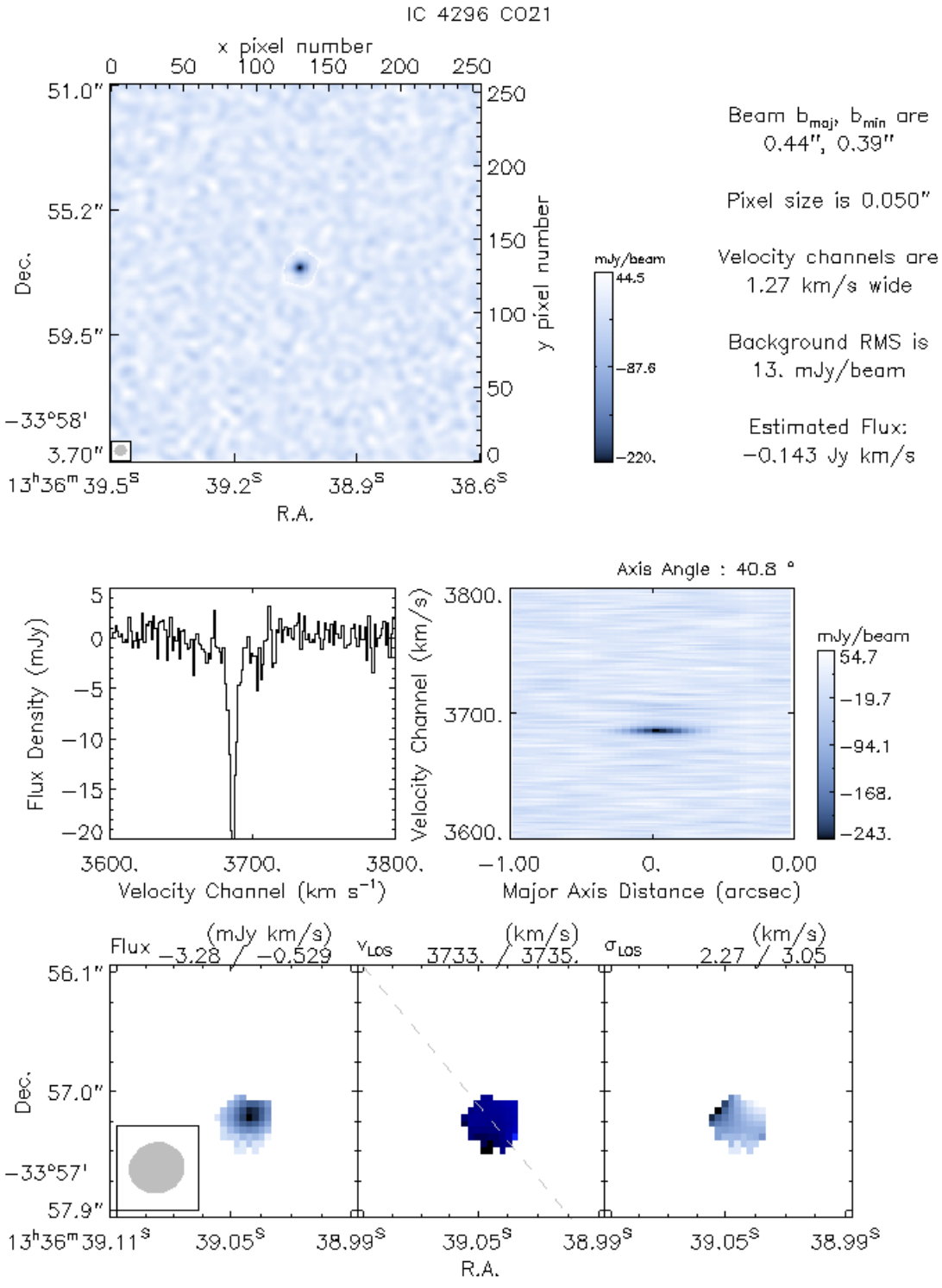

Figure A.6 IC4296 CO(2-1) archive data visualizations from Project 2013.1.00229.S

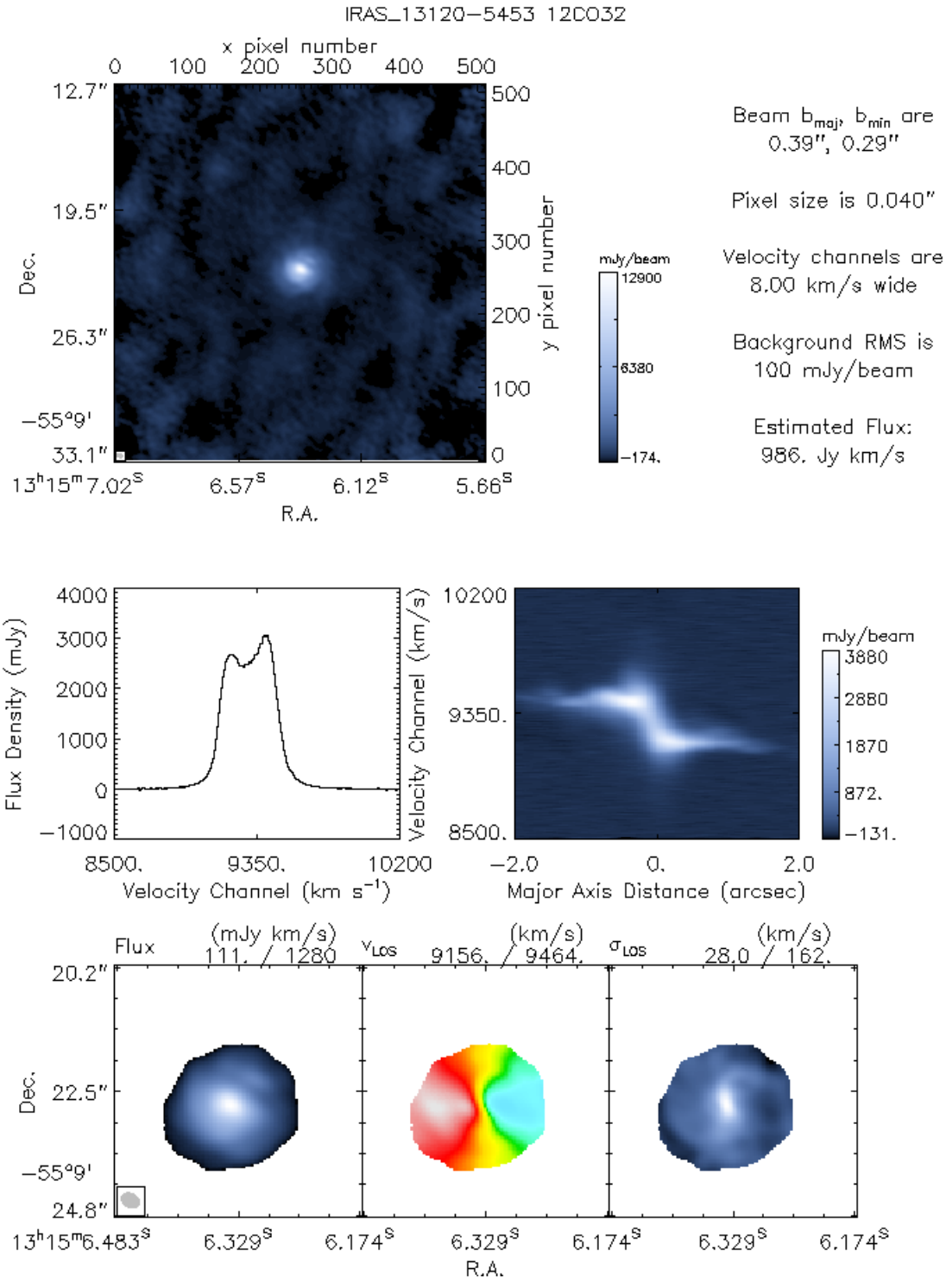

Figure A.7 IRAS 13120-5453 CO(3-2) archive data visualizations from Project 2013.1.00379.S

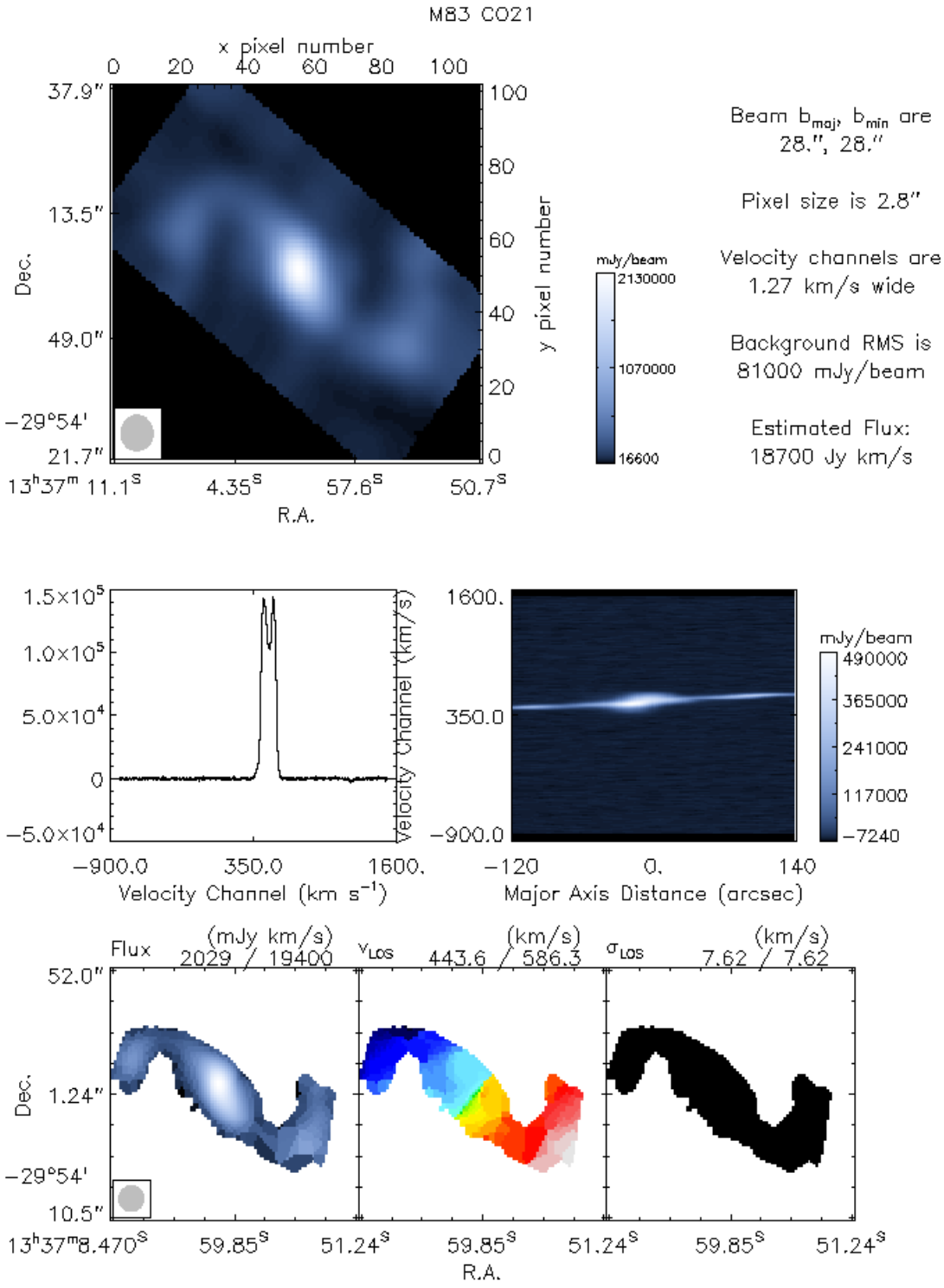

Figure A.8 M83 CO(2-1) archive data visualizations from Project 2013.1.01161.S

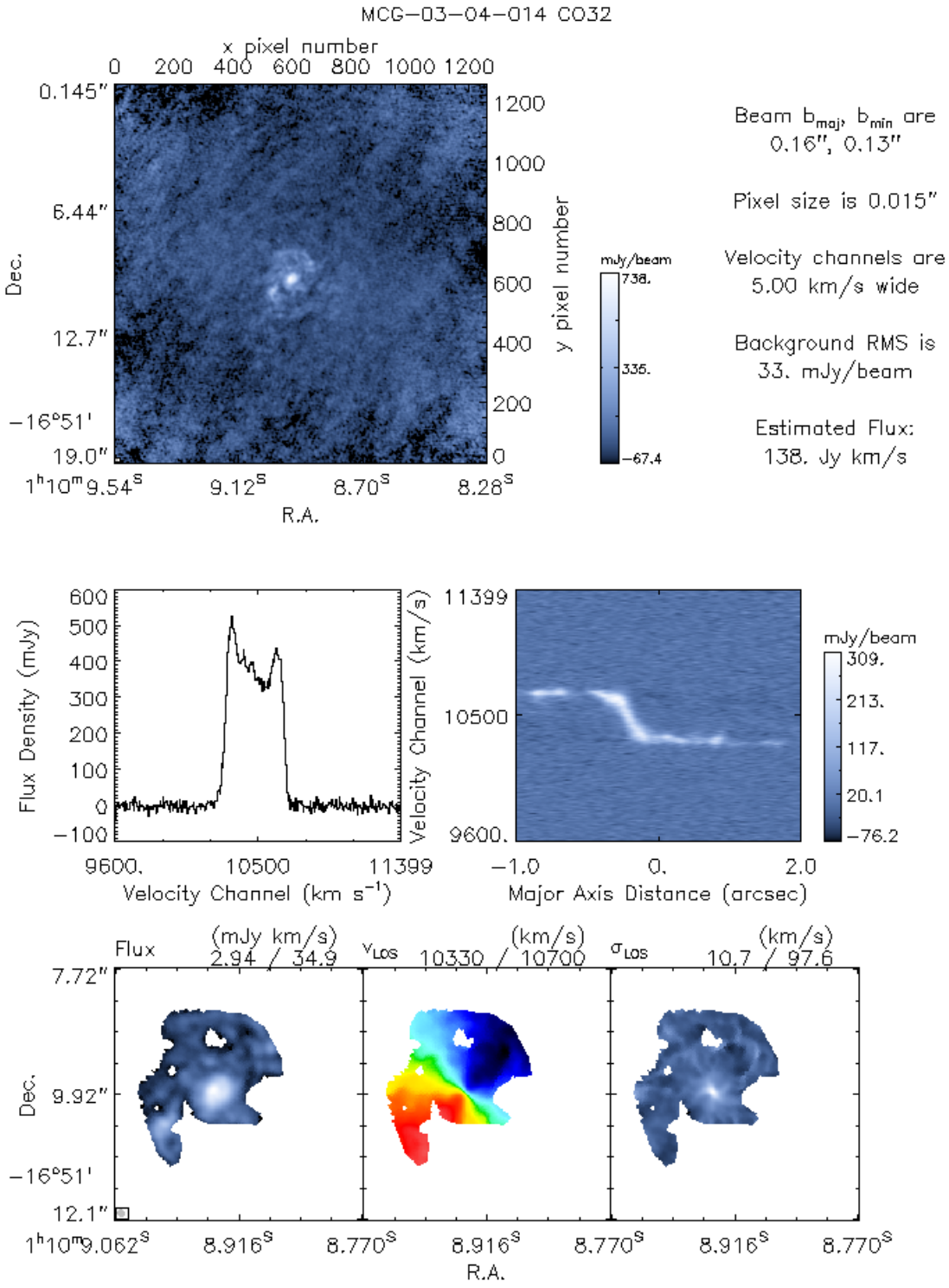

Figure A.9 MCG-03-04-014 CO(3-2) archive data visualizations from Project 2013.1.01165.S

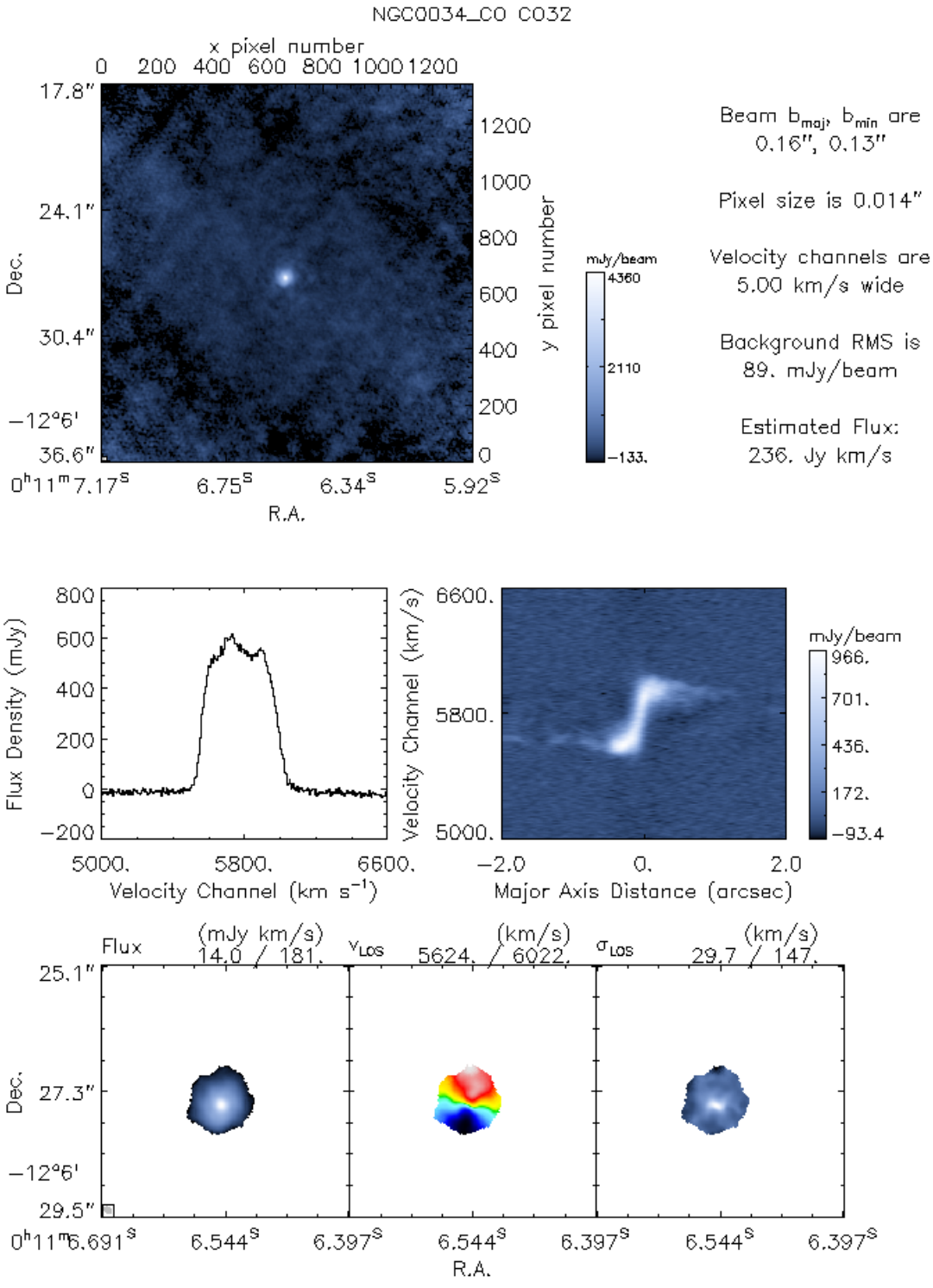

Figure A.10 NGC 34 CO(3-2) archive data visualizations from Project 2013.1.00814.S

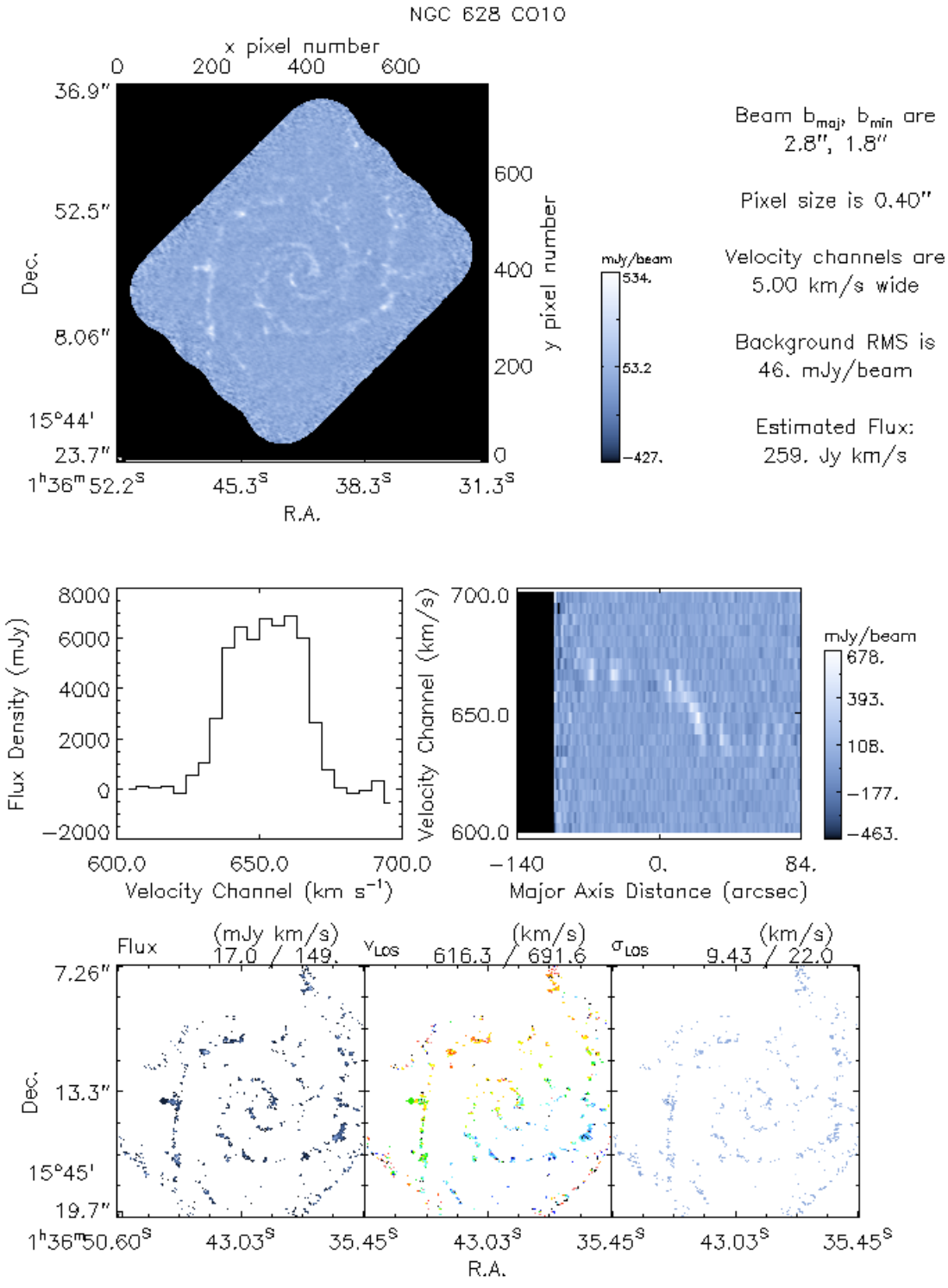

Figure A.11 NGC 628 CO(1-0) archive data visualizations from Project 2013.1.00532.S

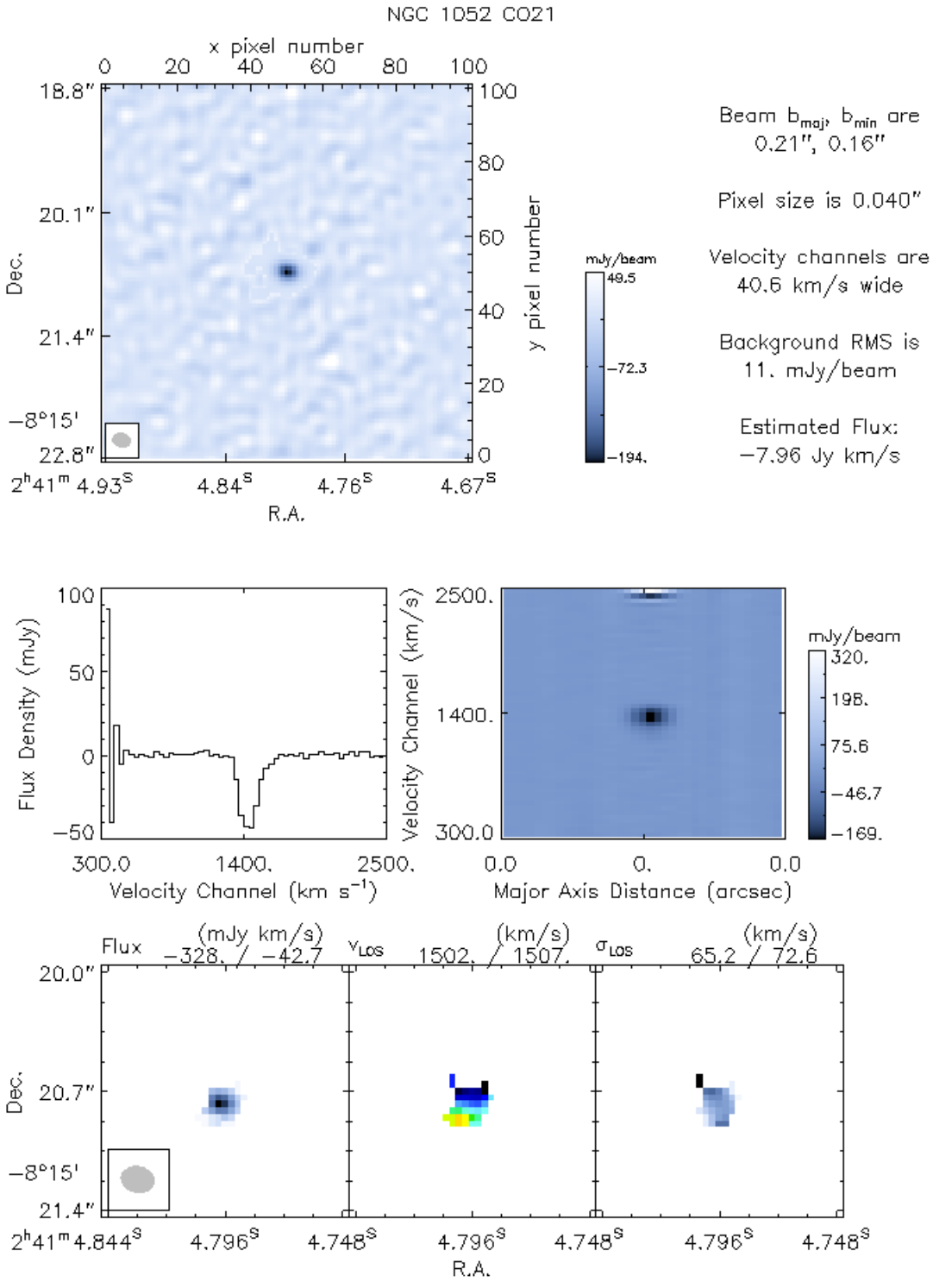

Figure A.12 NGC 1052 CO(2-1) archive data visualizations from Project 2013.1.01225.S

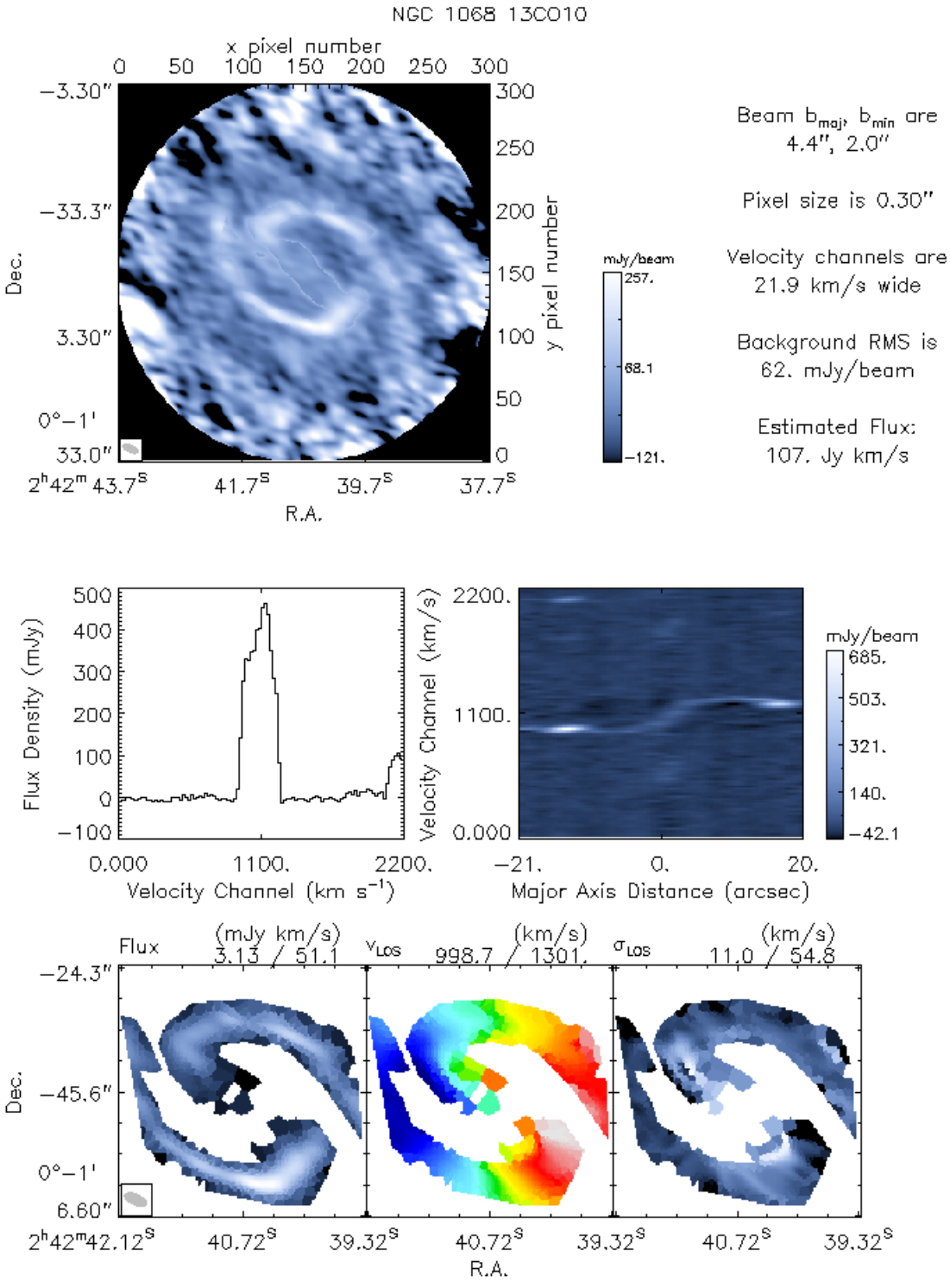

Figure A.13 NGC 1068 ^{13}CO(1-0) archive data visualizations from Project 2013.1.00060.S

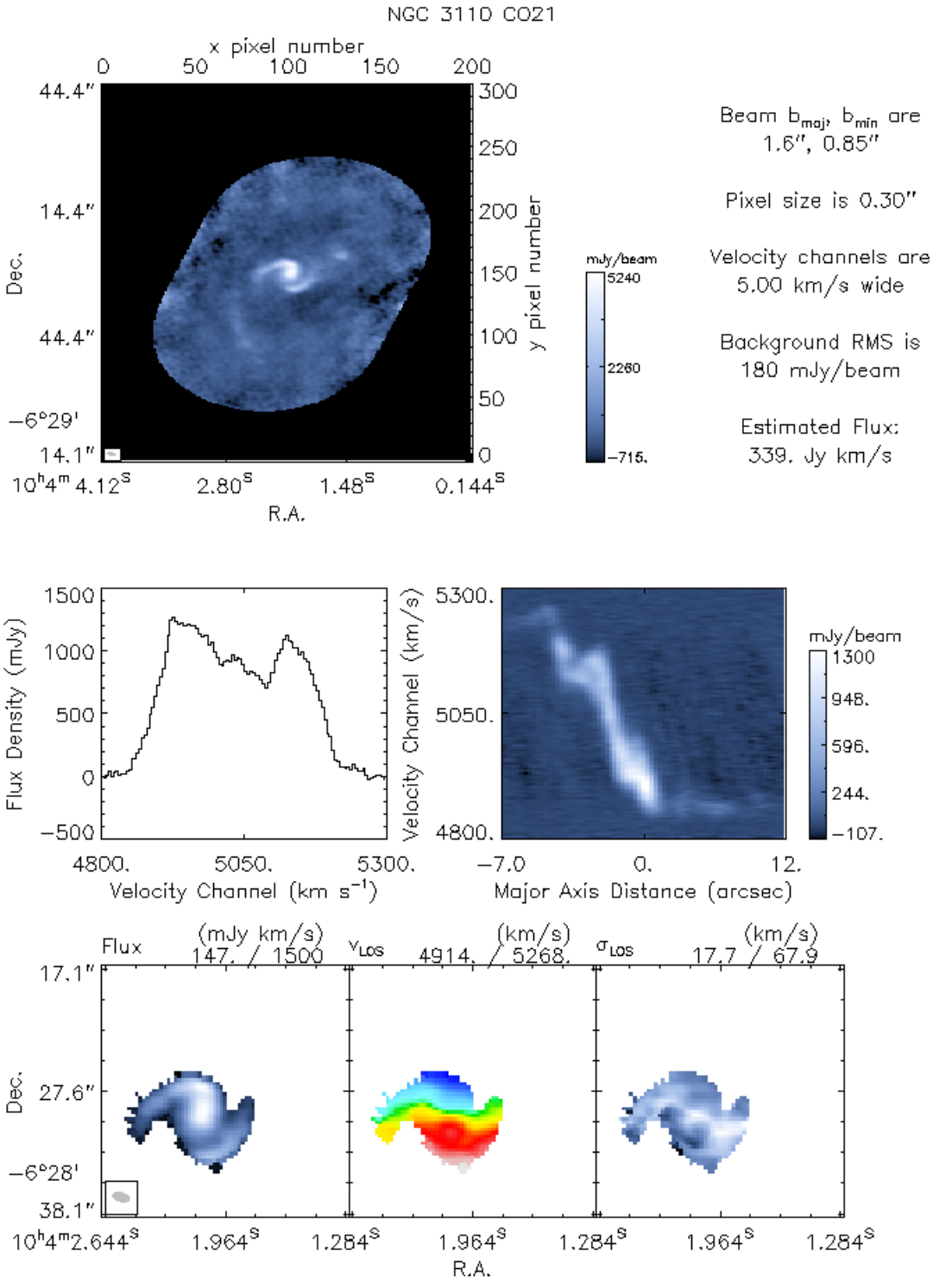

Figure A.14 NGC 3110 CO(2-1) archive data visualizations from Project 2013.1.01172.S